ON POROELASTIC AND PORO-ELASTO-PLASTIC HERTZIAN CONTACT PROBLEMS

A Thesis
Presented to
The Academic Faculty

by

Ming Liu

In Partial Fulfillment
of the Requirements for the Degree
Doctor of Philosophy in the
School of Civil and Environmental Engineering

Georgia Institute of Technology
April 2021

ON POROELASTIC AND PORO-ELASTO-PLASTIC HERTZIAN CONTACT PROBLEMS

Approved by:

Dr. Haiying Huang, Advisor
School of Civil and Environmental Engineering
Georgia Institute of Technology

Dr. Yuhang Hu
School of Mechanical Engineering
Georgia Institute of Technology

Dr. David Frost
School of Civil and Environmental Engineering
Georgia Institute of Technology

Dr. Paul Mayne
School of Civil and Environmental Engineering
Georgia Institute of Technology

Dr. Lauren Stewart
School of Civil and Environmental Engineering
Georgia Institute of Technology

Dr. Susan Burns
School of Civil and Environmental Engineering
Georgia Institute of Technology

Date Approved: 04/21/2021

ACKNOWLEDGEMENTS

The author wants first to express his deep gratitude to Dr. Haiying Huang. Not only the subjects for all chapters were suggested by Dr. Huang, but her constant guidance and help were also essential for carrying out these studies. Her inspiration and warm personality have won the author's highest respect and love.

The author would like to thank Drs. Paul Mayne, Yuhang Hu, Lauren Stewart, David Frost and Susan Burns for serving on his committee. Their comments and suggestions have improved the quality of this work.

During the preparation of this thesis, the author was very much benefited by the life stories of Xuesen Qian and John Nash. Their attitudes towards research and their perspectives on leading a valuable life have greatly motivated him during the hard time.

The author wants to thank his wife, Xin Wen, for her love and support; his dog, Pepper, for the companionship and comfort; his parents and parents in-law, for their support and encouragement; and his prior advisor, Dr. Yan Jin from China University of Petroleum Beijing, for introducing him to the field of geomechanics.

Partial financial support from Schlumberger and Halliburton and the communication opportunities with Exxonmobil Upstream Research Company are gratefully acknowledged.

Contents

List of Tables

List of Figures

SUMMARY

Contact between a rigid sphere and a linear poroelastic or poro-elasto-plastic half-space is examined in this work. The process of indentation by a rigid tool has been widely studied for its versatility as an experimental methodology to probe constitutive properties of materials of various kinds across multiple scales. Recently, spherical indentation has been applied to characterize poroelasticity of fully saturated porous media such as polymeric gels and hydrated bones via either displacement- or force-controlled tests. In principle, for a step loading test, if the solid and fluid constituents are incompressible, elastic constants can be determined from the undrained and drained responses based on the classical Hertzian contact solution, while the hydraulic diffusivity can be obtained from the transient response by matching the measured indentation force or displacement as a function of time against a master curve. Poroelastic contact problems have their roots in geomechanics and geotechnical engineering owing to our interests in ground settlement behaviors due to surface loading. After the theoretical frameworks for soil consolidation were laid out by Terzaghi and Biot, significant contributions have been made in developing general methods of solution as well as in treating particular cases such as strip loading or punch indentation in a consolidating half-space. Motivated by these theoretical and experimental advances, we set our research objectives to investigate the feasibility of poroelastic spherical indentation as a testing technique for determining the hydraulic diffusivity for geomaterials through an integrated theoretical and numerical approach.

With the aid of a variety of mathematical techniques, fully coupled theoretical solutions for spherical indentation into a poroelastic half-space with three distinct cases of surface drainage conditions when the indenter is subjected to step displacement loading are first derived. The solutions are obtained within the framework of Biot's theory using the McNamee-Gibson displacement function method. Specifically, we overcome the mathematical difficulties associated with evaluating integrals with highly oscillatory kernels by using alternative integral representations with exponentially decaying functions in the kernels. Special functions, such as the modified Struve and Bessel functions, and the method of contour integration are utilized to

aid the removal of the oscillation. Moreover, the method of successive substitution, instead of the method of quadrature previously used in the literature, is employed to solve the Fredholm integral equation of the second kind to improve solution accuracy. The theoretical analyses show that the normalized indentation force relaxation has a relatively weak dependence on a single derived material constant ω only. Master curves of indentation force relaxation can be constructed by fitting the full solution with an elementary function for convenient use of poroelasticity characterization in the laboratory.

A hydromechanically coupled finite element method (FEM) algorithm following a mixed continuous Galerkin formulation for displacement and pore pressure and incorporating a penalty-based frictionless contact scheme is constructed for modeling of spherical indentation in a poro-elasto-plastic medium in order to examine how factors such as plastic deformation, depth of penetration and loading rate affect the indentation responses. The fully saturated porous medium is assumed to be isotropic and elasto-perfectly plastic, obeying a Drucker-Prager yield criterion with an associative or non-associated flow rule. The Newton-Raphson method with the tangent stiffness scheme is adopted to deal with plasticity in the solid skeleton. A stabilization scheme, which permits equal-order interpolation for the displacement and pore pressure fields and suppresses pore pressure oscillation in the incompressible or nearly incompressible limit, is incorporated in this FEM algorithm.

Numerical simulations of poroelastic spherical indentation under step displacement loading with or without ramping are conducted to show that the normalized force relaxation responses from the numerical simulations can be very well captured by the theoretical solutions when the indentation strain and ramping duration are relatively small. Numerical results confirm that the normalized force relaxation behaviors are indeed affected by material properties through the material constant ω only. For indentation in a poro-elasto-plastic medium, it is shown that even though plasticity could occur immediately at the undrained limit, if the indentation strain and material strength are such that the maximum plastic strain remains at the location of the onset of plasticity as predicted by the poroelastic solutions and the plastic strain does not accumulate during the transient period, the normalized force relaxation behavior could still be

approximated as poroelastic.

Finally, a combined theoretical and numerical analysis is performed for poroelastic spherical indentation under step force loading. Results show that though the normalized transient displacement response is also affected by material properties through ω only, compared with the step displacement loading cases, the dependence on ω is relatively stronger under step force loading, indicating that the force-controlled poroelastic indentation test may be less reliable than the displacement-controlled test.

1 INTRODUCTION

1.1 Motivation and Objectives

The process of indentation by a rigid tool has been widely studied for its versatility as an experimental methodology to probe constitutive properties of materials of various kinds across multiple scales (Johnson, 1987; Cook and Pharr, 1990; Lawn, 1993, 1998; Marshall et al., 2015; Argatov and Mishuris, 2018). Hardness and elastic modulus of a material can be determined from the indentation force-displacement response, while mode I fracture toughness can be measured from the size of a well-defined crack system as a function of the indentation force. The advantages of the indentation tests are that they are non-destructive and relatively quick and easy to perform.

Recently, spherical indentation has been applied to characterize poroelasticity of fully saturated porous media such as polymeric gels and hydrated bones via either displacement- or force-controlled tests. In a displacement-controlled load relaxation test (see Fig. 1.1), the indenter is pressed instantaneously to a fixed depth and held until the indentation force approaches a horizontal asymptote (Hu et al., 2010, 2011, 2012; Chan et al., 2012; Kalcioglu et al., 2012), whereas in a step force loading or ramp-hold test, the indentation force is kept constant after reaching a prescribed level (Galli and Oyen, 2008, 2009; Oyen, 2008). In theory, for a step loading test, if both the fluid and solid phases are considered incompressible, elastic constants can be determined from the undrained and drained responses based on the classical Hertzian contact solution, while the hydraulic diffusivity can be obtained from the transient response by matching the measured indentation force or displacement as a function of time against a master curve. Such master curves for various indenter shapes under step displacement loading have been previously constructed through finite element simulations (Hu et al., 2010) and also semi-analytically for spherical indentation with step force loading (Agbezuge and Deresiewicz, 1974; Oyen, 2008). After the indentation force or displacement is normalized by the undrained and drained asymptotes, these master curves are generally fitted by elementary functions. Possibility of using spherical indentation to determine the hydraulic diffusivity was first suggested by

Agbezuge and Deresiewicz (1974). They outlined theoretical treatment for indentation with a rigid sphere subjected to a constant force for three distinct surface drainage conditions, namely, case I of a permeable indenter on a permeable half space, case II of an impermeable half space and case III of an impermeable indenter on a permeable half space. In literature, in addition to step loading tests, there are other types of indentation experiments with different loading methods to characterize poroelastic material. A literature review of the detailed experimental procedures is given in Section 1.2.

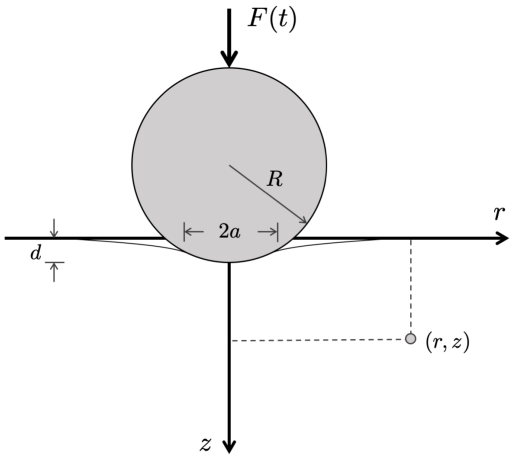

Figure 1.1: Schematic of spherical indentation.

Poroelastic contact problems have their roots in geomechanics and geotechnical engineering owing to our interests in ground settlement behaviors due to surface loading. After the theoretical frameworks for soil consolidation were laid out by Terzaghi (1943) and Biot (1941), significant contributions have been made in developing general methods of solution (Biot, 1956; De Josselin De Jong, 1957; McNamee and Gibson, 1960a,b; Schiffman and Fungaroli, 1965; Verruijt, 1971; Chiarella and Booker, 1975; Detournay and Cheng, 1993) as well as in treating particular cases such as strip loading or punch indentation in a consolidating half space (De Josselin De Jong, 1957; McNamee and Gibson, 1960a,b; Gibson and Mcnamee, 1963; Jana, 1965; Schiffman and Fungaroli, 1965; Gibson et al., 1970; Schiffman and Fungaroli, 1973; Agbezuge and Deresiewicz, 1974; Chiarella and Booker, 1975; Agbezuge, 1975, 1976; Deresiewicz, 1979;

Gaszynski and Szefer, 1978; Booker and Small, 1985; Vardoulakis and Harnpattanapanich, 1986; Harnpattanapanich and Vardoulakis, 1987; Mak et al., 1987; Selvadurai and Yue, 1994; Yue and Selvadurai, 1994, 1995; Lan and Selvadurai, 1996; Chen et al., 2005a,b; Singh et al., 2009; Chen and Abousleiman, 2010; Verruijt, 2013; Kim and Selvadurai, 2016; Selvadurai and Samea, 2020; Paria, 1957; Sanyal, 1972; Singh and Rani, 2006; Singh et al., 2007). Results from these theoretical works are however rather cumbersome since mathematical issues such as evaluating integrals with kernels that oscillate rapidly and solving the Fredholm integral equations of the second kind were not treated satisfactorily.

Hydraulic diffusivity, or the coefficient of consolidation in the context of Terzaghi's consolidation theory (Terzaghi, 1943), is one of the most important properties of geomaterials such as low-permeability rocks and fine-grained soils since it governs the time rate of deformation and pore pressure dissipation in hydromechanically coupled problems. For fully saturated soils, where the fluid and solid phases can be considered as incompressible, linear poroelastic response can be fully determined if the drained elastic constants and the coefficient of consolidation are known. Consolidation test in an oedometer or a triaxial cell is the current standard laboratory testing method for measuring the coefficient of consolidation. The advantage of these test configurations is that they correspond to a well-defined one-dimensional boundary value problem as described by Terzaghi's consolidation theory (Terzaghi, 1943; Olson, 1986). In both the conventional setups and variations such as the Rowe cell (Rowe and Barden, 1966), the test duration scales according to $t \sim H^2/c$, where H is the maximum length of the drainage path and c is the coefficient of consolidation. The testing time could be rather lengthy for a fine-grained soil.

For rocks, since bulk modulus of the fluid and solid phases could be comparable to that of the skeleton, two additional mechanical constants, the Biot coefficient α and the storage coefficient S, are also needed in order to fully describe the poroelastic response. Hydraulic

diffusivity is related to the hydraulic and mechanical properties through,

$$c = \frac{\kappa}{\mu} \frac{K + \frac{4}{3}G}{\alpha^2 + \left(K + \frac{4}{3}G\right) S} \tag{1.1}$$

where κ is the permeability; μ is the fluid viscosity; and K and G are the skeleton bulk and shear modulus, respectively.

In the laboratory, mechanical constants such as K, G, α and S can be determined using a combination of the drained, undrained and unjacketed tests under triaxial conditions (Hart and Wang, 1995). Meanwhile, transient pore pressure test (Hart, 2000) and the pressure oscillation method (Kranz et al., 1990) have been used to measure the hydraulic diffusivity of rocks. If the fluid viscosity is known, measuring the hydraulic diffusivity provides an indirect way to determine the permeability.

Rock permeability is generally measured using the classical steady state flow measurement, transient pressure pulse test (Brace et al., 1968) or pressure oscillation method (Kranz et al., 1990). Over the last few years, an isolated-cell pressure decay method utilizing crushed samples has also been developed specifically for tight shales (Suarez-Rivera et al., 2012). Nevertheless, a recent benchmark study on Grimsel granodiorite with participation from 24 laboratories around the world shows that there are large scatters in the measured permeability, depending on the specific methods, procedures and techniques (David et al., 2018a,b). Inconsistency in the results was also found in benchmark studies for shale (Tinni et al., 2012).

Developing an additional and potentially more efficient means to determine the hydraulic diffusivity, and indirectly the intrinsic permeability, through poroelastic indentation could therefore be of great value. As have been shown in Kalcioglu et al. (2012), a poroelastic indentation test could offer a few unique advantages. Firstly, the testing duration can be greatly shortened with the proper choices of the indenter size and the depth of penetration, since the testing time now scales according to $t \sim a^2/c$, where a is the contact radius. Secondly, both the mechanical and hydraulic properties can be measured from a single test. Finally, since the methodology is based on continuum mechanics and is not limited to a particular scale, the

testing method could in principle be applied to probe material properties at multiple scales, potentially bridging the gaps from micro-scale to macro-scale and *in situ*.

Application of poroelastic indentation for geomaterial characterization has never been explored. Motivated by these prior theoretical and experimental advances, we set our research objectives to investigate the feasibility of poroelastic indentation as a testing technique for determining the hydraulic diffusivity for geomaterials through an integrated theoretical and numerical approach. The scope of this research includes:

- Establishing a theoretical framework for poroelastic spherical indentation into a half space with the compressibility of constituents taken into account. We attempt to construct theoretical solutions for both step displacement and step force loading for the three distinct surface drainage conditions.

- Developing a fully coupled poro-elasto-plastic finite element method (FEM) algorithm and incorporating a frictionless contact scheme.

- Conducting numerical analysis to identify the parameter space where the material response can be appropriately described by the theoretical solutions and is not strongly affected by factors such as plastic deformation, indenter size, depth of penetration and loading rate.

1.2 Experimental Development

Depending on how the surface load is applied, the experimental approaches can be classified into four groups: step displacement loading (Mattice et al., 2006; Galli and Oyen, 2009; Galli et al., 2009; Hu et al., 2010; Han et al., 2011; Chan et al., 2012; Hu et al., 2012; Kalcioglu et al., 2012; Moeendarbary et al., 2013; Wahlquist et al., 2017; Islam and Oyen, 2021), step force loading (Bembey et al., 2006; Delavoipière et al., 2016), oscillatory loading (Han et al., 2011; Lai and Hu, 2017, 2018) and ramp loading (Esteki et al., 2019).

Different types of instruments have been used to conduct these experiments at various scales. Conventional load frames have generally been utilized to conduct the tests at the

macro-scale (mm) (Mattice et al., 2006; Hu et al., 2010, 2012; Kalcioglu et al., 2012; Islam and Oyen, 2021). At the nano- to micro-scale, commercial instrumented nanoindentation systems (Bembey et al., 2006; Galli et al., 2009; Wahlquist et al., 2017) and the atomic force microscope (AFM) (Han et al., 2011; Kalcioglu et al., 2012; Moeendarbary et al., 2013; Delavoipière et al., 2016; Lai and Hu, 2017, 2018) have both been used. The primary difference between the instrumented nanoindentation system and AFM is that the former adopts a step motor to directly actuate an indenter into the sample, while the latter actuates the tip indirectly via a calibrated cantilever (Oyen, 2014). The AFM system is thus easier to optimize for testing different classes of materials by adjusting the cantilever stiffness.

1.2.1 Step Displacement Loading Method

Feasibility of using step displacement loading for poroelastic characterization was demonstrated by Hu et al. (2010). Their experiment was conducted with a conical aluminum indenter with a half apex angle $\theta = 70°$ and a saturated alginate hydrogel. Indentation force relaxation was then recorded as a function of time. To minimize the effect of the initial loading rate, the ramping time is set to be much shorter than the relaxation time. Poroelastic constants were determined by overlapping the experimental data with the master curve for a conical indenter (see Eqs. 1.2-1.4), derived using finite element simulations and dimensional consideration.

The undrained and drained force asymptotes, $F(0)$ and $F(\infty)$, can be expressed as,

$$F(0) = \frac{8}{\pi} G d^2 \tan\theta \tag{1.2}$$

$$F(\infty) = \frac{4 G d^2 \tan\theta}{\pi (1-\nu)} \tag{1.3}$$

where d is the applied step indentation depth and ν the Poisson's ratio. The relationship obtained from numerical simulations for the normalized indentation force $F_n(t_*)$ as a function

of dimensionless time, $t_* = tc/a^2$, can be expressed as,

$$F_n(t_*) = \frac{F(t_*) - F(\infty)}{F(0) - F(\infty)} = 0.493 \exp\left(-0.822\sqrt{t_*}\right) + 0.507 \exp\left(-1.348 t_*\right) \tag{1.4}$$

Here, both the fluid and solid phases are considered incompressible. Shear modulus and Poisson's ratio can be determined from $F(0)$ and $F(\infty)$, respectively, while the hydraulic diffusivity can be determined by matching the experimental data with $F_n(t_*)$. Finite element simulations show that the normalized transient force response is not sensitive to the change of any material constants such as the Poisson's ratio, suggesting that the master curves are universal applicable. Master curves for other indenter shapes have also been reported in their study.

For fluid-filled porous media, both viscoelasticity and poroelasticity can result in indentation force relaxation. These two relaxation mechanisms are, however, distinct and can be distinguished from each other by their respective time scaling. Viscoelastic relaxation time is associated with the viscosity and elastic modulus of the material and is therefore independent of any length scale. This is in contrast to the quadratic relation between the relaxation time and the contact radius or indentation depth in poroelastic indentation ($t \sim a^2/c$).

Benefit of conducting the experiment at a smaller scale for significant time saving was demonstrated by Kalcioglu et al. (2012) using spherical indentation in PAAm hydrogel. Hydraulic diffusivity of the hydrogel is around 1.7×10^{-10} m^2/s. The testing duration for the case with an indenter of radius 1 cm at a depth of 100 μm is about 4.9×10^3 s, while it took less than 1 s for the case with an indenter of radius 22.5 μm at a depth of 4 μm. Favorable comparison was achieved between the two scales.

Spherical indentation into a poroelastic thin film was considered in Chan et al. (2012). Equations for the master curves were modified to account for the effect of finite thickness.

1.2.2 Step Force Loading Method

Step force loading test was conducted in Bembey et al. (2006) by pressing a spherical indenter into hydrated bones. Displacement of the indenter was then recorded as a function of time.

Their experimental data were originally used for a viscoelastic analysis. The transient response was later recognized as a result of poroelasticity and the data were then reanalyzed by Oyen (2008). The master curve constructed by fitting the semi-analytical solution from Agbezuge and Deresiewicz (1974) was used in Oyen (2008), i.e.,

$$d_n(t_*) = \frac{d(\infty) - d(t_*)}{d(\infty) - d(0)} = 0.928 - 0.928\left[1 + \left(\frac{t_*}{0.772}\right)^{2.0837}\right]^{-1} \tag{1.5}$$

where the dimensionless time is defined according to $t_* = ct/a^2(t)$, with $a(t) = \sqrt{Rd(t)}$; $d_n(t_*)$ is the transient indentation displacement normalized by its undrained and drained asymptotes $d(0)$ and $d(\infty)$,

$$d(0) = \left(\frac{3F}{16G\sqrt{R}}\right)^{\frac{2}{3}} \tag{1.6}$$

$$d(\infty) = \left[2(1-\nu)\right]^{\frac{2}{3}} d(0) \tag{1.7}$$

where F is the applied step force and R is the sphere radius. Shear modulus and the Poisson's ratio can be determined from $d(0)$ and $d(\infty)$, and the hydraulic diffusivity from matching the experimental data with Eq. 1.5. It should be noted that the semi-analytical solution in Agbezuge and Deresiewicz (1974) was obtained assuming $\nu = 0$. In addition, an assumption that treats the contact pressure as a slowly varing function of time is made to make the problem amenable to mathematical treatment. It is however unclear to us whether the assumption is legitimate or not and whether the result for $\nu = 0$ is also applicable to other cases with $\nu > 0$. This problem will be revisited in Section 7.3 using a combined theoretical and numerical approach.

Since it is rather difficult to apply the idealized step loading, a ramp-hold test was suggested by Galli and Oyen (2009). Instead of a single master curve, a database was constructed based on numerical simulations assuming various loading rates.

Application of the step loading test to thin hydrogel films was investigated by Delavoipière et al. (2016), where an asymptotic contact model (Ateshian et al., 1994; Delavoipière et al., 2016) was employed as the theoretical base.

1.2.3 Oscillatory Loading Method

An oscillatory loading method for spherical, conical and cylindrical indenters has been developed by Lai and Hu (2017). In this method, an indenter is first pressed to a fixed depth d_0. After the indentation force reaches a plateau F_0, an oscillation phase then follows. The indentation displacement is prescribed to be a sinusoidal function with a small amplitude δ, i.e., $d = d_0 + \delta \sin(\omega t)$. The corresponding indentation force can then be expressed as $F(t) = F_0 + F_a \sin(\omega t + \Delta)$, where ω and Δ denote the angular frequency and phase lag, respectively. A frequency sweep is performed to obtain the relationship for the frequency ω as a function of Δ. The peak frequency ω_c and the phase lag Δ_c were used to determine the material constants according to,

$$\nu = 0.5 - 0.027\Delta_c - 0.00136\Delta_c^2 \tag{1.8}$$

$$c = Rd_0 \frac{\omega_c}{\Delta_c} \tag{1.9}$$

$$G = \frac{3(1-\nu)}{8d_0\sqrt{Rd_0}} F_0 \tag{1.10}$$

The oscillation loading method can overcome the difficulty in applying the instantaneous loading. Therefore, it has great potential to become a reliable technique for characterizing poroelastic materials at the nano- to micro-scale.

1.2.4 Ramp Loading Method

A recent work by Esteki et al. (2019) proposes to conduct experiments through ramp-hold to take into account the loading rate effect. For each ramp-hold test, only the peak force or the peak displacement is used in data analysis. A series of ramp-hold tests is therefore needed to identify the poroelastic constants via data regression. Their master curve was contructed based on empirical correlation.

1.3 Research Outline and Thesis Structure

The thesis is organized as follows,

- Chapter 1 outlines the motivations and objectives of this research.
- Chapters 2, 3 and 4 present derivations of theoretical solutions for poroelastic spherical indentation via step displacement loading for three different types of surface drainage conditions, i.e., case I of a permeable indenter on a permeable half space, case II of an impermeable half space and case III of an impermeable indenter on a permeable half space. Effective mathematical techniques to overcome the difficulties in evaluating integrals with highly oscillatory kernels and solving the Fredholm integral equations of the second kind are developed. In addition to the Laplace and Hankel transforms which have been used in previous literature, Abel transform, the method of successive substitution for solving the Fredholm integral equation of the second kind, and Wynn's epsilon algorithm for accelerating convergence of an alternating series are some of the new techniques we adopted. Implications of the poroelastic solutions for incipient failure in form of tensile crack initiation and onset of plastic deformation are discussed. Behaviors of the normalized indentation force relaxation are analyzed. Master curves of indentation force relaxation are constructed by fitting the full solutions with an elementary function. In addition, for cases I and II, closed-form asymptotic solutions for the force relaxation response at both early and late times are derived.
- Chapters 5 and 6 implement a fully coupled finite element algorithm for poro-elasto-plasticity for both plane strain and cylindrically axisymmetric problems using MATLAB following the mixed continuous Galerkin formulation for displacement and pore pressure. To take into account interations, a penalty-based frictionless contact scheme is developed and incorporated into the algorithm. The finite element algorithm is first extensively benchmarked with poroelastic analytical solutions to the problems of Terzaghi, Mandel, Cryer, and De Leeuw and an analytic solution for one-dimensional poro-elasto-plastic

consolidation. Numerical results for poro-elasto-plastic indentation that if the plastic deformation is within a certain range, the normalized force relaxation behavior could still be approximated as poroelastic are shown next. Finally, parameters space where the soil response can be appropriately described by the theoretical solutions is constructed.

- Chapter 7 presents a combined theoretical and numerical analysis for poroelastic spherical indentation under step force loading. Two approaches are employed to approximate the contact radius responses. One is to assume that the contact radius remains constant and the other is to assume that the contact radius is time dependent and follows the Hertzian relationship. While the problem with the first approach is mathematically amenable and can be solved theoretically via the McNamee-Gibson displacement function method, the problem with the second approach involves a moving boundary condition and cannot be solved theoretically. Finite element simulations are performed to obtain the solution for the second approach.

- Chapter 8 summarizes the findings in this research and provides suggestions for future work.

2 POROELASTIC RESPONSE OF SPHERICAL INDENTATION INTO A HALF SPACE WITH A PERMEABLE SURFACE VIA STEP DISPLACEMENT

2.1 Introduction

General methods of solution for poroelasticity by means of potential functions were first discussed in Biot (1956) and De Josselin De Jong (1957). By expressing field variables as partial derivatives of the stress and/or displacement functions, governing equations can be reduced to canonical forms in terms of these functions. As is the case with linear elasticity, the stress function methods are relatively inconvenient in dealing with boundary conditions involving displacements and in ensuring uniqueness in the displacement fields. Their use for poroelastic contact problems has therefore been limited to the few cases when the half-space is subjected to tractions only (Paria, 1957; Sanyal, 1972).

Meanwhile, the displacement function method of McNamee and Gibson (McNamee and Gibson, 1960a,b) has shown to be robust for treating both plane strain and axisymmetric poroelastic contact problems subjected to normal loading. The original formulation of McNamee and Gibson assumes the solid and fluid phases are incompressible. The method was later generalized to account for compressible constituents by Verruijt (1971) and Detournay and Cheng (1993). The advantage of this method is that the governing equations are decoupled such that successive Laplace and Fourier/Hankel transforms can be applied to find the general solutions for the displacement functions in the Laplace domain and their exact solutions can be uniquely determined by the boundary conditions. Extension of the method for tangential loading over a half space was introduced in Schiffman and Fungaroli (1965) and Verruijt (1971).

In addition, an alternative direct method for solving axisymmetric problems was introduced by Chiarella and Booker (1975), where field variables are first expressed using integral representations in form of Laplace-Hankel transforms of unknown functions. The governing equations then become a system of ordinary differential equations (ODEs) for these functions. This ap-

proach is however less convenient than the McNamee-Gibson displacement function method since it also has issues with uniqueness.

In this work, we adopt the McNamee-Gibson displacement function method to consider the problem where a homogeneous, isotropic and linear poroelastic half space is subjected to step displacement loading under isothermal conditions. In this chapter, the surface drainage condition of case I as defined in Agbezuge and Deresiewicz (1974) is treated. Here we show that the mathematical issues in dealing with integrals with highly oscillatory kernels and solving Fredholm integral equations can in fact be overcome by using alternative integral representations with exponentially decaying functions in the kernels, and by employing the method of successive substitution to improve the accuracy in solving the Fredholm integral equations of the second kind.

Compressibility of both the fluid and solid phases is taken into account in our derivation. Constituent compressibility is particularly important when dealing with poroelastic response of geological materials such as rocks, where the bulk modulus of the solid phase could be comparable with that of the skeleton. Poroelastic characterization of rocks is crucial to the analyses of many geological processes and subsurface engineering applications in the fields of geomechanics, hydrogeology, and reservoir engineering (Wang, 2000). In addition, in drilling, the action of a single button in a drill bit pressing normally against a rock surface causing the rock underneath the bit to crush and fracture is essentially an indentation process (Fowell, 1993; Cook et al., 1984). Insights into the poroelastic effect on the indentation process could potentially help predict and improve the drilling efficiency.

Problem formulation and solution procedure are first introduced. Derivation to obtain the poroelastic fields is then shown. Implications of the poroelastic solution for incipient failure in form of tensile crack initiation and onset of plastic deformation are also discussed. Though derivation of this fully coupled poroelastic solution requires the aid of a variety of mathematical techniques, the result in terms of the normalized indentation force relaxation with time is remarkably simple and shows only relatively weak dependence on one derived material constant ω. Master curves of the normalized transient force response can be constructed by fitting the

theoretical solution using a simple elementary function, which lends itself to convenient use for material characterization in the laboratory. For the particular case when $\omega = 0$, closed-form asymptotic solutions for the force relaxation response at both early and late times are derived.

2.2 McNamee-Gibson Displacement Function Method

Governing equations for an axisymmetric fully poroelastic problem in a half space ($z \geq 0$) can be written using the displacement functions $\mathcal{D}$ and $\mathcal{F}$ (McNamee and Gibson, 1960a; Verruijt, 2013), which satisfy,

$$\frac{\partial}{\partial t}\nabla^2\mathcal{D} = c\nabla^2\nabla^2\mathcal{D} \tag{2.1}$$

$$\nabla^2\mathcal{F} = 0 \tag{2.2}$$

where,

$$\nabla^2 = \frac{\partial^2}{\partial r^2} + \frac{1}{r}\frac{\partial}{\partial r} + \frac{\partial^2}{\partial z^2} \tag{2.3}$$

$$c = \frac{\kappa\left(K + \frac{4}{3}G\right)}{\left[\alpha^2 + S\left(K + \frac{4}{3}G\right)\right]\mu} \tag{2.4}$$

$$\alpha = 1 - \frac{K}{K_s} \tag{2.5}$$

$$S = \frac{n}{K_f} + \frac{\alpha - n}{K_s} \tag{2.6}$$

The linear poroelastic response is described by the following list of independent material constants: $\kappa -$ permeability, $\mu -$ fluid viscosity, $K -$ skeleton bulk modulus, $G -$ skeleton shear modulus, $n -$ porosity, $K_f -$ fluid bulk modulus, $K_s -$ solid bulk modulus. In addition to the diffusion coefficient, c, the Biot coefficient, α, and the storage coefficient, S, two other derived material constants, η and ϕ, are defined to facilitate the derivation,

$$\eta = \frac{K}{2G} + \frac{2}{3} \tag{2.7}$$

$$\phi = \frac{\alpha^2 + S\left(K + \frac{4}{3}G\right)}{\alpha^2 + S\left(K + \frac{1}{3}G\right)} \tag{2.8}$$

Pore pressure, stresses and displacements can be directly expressed using displacement functions $\mathcal{D}$ and $\mathcal{F}$,

$$u_r = -\frac{\partial \mathcal{D}}{\partial r} + z\frac{\partial \mathcal{F}}{\partial r} \tag{2.9}$$

$$u_z = -\frac{\partial \mathcal{D}}{\partial z} + z\frac{\partial \mathcal{F}}{\partial z} + (1-2\phi)\,\mathcal{F} \tag{2.10}$$

$$\frac{\alpha p}{2G} = -\eta\nabla^2\mathcal{D} + [\phi + 2\eta\,(1-\phi)]\,\frac{\partial \mathcal{F}}{\partial z} \tag{2.11}$$

$$\frac{\sigma_z}{2G} = -\nabla^2\mathcal{D} + \frac{\partial^2 \mathcal{D}}{\partial z^2} - z\frac{\partial^2 \mathcal{F}}{\partial z^2} + \phi\frac{\partial \mathcal{F}}{\partial z} \tag{2.12}$$

$$\frac{\sigma_r}{2G} = -\nabla^2\mathcal{D} + \frac{\partial^2 \mathcal{D}}{\partial r^2} - z\frac{\partial^2 \mathcal{F}}{\partial r^2} + (2-\phi)\,\frac{\partial \mathcal{F}}{\partial z} \tag{2.13}$$

$$\frac{\sigma_\theta}{2G} = -\nabla^2\mathcal{D} + \frac{1}{r}\frac{\partial \mathcal{D}}{\partial r} - \frac{z}{r}\frac{\partial \mathcal{F}}{\partial r} + (2-\phi)\,\frac{\partial \mathcal{F}}{\partial z} \tag{2.14}$$

$$\frac{\sigma_{zr}}{2G} = \frac{\partial^2 \mathcal{D}}{\partial r \partial z} - z\frac{\partial^2 \mathcal{F}}{\partial r \partial z} - (1-\phi)\,\frac{\partial \mathcal{F}}{\partial r} \tag{2.15}$$

where u_r and u_z are the radial and vertical displacements; p is the pore pressure; and σ_z, σ_r, σ_θ, σ_{zr} are stress components. Compression positive is adopted in Chapters 2, 3, 4 and 7 for the sign convention. Expressions for components of the flux can be readily obtained after applying Darcy's law, i.e.,

$$q_z = -\frac{\kappa}{\mu}\frac{\partial p}{\partial z} = \frac{2G\kappa}{\alpha\mu}\left\{\eta\frac{\partial}{\partial z}\nabla^2\mathcal{D} - [\phi + 2\eta\,(1-\phi)]\,\frac{\partial^2 \mathcal{F}}{\partial z^2}\right\} \tag{2.16}$$

General solutions for Eqs. 2.1 and 2.2 can be obtained from Hankel transform in the Laplace domain. After neglecting the terms unbounded at infinity, we obtain,

$$\overline{\mathcal{D}} = \int_0^\infty \begin{bmatrix} A_1\,(s,\xi)\exp\,(-z\xi) \\ +A_2\,(s,\xi)\exp\left(-z\sqrt{\xi^2+\lambda}\right) \end{bmatrix} J_0\,(r\xi)\,d\xi \tag{2.17}$$

$$\overline{\mathcal{F}} = \int_0^\infty B_1\,(s,\xi)\exp\,(-z\xi)\,J_0\,(r\xi)\,d\xi \tag{2.18}$$

where $\lambda = s/c$ and s is the Laplace variable; $J_v\,(\cdot)$ is the Bessel function of the first kind of

order v; A_1, A_2 and B_1 are functions of s and ξ to be determined from the boundary conditions. The overbar is used here to denote the functions in the Laplace domain.

2.3 Problem Formulation

To describe spherical indentation into a semi-infinite domain with a permeable surface via step displacement loading, we can express the mechanical and drainage boundary conditions in terms of surface displacement u_z, stresses σ_z and σ_{zr}, and pore pressure p as listed in Table 2.1, where d is the depth of indentation; R is the radius of the indenter; a is the contact radius; and $\mathcal{H}(t)$ is the Heaviside step function. We assume the contact is frictionless. Radial displacement on the surface is therefore not constrained.

At the two limits when the domain is either fully undrained ($t = 0$) or drained ($t \to \infty$), the problem defined here is the same as Hertzian contact. The contact radius a can therefore be expressed as $a = \sqrt{Rd}$ (Love, 1929; Johnson, 1987; Liu and Huang, 2016). For the transient period, in order to make the problem amenable to mathematical treatment, we follow the argument (Agbezuge and Deresiewicz, 1974; Hu et al., 2010) that since the relation for a, d and R is purely geometrical at the two limits, it is reasonable to hypothesize that $a = \sqrt{Rd}$ still holds at $t > 0$. Strictly speaking, poroelastic indentation with a rigid sphere is a moving boundary problem. Nevertheless, as will be shown in Chapter 6, the assumption of a fixed contact radius is valid if the ratio of the depth of penetration over the indenter radius is small.

	time domain	Laplace domain
$0 \le r \le a_-$	$u_z = \left(d - \dfrac{r^2}{2R}\right)\mathcal{H}(t)$	$\overline{u}_z = s^{-1}\left(d - \dfrac{r^2}{2R}\right)$
	$\sigma_{zr} = 0,\ p = 0$	$\overline{\sigma}_{zr} = 0,\ \overline{p} = 0$
$r \ge a_+$	$\sigma_z = \sigma_{zr} = 0,\ p = 0$	$\overline{\sigma}_z = \overline{\sigma}_{zr} = 0,\ \overline{p} = 0$

Table 2.1: Boundary conditions.

Matching the poroelastic fields with the boundary conditions in the Laplace domain yields

the following equations,

$$A_1\xi + A_2\sqrt{\xi^2+\lambda} + B_1\left(1-\phi\right) = 0 \tag{2.19}$$

$$A_2 + \frac{\phi + 2\eta\left(1-\phi\right)}{\eta\lambda} B_1\xi = 0 \tag{2.20}$$

and a dual integral equation containing only the unknown B_1,

$$\int_0^\infty B_1 J_0\left(r\xi\right) d\xi = \left(s\phi\right)^{-1}\left(\frac{r^2}{2R} - d\right), \qquad 0 \le r \le a_- \tag{2.21}$$

$$\int_0^\infty \left[1 + \omega H\left(s,\xi\right)\right] \xi B_1 J_0\left(r\xi\right) d\xi = 0, \qquad r \ge a_+ \tag{2.22}$$

where,

$$H\left(s,\xi\right) = 1 + \frac{2\xi^2}{\lambda}\left(1 - \frac{\sqrt{\xi^2+\lambda}}{\xi}\right) \tag{2.23}$$

$$\omega = \frac{\phi + 2\eta\left(1-\phi\right)}{\phi\left(2\eta - 1\right)} \tag{2.24}$$

The problem now reduces to first finding B_1 through Eqs. 2.21-2.22 and then A_1 and A_2 from Eqs. 2.19-2.20.

Constant ω can be expressed explicitly using other material constants,

$$\omega = \alpha^2\left(1-2\nu\right)\left(\alpha^2 + 2SG\frac{1-\nu}{1-2\nu}\right)^{-1} \tag{2.25}$$

where ν is the drained Poisson's ratio. Since $0 \le \alpha \le 1$, $S \ge 0$, $G \ge 0$ and $0 \le \nu \le 0.5$, the theoretical range of ω is $[0,1]$. If both the fluid and solid phases are incompressible, ω becomes a function of ν only, $\omega = 1 - 2\nu$.

	material	ω		material	ω
1	Ruhr sandstone	0.2544	9	Boise sandstone	0.1792
2	Tennessee marble	0.0213	10	Gulf of Mexico shale	0.4174
3	Charcoal granite	0.0308	11	Danian chalk	0.2019
4	Berea sandstone	0.1637	12	hard sediment	0.4904
5	Westerly granite	0.1206	13	soft sediment	0.4881
6	Weber sandstone	0.1665	14	Abyssal red clay	0.0036
7	Ohio sandstone	0.1372	15	rock salt	0.0322
8	Pecos sandstone	0.2156	16	coarse sand	0.3333

Table 2.2: A list of poroelastic materials from Cheng (2016) and their ω values.

Based on the material constants listed in Cheng (2016), the values of ω for sixteen saturated poroelastic media appear to fall within the range between 0 and 0.5, see Table 2.2. The saturating fluid is kerosene for Boise sandstone (No. 9) and salt water for Abyssal red clay (No. 14). All the others are saturated in water. For the saturated hydrogel in Hu et al. (2010), $\omega = 0.44$.

2.4 Solution Procedure

2.4.1 Fredholm Integral Equation of the Second Kind

Noble (1963) showed that the pair of dual integral equations in Eqs. 2.21-2.22 can be reduced to a Fredholm integral equation of the second kind. By applying the following Sonine's integrals to Eqs. 2.21-2.22, respectively,

$$J_{\frac{1}{2}}(x\xi) = \sqrt{\frac{2\xi}{\pi x}} \int_0^x J_0(r\xi) \frac{rdr}{\sqrt{x^2 - r^2}} \tag{2.26}$$

$$J_{-\frac{1}{2}}(x\xi) = \sqrt{\frac{2\xi}{\pi x}} \int_x^\infty J_0(r\xi) \frac{rdr}{\sqrt{r^2 - x^2}} \tag{2.27}$$

we obtain,

$$\int_0^\infty B_1 \xi^{-\frac{1}{2}} J_{\frac{1}{2}}(x\xi)\, d\xi = (s\phi R)^{-1} \sqrt{\frac{2}{\pi x}} \left(\frac{x^3}{3} - xRd\right), \qquad 0 \le x \le a_- \tag{2.28}$$

and,

$$\int_0^\infty \left[1+\omega H\left(s,\xi\right)\right] B_1 \xi^{\frac{1}{2}} J_{-\frac{1}{2}}\left(x\xi\right) d\xi = 0, \qquad x \geq a_+ \tag{2.29}$$

In order to make the orders of the Bessel functions and the powers of ξ identical in the above equations, both sides of Eq. 2.28 are first multiplied by $x^{\frac{1}{2}}$ and then differentiated with respect to x,

$$\int_0^\infty B_1 \xi^{\frac{1}{2}} J_{-\frac{1}{2}}\left(x\xi\right) d\xi = \left(s\phi R\right)^{-1} \sqrt{\frac{2}{\pi x}} \left(x^2 - Rd\right), \qquad 0 \leq x \leq a_- \tag{2.30}$$

Define $\theta\left(s,x\right)$ as an unknown function of s and x in the Laplace domain according to,

$$\int_0^\infty B_1 \xi^{\frac{1}{2}} J_{-\frac{1}{2}}\left(x\xi\right) d\xi = \sqrt{\frac{2}{\pi}} \left(s\phi R\right)^{-1} \theta\left(s,x\right), \qquad x \geq a_+ \tag{2.31}$$

Since the left hand sides of Eqs. 2.30 and 2.31 are identical, the expression on the left is defined for all x. It follows from inverse Hankel transform,

$$\begin{aligned} B_1 \xi^{-\frac{1}{2}} = &\sqrt{\frac{2}{\pi}} \left(s\phi R\right)^{-1} \int_0^a m^{\frac{1}{2}} \left(m^2 - Rd\right) J_{-\frac{1}{2}}\left(m\xi\right) dm \\ &+\sqrt{\frac{2}{\pi}} \left(s\phi R\right)^{-1} \int_a^\infty m\theta\left(s,m\right) J_{-\frac{1}{2}}\left(m\xi\right) dm \end{aligned} \tag{2.32}$$

Substituting Eq. 2.32 into Eq. 2.29 gives a Fredholm integral equation of the second kind for $\theta\left(s,x\right)$,

$$\begin{aligned} &\theta\left(s,x\right) + \omega \int_a^\infty \left[m \int_0^\infty \xi H\left(s,\xi\right) J_{-\frac{1}{2}}\left(x\xi\right) J_{-\frac{1}{2}}\left(m\xi\right) d\xi\right] \theta\left(s,m\right) dm \\ &= \omega \int_0^a m^{-\frac{1}{2}} \left(Rd - m^2\right) \left[m \int_0^\infty \xi H\left(s,\xi\right) J_{-\frac{1}{2}}\left(x\xi\right) J_{-\frac{1}{2}}\left(m\xi\right) d\xi\right] dm \end{aligned} \tag{2.33}$$

Eq. 2.33 extends the definition of $\theta\left(s,x\right)$ from $x \geq a_+$ to $x \geq 0$.

For convenience, the following dimensionless variables are introduced,

$$\begin{gathered} x_* = x/a \qquad m_* = m/a \qquad r_* = r/a \qquad z_* = z/a \\ \xi_* = \xi a \qquad s_* = \lambda a^2 \qquad t_* = tc/a^2 \end{gathered} \tag{2.34}$$

Denote function $\theta_1(s_*, x_*)$ as the normalized $\theta(s, x)$ according to,

$$\theta_1(s_*, x_*) = \theta(s, x)\, a^{-\frac{3}{2}} \tag{2.35}$$

Eq. 2.33 can be rewritten as,

$$\theta_1(s_*, x_*) + \omega \int_1^\infty N(s_*, x_*, m_*)\, \theta_1(s_*, m_*)\, dm_* = \omega M(s_*, x_*) \tag{2.36}$$

where,

$$N(s_*, x_*, m_*) = m_* \int_0^\infty \xi_* H_1(s_*, \xi_*)\, J_{-\frac{1}{2}}(x_* \xi_*)\, J_{-\frac{1}{2}}(m_* \xi_*)\, d\xi_* \tag{2.37}$$

$$M(s_*, x_*) = \int_0^1 m_*^{-\frac{1}{2}} \left(1 - m_*^2\right) N(s_*, x_*, m_*)\, dm_* \tag{2.38}$$

$$H_1(s_*, \xi_*) = 1 + \frac{2\xi_*^2}{s_*} \left(1 - \frac{\sqrt{\xi_*^2 + s_*}}{\xi_*}\right) \tag{2.39}$$

Now $\theta_1(s_*, x_*)$ is the unknown to be determined. Once it is known, all the field quantities can be expressed in the Laplace domain in terms of $\theta_1(s_*, x_*)$. It is noted that $\theta_1(s_*, x_*)$ is influenced by the material properties only through ω. Prior to finding the solution to Eq. 2.36, function $N(s_*, x_*, m_*)$ needs to be evaluated. Methodologies for evaluating $N(s_*, x_*, m_*)$ and then $M(s_*, x_*)$ and $\theta_1(s_*, x_*)$ are outlined next.

2.4.2 Alternative Expression for $N(s_*, x_*, m_*)$

Though uniformly convergent, $N(s_*, x_*, m_*)$ in Eq. 2.37 has an oscillatory integral kernel over an unbounded interval. As x_* and m_* become large, the rapidly oscillating integrand could result in unstable numerical integration. Yue and Selvadurai (1994) separated the integrand

into two parts so that one deals with its asymptote as $s_*^{-1}\xi_*^2 \to \infty$, the integral of which can be expressed in closed-form, and the other is the difference between the integrand and its asymptote, which reduces to zero relatively faster and thus can be numerically treated more effectively. Lan and Selvadurai (1996) used a function to fit $H_1(s_*, \xi_*)$. The fitting function is chosen in such a way that a closed-form solution can be obtained for $N(s_*, x_*, m_*)$.

In this study, we take a different approach by expressing $N(s_*, x_*, m_*)$ using an alternative integral expression. Indeed, $N(s_*, x_*, m_*)$ can be rewritten using one of the integral representations of the modified Struve functions (Olver, 2010), in which the oscillatory nature is no longer present. Since $J_{-\frac{1}{2}}(y) = \sqrt{2/\pi y}\cos y$, $N(s_*, x_*, m_*)$ can be rewritten as,

$$N(s_*, x_*, m_*) = \frac{1}{\pi}\sqrt{\frac{m_*}{x_*}}\int_0^\infty H_1(s_*, \xi_*)\begin{bmatrix}\cos(x_*\xi_* - m_*\xi_*) \\ +\cos(x_*\xi_* + m_*\xi_*)\end{bmatrix} d\xi_* \tag{2.40}$$

Integration by parts three times on the right hand side (RHS) of Eq. 2.40 gives,

$$\begin{aligned}\text{RHS} = \frac{2}{\pi}\left(\frac{m_*}{x_*}\right)^{\frac{1}{2}}\Bigg\{&(x_* - m_*)^{-2}\left[s_*^{-\frac{1}{2}} - \frac{3s_*}{x_* - m_*}\int_0^\infty \left(\xi_*^2 + s_*\right)^{-\frac{5}{2}}\sin\left[(x_* - m_*)\,\xi_*\right]d\xi_*\right] \\ &+ (x_* + m_*)^{-2}\left[s_*^{-\frac{1}{2}} - \frac{3s_*}{x_* + m_*}\int_0^\infty \left(\xi_*^2 + s_*\right)^{-\frac{5}{2}}\sin\left[(x_* + m_*)\,\xi_*\right]d\xi_*\right]\Bigg\}\end{aligned} \tag{2.41}$$

Though the integrals in Eq. 2.41 still contain oscillatory terms, the integrals are related to the modified Struve function through,

$$\int_0^\infty \left(\xi_*^2 + s_*\right)^{-\frac{5}{2}}\sin(y\xi_*)\,d\xi_* = -\frac{\pi}{6}y\,|y|\,s_*^{-1}\mathrm{M}_{-2}\left(|y|\,s_*^{\frac{1}{2}}\right) \tag{2.42}$$

where $\mathrm{M}_v(\cdot)$ is the modified Struve function of the second kind of order v. According to Olver (2010), Eq. 2.42 holds, provided that $|y|\,s_*^{\frac{1}{2}} \geq 0$. This requirement is fulfilled since $|y| \geq 0$ and $s_* \geq 0$ in the Stehfest algorithm (Stehfest, 1970) for the inverse Laplace transform.

According to the recurrence relationship for the modified Struve function, we have,

$$\mathrm{M}_{-2}(y) = \mathrm{M}_0(y) - \frac{2}{y}\mathrm{M}_1(y) - \frac{2}{\pi y} \tag{2.43}$$

Functions $\mathrm{M}_0(y)$ and $\mathrm{M}_1(y)$ can be expressed through integral representations that do not contain oscillatory terms,

$$\mathrm{M}_0(y) = -\frac{2}{\pi}\int_0^1 \exp(-y\zeta)\left(1-\zeta^2\right)^{-\frac{1}{2}} d\zeta \tag{2.44}$$

$$\mathrm{M}_1(y) = -\frac{2}{\pi}y\int_0^1 \exp(-y\zeta)\left(1-\zeta^2\right)^{\frac{1}{2}} d\zeta \tag{2.45}$$

The integrals in Eqs. 2.44 and 2.45 have an exponentially decaying function in the kernels and a finite integral upper limit, and thus can be numerically integrated efficiently and effectively.

In addition, we can use the asymptotic behaviors of $\mathrm{M}_0(y)$ and $\mathrm{M}_1(y)$ for approximation, if the numerical integration cannot return satisfactory results at small or large y, e.g.,

$$\lim_{y\to 0}\mathrm{M}_0(y) = -1 + \frac{2}{\pi}y - \frac{1}{4}y^2 + \frac{2}{9\pi}y^3 \tag{2.46}$$

$$\lim_{y\to \infty}\mathrm{M}_0(y) = -\frac{2}{\pi y} - \frac{2}{\pi y^3} - \frac{18}{\pi y^5} \tag{2.47}$$

$$\lim_{y\to 0}\mathrm{M}_1(y) = -\frac{1}{2}y + \frac{2}{3\pi}y^2 - \frac{1}{16}y^3 \tag{2.48}$$

$$\lim_{y\to \infty}\mathrm{M}_1(y) = -\frac{2}{\pi} + \frac{2}{\pi y^2} + \frac{6}{\pi y^4} \tag{2.49}$$

It follows from Eqs. 2.41-2.45 that an alternative expression for $N(s_*, x_*, m_*)$ can be written as,

$$N(s_*, x_*, m_*) = \sqrt{\frac{s_* m_*}{x_*}}\left[\frac{\mathrm{M}_0(y_1)}{y_1} + \frac{\mathrm{M}_0(y_2)}{y_2} - \frac{2\mathrm{M}_1(y_1)}{y_1^2} - \frac{2\mathrm{M}_1(y_2)}{y_2^2}\right] \tag{2.50}$$

where $y_1 = |x_* - m_*|\, s_*^{\frac{1}{2}}$ and $y_2 = (x_* + m_*)\, s_*^{\frac{1}{2}}$.

Some asymptotic expressions of $N(s_*, x_*, m_*)$ are straightforward to obtain,

$$\lim_{s_* \to \infty} N(s_*, x_*, m_*) = \delta(m_* - x_*) \tag{2.51}$$

$$\lim_{s_* \to 0} N(s_*, x_*, m_*) = 0 \tag{2.52}$$

$$\lim_{x_* \to \infty} N(s_*, x_*, m_*) = \frac{4}{\pi} \sqrt{\frac{m_*}{s_* x_*^5}} \tag{2.53}$$

Comparison between direct numerical integration of Eq. 2.40 with the oscillatory kernel and the alternative expression in Eq. 2.50 at $x_* = 1$, $s_* = 5,000$ and $s_* = 500,000$ are shown in Fig. 2.1. The results in both cases are obtained by directly using the "integral" command in MATLAB. Direct integration of Eq. 2.40 yields highly oscillatory results at large s_* (small t_*) and fails to capture the Dirac function behavior at $m_* = x_*$, which is expected for $N(s_*, x_*, m_*)$ at large s_* according to Eq. 2.51. In contrast, the alternative expression with the modified Struve functions is well behaved and approaches $\delta(m_* - x_*)$ at large s_*.

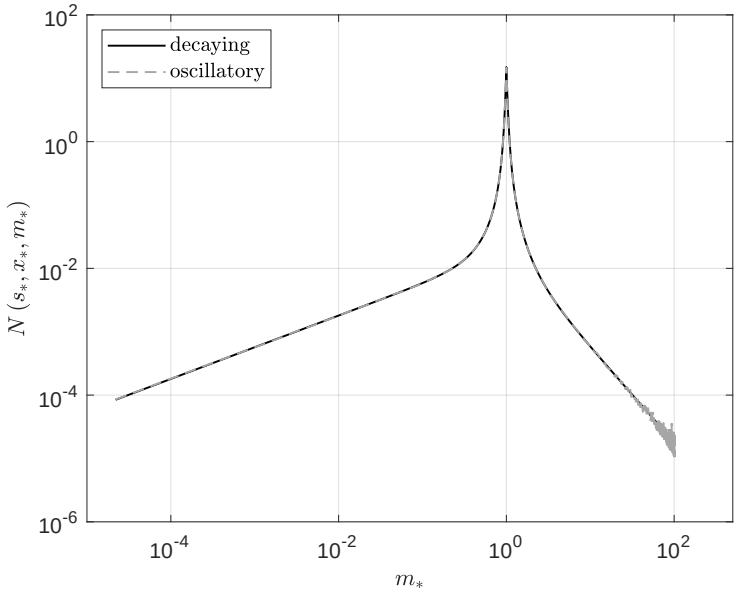

(a) $s_* = 5,000$

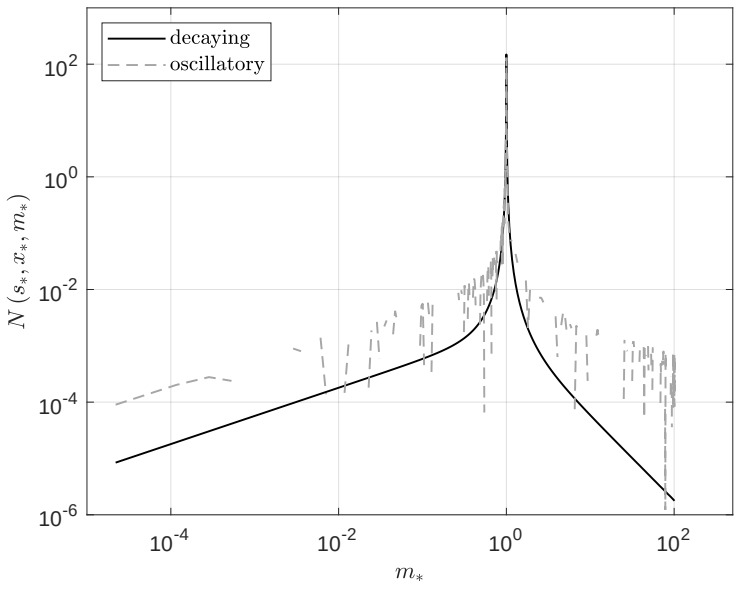

(b) $s_* = 500,000$

Figure 2.1: Comparison between direct numerical integration of the oscillatory kernel and the alternative expression with the modified Struve functions for $N(s_*, x_*, m_*)$ at $x_* = 1$.

Using the alternative expression for $N(s_*, x_*, m_*)$, a closed-form solution for $M(s_*, x_*)$ consisting of special functions such as the hypergeometric functions can be obtained, see Appendix A.4. However, the exact expression of $M(s_*, x_*)$ is cumbersome and barely offers any advantage over direct numerical evaluation of Eq. 2.38 in terms of computational speed and accuracy. Indeed, as long as sufficient integration points are added in the vicinity of the peak in $N(s_*, x_*, m_*)$, direct numerical integration to determine $M(s_*, x_*)$ is rather efficient. The relative error from direct numerical integration is smaller than 10^{-5} in this study.

2.4.3 Method of Successive Substitution

To solve for $\theta_1(s_*, x_*)$ in Eq. 2.36, we adopt the method of successive substitution (Zemyan, 2012) by letting,

$$\theta_1(s_*, x_*) = -\sum_{n=0}^{\infty} (-\omega)^{n+1} a_n(s_*, x_*) \tag{2.54}$$

where,

$$a_0(s_*, x_*) = M(s_*, x_*) \tag{2.55}$$

$$a_n(s_*, x_*) = \int_1^{\infty} N(s_*, x_*, m_*)\, a_{n-1}(s_*, m_*)\, dm_*, \qquad n = 1, 2, 3... \tag{2.56}$$

Numerical integration for the improper integral in Eq. 2.56 is performed by substituting its infinite upper bound with a sufficiently large value (say, 100), and assigning adequate integration points in the vicinity of the peak in $N(s_*, x_*, m_*)$. Summation of the infinite series is also replaced by a partial sum. It is observed that when $\omega \leq 0.5$ as in the cases for the porous media in Table 2.2, the series converges rather fast and the partial sum with only 20 terms is sufficient to give a satisfactory approximation for any values of s_* and x_*. For example, when $s_* = 500,000$ and $\omega = 0.25$, at $x_* = 1$, a_n decreases with the increase of n and the largest term is $a_0 = 0.01$. This means that the largest truncation error of the partial sum with 20 terms is $0.01 \sum_{n=21}^{\infty} \omega^n \approx 3 \times 10^{-15}$, much smaller than $\theta_1 = 0.00232$ at $x_* = 1$.

By substituting Eq. 2.53 into Eqs. 2.36 and 2.38, the asymptotes of $\theta_1(s_*, x_*)$ and

$M(s_*, x_*)$ at $x_* \to \infty$ can be expressed explicitly,

$$\lim_{x_* \to \infty} \log\left[\theta_1(s_*, x_*)\right] = -\frac{5}{2}\log(x_*) + C_1 \tag{2.57}$$

$$\lim_{x_* \to \infty} \log\left[M(s_*, x_*)\right] = -\frac{5}{2}\log(x_*) + C_2 \tag{2.58}$$

where C_1 and C_2 are constants and equal to,

$$C_1 = \log\left[\frac{8\omega}{3\pi\sqrt{s_*}}\left(1 - \frac{3}{2}\int_1^\infty m_*^{\frac{1}{2}}\theta_1(s_*, m_*)\, dm_*\right)\right] \tag{2.59}$$

$$C_2 = \log\left(\frac{8}{3\pi\sqrt{s_*}}\right) \tag{2.60}$$

The limits of $\theta_1(s_*, x_*)$ at $s_* \to 0$ and $s_* \to \infty$ can be determined after substituting Eqs. 2.51 and 2.52 into Eq. 2.36,

$$\lim_{s_* \to \infty} \theta_1(s_*, x_*) = \begin{cases} \dfrac{\omega\left(1 - x_*^2\right)}{\sqrt{x_*}}, & 0 \le x_* \le 1 \\ 0, & x_* > 1 \end{cases} \tag{2.61}$$

$$\lim_{s_* \to 0} \theta_1(s_*, x_*) = 0, \qquad x_* \ge 0 \tag{2.62}$$

A comparison between the method of successive substitution and the method of quadrature for determining $\theta_1(s_*, x_*)$ is shown in Fig. 2.2 for $s_* = 500,000$ and $\omega = 0.25$. The method of quadrature was previously used in the literature (Agbezuge and Deresiewicz, 1974; Chiarella and Booker, 1975; Yue and Selvadurai, 1995; Lan and Selvadurai, 1996). The method of successive substitution is able to recover the analytical asymptote of $\theta_1(s_*, x_*)$ at large x_*. As indicated by Eqs. 2.57 and 2.58, when $x_* \to \infty$, $\theta_1(s_*, x_*)$ and $M(s_*, x_*)$ should be parallel to each other with a slope of $-5/2$ in the log-log scale. The deficiency in the quadrature method is likely due to the fact that the information around the peak of $N(s_*, x_*, m_*)$ when x_* is large is not adequately captured.

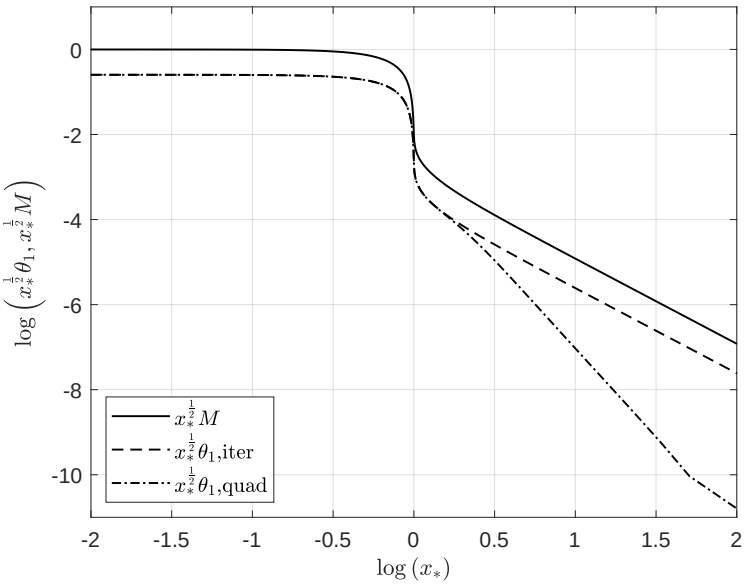

Figure 2.2: Comparison between the method of successive substitution ("iter") and the method of quadrature ("quad") for $\theta_1(s_*, x_*)$ at $s_* = 500,000$ and $\omega = 0.25$.

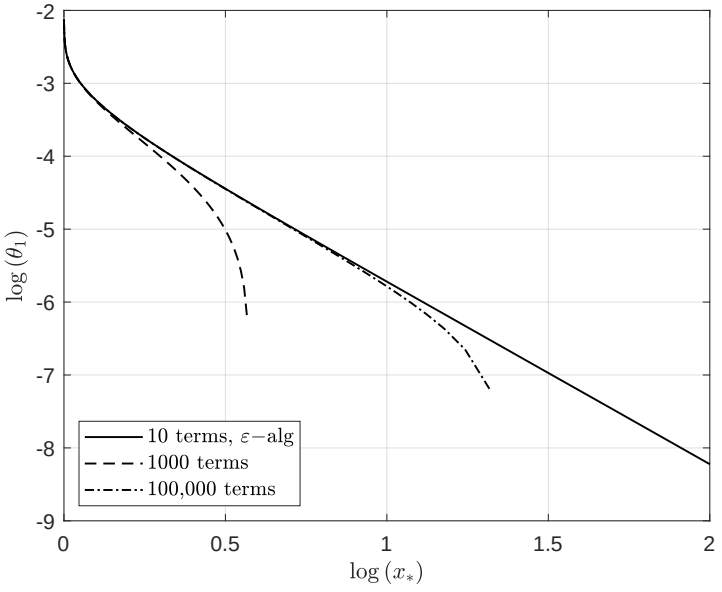

Figure 2.3: Comparison between the partial sum results with $1,000$ and $100,000$ terms and the accelerated result using the $\varepsilon-$algorithm for $\theta_1(s_*, x_*)$ for $\omega = 1$ and $s_* = 500,000$.

Theoretically, the value of ω could be close or equal to 1. In that case, the alternating series in Eq. 2.54 converges slowly. Wynn's epsilon algorithm (Wynn, 1956) is employed here to accelerate the convergence for the method's effectiveness in dealing with an alternating series. Fig. 2.3 presents a comparison between the accelerated result using the $\varepsilon-$algorithm based on the first 10 terms in the series only and the partial sum results with $1,000$ and $100,000$ terms for $\omega = 1$ and $s_* = 500,000$. It shows that the accelerated result is well behaved and acts like an upper bound for the results from the partial sum.

2.5 Poroelastic Fields

Poroelastic fields on the surface and inside the half space can now be expressed in terms of $\theta_1(s_*, x_*)$ in the Laplace domain by directly substituting the displacement functions $\overline{\mathcal{D}}$ and $\overline{\mathcal{F}}$ into Eqs. 2.9-2.16. However, these expressions from direct substitution all contain integrals with oscillatory kernels. As will be shown later in Section 2.5.1, direct evaluation of these integrals could yield nonsmooth results at small depth. As such, a second set of expressions is derived with the aid of Abel transform (Bracewell, 1986; Poularikas, 2018) and Sonine's integral (Noble, 1963). For the second set, the expressions for the surface and inside the half space are listed separately.

The first pair of forward and inverse Abel transform used in this study is,

$$F(x) = 2\int_x^\infty f(r)\frac{rdr}{\sqrt{r^2-x^2}} \tag{2.63}$$

$$f(r) = -\frac{1}{\pi}\int_r^\infty F'(x)\frac{dx}{\sqrt{x^2-r^2}} \tag{2.64}$$

The inverse transform in Eq. 2.64 is applicable only if $F(x)$ is continuous. Generalization to account for discontinuity in $F(x)$, for example, at $x = 1$, $F(x_-) - F(x_+) = C$ where C is a constant, can be expressed as,

$$f(r) = -\frac{1}{\pi}\int_r^\infty \frac{d\left[F(x) - C\mathcal{H}(1-x)\right]}{dx}\frac{dx}{\sqrt{x^2-r^2}} + \frac{C\mathcal{H}(1-r)}{\pi\sqrt{1-r^2}} \tag{2.65}$$

The second pair of forward and inverse Abel transform, which will be used for the derivations for cases II and III, is,

$$F(r) = 2\int_0^r f(x)\frac{dx}{\sqrt{r^2-x^2}} \tag{2.66}$$

$$f(x) = \frac{1}{\pi}\frac{d}{dx}\left[\int_0^x F(r)\frac{rdr}{\sqrt{x^2-r^2}}\right] \tag{2.67}$$

The formula below, derived from Sonine's finite integral (Noble, 1963), will also be used,

$$J_{-\frac{1}{2}}(x\xi) = \sqrt{\frac{2}{\pi x\xi}} - \sqrt{\frac{2x\xi}{\pi}}\int_0^x J_1(r\xi)\frac{dr}{\sqrt{x^2-r^2}} \tag{2.68}$$

$$J_{\frac{1}{2}}(x\xi) = \sqrt{\frac{2x\xi}{\pi}}\int_x^\infty J_1(r\xi)\frac{dr}{\sqrt{r^2-x^2}} \tag{2.69}$$

In addition, two techniques are used to rewrite the integrals in the second set of expressions. The first one is to express the integrals alternatively using the modified Bessel functions of the second kind (Bateman, 1954), for example,

$$\int_0^\infty \exp\left(-z\sqrt{\xi^2+s}\right)\frac{\cos(y\xi)}{\sqrt{\xi^2+s}}d\xi = \mathrm{K}_0\left[\sqrt{s\left(y^2+z^2\right)}\right] \tag{2.70}$$

where $\mathrm{K}_v(\cdot)$ is the modified Bessel functions of the second kind of order v. One of the integral representations of $\mathrm{K}_v(\cdot)$ does not contain an oscillatory kernel. For example,

$$\mathrm{K}_v(y) = \frac{\sqrt{\pi}\left(\frac{1}{2}y\right)^v}{\Gamma\left(v+\frac{1}{2}\right)}\int_1^\infty \exp(-y\zeta)\left(\zeta^2-1\right)^{v-\frac{1}{2}}d\zeta \tag{2.71}$$

where $\mathrm{Re}(v) > -\frac{1}{2}$ and $\mathrm{Re}(y) > 0$. Other identities can also be obtained after taking derivatives of Eq. 2.70 with respect to y or z. The second technique is the method of contour integration, see details in Appendix A.2.

Poroelastic fields in the time domain can be obtained by using the Stehfest algorithm (Stehfest, 1970) for inverse Laplace transform with six expansion terms. Derivation of the pore pressure $\overline{p}$, vertical stress $\overline{\sigma}_z$ and displacement $\overline{u}_z$ is shown next. Details of the other non-trivial stresses and displacements are given in Appendix A.1. Their undrained and drained

asymptotes, which correspond to the undrained and drained responses of the Hertzian contact, are given in Appendix A.1.5.

Skeleton shear modulus, G	0.76 GPa
Skeleton compression modulus, K	1.1 GPa
Solid compression modulus, K_s	34 GPa
Fluid compression modulus, K_f	2.25 GPa
Porosity, n	0.3
Permeability, κ	$1 \times 10^{-19}\,\mathrm{m}^2$

Table 2.3: Material constants of the Gulf of Mexico shale (Cheng, 2016).

Material properties of the Gulf of Mexico shale as listed in Cheng (2016), see Table 2.3, are used for the subsequent calculation of the field quantities and the incipient failure analysis. Viscosity of the saturating fluid is taken to be $\mu = 1$ cp. Values of the drained and undrained Poisson's ratios are $\nu = 0.219$ and $\nu_u = 0.449$, which correspond to $\omega = 0.4174$. Radius of the spherical indenter is taken as $R = 50$ mm and the indentation depth $d = 0.1$ mm and the corresponding contact radius is $a = 2.23$ mm for this example case.

2.5.1 Pore Pressure

Expression 1 Substituting Eqs. 2.17-2.20 and 2.32 into Eq. 2.11 gives,

$$\begin{aligned}\alpha\overline{p} = \frac{2G\left(2\eta-1\right)a^3}{cRs_*}\Bigg[\omega\int_0^1\left(m_*^2-1\right)N_p\left(s_*,r_*,m_*,z_*\right)dm_* \\ +\omega\int_1^\infty m_*^{\frac{1}{2}}\theta_1\left(s_*,m_*\right)N_p\left(s_*,r_*,m_*,z_*\right)dm_*\Bigg]\end{aligned} \tag{2.72}$$

where,

$$\begin{aligned}N_p\left(s_*,r_*,m_*,z_*\right) = \frac{2}{\pi}\int_0^\infty \xi_*\Big[\exp\left(-z_*\sqrt{\xi_*^2+s_*}\right) \\ -\exp\left(-z_*\xi_*\right)\Big]\cos\left(m_*\xi_*\right)J_0\left(r_*\xi_*\right)d\xi_*\end{aligned} \tag{2.73}$$

Expression 2 An alternative expression for the pore pressure field can be derived by first applying Sonine's integral in Eq. 2.27 to Eq. 2.72,

$$\int_{x_*}^{\infty} \alpha\overline{p} \frac{r_* dr_*}{\sqrt{r_*^2 - x_*^2}} = \frac{2G\left(2\eta - 1\right) a^3}{cRs_*} \left[\omega \int_0^1 \left(m_*^2 - 1\right) N_{px}\left(s_*, x_*, m_*, z_*\right) dm_* + \omega \int_1^{\infty} m_*^{\frac{1}{2}} \theta_1\left(s_*, m_*\right) N_{px}\left(s_*, x_*, m_*, z_*\right) dm_*\right] \tag{2.74}$$

where,

$$N_{px}\left(s_*, x_*, m_*, z_*\right) = \frac{2}{\pi} \int_0^{\infty} \left[\exp\left(-z_* \sqrt{\xi_*^2 + s_*}\right) - \exp\left(-z_* \xi_*\right)\right] \cos\left(m_* \xi_*\right) \cos\left(x_* \xi_*\right) d\xi_* \tag{2.75}$$

Since the right hand side of Eq. 2.74 is continuous at $x_* \geq 0$, applying the inverse Abel transform in Eq. 2.64 gives,

$$\alpha\overline{p} = -\frac{4\left(2\eta - 1\right) Ga^3}{\pi cRs_*} \int_{r_*}^{\infty} \frac{\theta_p\left(s_*, x_*, z_*\right) dx_*}{\sqrt{x_*^2 - r_*^2}} \tag{2.76}$$

where,

$$\theta_p\left(s_*, x_*, z_*\right) = \omega \int_0^1 \left(m_*^2 - 1\right) N_{px,x}\left(s_*, x_*, m_*, z_*\right) dm_* + \omega \int_1^{\infty} m_*^{\frac{1}{2}} \theta_1\left(s_*, m_*\right) N_{px,x}\left(s_*, x_*, m_*, z_*\right) dm_* \tag{2.77}$$

and $N_{px,x} = \partial N_{px} / \partial x_*$,

$$N_{px,x}\left(s_*, x_*, m_*, z_*\right) = -\frac{2}{\pi} \int_0^{\infty} \xi_* \left[\exp\left(-z_* \sqrt{\xi_*^2 + s_*}\right) - \exp\left(-z_* \xi_*\right)\right] \cos\left(m_* \xi_*\right) \sin\left(x_* \xi_*\right) d\xi_* \tag{2.78}$$

Here the first term in $N_{px,x}$ can be evaluated with the aid of the modified Bessel function while

the second term gives an elementary antiderivative, i.e.,

$$
\begin{aligned}
N_{px,x}\left(s_*, x_*, m_*, z_*\right) = & -\frac{1}{\pi} s_*^{\frac{1}{2}} \left[\frac{\left(x_*+m_*\right)^2 - z_*^2}{\left(\left(x_*+m_*\right)^2 + z_*^2\right)^{\frac{3}{2}}}\right] \mathrm{K}_1\left[\sqrt{s_*\left(x_*+m_*\right)^2 + s_* z_*^2}\right] \\
& -\frac{1}{\pi} s_* \left[\frac{\left(x_*+m_*\right)^2}{\left(x_*+m_*\right)^2 + z_*^2}\right] \mathrm{K}_0\left[\sqrt{s_*\left(x_*+m_*\right)^2 + s_* z_*^2}\right] + \frac{1}{\pi} \frac{\left(x_*+m_*\right)^2 - z_*^2}{\left[\left(x_*+m_*\right)^2 + z_*^2\right]^2} \\
& -\frac{1}{\pi} s_*^{\frac{1}{2}} \left[\frac{\left(x_*-m_*\right)^2 - z_*^2}{\left(\left(x_*-m_*\right)^2 + z_*^2\right)^{\frac{3}{2}}}\right] \mathrm{K}_1\left[\sqrt{s_*\left(x_*-m_*\right)^2 + s_* z_*^2}\right] \\
& -\frac{1}{\pi} s_* \left[\frac{\left(x_*-m_*\right)^2}{\left(x_*-m_*\right)^2 + z_*^2}\right] \mathrm{K}_0\left[\sqrt{s_*\left(x_*-m_*\right)^2 + s_* z_*^2}\right] + \frac{1}{\pi} \frac{\left(x_*-m_*\right)^2 - z_*^2}{\left[\left(x_*-m_*\right)^2 + z_*^2\right]^2}
\end{aligned}
\tag{2.79}
$$

Note that for the sake of brevity, explicit expressions for similar integrals in the sections below will be omitted.

Pore pressure in the time domain can be determined after taking the inverse Laplace transform. For example, for Eq. 2.76,

$$
\alpha p = -\frac{4G\left(2\eta - 1\right) a}{\pi R} \int_{r_*}^{\infty} \frac{\mathcal{L}^{-1}\left[s_*^{-1} \theta_p\left(s_*, x_*, z_*\right)\right] dx_*}{\sqrt{x_*^2 - r_*^2}} \tag{2.80}
$$

Here $\mathcal{L}^{-1}$ denotes the inverse Laplace transform with respect to s_*.

$$
\mathcal{L}^{-1}\left[\cdot\right] = \frac{1}{2\pi i} \int_{\gamma - i\infty}^{\gamma + i\infty} \left[\cdot\right] \exp\left(s_* t_*\right) ds_* \tag{2.81}
$$

Both Eqs. 2.72 and 2.76 can be used to determine the pore pressure field inside the half space ($z_* > 0$) in the Laplace domain. While it is easier to program with Eq. 2.72 in MATLAB, the result from direct numerical integration at some depths when $z_* < 0.05$ is not as smooth as that based on Eq. 2.76, see the inset in Fig. 2.4 showing the pore pressure distribution along the contact axis. The results are obtained with the properties of the Gulf of Mexico shale at $t_* = 10^{-4}$. The discrepancy at small z_* is because that as z_* becomes smaller, the oscillatory integrand in N_p approaches to zero slower than the case when z_* is relatively large. However,

the two algorithms yield excellent agreement when $z_* \geq 0.05$.

There are benefits in having both sets of expressions. On the one hand, Eq. 2.72 has the advantage in calculating the pore pressure at a specific location when $z_* \geq 0.05$ since the algorithm is less time consuming. On the other hand, Eq. 2.76 is more efficient in determining the full pore pressure field since once θ_p is computed for all x_*, the pore pressure at any position can be conveniently calculated all at once.

Fig. 2.5 shows the pore pressure distributions along the contact axis at various times from Eq. 2.72 for $z_* > 0.05$ and Eq. 2.76 for $z_* \leq 0.05$. Since a permeable surface is assumed, the pore pressure on the surface drops from the undrained asymptote to zero instantaneously. Along the contact axis, the pore pressure exhibits the Mandel-Cryer effect (Detournay and Cheng, 1993), where the pore pressure rises above the initial value at $t_* = 0_+$ before its dissipation, see the inset in Fig. 2.5.

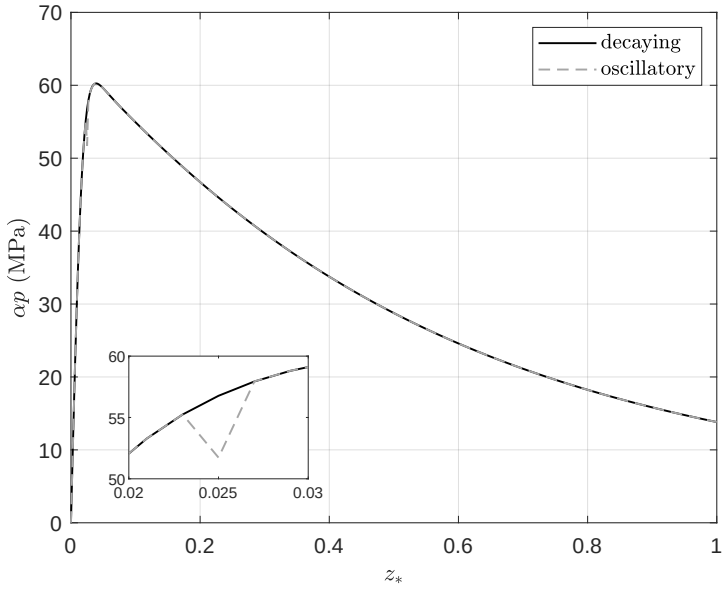

Figure 2.4: Pore pressure along the contact axis at $t_* = 10^{-4}$; evaluated based on Eq. 2.72 (dashed line) and Eq. 2.76 (solid line).

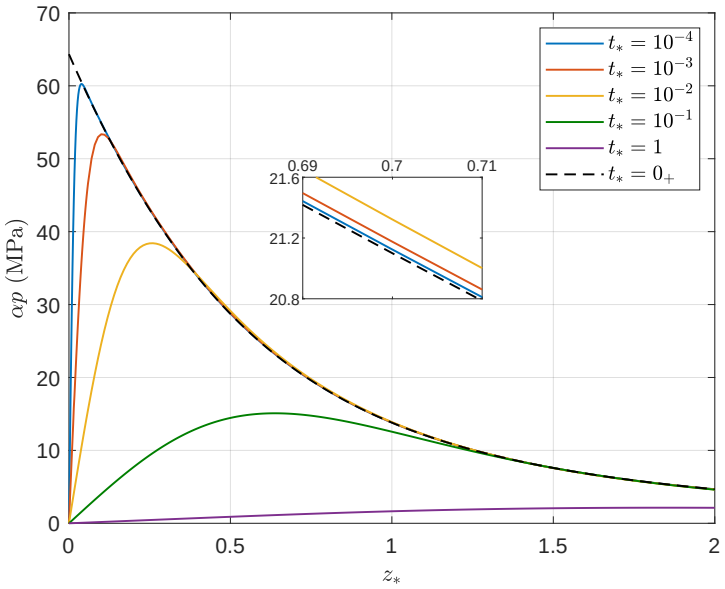

Figure 2.5: Distribution of the pore pressure along the contact axis.

2.5.2 Vertical Stress

Expression 1 The vertical stress field can be obtained after substituting Eqs. 2.17-2.20 and 2.32 into Eq. 2.12,

$$\begin{aligned}\overline{\sigma}_z = \frac{2Ga^3}{c\phi R s_*}\Bigg[&\int_0^1 \left(m_*^2 - 1\right) N_{sz}\left(s_*, r_*, m_*, z_*\right) dm_* \\ &+ \int_1^\infty m_*^{\frac{1}{2}} \theta_1\left(s_*, m_*\right) N_{sz}\left(s_*, r_*, m_*, z_*\right) dm_*\Bigg]\end{aligned} \tag{2.82}$$

where,

$$\begin{aligned}N_{sz}\left(s_*, r_*, m_*, z_*\right) = -\frac{2}{\pi}\int_0^\infty \xi_* \Bigg\{&\left(1 + z_*\xi_*\right)\exp\left(-z_*\xi_*\right) \\ +\frac{2\omega}{1+\omega}\left(\frac{\xi_*^2}{s_*}\right)&\left[\exp\left(-z_*\sqrt{\xi_*^2 + s_*}\right) - \frac{\sqrt{\xi_*^2 + s_*}}{\xi_*}\exp\left(-z_*\xi_*\right)\right]\Bigg\}\cos\left(m_*\xi_*\right) J_0\left(r_*\xi_*\right) d\xi_*\end{aligned} \tag{2.83}$$

Expression 2 Similar to the treatment for the pore pressure, an alternative expression for $\overline{\sigma}_z$ can be obtained by first applying Eq. 2.27 to Eq. 2.82,

$$\int_{x_*}^{\infty} \overline{\sigma}_z \frac{r_* dr_*}{\sqrt{r_*^2 - x_*^2}} = \frac{2Ga^3}{c\phi R s_*} \left[\int_0^1 \left(m_*^2 - 1 \right) N_{szx} \left(s_*, x_*, m_*, z_* \right) dm_* + \int_1^{\infty} m_*^{\frac{1}{2}} \theta_1 \left(s_*, m_* \right) N_{szx} \left(s_*, x_*, m_*, z_* \right) dm_* \right] \tag{2.84}$$

where,

$$N_{szx} \left(s_*, x_*, m_*, z_* \right) = -\frac{2}{\pi} \int_0^{\infty} \left\{ \left(1 + z_* \xi_* \right) \exp \left(-z_* \xi_* \right) + \frac{2\omega}{1+\omega} \left(\frac{\xi_*^2}{s_*} \right) \left[\exp \left(-z_* \sqrt{\xi_*^2 + s_*} \right) - \frac{\sqrt{\xi_*^2 + s_*}}{\xi_*} \exp \left(-z_* \xi_* \right) \right] \right\} \cos \left(m_* \xi_* \right) \cos \left(x_* \xi_* \right) d\xi_* \tag{2.85}$$

Inside the half space ($z_* > 0$), the vertical stress $\overline{\sigma}_z$ is continuous at $x_* \geq 0$. Applying the inverse Abel transform in Eq. 2.64 to Eq. 2.84 gives,

$$\overline{\sigma}_z = -\frac{4Ga^3}{\pi c\phi R s_*} \int_{r_*}^{\infty} \frac{\theta_{sz} \left(s_*, x_*, z_* \right) dx_*}{\sqrt{x_*^2 - r_*^2}} \tag{2.86}$$

where,

$$\theta_{sz} \left(s_*, x_*, z_* \right) = \int_0^1 \left(m_*^2 - 1 \right) N_{szx,x} \left(s_*, x_*, m_*, z_* \right) dm_* + \int_1^{\infty} m_*^{\frac{1}{2}} \theta_1 \left(s_*, m_* \right) N_{szx,x} \left(s_*, x_*, m_*, z_* \right) dm_* \tag{2.87}$$

and $N_{szx,x} = \partial N_{szx} / \partial x_*$,

$$N_{szx,x} \left(s_*, x_*, m_*, z_* \right) = \frac{2}{\pi} \int_0^{\infty} \xi_* \left\{ \left(1 + z_* \xi_* \right) \exp \left(-z_* \xi_* \right) + \frac{2\omega}{1+\omega} \frac{\xi_*^2}{s_*} \left[\exp \left(-z_* \sqrt{\xi_*^2 + s_*} \right) - \frac{\sqrt{\xi_*^2 + s_*}}{\xi_*} \exp \left(-z_* \xi_* \right) \right] \right\} \cos \left(m_* \xi_* \right) \sin \left(x_* \xi_* \right) d\xi_* \tag{2.88}$$

The first term in $N_{szx,x}$ has an elementary antiderivative. The second term can be expressed alternatively using the modified Bessel function. The last term can be evaluated with the aid of the method of contour integration, see Appendix A.2.

On the surface ($z_* = 0$), the vertical stress $\overline{\sigma}_z$ is non-trivial only when $r_* \leq 1$. Eq. 2.84 becomes,

$$\int_{x_*}^{\infty} \overline{\sigma}_z \frac{r_* dr_*}{\sqrt{r_*^2 - x_*^2}} = \frac{G\left(2\eta - 1\right) a^3}{c\eta R s_*} \left[1 - x_*^2 + x_*^{\frac{1}{2}} \theta_1\left(s_*, x_*\right)\right], \qquad x_* \leq 1_- \tag{2.89}$$

$$\int_{x_*}^{\infty} \overline{\sigma}_z \frac{r_* dr_*}{\sqrt{r_*^2 - x_*^2}} = 0, \qquad x_* \geq 1_+ \tag{2.90}$$

Since $\theta_1\left(s_*, 1\right)$ is positive at $s_* > 0$ (except $s_* \to \infty$), the right hand side of Eq. 2.89 is nonzero at $x_* = 1$, suggesting that the integrals above are discontinuous at $x_* = 1$. Inverse Abel transform in Eq. 2.65 is therefore applied to Eqs. 2.89 and 2.90 to obtain the contact pressure,

$$\overline{\sigma}_z = \frac{2G\left(2\eta - 1\right) a^3}{\pi c\eta R s_*} \begin{bmatrix} 2\sqrt{1 - r_*^2} + \dfrac{\theta_1\left(s_*, 1\right)}{\sqrt{1 - r_*^2}} \\ -\displaystyle\int_{r_*}^{1} \theta_3\left(s_*, x_*\right) \frac{dx_*}{\sqrt{x_*^2 - r_*^2}} \end{bmatrix}, \qquad r_* \leq 1 \tag{2.91}$$

where,

$$\theta_3\left(s_*, x_*\right) = \frac{\partial}{\partial x_*} \left[x_*^{\frac{1}{2}} \theta_1\left(s_*, x_*\right)\right] \tag{2.92}$$

The expression for evaluating $\theta_3\left(s_*, x_*\right)$ is given in Appendix A.3.

Contact pressure for the example case is shown in Fig. 2.6. The contact pressure from the full poroelastic solution reduces to the classical Hertzian solution at $t_* = 0_+$ and $t_* \to \infty$. At an intermediate time, the contact pressure is bounded by the two limits except near the contact edge around $r_* = 1$, where the contact pressure is in fact singular. Existence of such a singularity can be attributed to the assumption of a fixed contact radius a. The underlying reason can be found in the transient response of the surface displacement. As shown in Fig. 2.7, the fixed contact radius assumption allows a kink in the vertical displacement to develop at $r_* = 1$ at intermediate times.

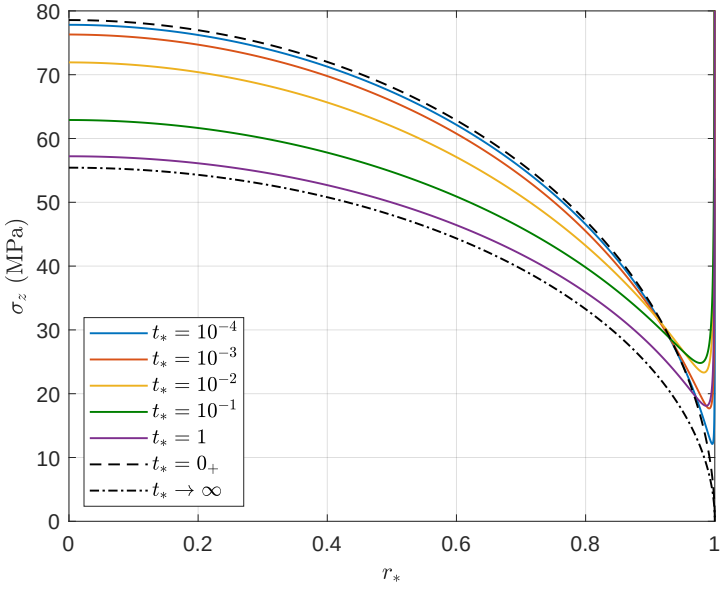

Figure 2.6: Distribution of the contact pressure at various dimensionless times.

2.5.3 Vertical Displacement

Expression 1 Vertical displacement $\overline{u}_z$ can be obtained after substituting Eqs. 2.17-2.20 and 2.32 into Eq. 2.10,

$$\begin{aligned}\overline{u}_z = \frac{a^4}{c\phi R s_*}\Bigg[&\int_0^1 \left(m_*^2 - 1\right) N_{uz}\left(s_*, r_*, m_*, z_*\right) dm_* \\ &+ \int_1^\infty m_*^{\frac{1}{2}} \theta_1\left(s_*, m_*\right) N_{uz}\left(s_*, r_*, m_*, z_*\right) dm_*\Bigg]\end{aligned} \tag{2.93}$$

where,

$$\begin{aligned}N_{uz}\left(s_*, r_*, m_*, z_*\right) = -\frac{2}{\pi}\int_0^\infty \Bigg\{&\left(\phi + z_*\xi_*\right)\exp\left(-z_*\xi_*\right) \\ &+ \frac{2\omega}{1+\omega}\frac{\xi_*\sqrt{\xi_*^2 + s_*}}{s_*}\left[\exp\left(-z_*\sqrt{\xi_*^2 + s_*}\right) - \exp\left(-z_*\xi_*\right)\right]\Bigg\}\cos\left(m_*\xi_*\right) J_0\left(r_*\xi_*\right) d\xi_*\end{aligned} \tag{2.94}$$

Expression 2 Applying Eq. 2.27 to Eq. 2.93 gives,

$$\int_{x_*}^{\infty} \overline{u}_z \frac{r_* dr_*}{\sqrt{r_*^2 - x_*^2}} = \frac{a^4}{c\phi R s_*} \left[\int_0^1 \left(m_*^2 - 1 \right) N_{uzx} \left(s_*, x_*, m_*, z_* \right) dm_* + \int_1^{\infty} m_*^{\frac{1}{2}} \theta_1 \left(s_*, m_* \right) N_{uzx} \left(s_*, x_*, m_*, z_* \right) dm_* \right] \tag{2.95}$$

where,

$$N_{uzx} \left(s_*, x_*, m_*, z_* \right) = -\frac{2}{\pi} \int_0^{\infty} \left\{ \xi_*^{-1} \left(\phi + z_* \xi_* \right) \exp \left(-z_* \xi_* \right) + \frac{2\omega}{1+\omega} \frac{\sqrt{\xi_*^2 + s_*}}{s_*} \left[\exp \left(-z_* \sqrt{\xi_*^2 + s_*} \right) - \exp \left(-z_* \xi_* \right) \right] \right\} \cos \left(m_* \xi_* \right) \cos \left(x_* \xi_* \right) d\xi_* \tag{2.96}$$

Inside the half space, applying Eq. 2.64 to Eq. 2.95 gives,

$$\overline{u}_z = -\frac{2a^4}{\pi c\phi R s_*} \int_{r_*}^{\infty} \frac{\theta_{uz} \left(s_*, x_*, z_* \right) dx_*}{\sqrt{x_*^2 - r_*^2}} \tag{2.97}$$

where,

$$\theta_{uz} \left(s_*, x_*, z_* \right) = \int_0^1 \left(m_*^2 - 1 \right) N_{uzx,x} \left(s_*, x_*, m_*, z_* \right) dm_* + \int_1^{\infty} m_*^{\frac{1}{2}} \theta_1 \left(s_*, m_* \right) N_{uzx,x} \left(s_*, x_*, m_*, z_* \right) dm_* \tag{2.98}$$

and $N_{uzx,x} = \partial N_{uzx} / \partial x_*$,

$$N_{uzx,x} \left(s_*, x_*, m_*, z_* \right) = \frac{2}{\pi} \int_0^{\infty} \left\{ \left(\phi + z_* \xi_* \right) \exp \left(-z_* \xi_* \right) + \frac{2\omega}{1+\omega} \frac{\xi_* \sqrt{\xi_*^2 + s_*}}{s_*} \left[\exp \left(-z_* \sqrt{\xi_*^2 + s_*} \right) - \exp \left(-z_* \xi_* \right) \right] \right\} \cos \left(m_* \xi_* \right) \sin \left(x_* \xi_* \right) d\xi_* \tag{2.99}$$

On the surface ($z_* = 0$), N_{uz} can be expressed in a closed form,

$$N_{uz} \left(s_*, r_*, m_*, 0 \right) = -\frac{2\phi}{\pi \sqrt{r_*^2 - m_*^2}} \mathcal{H} \left(r_* - m_* \right) \tag{2.100}$$

Substituting Eq. 2.100 into Eq. 2.93 gives,

$$\overline{u}_z = \frac{a^4}{cRs_*}\left(1 - \frac{r_*^2}{2}\right) \qquad r_* \leq 1 \tag{2.101}$$

and,

$$\overline{u}_z = \frac{a^4}{\pi cRs_*}\left[\begin{array}{l} \sqrt{r_*^2 - 1} + \left(2 - r_*^2\right)\arcsin\left(\dfrac{1}{r_*}\right) \\ -2\displaystyle\int_1^{r_*} m_*^{\frac{1}{2}}\theta_1\left(s_*, m_*\right)\frac{dm_*}{\sqrt{r_*^2 - m_*^2}} \end{array}\right] \qquad r_* \geq 1 \tag{2.102}$$

Vertical and radial displacement expressions in Eqs. 2.101-2.102 and Eqs. A.16-A.17 allow us to examine how the surface displacement evolves with time and differs from that of the case if the frictionless contact with a rigid sphere were to be modeled. At a given time, the plot of u_z vs. $\left(r + u_r\right)/a$ at $z = 0$ could be viewed as the profile of the displaced surface. Denote $\delta_r\left(t_*\right)$ as the radial distance between the displaced surface and the spherical indenter profile for $r_* \leq 1$ at $z = 0$. At the undrained and drained limits,

$$\delta_r\left(0\right) = \frac{4d\left(\phi - 1\right)}{3\pi\phi r_*}\left[1 - \left(1 - r_*^2\right)^{\frac{3}{2}}\right] = \frac{2d\left(1 - 2\nu_u\right)}{3\pi\left(1 - \nu_u\right)r_*}\left[1 - \left(1 - r_*^2\right)^{\frac{3}{2}}\right] \tag{2.103}$$

$$\delta_r\left(\infty\right) = \frac{2d}{3\pi\eta r_*}\left[1 - \left(1 - r_*^2\right)^{\frac{3}{2}}\right] = \frac{2d\left(1 - 2\nu\right)}{3\pi\left(1 - \nu\right)r_*}\left[1 - \left(1 - r_*^2\right)^{\frac{3}{2}}\right] \tag{2.104}$$

Depending on the drained and undrained Poisson's ratios, ν and ν_u, responses of the surface displacement can indeed be categorized into three distinct types.

When $\nu = \nu_u = 0.5$, radial displacement $u_r = 0$ on the surface ($\omega = 0$, $\phi = 1$ and $1/\eta = 0$). This is the peculiar case when the problem is actually not time-dependent and in essence the same as the Hertzian contact problem. Therefore, the surface displacement profile always conforms to that of a rigid sphere as long as the Hertzian assumption of parabolic surface displacement remains valid at small depth. Interestingly, this case of $\omega = 0$ is not all trivial as far as time dependence is concerned. As shown in Sections 2.7.2, mathematically, it still gives a meaningful expression for the normalized transient indentation force response, where the early and late time asymptotes can be found in closed-form.

When $\nu < 0.5$ and $\nu_u = 0.5$, namely, when the skeleton is compressible while the constituents are incompressible ($\phi = 1$), $u_r = 0$ and $\delta_r(0) = 0$ at the undrained limit, but $\delta_r(\infty) > 0$. Evolution of the displaced surface is shown in Fig. 2.7(a) where position of the spherical indenter is marked by a solid line. The contact edge for the deformed surface is marked by an empty circle. Results in Fig. 2.7(a) are calculated with $K_s \to \infty$ and $K_f \to \infty$ while all other parameters remain the same as those in Table 2.3. At the undrained limit, the displaced surface profile conforms to that of the spherical indenter and the free surface at $r_* > 1$ is beneath the indenter. During the transient phase ($t_* > 0$), the contact surface shifts to the left and is now above the indenter position and the free surface outside of the contact region rises and subsides to eventually approach the solution at the drained limit. This means if the frictionless contact between the indenter and the half space were to be modeled, edge of the contact will gradually move outwards from $r_* = 1$ and then recede back at the drained limit. We could expect that the contact radius to become time-dependent. Note that $\delta_r(0)$ and $\delta_r(\infty)$ are not affected by the surface drainage condition. In addition, it can be observed that a kink in the displacement profile develops at the contact edge during the transient phase, which in turn gives rise to the stress singularity observed in Fig. 2.6.

When $\nu < 0.5$ and $\nu_u < 0.5$, namely, when the constituents are now compressible, instantaneous radial displacement is no longer zero and $\delta_r(0) > 0$, see Fig. 2.7(b) showing the results with properties of the Gulf of Mexico shale in Table 2.3. As such, even at $t_* = 0_+$, the surface displacement profile no longer coincides with that of the spherical indenter, and a kink appears in the displacement profile during the transient phase.

The reason that the displaced surface profile deviates from that of the spherical indenter can be attributed to the fact only normal displacement is prescribed within $r_* \leq 1$ in modeling the indentation action. To what a degree the theoretical solution derived in this work differs from the case when the frictionless contact with a rigid sphere will be investigated numerically in Chapter 6. It will be shown the theoretical solution especially the integrated response such as the indentation force remains valid as long as the indentation strain d/R is small, with which the discrepancy in the surface displacement is not significant.

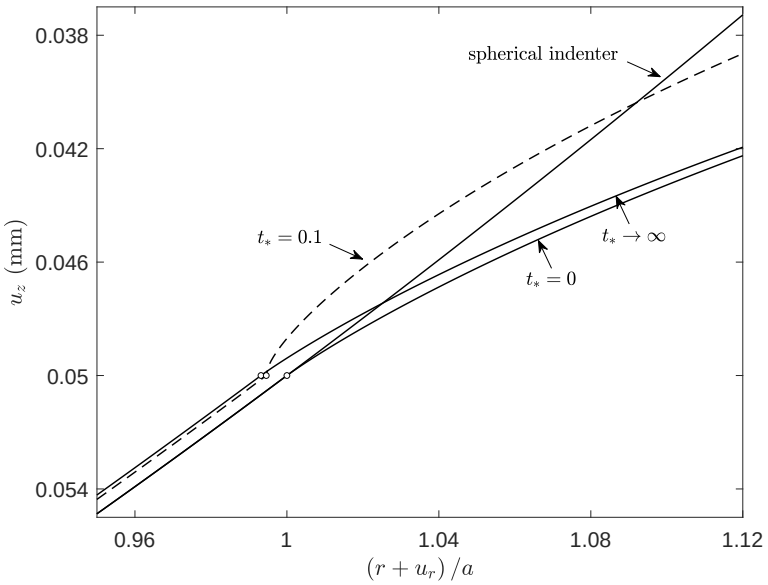

(a) incompressible constituents, $\nu = 0.219$ and $\nu_u = 0.5$

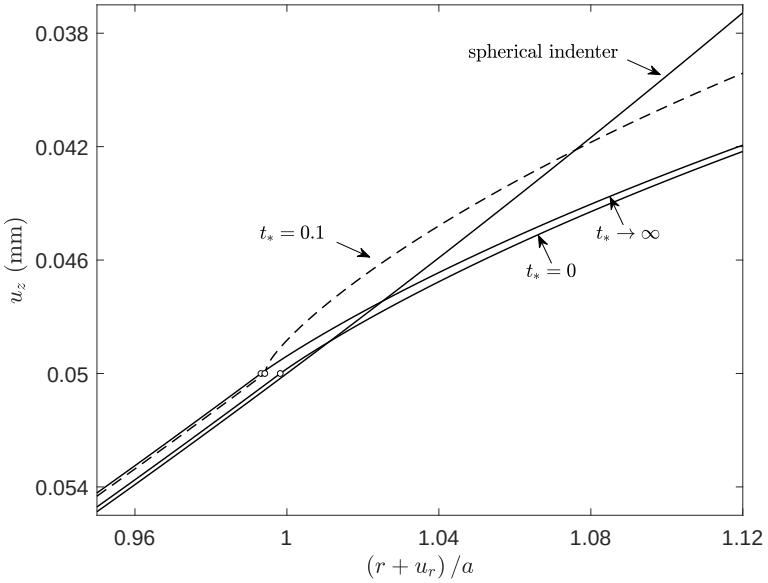

(b) compressible constituents, $\nu = 0.219$ and $\nu_u = 0.449$

Figure 2.7: Comparison of surface displacement profiles at the undrained and drained limits ($t_* = 0_+$, $t_* \to \infty$) and at $t_* = 0.1$ from case I; the material points at the contact edge are marked by the empty circles.

2.6 Incipient Failure

Incipient failure in form of tensile fracturing and plastic deformation could take place in spherical indentation. It is therefore of interest to examine how poroelasticity could affect potential development of the indentation crack system and plastic failure. Biot's effective stress definition, $\sigma'_{ij} = \sigma_{ij} - \alpha p$, is adopted in the analysis below.

2.6.1 Cone Crack Initiation

The classical Hertzian cone crack initiates on the surface as a ring crack slightly outside of the contact area and propagates stably downwards to form a cone (Lawn, 1998). Since the pore pressure is zero on the surface in this problem, the effective stresses equal to the total stresses. As shown in Fig. 2.8, the total/effective radial stress at the contact edge ($r_* = 1_+$) is always in tension. At $t_* = 5 \times 10^{-5}$, $\sigma_r = -8.16$ MPa. Magnitude of the radial stress then increases with time to reach its maximum, $\sigma_r = -16.12$ MPa at $t_* = 0.03$. Eventually, the radial stress asymptotes to $\sigma_r = -10.40$ MPa at late time. Since tensile strength of a shale is usually smaller than 10 MPa, a cone crack is very likely to occur in this case. In addition, the fact that the largest radial stress magnitude occurs at an intermediate time suggests that even if a cone crack does not initiate immediately when the indenter gets in contact with the porous medium, it may still appear after a certain time. However, it should be mentioned that these results should be understood with the fixed contact radius assumption in mind. How the tensile stress distribution will be affected by a moving contact boundary will need to be examined in future work.

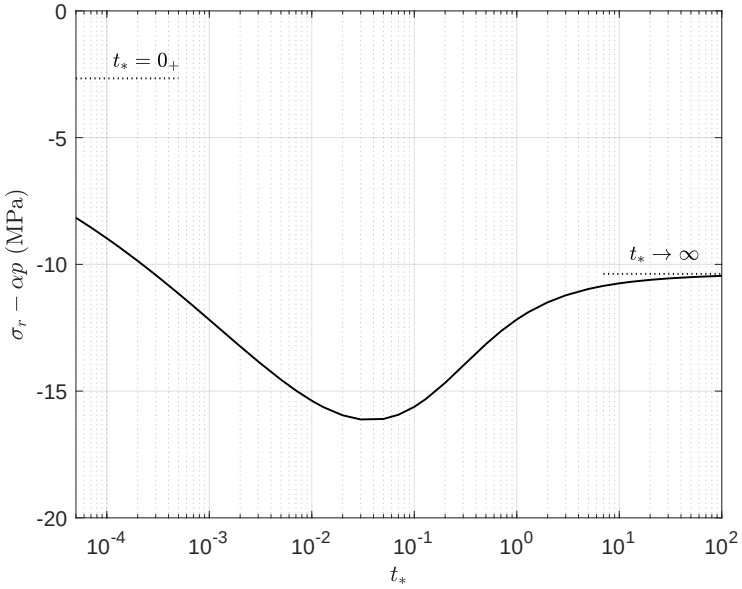

Figure 2.8: Variation of the total/effective radial stress with the dimensionless time at $r_* = 1_+$ on the surface (right outside of the contact area).

2.6.2 Median Crack Initiation

According to the Hertzian solution, variation of the radial or tangential stress along the contact axis is not monotonic and the maximum tensile stress occurs beneath the surface. Theoretically, a penny-shaped median crack may therefore nucleate from this location. Distribution of the total radial stress along the contact axis from the poroelastic solution is shown in Fig. 2.9. Since a permeable boundary is assumed on the surface, the radial stress on the surface drops almost instantaneously from the undrained asymptote to a value slightly below the drained asymptote.

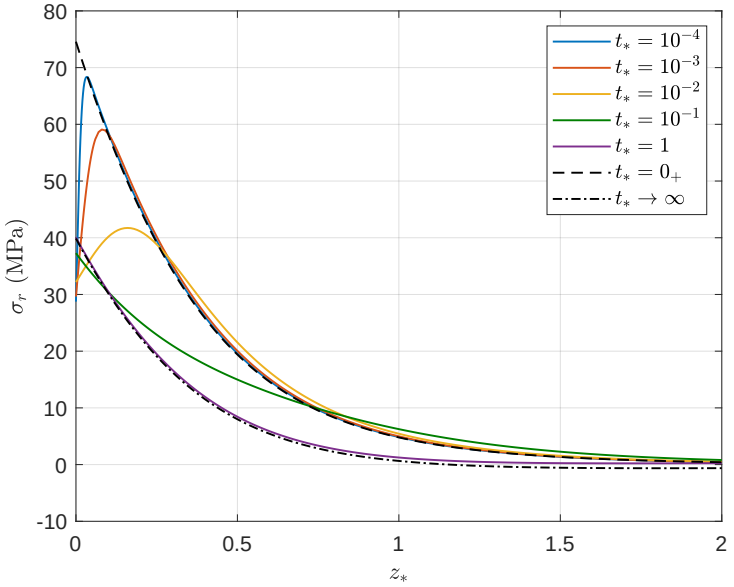

Figure 2.9: Variation of the radial stress along the contact axis.

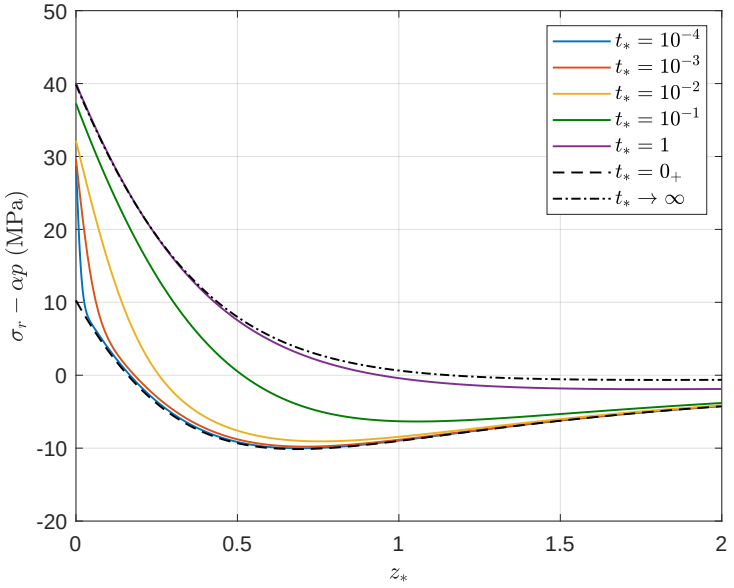

Figure 2.10: Variation of the effective radial stress along the contact axis.

The total stress reaches its maximum in tension at $z_* = 4.76$ with $\nu_u = 0.449$ at $t_* = 0_+$ and $z_* = 1.83$ with $\nu = 0.219$ at $t_* \to \infty$, respectively. Meanwhile, the effective radial stress distribution in Fig. 2.10 shows at $t_* = 0_+$, a maximum in tension, $\sigma_r' = -10.129$ MPa, is reached at $z_* = 0.69$. This magnitude is much larger than the tension maxima for the total radial stress at the drained and undrained limits. Since this maximum tensile stress occurs at the undrained limit, it is not affected by the surface drainage condition. This indicates that for all three surface drainage cases, due to the poroelastic effect, the median crack is more likely to be induced at an early time at a depth much smaller, compared with what is predicted by the Hertzian solution with either drained or undrained properties.

2.6.3 Onset of Plastic Deformation

At a given location, the maximum shear stress, $(\sigma_z - \sigma_r)/2$, can be used to infer the possibility of incipient plastic yielding. The Hertzian solution predicts plastic yielding to occur first only beneath the surface, see the dashed curves for $t_* = 0_+$ and ∞ in Fig. 2.11. However, the early time isochrones from the poroelastic solution reveal that the shear stress near the surface is in fact comparable to the maxima around $z_* = 0.5$ on the contact axis. This suggests that plastic deformation could take place almost instantaneously on the contact surface as well as inside the domain. However, it should be noted that in addition to the shear stress, failure for materials such as rocks could also depend on the effective mean stress. Since the effective mean stress is the most compressive right beneath the indenter, plastic deformation may not necessarily occur near the contact surface if the material behavior is governed by a pressure-sensitive failure criterion such as Mohr-Coulomb or Drucker-Prager.

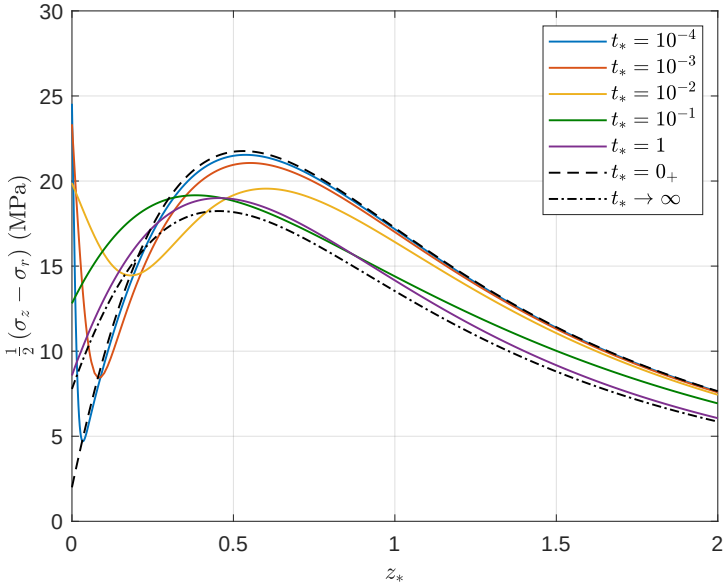

Figure 2.11: Variation of the maximum shear stress along the contact axis.

2.7 Indentation Force Relaxation

2.7.1 Master Curves

The ratio between the undrained and drained asymptotes of the contact pressure (see Section 2.5.2) can be expressed as,

$$\left.\frac{\lim\limits_{t\to 0}\sigma_z}{\lim\limits_{t\to\infty}\sigma_z}\right|_{z_*=0} = \frac{2\eta}{(2\eta-1)\,\phi} = 1+\omega \tag{2.105}$$

Since the contact radius is assumed to remain fixed in this model, the ratio of the indentation forces at the undrained and drained states is also,

$$\frac{F(0)}{F(\infty)} = 1+\omega \tag{2.106}$$

where $F(t)$ is the indentation force as a function of time. Indeed, integrating the normal stress over the contact area at $t_* = 0_+$ and $t \to \infty$, the Hertzian solutions for the indentation force

are recovered,

$$F(0) = \frac{16Ga^3}{3\phi R} \tag{2.107}$$

$$F(\infty) = \frac{8G(2\eta - 1)a^3}{3\eta R} \tag{2.108}$$

A normalized indentation force $F_n(t_*)$ can be defined in a similar fashion to the degree of consolidation in Terzaghi's one-dimensional consolidation theory (Terzaghi, 1943), i.e.,

$$F_n(t_*) = \frac{F(t_*) - F(\infty)}{F(0) - F(\infty)} \tag{2.109}$$

where $F_n(0) = 1$ and $F_n(\infty) = 0$. The explicit expression for $F_n(t_*)$ is,

$$F_n(t_*) = \frac{3}{2\omega}\mathcal{L}^{-1}\left[s_*^{-1}\int_0^1 x_*^{\frac{1}{2}}\theta_1(s_*, x_*)\,dx_*\right] \tag{2.110}$$

Eq. 2.110 shows that the normalized transient force response is affected by material properties only through constant ω. Moreover, as shown in Fig. 2.12, relaxation of the normalized indentation force does not appear to be very sensitive to ω. Indeed, the dimensionless time $t_{*0.5}$ at which $F_n(t_{*0.5}) = 0.5$ varies only within a narrow range, $t_{*0.5} \in [0.0966, 0.1304]$ for $\omega \in [0, 1]$, see Fig. 2.13. In addition, it should be noted that though at $\omega = 0$, the indentation force remains constant and $F_n(t_*)$ appears to become indefinite, mathematically, the limit of $F_n(t_*)$ at $\omega = 0$ exists and can still be calculated with our algorithms.

If the solid and fluid phases can be assumed as incompressible, we have $\omega = 1 - 2\nu$. The normalized force relaxation behavior is now affected by the Poisson's ratio only. Effect of the Poisson's ratio on the force relaxation response was previously observed in the numerical analysis of poroelastic indentation with a flat punch in plane strain (Bouklas et al., 2015). Nevertheless, the insensitivity to ω shown in Fig. 2.12 signifies that the dependence of $F_n(t_*)$ on ν is rather weak. That could perhaps explain though the effect of the Poisson's ratio is not accounted for in the master curves constructed based on numerical analysis, e.g., Hu et al. (2010), those master curves still provide consistent interpretation for their experimental results.

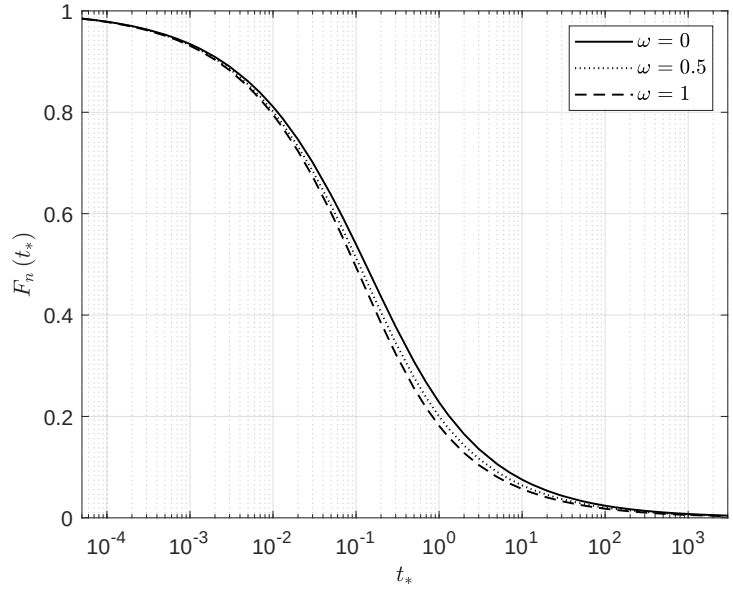

Figure 2.12: Relaxation of the normalized indentation force with the dimensionless time.

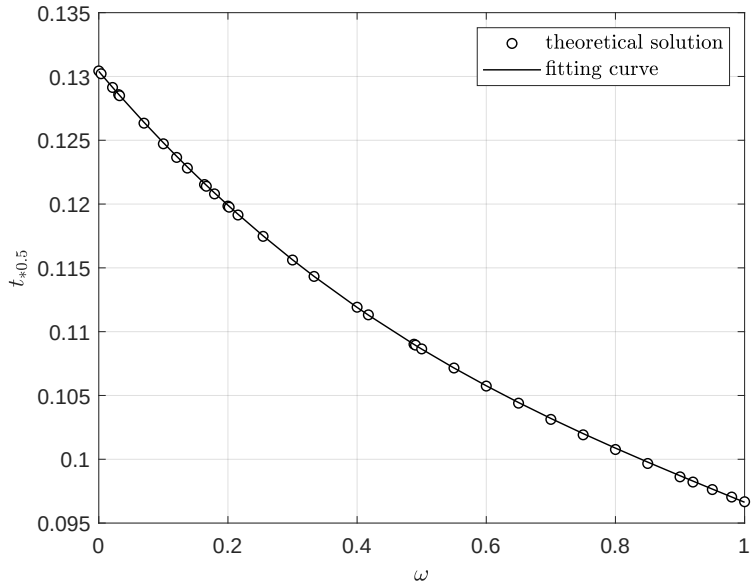

Figure 2.13: Dimensionless time $t_{*0.5}$ as a function of ω, fitted by $t_{*0.5} = 0.1304 - 0.05968\omega + 0.03869\omega^2 - 0.01278\omega^3$.

The force relaxation response from our theoretical solution, see Fig. 2.12, can be fitted by a four-parameter function $f_n(t_*)$,

$$f_n(t_*) = \frac{1}{2}\left(\frac{1}{1+a_1 t_*^{b_1}} + \frac{1}{1+a_2 t_*^{b_2}}\right) \tag{2.111}$$

The fitting parameters a_1, b_1, a_2, b_2 are listed in Table 2.4 for $\omega \in [0,1]$. Indeed, this elementary function gives an excellent approximation and the coefficient of determination for all ω is $R^2 = 1$. Therefore, the fitting function in Eq. 2.111 with the parameters from Table 2.4 can be readily used as the basis for experimental analysis. Insensitivity of the force relaxation response to ω means that these master curves can be a rather reliable means for determining diffusivity c, since the end result will not be much affected by the uncertainty in ω. Consequently, for an arbitrary ω, linear interpolation with the data in Table 2.4 can simply be used to find the fitting parameters.

ω	a_1	b_1	a_2	b_2
0	2.945	0.4636	3.906	0.733
0.1	3.013	0.4646	4.127	0.743
0.3	3.149	0.467	4.536	0.761
0.44	3.239	0.4686	4.801	0.773
0.5	3.278	0.4694	4.912	0.778
0.7	3.402	0.4718	5.262	0.793
0.9	3.52	0.474	5.589	0.806
1	3.58	0.4752	5.745	0.813

Table 2.4: Values of the fitting parameters for the force relaxation curves.

A protocol of data interpretation for this type of indentation experiment can be established as follows. The two force asymptotes can be used to determine material constants G/ϕ, $G(2\eta-1)/\eta$ and the ratio of the two asymptotes gives constant ω. Once ω is known, hydraulic diffusivity c can be determined by matching the transient force response with the fitting function $f_n(t_*)$. In addition, if the undrained and drained asymptotes can be clearly identified from the experimental data, the diffusion coefficient c can also be computed from $t_{*0.5}$ via the fitting function, $t_{*0.5} = 0.13 - 0.0597\omega + 0.0387\omega^2 - 0.0128\omega^3$.

2.7.2 Asymptotic Behaviors

While the Hertzian solution gives the indentation force asymptotes at $t_* = 0_+$ and ∞, closed-form asymptotic expressions beyond these two limits can be derived for the particular case of $\omega = 0$.

Substituting Eq. 2.54 into Eq. 2.110 and setting $\omega = 0$ gives,

$$F_n(t_*) = \frac{3}{2}\mathcal{L}^{-1}\left[s_*^{-1}\int_0^1 x_*^{\frac{1}{2}} M(s_*, x_*)\, dx_*\right] \tag{2.112}$$

The integral in Eq. 2.112 can be expressed explicitly using the modified Struve function and the generalized hypergeometric functions. Detailed derivation can be found in Appendix A.4.

$$\int_0^1 x_*^{\frac{1}{2}} M(s_*, x_*)\, dx_* = \frac{2}{3} - \frac{4}{\pi\sqrt{s_*}} + \frac{2}{s_*}\left[1 - \mathrm{F}(s_*)\right] \tag{2.113}$$

where,

$$\mathrm{F}(s_*) = \mathrm{F}_{1,2}\left[\begin{matrix} 0.5 \\ (1, 1.5) \end{matrix}, s_*\right] - \frac{2}{\pi} s_*^{\frac{1}{2}} \mathrm{F}_{2,3}\left[\begin{matrix} (1,1) \\ (1.5, 1.5, 2) \end{matrix}, s_*\right] \tag{2.114}$$

with $\mathrm{F}_{1,2}[\cdot]$ and $\mathrm{F}_{2,3}[\cdot]$ being two generalized hypergeometric functions.

Asymptotic expressions for indentation force relaxation at early and late times can be obtained by applying inverse Laplace transform to the integrals above when $s_* \to \infty$ and $s_* \to 0$ (Bateman, 1954; Olver, 2010). The first few terms at $\omega = 0$ can be expressed as follows.

- early time ($t_* \to 0$),

$$\begin{aligned} \lim_{t_* \to 0} F_n(t_*) &= 1 - \frac{12}{\pi}\left(\frac{t_*}{\pi}\right)^{\frac{1}{2}} + 3t_* \\ &+ 2\left(\frac{t_*}{\pi}\right)^{\frac{3}{2}} \ln t_* - 2\left(\gamma + 2\ln 2 + \frac{8}{3}\right)\left(\frac{t_*}{\pi}\right)^{\frac{3}{2}} + \frac{\pi}{5}\left(\frac{t_*}{\pi}\right)^{\frac{5}{2}} \end{aligned} \tag{2.115}$$

  where $\gamma = 0.57721...$ is the Euler constant.

- late time ($t_* \to \infty$),

$$\lim_{t_* \to \infty} F_n(t_*) = \pi^{-\frac{3}{2}} \left(\frac{4}{3} t_*^{-\frac{1}{2}} - \frac{16}{225} t_*^{-\frac{3}{2}} + \frac{8}{1225} t_*^{-\frac{5}{2}} - \frac{64}{99225} t_*^{-\frac{7}{2}} \right) \tag{2.116}$$

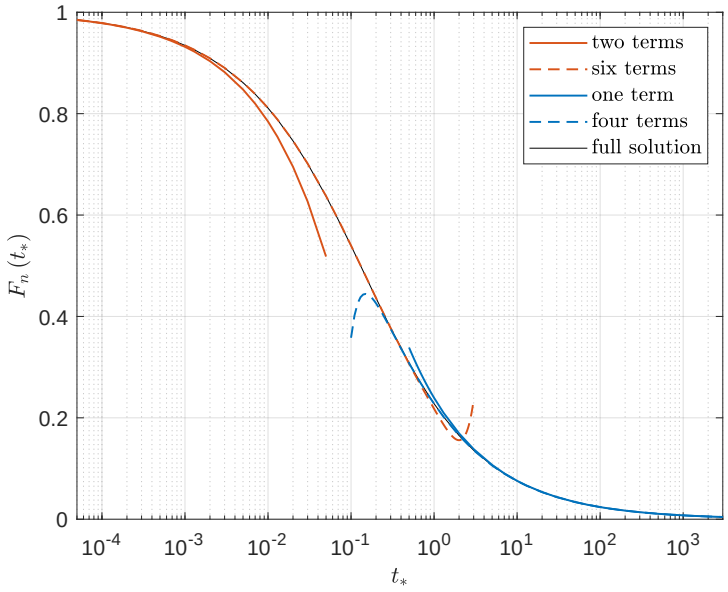

Figure 2.14: Comparison of the asymptotic expressions with the full solutions for the normalized indentation force $F_n(t_*)$ at $\omega = 0$.

Fig. 2.14 shows that these asymptotes capture the force relaxation behavior at $\omega = 0$ remarkbly well not just for the very small and large times. A combination of the six-term early time asymptote with the four-term late time asymptote could provide an excellent approximation to the full solution for the entire time range. For the general case when $\omega \neq 0$, closed-form asymptotic expressions cannot be obtained. A comparison of the early time behaviors from the full solution for $\omega = 0$, 0.5 and 1 is shown in Fig. 2.15(a) in a log-log scale. It seems that constant ω barely has any influence on the early time responses. Indeed, given a tolerance of 1%, the first two-term in Eq. 2.115 remains valid up to $t_* = 5 \times 10^{-3}$ and 7×10^{-3} for $\omega = 0.5$ and 1, respectively. At late times, the force relaxation curves appear to be parallel to each other, see Fig. 2.15(b), suggesting $F_n(t_*) \sim t_*^{-\frac{1}{2}}$ is the dominant behavior when t_* is large.

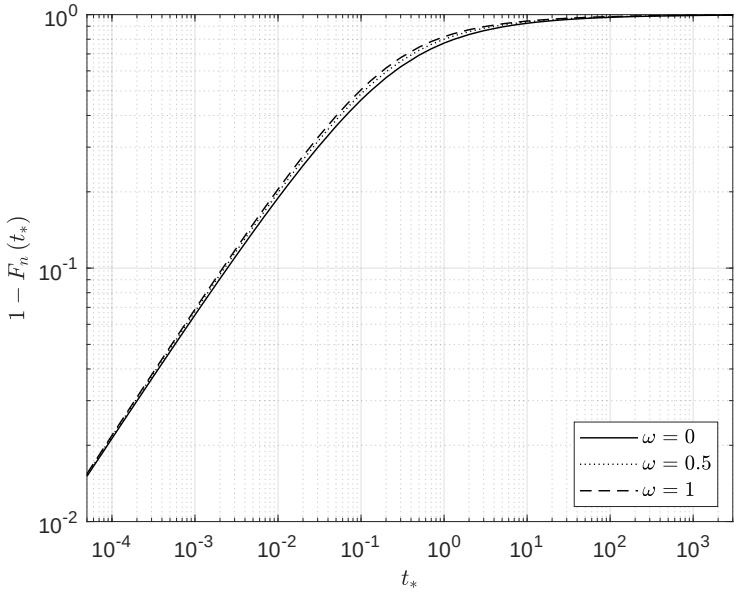

(a) early time behaviors

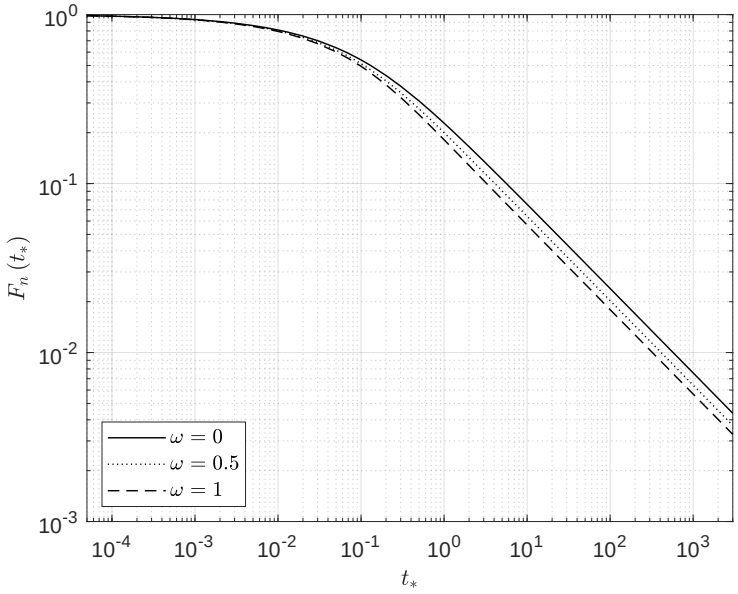

(b) late time behaviors

Figure 2.15: Asymptotic behaviors of the normalized indentation force at $\omega = 0$, 0.5 and 1 for case I.

3 POROELASTIC RESPONSE OF SPHERICAL INDENTATION INTO A HALF SPACE WITH AN IMPERMEABLE SURFACE VIA STEP DISPLACEMENT

3.1 Introduction

The problem of poroelastic spherical indentation into a half space with an impermeable surface via step displacement is dealt with in this chapter. As far as the method of solution is concerned, since change in the drainage condition from case I to case II does not cause any structural change in the dual integral equations for determining the unknowns for the full solution, the mathematical techniques and solution procedure we previously developed can be readily applied here.

Formulation of the problem and derivation of the solution for the poroelastic fields are first presented. Effects of poroelasticity on incipient failures in the context of initiation of the indentation crack systems and onset of plasticity are then analyzed. Master curves of indentation force relaxation are constructed. For the particular case of $\omega = 0$, closed-form asymptotic expressions of the transient indentation force response are derived for both early and late times.

3.2 Problem Formulation

The boundary condition for case II surface drainage can be written in terms of vertical displacement u_z, stresses σ_z and σ_{zr}, and normal flux q_z on the surface, see Table 3.1, where $\mathcal{H}(t)$ is the Heaviside step function.

In the McNamee-Gibson displacement function method, poroelastic fields including pore pressure, stresses and displacements can be directly expressed using displacement functions $\mathcal{D}$ and $\mathcal{F}$, which satisfy two partial differential equations. Solutions for $\mathcal{D}$ and $\mathcal{F}$ are obtained from Hankel transform in the Laplace domain, which can be expressed in integral forms in terms of three unknowns A_1, A_2 and B_1. Detailed equation expressions and explanations of all

material constants therein can be found in Section 2.2.

	time domain	Laplace domain
$0 \leq r \leq a_-$	$u_z = \left(d - \frac{r^2}{2R}\right)\mathcal{H}(t)$	$\overline{u}_z = s^{-1}\left(d - \frac{r^2}{2R}\right)$
	$\sigma_{zr} = 0,\ q_z = 0$	$\overline{\sigma}_{zr} = 0,\ \overline{q}_z = 0$
$r \geq a_+$	$\sigma_z = \sigma_{zr} = 0,\ q_z = 0$	$\overline{\sigma}_z = \overline{\sigma}_{zr} = 0,\ \overline{q}_z = 0$

Table 3.1: Boundary conditions.

Matching the poroelastic fields with the boundary conditions in the Laplace domain yields the following equations,

$$A_1\xi + A_2\sqrt{\xi^2+\lambda} + B_1(1-\phi) = 0 \tag{3.1}$$

$$A_2\sqrt{\xi^2+\lambda} + \frac{\phi + 2\eta(1-\phi)}{\eta\lambda}B_1\xi^2 = 0 \tag{3.2}$$

and a dual integral equation that contains only the unknown B_1,

$$\int_0^\infty B_1 J_0(r\xi)\,d\xi = (s\phi)^{-1}\left(\frac{r^2}{2R} - d\right), \qquad 0 \leq r \leq a_- \tag{3.3}$$

$$\int_0^\infty [1 + \omega H(s,\xi)]\,\xi B_1 J_0(r\xi)\,d\xi = 0, \qquad r \geq a_+ \tag{3.4}$$

where,

$$H(s,\xi) = 1 + \frac{2\xi^2}{\lambda}\left(\frac{\xi}{\sqrt{\xi^2+\lambda}} - 1\right) \tag{3.5}$$

The problem now reduces to first finding B_1 through Eqs. 3.3-3.4 and then A_1 and A_2 from Eqs. 3.1-3.2.

3.3 Solution Procedure

3.3.1 Fredholm Integral Equation of the Second Kind

According to Noble (1963), the pair of dual integral equations in Eqs. 3.3 and 3.4 can be reduced to a Fredholm integral equation of the second kind. As shown in Section 2.4.1, the

solution of the dual integral equation can be expressd as,

$$\begin{aligned} B_1\xi^{-\frac{1}{2}} = &\sqrt{\frac{2}{\pi}}\left(s\phi R\right)^{-1}\int_0^a m^{\frac{1}{2}}\left(m^2 - Rd\right)J_{-\frac{1}{2}}\left(m\xi\right)dm \\ &+\sqrt{\frac{2}{\pi}}\left(s\phi R\right)^{-1}\int_a^\infty m\theta\left(s,m\right)J_{-\frac{1}{2}}\left(m\xi\right)dm \end{aligned} \tag{3.6}$$

where $\theta\left(s,m\right)$ satisfies a Fredholm integral equation of the second kind.

Based on the dimensionless variables defined in Eqs. 2.34 and 2.35, the Fredholm integral equation for $\theta_1\left(s_*,x_*\right)$ is given by,

$$\theta_1\left(s_*,x_*\right) + \omega\int_1^\infty N\left(s_*,x_*,m_*\right)\theta_1\left(s_*,m_*\right)dm_* = \omega M\left(s_*,x_*\right) \tag{3.7}$$

where,

$$N\left(s_*,x_*,m_*\right) = m_*\int_0^\infty \xi_* H_1\left(s_*,\xi_*\right)J_{-\frac{1}{2}}\left(x_*\xi_*\right)J_{-\frac{1}{2}}\left(m_*\xi_*\right)d\xi_* \tag{3.8}$$

$$M\left(s_*,x_*\right) = \int_0^1 m_*^{-\frac{1}{2}}\left(1-m_*^2\right)N\left(s_*,x_*,m_*\right)dm_* \tag{3.9}$$

$$H_1\left(s_*,\xi_*\right) = 1 + \frac{2\xi_*^2}{s_*}\left(\frac{\xi_*}{\sqrt{\xi_*^2+s_*}} - 1\right) \tag{3.10}$$

Now $\theta_1\left(s_*,x_*\right)$ is the unknown to be determined. Once it is known, all field quantities can be expressed in the Laplace domain in terms of $\theta_1\left(s_*,x_*\right)$. Note that $\theta_1\left(s_*,x_*\right)$ is influenced by the material properties only through ω.

3.3.2 Alternative Expression for $N\left(s_*,x_*,m_*\right)$

Prior to finding the solution to Eq. 3.7, functions $N\left(s_*,x_*,m_*\right)$ and $M\left(s_*,x_*\right)$ need to be evaluated. The integral kernel in Eq. 3.8 for $N\left(s_*,x_*,m_*\right)$ is highly oscillatory. However, we can rewrite the integral alternatively using two modified Struve functions of the second kind,

$\mathrm{M}_0(\cdot)$ and $\mathrm{M}_1(\cdot)$,

$$N(s_*, x_*, m_*) = \sqrt{\frac{s_* m_*}{x_*}} \left\{ \left[\frac{2}{\pi} - \frac{\mathrm{M}_0(y_1)}{y_1} + \left(1 + \frac{2}{y_1^2}\right) \mathrm{M}_1(y_1) \right] + \left[\frac{2}{\pi} - \frac{\mathrm{M}_0(y_2)}{y_2} + \left(1 + \frac{2}{y_2^2}\right) \mathrm{M}_1(y_2) \right] \right\} \tag{3.11}$$

where $y_1 = |x_* - m_*| \, s_*^{\frac{1}{2}}$ and $y_2 = (x_* + m_*) \, s_*^{\frac{1}{2}}$.

One type of the integral representations of $\mathrm{M}_0(\cdot)$ and $\mathrm{M}_1(\cdot)$ has an exponential decaying integrand and a bounded upper limit, see Eqs. 2.44-2.49. Consequently, asymptotes for $N(s_*, x_*, m_*)$ at the undrained and drained limits and in the far-field can be expressed as,

$$\lim_{s_* \to \infty} N(s_*, x_*, m_*) = \delta(m_* - x_*) \tag{3.12}$$

$$\lim_{s_* \to 0} N(s_*, x_*, m_*) = 0 \tag{3.13}$$

$$\lim_{x_* \to \infty} N(s_*, x_*, m_*) = \frac{24}{\pi} \sqrt{\frac{m_*}{s_*^3 x_*^9}} \tag{3.14}$$

where $\delta(\cdot)$ is the Dirac delta function. In contrast to Eq. 3.8, the alternative expression for $N(s_*, x_*, m_*)$ in Eq. 3.11 can be numerically integrated efficiently and effectively. The numerical integration results are very well behaved at large s_* even when $N(s_*, x_*, m_*)$ is approaching the Dirac delta function at $m_* = x_*$.

Closed form solutions for $M(s_*, x_*)$ can be derived based on its alternative expression for $N(s_*, x_*, m_*)$. In case I, the closed form expression consists of special functions such as hypergeometric functions, which barely offers any advantage over direct numerical integration. In contrast, in case II, the exact expression of $M(s_*, x_*)$ is simpler since it is composed of special functions only with $\mathrm{M}_0(\cdot)$ and $\mathrm{M}_1(\cdot)$. The expression is given in Appendix B.3.

3.3.3 Method of Successive Substitution

To solve for $\theta_1(s_*, x_*)$ in Eq. 3.7, we adopt the method of successive substitution (Zemyan, 2012) by letting,

$$\theta_1(s_*, x_*) = -\sum_{n=0}^{\infty} (-\omega)^{n+1} a_n(s_*, x_*) \tag{3.15}$$

where,

$$a_0(s_*, x_*) = M(s_*, x_*) \tag{3.16}$$

$$a_n(s_*, x_*) = \int_1^{\infty} N(s_*, x_*, m_*) a_{n-1}(s_*, m_*) dm_*, \qquad n = 1, 2, 3... \tag{3.17}$$

As has been shown in Section 2.4.3, an advantage of the method of successive substitution is that it is able to reflect the asymptotic behavior of $\theta_1(s_*, x_*)$ at $x_* \to \infty$. Now the expression of $\theta_1(s_*, x_*)$ is given in terms of a sum of an alternating series. While the series converges rather fast when $\omega \leq 0.5$ and a partial sum with the first 20 terms is sufficient to give a satisfactory approximation for any values of s_* and x_*, when ω is close or equal to 1, it converges relatively slowly. In this case, Wynn's epsilon algorithm (Wynn, 1956) can be employed to accelerate the convergence.

By substituting Eq. 3.14 into Eqs. 3.7 and 3.9, the asymptotes of $\theta_1(s_*, x_*)$ and $M(s_*, x_*)$ at $x_* \to \infty$ can be expressed explicitly,

$$\lim_{x_* \to \infty} \log[\theta_1(s_*, x_*)] = -\frac{9}{2} \log(x_*) + C_1 \tag{3.18}$$

$$\lim_{x_* \to \infty} \log[M(s_*, x_*)] = -\frac{9}{2} \log(x_*) + C_2 \tag{3.19}$$

where C_1 and C_2 are constants and equal to,

$$C_1 = \log\left[\frac{16\omega}{\pi\sqrt{s_*^3}}\left(1 - \frac{3}{2}\int_1^{\infty} m_*^{\frac{1}{2}} \theta_1(s_*, m_*) dm_*\right)\right] \tag{3.20}$$

$$C_2 = \log\left(\frac{16}{\pi\sqrt{s_*^3}}\right) \tag{3.21}$$

Additionally, combining Eqs. 3.12 and 3.13 with Eq. 3.7 gives,

$$\lim_{s_* \to \infty} \theta_1 (s_*, x_*) = \begin{cases} \dfrac{\omega \left(1 - x_*^2\right)}{\sqrt{x_*}}, & 0 \leq x_* \leq 1 \\ 0, & x_* > 1 \end{cases} \tag{3.22}$$

$$\lim_{s_* \to 0} \theta_1 (s_*, x_*) = 0, \qquad x_* \geq 0 \tag{3.23}$$

3.4 Poroelastic Fields

Poroelastic fields on the surface and inside the half space can now be expressed in terms of $\theta_1 (s_*, x_*)$ in the Laplace domain from direct substitution of the displacement functions $\overline{\mathcal{D}}$ and $\overline{\mathcal{F}}$ into Eqs. 2.9-2.16. However, these expressions from direct substitution all contain improper integrals with oscillatory kernels involving Bessel functions of the first kind $J_v (\cdot)$. Direct evaluation of these integrals could yield nonsmooth results at small depth. Oscillation in these integrals can however be removed with the aid of Abel transform (Bracewell, 1986; Poularikas, 2018), Sonine's integrals (Noble, 1963) and the use of integral representations of special functions with non-oscillatory kernels. These equations can be found from Eqs. 2.26, 2.27 and Section 2.5.

In this section, two sets of expressions, one from direct substitution and the other with the oscillatory kernels removed, are both presented for the pore pressure $\overline{p}$, vertical stress $\overline{\sigma}_z$ and displacement $\overline{u}_z$. Details for the other non-trivial field variables are given in Appendix B.1. The undrained and drained asymptotes, which correspond to the undrained and drained responses of the Hertzian contact, are the same as those for the case I solution and can be found in Appendix A.1.5.

Stehfest numerical algorithm (Stehfest, 1970) with 6 expansion terms for inverse Lapalace transform is then used to compute the poroelastic fields in the time domain. All calculations are performed based on the material properties according to the Gulf of Mexico shale (Cheng, 2016), see Table 2.3. Viscosity of the saturating fluid is taken to be $\mu = 1$ cp. Values of the drained and undrained Poisson's ratios are $\nu = 0.219$ and $\nu_u = 0.449$, which correspond to

$\omega = 0.4174$. Given radius of the indenter $R = 50$ mm and the indentation depth $d = 0.1$ mm, the corresponding contact radius is $a = 2.23$ mm for this example case.

3.4.1 Pore Pressure

Expression 1 Substituting Eqs. 2.17, 2.18, 3.1, 3.2 and 3.6 into Eq. 2.11 gives,

$$\begin{aligned}\alpha\overline{p} = \frac{2G\left(2\eta-1\right)a^3}{cRs_*}\Bigg[&\omega\int_0^1\left(m_*^2-1\right)N_p\left(s_*,r_*,m_*,z_*\right)dm_* \\ &+\omega\int_1^\infty m_*^{\frac{1}{2}}\theta_1\left(s_*,m_*\right)N_p\left(s_*,r_*,m_*,z_*\right)dm_*\Bigg]\end{aligned} \tag{3.24}$$

where,

$$\begin{aligned}N_p\left(s_*,r_*,m_*,z_*\right) = \frac{2}{\pi}\int_0^\infty \xi_*\Bigg[&\frac{\xi_*}{\sqrt{\xi_*^2+s_*}}\exp\left(-z_*\sqrt{\xi_*^2+s_*}\right) \\ &-\exp\left(-z_*\xi_*\right)\Bigg]\cos\left(m_*\xi_*\right)J_0\left(r_*\xi_*\right)d\xi_*\end{aligned} \tag{3.25}$$

Along the contact axis, with $r_* = 0$ and $J_0\left(r_*\xi_*\right) = 1$, $N_p\left(s_*,0,m_*,z_*\right)$ can be expressed explicitly since the first term in Eq. 3.25 can be evaluated with the aid of the modified Bessel functions (see Eqs. 2.70 and 2.71) and the second term has an elementary antiderivative, i.e.,

$$\begin{aligned}N_p\left(s_*,0,m_*,z_*\right) = &-\frac{2}{\pi}s_*^{\frac{1}{2}}\left[\frac{m_*^2-z_*^2}{\left(m_*^2+z_*^2\right)^{\frac{3}{2}}}\right]\mathrm{K}_1\left[\sqrt{s_*\left(m_*^2+z_*^2\right)}\right] \\ &-\frac{2}{\pi}s_*\left(\frac{m_*^2}{m_*^2+z_*^2}\right)\mathrm{K}_0\left[\sqrt{s_*\left(m_*^2+z_*^2\right)}\right]+\frac{2}{\pi}\left[\frac{m_*^2-z_*^2}{\left(m_*^2+z_*^2\right)^2}\right]\end{aligned} \tag{3.26}$$

It is therefore convenient to use Eqs. 3.24 and 3.26 to calculate the pore pressure along the contact axis. Note that for the sake of brevity, explicit expressions for similar integrals in the sections below will be omitted.

Expression 2 An alternative expression for the pore pressure field can be derived by first applying Sonine's finite integral in Eq. 2.26 to Eq. 3.24,

$$\int_0^{x_*} \alpha\overline{p} \frac{r_* dr_*}{\sqrt{x_*^2 - r_*^2}} = \frac{2G\left(2\eta - 1\right) a^3}{cRs_*} \left[\omega \int_0^1 \left(m_*^2 - 1\right) N_{px}\left(s_*, x_*, m_*, z_*\right) dm_* + \omega \int_1^\infty m_*^{\frac{1}{2}} \theta_1\left(s_*, m_*\right) N_{px}\left(s_*, x_*, m_*, z_*\right) dm_*\right] \tag{3.27}$$

where,

$$N_{px}\left(s_*, x_*, m_*, z_*\right) = \frac{2}{\pi} \int_0^\infty \left[\frac{\xi_*}{\sqrt{\xi_*^2 + s_*}} \exp\left(-z_* \sqrt{\xi_*^2 + s_*}\right) - \exp\left(-z_* \xi_*\right)\right] \cos\left(m_* \xi_*\right) \sin\left(x_* \xi_*\right) d\xi_* \tag{3.28}$$

Differentiating both sides of Eq. 3.27 with respect to x_* and applying the Abel transform in Eq. 2.66 gives,

$$\alpha\overline{p} = \frac{4G\left(2\eta - 1\right) a^3}{\pi cRs_*} \int_0^{r_*} \frac{\theta_p\left(s_*, x_*, z_*\right) dx_*}{\sqrt{r_*^2 - x_*^2}} \tag{3.29}$$

where,

$$\theta_p\left(s_*, x_*, z_*\right) = \omega \int_0^1 \left(m_*^2 - 1\right) N_{px,x}\left(s_*, x_*, m_*, z_*\right) dm_* + \omega \int_1^\infty m_*^{\frac{1}{2}} \theta_1\left(s_*, m_*\right) N_{px,x}\left(s_*, x_*, m_*, z_*\right) dm_* \tag{3.30}$$

and $N_{px,x} = \partial N_{px} / \partial x_*$,

$$N_{px,x}\left(s_*, x_*, m_*, z_*\right) = \frac{2}{\pi} \int_0^\infty \xi_* \left[\frac{\xi_*}{\sqrt{\xi_*^2 + s_*}} \exp\left(-z_* \sqrt{\xi_*^2 + s_*}\right) - \exp\left(-z_* \xi_*\right)\right] \cos\left(m_* \xi_*\right) \cos\left(x_* \xi_*\right) d\xi_* \tag{3.31}$$

Both the pore pressure on the surface ($z_* = 0$) and inside the half space ($z_* > 0$) can be calculated using Eq. 3.29, where the oscillation nature in Eq. 3.31 can be removed with the aid of the modified Bessel functions. Explicit expression for $N_{px,x}$ can be rewritten using $\mathrm{K}_v\left(\cdot\right)$.

Pore pressure in the time domain can be determined after taking the inverse Laplace trans-

form to Eq. 3.29,

$$\alpha p = \frac{4G\,(2\eta - 1)\,a}{\pi R} \int_0^{r_*} \frac{\mathcal{L}^{-1}\left[s_*^{-1}\theta_p\left(s_*, x_*, z_*\right)\right] dx_*}{\sqrt{r_*^2 - x_*^2}} \tag{3.32}$$

Distribution of the pore pressure along the contact axis, calculated using Eqs. 3.24 and 3.26, is shown in Fig. 3.1 for various dimensionless times. The pore pressure is the largest at the contact origin and decreases monotonically with depth. The Mandel-Cryer effect, where the pore pressure rises above the initial value at $t_* = 0$ before its dissipation, is observed at early times (see the inset).

The Mandel-Cryer effect is more evident at the contact edge, where the magnitude of pore pressure increases from 5.39 MPa at $t_* = 5\times10^{-5}$, to its maximum of 13.9 MPa at $t_* = 3\times10^{-2}$, and eventually dissipates to 0 MPa, see Fig. 3.2. The pore pressure in Fig. 3.2 is calculated using Eq. 3.29. The strong Mandel-Cryer effect is likely a manifestation of the normal stress singularity developed at the contact edge during the transient phase.

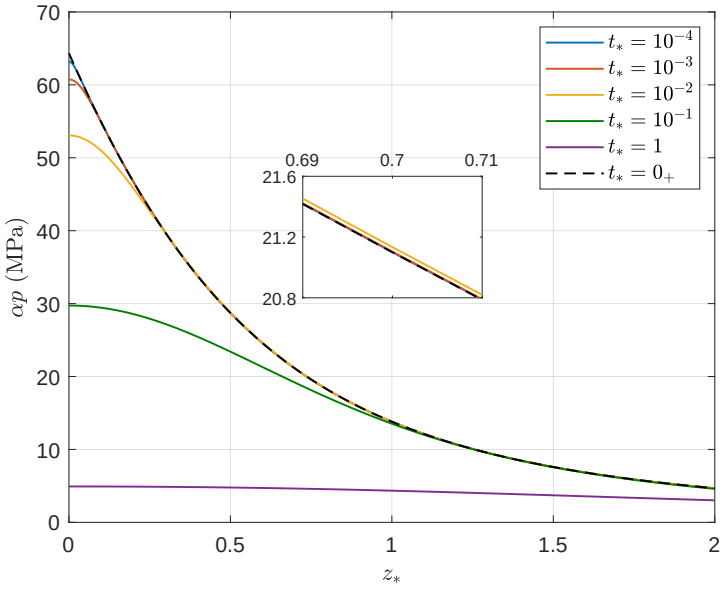

Figure 3.1: Distribution of the pore pressure along the contact axis.

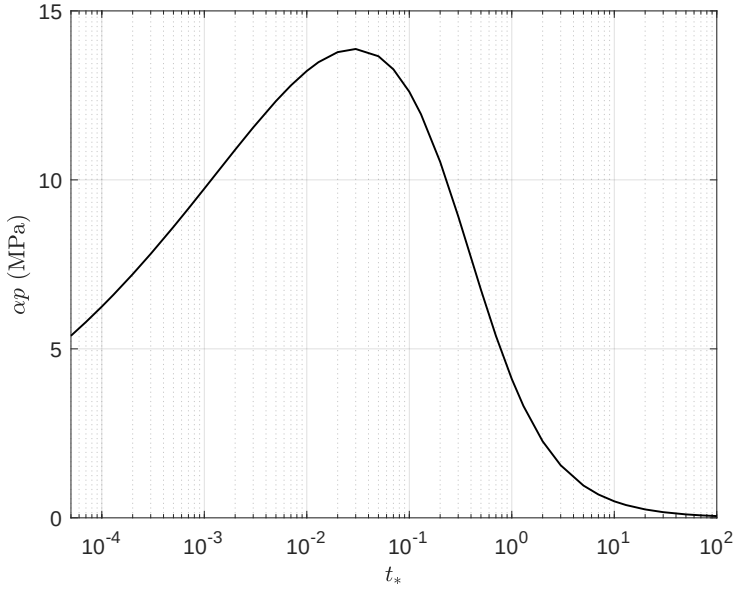

Figure 3.2: Variation of the pore pressure at the contact edge.

3.4.2 Vertical Stress

Expression 1 The vertical stress field can be obtained after substituting Eqs. 2.17, 2.18, 3.1, 3.2 and 3.6 into Eq. 2.12,

$$\begin{aligned}\overline{\sigma}_z = \frac{2Ga^3}{c\phi R s_*}\Bigg[&\int_0^1 \left(m_*^2 - 1\right) N_{sz}\left(s_*, r_*, m_*, z_*\right) dm_* \\ &+ \int_1^\infty m_*^{\frac{1}{2}} \theta_1\left(s_*, m_*\right) N_{sz}\left(s_*, r_*, m_*, z_*\right) dm_*\Bigg]\end{aligned} \tag{3.33}$$

where,

$$\begin{aligned}N_{sz}\left(s_*, r_*, m_*, z_*\right) = -\frac{2}{\pi}\int_0^\infty \xi_* \Bigg\{ &\left(1 + z_*\xi_*\right)\exp\left(-z_*\xi_*\right) \\ + \frac{2\omega}{1+\omega}\left(\frac{\xi_*^2}{s_*}\right)&\left[\frac{\xi_*}{\sqrt{\xi_*^2 + s_*}}\exp\left(-z_*\sqrt{\xi_*^2 + s_*}\right) - \exp\left(-z_*\xi_*\right)\right]\Bigg\}\cos\left(m_*\xi_*\right) J_0\left(r_*\xi_*\right) d\xi_*\end{aligned} \tag{3.34}$$

At $r_* = 0$, the first and last terms in N_{sz} can be written using elementary antiderivatives while the second term can be evaluated with the aid of the modified Bessel function.

Expression 2 On the surface ($z_* = 0$), the procedure to derive the second set expression for the normal stress is to apply first Sonine's integral in Eq. 2.27 and then the inverse Abel transform in Eq. 2.65 to Eq. 3.33 successively. We obtain,

$$\overline{\sigma}_z = \frac{2G\left(2\eta-1\right)a^3}{\pi c\eta R s_*}\left[\begin{array}{c} 2\sqrt{1-r_*^2}+\dfrac{\theta_1\left(s_*,1\right)}{\sqrt{1-r_*^2}} \\ -\displaystyle\int_{r_*}^{1}\theta_3\left(s_*,x_*\right)\frac{dx_*}{\sqrt{x_*^2-r_*^2}} \end{array}\right], \qquad r_* \le 1 \tag{3.35}$$

where,

$$\theta_3\left(s_*,x_*\right) = \frac{\partial}{\partial x_*}\left[x_*^{\frac{1}{2}}\theta_1\left(s_*,x_*\right)\right] \tag{3.36}$$

See Appendix B.2 for the expression of $\theta_3\left(s_*,x_*\right)$.

Inside the half space ($z_* > 0$), the vertical stress $\overline{\sigma}_z$ can be obtained by applying Eqs. 2.26 and 2.66 successively to Eq. 3.33,

$$\overline{\sigma}_z = \frac{4Ga^3}{\pi c\phi R s_*}\int_0^{r_*}\frac{\theta_{sz}\left(s_*,x_*,z_*\right)dx_*}{\sqrt{r_*^2-x_*^2}} \tag{3.37}$$

where,

$$\begin{aligned}\theta_{sz}\left(s_*,x_*,z_*\right) = &\int_0^1\left(m_*^2-1\right)N_{szx,x}\left(s_*,x_*,m_*,z_*\right)dm_* \\ &+\int_1^\infty m_*^{\frac{1}{2}}\theta_1\left(s_*,m_*\right)N_{szx,x}\left(s_*,x_*,m_*,z_*\right)dm_*\end{aligned} \tag{3.38}$$

and,

$$\begin{aligned}N_{szx,x}\left(s_*,x_*,m_*,z_*\right) = -\frac{2}{\pi}\int_0^\infty \xi_*\Bigg\{&\left(1+z_*\xi_*\right)\exp\left(-z_*\xi_*\right) \\ +\frac{2\omega}{1+\omega}\left(\frac{\xi_*^2}{s_*}\right)&\left[\frac{\xi_*}{\sqrt{\xi_*^2+s_*}}\exp\left(-z_*\sqrt{\xi_*^2+s_*}\right)-\exp\left(-z_*\xi_*\right)\right]\Bigg\}\cos\left(m_*\xi_*\right)\cos\left(x_*\xi_*\right)d\xi_*\end{aligned} \tag{3.39}$$

Fig. 3.3 shows the contact stress distribution at various different times. Overall, the distribution is similar to that in case I, see Fig. 2.6. At the two time limits, the contact stress reduces to the classical Hertzian solution; at transient times, the contact stress near the contact

edge becomes singular. The singularity is due to the assumption of a fixed contact radius a, which is responsible for the kink in the surface profiles at transient times, see Fig. 3.4.

There is however a slight difference in the normal stress responses between the two cases. Since the largest excess pore pressure is produced instantaneously right beneath the contact area, at early time, it is the drainage condition inside the contact area controlling the primary drainage path and therefore the poroelastic response. Compared with case I where the surface is fully permeable, imposition of a fully impermeable surface effectively delays pore pressure dissipation at early time. As a result, the isochrone of the contact stress remains relatively close to the undrained asymptote even at $t_* = 10^{-2}$. As the pore pressure dissipates, the contact stess then gradually approaches the Hertzian solution at the drained limit.

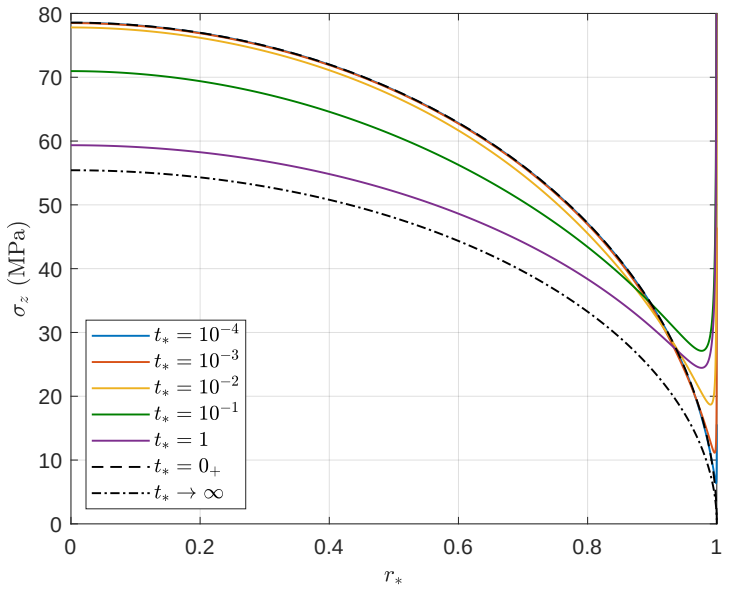

Figure 3.3: Distribution of the contact stress at various dimensionless times.

3.4.3 Vertical Displacement

Expression 1 Vertical displacement $\overline{u}_z$ can be obtained after substituting Eqs. 2.17, 2.18, 3.1, 3.2 and 3.6 into Eq. 2.10,

$$\begin{aligned}\overline{u}_z = \frac{a^4}{c\phi R s_*}\Bigg[&\int_0^1 \left(m_*^2 - 1\right) N_{uz}\left(s_*, r_*, m_*, z_*\right) dm_* \\ &+ \int_1^\infty m_*^{\frac{1}{2}} \theta_1\left(s_*, m_*\right) N_{uz}\left(s_*, r_*, m_*, z_*\right) dm_*\Bigg]\end{aligned} \tag{3.40}$$

where,

$$\begin{aligned}N_{uz}\left(s_*, r_*, m_*, z_*\right) = -\frac{2}{\pi}\int_0^\infty \Bigg\{&\left(\phi + z_*\xi_*\right)\exp\left(-z_*\xi_*\right) \\ +\frac{2\omega}{1+\omega}\left(\frac{\xi_*^2}{s_*}\right)&\left[\exp\left(-z_*\sqrt{\xi_*^2 + s_*}\right) - \exp\left(-z_*\xi_*\right)\right]\Bigg\}\cos\left(m_*\xi_*\right) J_0\left(r_*\xi_*\right) d\xi_*\end{aligned} \tag{3.41}$$

On the surface ($z_* = 0$), N_{uz} can be expressed in a closed form,

$$N_{uz}\left(s_*, r_*, m_*, 0\right) = -\frac{2}{\pi}\frac{\phi}{\sqrt{r_*^2 - m_*^2}}\mathcal{H}\left(r_* - m_*\right) \tag{3.42}$$

Substituting Eq. 3.42 into Eq. 3.40 gives,

$$\overline{u}_z = \frac{a^4}{cRs_*}\left(1 - \frac{r_*^2}{2}\right), \qquad r_* \le 1 \tag{3.43}$$

and,

$$\overline{u}_z = \frac{a^4}{\pi cRs_*}\left[\begin{array}{l}\sqrt{r_*^2 - 1} + \left(2 - r_*^2\right)\arcsin\left(\dfrac{1}{r_*}\right) \\ -2\displaystyle\int_1^{r_*} m_*^{\frac{1}{2}}\theta_1\left(s_*, m_*\right)\frac{dm_*}{\sqrt{r_*^2 - m_*^2}}\end{array}\right], \qquad r_* \ge 1 \tag{3.44}$$

Expression 2 Applying Eqs. 2.26 and 2.66 successively to Eq. 3.40 gives the vertical displacement inside the half space ($z_* > 0$),

$$\overline{u}_z = \frac{2a^4}{\pi c\phi R s_*}\int_0^{r_*}\frac{\theta_{uz}\left(s_*, x_*, z_*\right) dx_*}{\sqrt{r_*^2 - x_*^2}} \tag{3.45}$$

where,

$$\theta_{uz}\left(s_*, x_*, z_*\right) = \int_0^1 \left(m_*^2 - 1\right) N_{uzx,x}\left(s_*, x_*, m_*, z_*\right) dm_* + \int_1^\infty m_*^{\frac{1}{2}} \theta_1\left(s_*, m_*\right) N_{uzx,x}\left(s_*, x_*, m_*, z_*\right) dm_* \tag{3.46}$$

and,

$$N_{uzx,x}\left(s_*, x_*, m_*, z_*\right) = -\frac{2}{\pi} \int_0^\infty \left\{ \left(\phi + z_*\xi_*\right) \exp\left(-z_*\xi_*\right) + \frac{2\omega}{1+\omega} \left(\frac{\xi_*^2}{s_*}\right) \left[\exp\left(-z_*\sqrt{\xi_*^2 + s_*}\right) - \exp\left(-z_*\xi_*\right)\right] \right\} \cos\left(m_*\xi_*\right) \cos\left(x_*\xi_*\right) d\xi_* \tag{3.47}$$

Vertical and radial displacement expressions in Eqs. 3.43-3.44 and Eqs. B.14-B.15 allow us to examine how the surface displacement evolves with time and differs from that of the case if the frictionless contact with a rigid sphere were to be modeled. Displaced surface profiles for case II, as shown in Fig. 3.4, are very similar to those from case I except that at a given transient time, the surface within the contact in case I displaces further to the left and closer to the drained limit than that in case II.

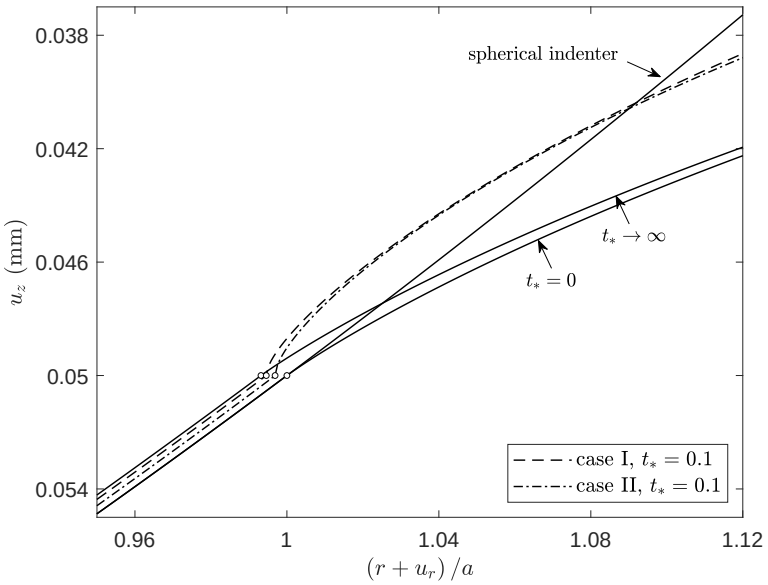

(a) incompressible constituents, $\nu = 0.219$ and $\nu_u = 0.5$

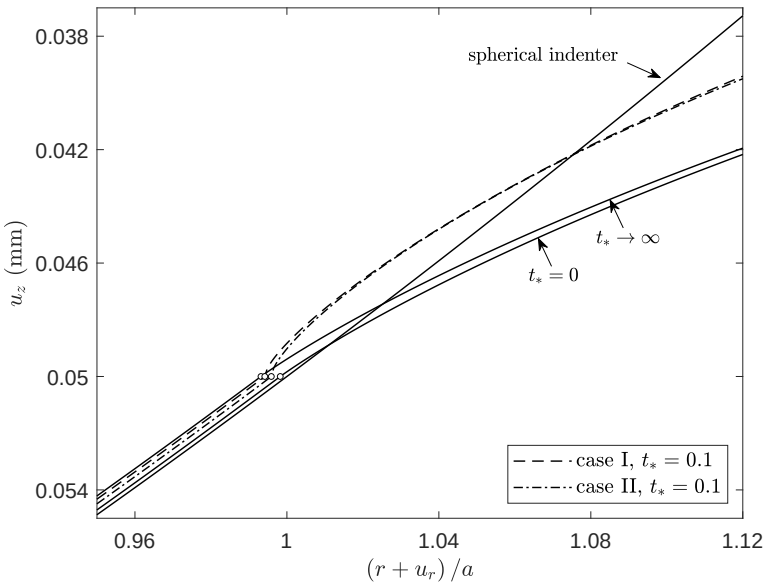

(b) compressible constituents, $\nu = 0.219$ and $\nu_u = 0.449$

Figure 3.4: Comparison of surface displacement profiles at the undrained and drained limits ($t_* = 0_+$, $t_* \to \infty$) and at $t_* = 0.1$ from cases I and II; the material points at the contact edge are marked by the empty circles.

3.5 Incipient Failure

How poroelasticity affects the potential development of the indentation crack systems and plastic failure is investigated here. Biot's effective stress definition, $\sigma'_{ij} = \sigma_{ij} - \alpha p$, is adopted in the analysis below.

3.5.1 Cone Crack Initiation

Tensile stress in the radial direction right outside of the contact area could be the cause for initiation of a ring crack on the surface, which may results in the formation of a Hertzian cone crack (Lawn, 1998). Variations of the effective radial stress with time at $r_* = 1$ are shown in Fig. 3.5 for both cases I and II surface drainage conditions. In both cases, the tensile stress first increases and then decreases to finally approach to the late time asymptote. At very early time, the effective tensile stress is larger in case I, suggesting that if the tensile strength of a material is small, case I is more prone to form the cone/ring crack system instantaneously after indentation. However, the effective tensile stress becomes larger in case II after $t_* \sim 3 \times 10^{-3}$. If the tensile strength is relatively large, the ring/cone crack system is more likely to occur in case II when the surface is fully impermeable.

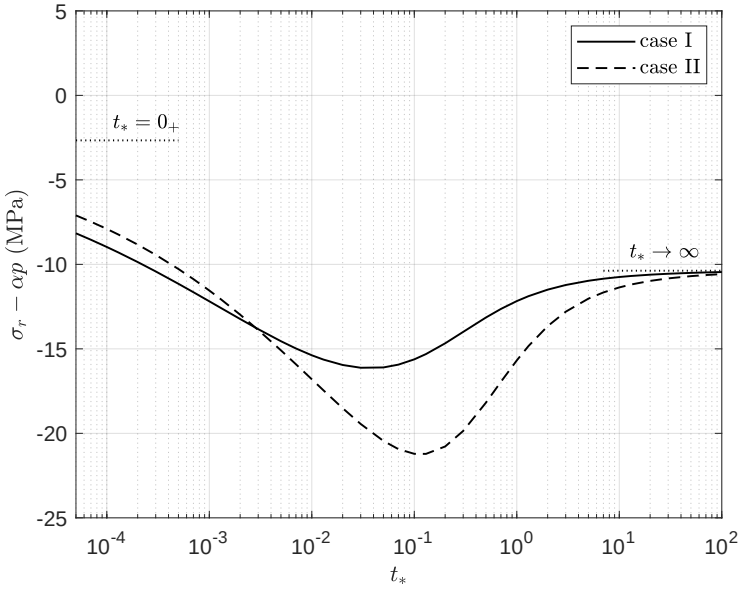

Figure 3.5: Variation of the effective radial stress with the dimensionless time at $r_* = 1_+$ on the surface (right outside of the contact area).

3.5.2 Median Crack Initiation

Tensile stress generated along the contact axis beneath the surface could result in nucleation of a penny-shaped median crack, which could potentially grow to become a radial crack. The total and effective radial stress distributions here are similar to those in case I, except that at early time and small depth, since an impermeable boundary is imposed on the surface, the total radial stress decreases monotonically with depth. In contrast, in case I, because a permeable boundary is assumed, the total radial stress on the surface drops instantaneously after indentation from the undrained asymptote to a value slightly below the drained asymptote. As a result, variation of the total radial stress with depth in case I is non-monotonic.

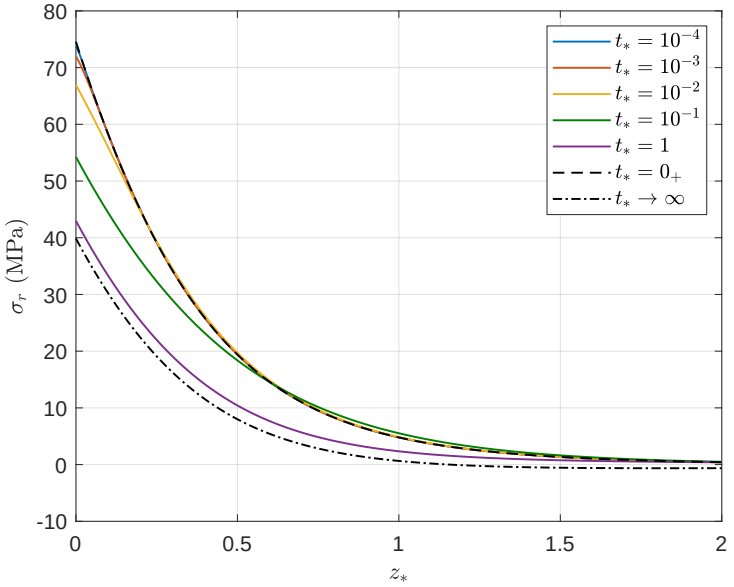

Figure 3.6: Variation of radial stress along the contact axis.

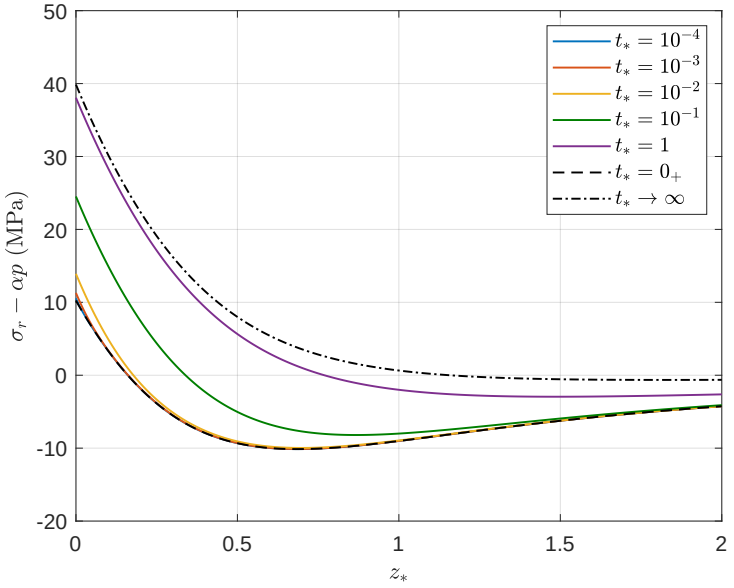

Figure 3.7: Variation of effective radial stress along the contact axis.

3.5.3 Onset of Plastic Deformation

The maximum shear stress on the contact axis, $(\sigma_z - \sigma_r)/2$, can be used to infer the possibility of incipient plastic yielding. Fig. 3.8 shows that the maximum value occurs at the undrained limit at a depth beneath the surface. This indicates that if plastic yielding were to occur, it will start from inside the domain. In addition, it is possible that the material strength is relatively high, plastic deformation occurs only at the undrained limit and there will be no further accumulation during the transient phase. Distribution of the shear stress shown here with case II surface drainage condition does differ slightly from that of case I in that at the intermediate times, there could be another shear stress maximum on the surface when it is fully permeable. However, numerical analysis will be needed in order to gain a comprehensive understanding of the poro-elasto-plastic indentation process.

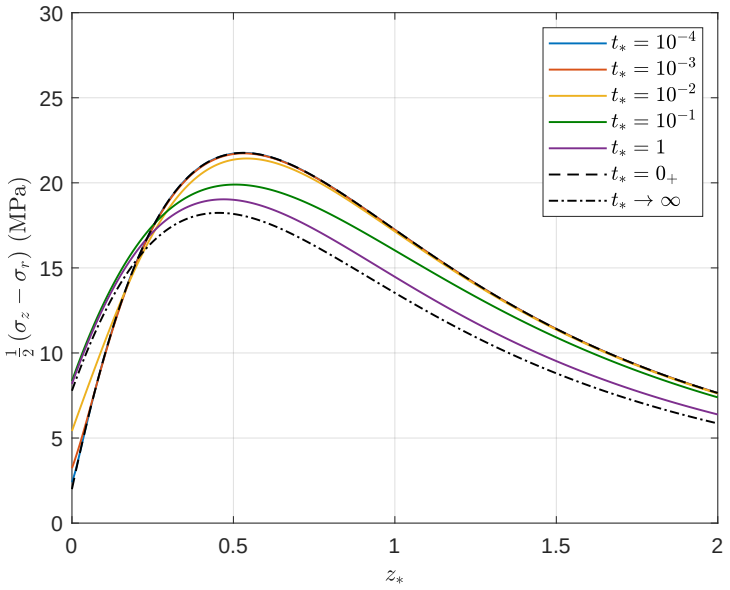

Figure 3.8: Variation of the maximum shear stress along the contact axis.

3.6 Indentation Force Relaxation

3.6.1 Master Curves

Following the normalization method in Section 2.7.1, explicit expression of the normalized indentation force $F_n(t_*)$ can be derived as,

$$F_n(t_*) = \frac{3}{2\omega}\mathcal{L}^{-1}\left[s_*^{-1}\int_0^1 x_*^{\frac{1}{2}}\theta_1(s_*, x_*)\,dx_*\right] \tag{3.48}$$

The general form of $F_n(t_*)$ here is the same as that for case I. The difference bewteen the two lies in the specific expression of $\theta_1(s_*, x_*)$. Eq. 3.48 indicates that the normalized force relaxation response is a function of material constant ω only. The force relaxation behaviors at $\omega = 0, 0.5, 1$ are plotted for both cases I and II drainage conditions in Fig. 3.9. As expected, the normalized force relaxation response is slower in case II, which can be attributed to the fact that the drainage path and the corresponding relaxation time are longer when the surface is fully impermeable. It is important to note that dependence of the normalized force relaxation response on constant ω is relatively weak for both two cases. Consider the values of ω from data reported in the literature for sands, clays and rocks fall within $[0, 0.5]$, see Section 2.3. From a practical point of view, dependence of $F_n(t_*)$ on ω could be even weaker.

The force relaxation response from our theoretical solution for case II can be fitted using a four-parameter function, i.e., Eq. 2.111. The fitting parameters a_1, b_1, a_2, b_2 are listed in Table 3.2. Indeed, this elementary function gives an excellent approximation and the coefficient of determination for all the cases is $R^2 = 1$.

As far as data interpretation for laboratory characterization is concerned, the two force asymtotes, $F(0)$ and $F(\infty)$, can be used to determine material constants G/ϕ and $G(2\eta - 1)/\eta$ and the ratio of the two asymptotes gives constant ω. Once ω is known, hydraulic diffusivity c can be determined by matching the normalized transient force response from the experiment with the master curve from the theoretical solution. In addition, if the undrained and drained asymptotes can be clearly identified from the experimental data, the diffusion coefficient c can

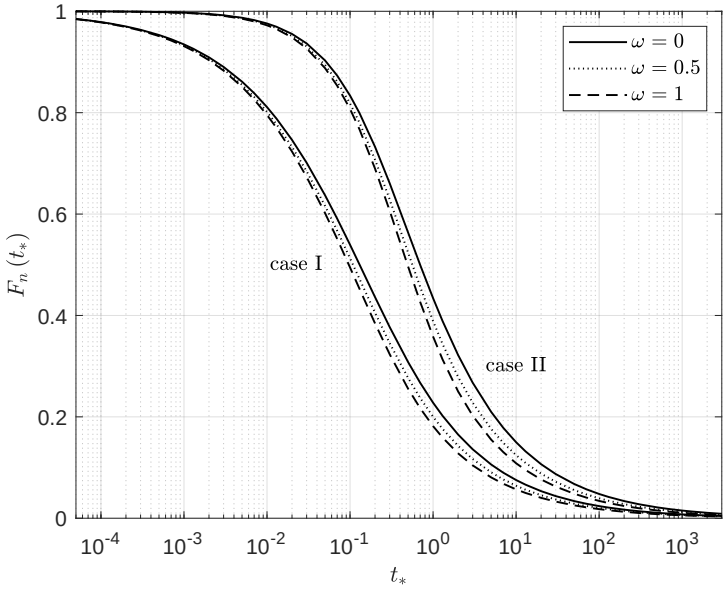

Figure 3.9: Relaxation of the normalized indentation force with the dimensionless time for cases I and II with $\omega = 0$, 0.5 and 1.

ω	a_1	b_1	a_2	b_2
0	0.631	0.609	3	1.097
0.1	0.666	0.6102	3.143	1.115
0.3	0.727	0.613	3.422	1.145
0.44	0.768	0.6136	3.613	1.189
0.5	0.785	0.6158	3.672	1.172
0.7	0.838	0.6186	3.899	1.195
0.9	0.888	0.622	4.109	1.215
1	0.913	0.6238	4.203	1.225

Table 3.2: Values of the fitting parameters for the force relaxation curves.

also be computed from $t_{*0.5}$ via the fitting function, $t_{*0.5} = 0.697 - 0.387\omega + 0.281\omega^2 - 0.1\omega^3$, where $t_{*0.5}$ denotes the dimensionless time at which $F_n(t_*) = 0.5$.

3.6.2 Asymptotic Behaviors

While the Hertzian solution gives the indentation force asymptotes at $t_* = 0_+$ and ∞, closed-form asymptotic expressions beyond these two limits can be derived for the particular case of $\omega = 0$ for both cases I and II. Expressions for case I are already given in Section 2.7.2. Here we provide the expressions for case II.

Substituting Eq. 3.15 into Eq. 3.48 and setting $\omega = 0$ gives,

$$F_n(t_*) = \frac{3}{2}\mathcal{L}^{-1}\left[s_*^{-1}\int_0^1 x_*^{\frac{1}{2}} M(s_*, x_*)\, dx_*\right] \tag{3.49}$$

The integral in Eq. 3.49 can be expressed explicitly using the modified Struve function and the generalized hypergeometric functions. Detailed derivation procedures can be found in Appendix B.3,

$$\int_0^1 x_*^{\frac{1}{2}} M(s_*, x_*)\, dx_* = \frac{2}{3} + \frac{2}{s_*}\left[-1 + \mathrm{M}_0\left(2\sqrt{s_*}\right) + 2\mathrm{F}(s_*)\right] \tag{3.50}$$

where,

$$\mathrm{F}(s_*) = \mathrm{F}_{1,2}\left[\begin{matrix} 0.5 \\ (1, 1.5)\end{matrix}, s_*\right] - \frac{2}{\pi} s_*^{\frac{1}{2}} \mathrm{F}_{2,3}\left[\begin{matrix} (1,1) \\ (1.5, 1.5, 2)\end{matrix}, s_*\right] \tag{3.51}$$

with $\mathrm{F}_{1,2}[\cdot]$ and $\mathrm{F}_{2,3}[\cdot]$ being two generalized hypergeometric functions.

Asymptotic expressions for indentation force relaxation at early and late times can be obtained by applying inverse Laplace transform to the integrals above when $s_* \to \infty$ and $s_* \to 0$ (Bateman, 1954; Olver, 2010). The first few terms at $\omega = 0$ can be expressed as follows.

- case II, early time ($t_* \to 0$),

$$\begin{aligned} \lim_{t_* \to 0} F_n(t_*) &= 1 - 3t_* - 4\left(\frac{t_*}{\pi}\right)^{\frac{3}{2}} \ln(t_*) \\ &+4\left(\gamma + 2\ln 2 + \frac{5}{3}\right)\left(\frac{t_*}{\pi}\right)^{\frac{3}{2}} - \frac{4\pi}{5}\left(\frac{t_*}{\pi}\right)^{\frac{5}{2}} - \frac{27\pi^2}{70}\left(\frac{t_*}{\pi}\right)^{\frac{7}{2}} \end{aligned} \tag{3.52}$$

where $\gamma = 0.57721...$ is the Euler constant.

- case II, late time ($t_* \to \infty$),

$$\lim_{t_* \to \infty} F_n(t_*) = \pi^{-\frac{3}{2}} \left(\frac{8}{3} t_*^{-\frac{1}{2}} - \frac{64}{225} t_*^{-\frac{3}{2}} + \frac{48}{1225} t_*^{-\frac{5}{2}} - \frac{512}{99225} t_*^{-\frac{7}{2}} \right) \tag{3.53}$$

Fig. 3.10 shows that these asymptotes capture the force relaxation behaviors remarkbly well not just for the very small and large times. The valid ranges of the asymptotic expressions in Eqs. 2.115-2.116 and Eqs. 3.52-3.53 for a tolerance of 1% are given in Table 3.3. Indeed, for both cases I and II, a combination of the six-term early time asymptote with the four-term late time asymptote could provide an excellent approximation to the full solution for the entire time range.

For the general case when $\omega \neq 0$, closed-form asymptotic expressions cannot be obtained. A comparison of the early time behaviors from the full solution for $\omega = 0$, 0.5 and 1 is shown in Fig. 3.11(a) in a log-log scale for both cases I and II. It seems that constant ω barely has any influence on the early time responses. Indeed, given a tolerance of 1%, for case II, the first two-term in Eq. 3.52 is valid till $t_* = 0.013$ and 0.02 for $\omega = 0.5$ and 1. At late times, the force relaxation curves appear to be parallel to each other, see Fig. 3.11(b), suggesting $F_n(t_*) \sim t_*^{-\frac{1}{2}}$ is the dominant behavior when t_* is large.

		case I	case II
early time	2-term	$[0, 0.003]$	$[0, 0.013]$
	6-term	$[0, 0.7]$	$[0, 0.7]$
late time	1-term	$[5, \infty)$	$[10, \infty)$
	4-term	$[0.5, \infty)$	$[0.7, \infty)$

Table 3.3: Validity ranges of the asymptotic expressions in Eqs. 2.115-2.116 and Eqs. 3.52-3.53 for $\omega = 0$ with a tolerance of 1%.

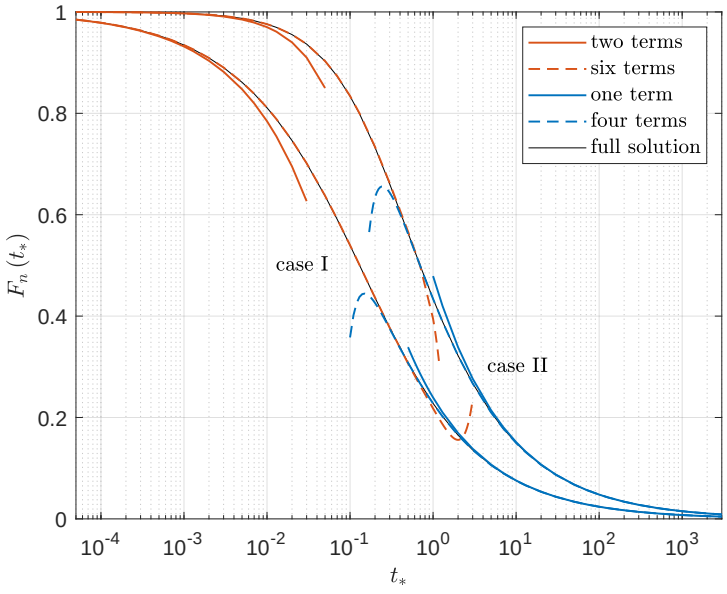

Figure 3.10: Comparison of the asymptotic expressions with the full solutions for the normalized indentation force $F_n(t_*)$ at $\omega = 0$ for cases I and II.

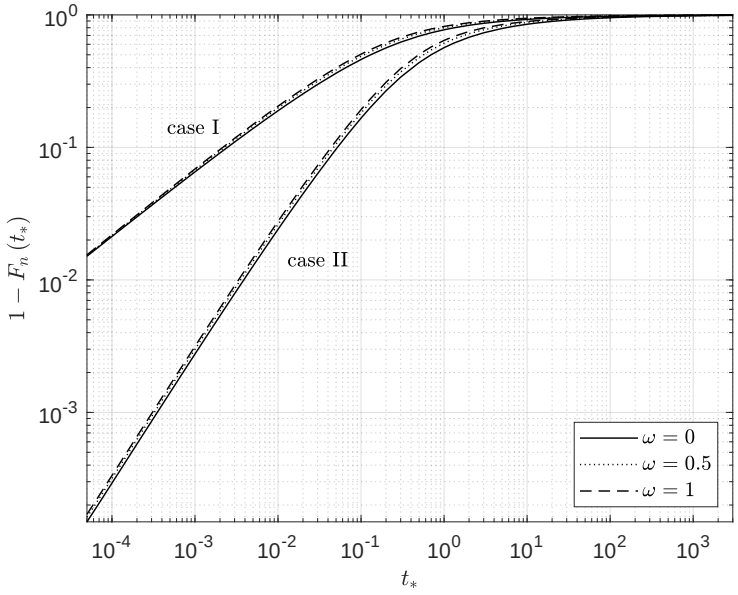

(a) early time behaviors

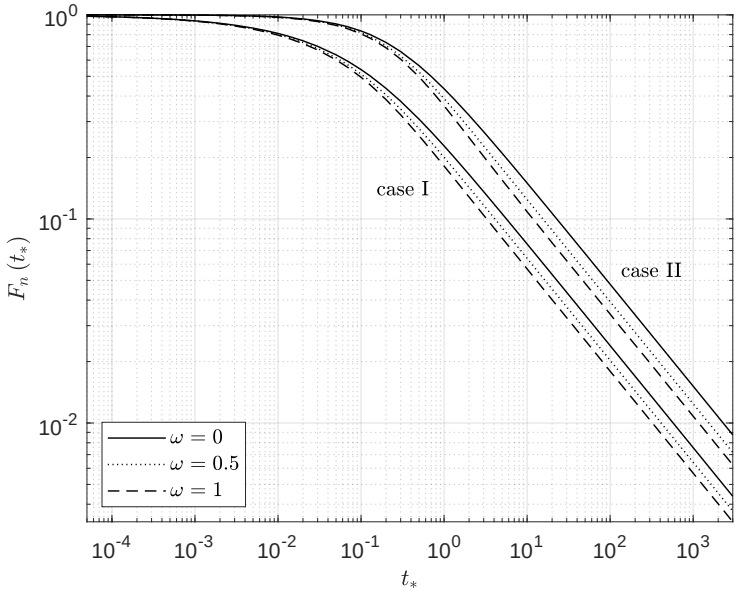

(b) late time behaviors

Figure 3.11: Asymptotic behaviors of the normalized indentation force at $\omega = 0$, 0.5 and 1 for cases I and II.

4 POROELASTIC RESPONSE OF SPHERICAL INDENTATION INTO A HALF SPACE WITH A MIXED DRAINAGE SURFACE VIA STEP DISPLACEMENT

4.1 Introduction

Depending on the material types, the exact nature of drainage between an indenter and a soil surface could be open to interpretation. The contact between an indenter made of stainless steel and a saturated fine-grained soil may be more likely impermeable, while the outer free surface may be more likely permeable. This gives the case III surface drainage condition. In this chapter, we extend our theoretical analysis based on the McNamee-Gibson displacement function method to treat the poroelastic spherical indentation by step displacement loading with case III surface drainage condition. Solution procedures in case III differ from those in cases I and II in that not only unknown B_1, but also A_2 needs to be determined from a Fredholm integral equations of the second kind. While we still employ the same suite of mathematical techniques, the solution procedure is now different from the previous two cases. Here we first present solution procedures and the expression of poroelastic fields. Next we examine the theoretical results for normalized indentation force at different ω. These results are further fitted with an elementary function in order to be conveniently used in the laboratory. Though for case III we are unable to derive closed-form asymptotic expressions of the transient indentation force response at $\omega = 0$, some asymptotic behaviors can still be extracted by comparing with the full solutions from all three cases.

4.2 Problem Formulation

The boundary condition for case III surface drainage can be written in terms of vertical displacement u_z, stresses σ_z and σ_{zr}, pore pressure p and normal flux q_z on the surface, see Table 4.1, where $\mathcal{H}(t)$ is the Heaviside step function.

	time domain	Laplace domain
$0 \leq r \leq a_-$	$u_z = \left(d - \frac{r^2}{2R}\right)\mathcal{H}(t)$	$\overline{u}_z = s^{-1}\left(d - \frac{r^2}{2R}\right)$
	$\sigma_{zr} = 0,\ q_z = 0$	$\overline{\sigma}_{zr} = 0,\ \overline{q}_z = 0$
$r \geq a_+$	$\sigma_z = \sigma_{zr} = 0,\ p = 0$	$\overline{\sigma}_z = \overline{\sigma}_{zr} = 0,\ \overline{p} = 0$

Table 4.1: Boundary conditions.

Matching the poroelastic fields expressed in Eqs. 2.9-2.16 with the boundary conditions in the Laplace domain in Table 4.1 yields the following equations,

$$A_1\xi + A_2\sqrt{\xi^2+\lambda} + B_1(1-\phi) = 0 \tag{4.1}$$

and two sets of dual integral equations. One is,

$$\int_0^\infty B_1 J_0(r\xi)\,d\xi = (s\phi)^{-1}\left(\frac{r^2}{2R} - d\right), \qquad 0 \leq r \leq a_- \tag{4.2}$$

$$\int_0^\infty \left(A_2\xi^2 - A_2\xi\sqrt{\xi^2+\lambda} - B_1\xi\right) J_0(r\xi)\,d\xi = 0, \qquad r \geq a_+ \tag{4.3}$$

and the other is,

$$\int_0^\infty \left(\frac{1+\omega}{2\omega}\lambda A_2\sqrt{\xi^2+\lambda} + B_1\xi^2\right) J_0(r\xi)\,d\xi = 0, \qquad 0 \leq r \leq a_- \tag{4.4}$$

$$\int_0^\infty \left(\frac{1+\omega}{2\omega}\lambda A_2 + B_1\xi\right) J_0(r\xi)\,d\xi = 0, \qquad r \geq a_+ \tag{4.5}$$

To facilitate derivation, A_2 and B_1 are replaced with C_1 and C_2 according to,

$$\begin{aligned} C_1 &= B_1 \\ C_2 &= \frac{1+\omega}{2\omega}\lambda A_2\sqrt{\xi^2+\lambda} + B_1\xi^2 \end{aligned} \tag{4.6}$$

Substituting C_1 and C_2 for A_2 and B_1, Eqs. 4.2 and 4.3 become,

$$\int_0^\infty C_1 J_0(r\xi)\, d\xi = (s\phi)^{-1}\left(\frac{r^2}{2R} - d\right), \qquad 0 \le r \le a_- \tag{4.7}$$

$$\int_0^\infty \left\{C_1\xi\left[1 + \omega H_a(s,\xi)\right] + \omega C_2 \xi^{-1}\left[1 - H_a(s,\xi)\right]\right\} J_0(r\xi)\, d\xi = 0, \qquad r \ge a_+ \tag{4.8}$$

where,

$$H_a(s,\xi) = 1 + \frac{2\xi^2}{\lambda}\left(\frac{\xi}{\sqrt{\xi^2+\lambda}} - 1\right) \tag{4.9}$$

And Eqs. 4.4 and 4.5 become,

$$\int_0^\infty C_2 J_0(r\xi)\, d\xi = 0, \qquad 0 \le r \le a_- \tag{4.10}$$

$$\int_0^\infty \left\{C_1\xi^2 H_b(s,\xi) + C_2\left[1 - H_b(s,\xi)\right]\right\} \xi^{-1} J_0(r\xi)\, d\xi = 0, \qquad r \ge a_+ \tag{4.11}$$

where,

$$H_b(s,\xi) = 1 - \frac{\xi}{\sqrt{\xi^2+\lambda}} \tag{4.12}$$

The problem now reduces to first find C_1 and C_2 from Eqs. 4.7-4.12 and then A_1, A_2 and B_1 from Eqs. 4.1 and 4.6.

4.3 Solution Procedure

4.3.1 Fredholm Integral Equation of the Second Kind

Noble's method (Noble, 1963) is used to reduce the two sets of dual integral equations to a set of coupled Fredholm integral equations of the second kind. By applying the Sonine's integral, Eqs. 2.26 and 2.27, to Eqs. 4.7 and 4.8, respectively, we obtain,

$$\int_0^\infty C_1 \xi^{-\frac{1}{2}} J_{\frac{1}{2}}(x\xi)\, d\xi = (s\phi R)^{-1}\sqrt{\frac{2}{\pi x}}\left(\frac{x^3}{3} - xRd\right), \qquad 0 \le x \le a_- \tag{4.13}$$

and,

$$\int_0^\infty \left\{C_1\xi\left[1+\omega H_a\left(s,\xi\right)\right]+\omega C_2\xi^{-1}\left[1-H_a\left(s,\xi\right)\right]\right\}\xi^{-\frac{1}{2}}J_{-\frac{1}{2}}\left(x\xi\right)d\xi=0, \qquad x\geq a_+ \quad (4.14)$$

In order to make the orders of the Bessel functions identical in the two equations above, both sides of Eq. 4.13 are first multiplied by $x^{\frac{1}{2}}$ and then differentiated with respect to x,

$$\int_0^\infty C_1\xi^{\frac{1}{2}}J_{-\frac{1}{2}}\left(x\xi\right)d\xi=\left(s\phi R\right)^{-1}\sqrt{\frac{2}{\pi x}}\left(x^2-Rd\right), \qquad 0\leq x\leq a_- \quad (4.15)$$

Define $\theta_a\left(s,x\right)$ as an unknown function of s and x in the Laplace domain according to,

$$\int_0^\infty C_1\xi^{\frac{1}{2}}J_{-\frac{1}{2}}\left(x\xi\right)d\xi=\sqrt{\frac{2}{\pi}}\left(s\phi R\right)^{-1}\theta_a\left(s,x\right), \qquad x\geq a_+ \quad (4.16)$$

Since the left hand sides of Eqs. 4.15 and 4.16 are identical, the expression on the left is defined for all x. It follows from inverse Hankel transform,

$$\begin{aligned} C_1\xi^{-\frac{1}{2}}=&\sqrt{\frac{2}{\pi}}\left(s\phi R\right)^{-1}\int_0^a m^{\frac{1}{2}}\left(m^2-Rd\right)J_{-\frac{1}{2}}\left(m\xi\right)dm \\ &+\sqrt{\frac{2}{\pi}}\left(s\phi R\right)^{-1}\int_a^\infty m\theta_a\left(s,m\right)J_{-\frac{1}{2}}\left(m\xi\right)dm \end{aligned} \quad (4.17)$$

By applying Eqs. 2.26 and 2.27 to Eqs. 4.10 and 4.11 respectively, we obtain,

$$\int_0^\infty C_2\xi^{-\frac{1}{2}}J_{\frac{1}{2}}\left(x\xi\right)d\xi=0, \qquad 0\leq x\leq a_- \quad (4.18)$$

and,

$$\int_0^\infty \left\{C_1\xi^2H_b\left(s,\xi\right)+C_2\left[1-H_b\left(s,\xi\right)\right]\right\}\xi^{-\frac{3}{2}}J_{-\frac{1}{2}}\left(x\xi\right)d\xi=0, \qquad x\geq a_+ \quad (4.19)$$

Similarly, both sides of Eq. 4.19 are first multiplied by $x^{\frac{1}{2}}$ and then differentiated with

respect to x so that the orders of the Bessel functions become identical to Eq. 4.18,

$$\int_0^\infty \left\{C_1\xi^2 H_b(s,\xi) + C_2\left[1 - H_b(s,\xi)\right]\right\} \xi^{-\frac{1}{2}} J_{\frac{1}{2}}(x\xi)\, d\xi = 0, \qquad x \geq a_+ \tag{4.20}$$

Define $\theta_b(s,x)$ as an unknown function of s and x in the Laplace domain according to,

$$\int_0^\infty C_2 \xi^{-\frac{1}{2}} J_{\frac{1}{2}}(x\xi)\, d\xi = \sqrt{\frac{2}{\pi}} (s\phi R)^{-1} \theta_b(s,x), \qquad x \geq a_+ \tag{4.21}$$

Applying inverse Hankel transform to Eqs. 4.18 and 4.21 gives,

$$C_2 \xi^{-\frac{3}{2}} = \sqrt{\frac{2}{\pi}} (s\phi R)^{-1} \int_a^\infty m\theta_b(s,m)\, J_{\frac{1}{2}}(m\xi)\, dm \tag{4.22}$$

Substituting both Eqs. 4.17 and 4.22 into Eqs. 4.14 and 4.20 gives a set of coupled Fredholm integral equations of the second kind for $\theta_{1a}(s_*, x_*)$ and $\theta_{1b}(s_*, x_*)$,

$$\theta_{1a}(s_*,x_*) + \begin{bmatrix} \omega \int_1^\infty N_a(s_*,x_*,m_*)\, \theta_{1a}(s_*,m_*)\, dm_* \\ +\omega \int_1^\infty N_b(s_*,x_*,m_*)\, \theta_{1b}(s_*,m_*)\, dm_* \end{bmatrix} = \omega M_a(s_*,x_*) \tag{4.23}$$

$$\theta_{1b}(s_*,x_*) + \begin{bmatrix} \int_1^\infty N_d(s_*,x_*,m_*)\, \theta_{1a}(s_*,m_*)\, dm_* \\ -\int_1^\infty N_c(s_*,x_*,m_*)\, \theta_{1b}(s_*,m_*)\, dm_* \end{bmatrix} = M_b(s_*,x_*) \tag{4.24}$$

Variables in the equations above are made dimensionless according to $\theta_{1a}(s_*,x_*) = \theta_a(s,x)\, a^{-\frac{3}{2}}$, $\theta_{1b}(s_*,x_*) = \theta_b(s,x)\, a^{-\frac{1}{2}} s_*^{-\frac{1}{2}}$ and those defined in Eq. 2.34.

Now $\theta_{1a}(s_*,x_*)$ and $\theta_{1b}(s_*,x_*)$ are the unknowns to be determined. Once they are known, all field quantities can be expressed in the Laplace domain in terms of $\theta_{1a}(s_*,x_*)$ and $\theta_{1b}(s_*,x_*)$. Other functions in Eqs. 4.23 and 4.24 are given by,

$$M_a(s_*,x_*) = \int_0^1 m_*^{-\frac{1}{2}} \left(1 - m_*^2\right) N_a(s_*,x_*,m_*)\, dm_* \tag{4.25}$$

$$M_b(s_*, x_*) = \int_0^1 m_*^{-\frac{1}{2}} \left(1 - m_*^2\right) N_d(s_*, x_*, m_*)\, dm_* \tag{4.26}$$

$$N_a(s_*, x_*, m_*) = m_* \int_0^\infty \xi_* H_{1a}(s_*, \xi_*)\, J_{-\frac{1}{2}}(x_*\xi_*)\, J_{-\frac{1}{2}}(m_*\xi_*)\, d\xi_* \tag{4.27}$$

$$N_b(s_*, x_*, m_*) = 2s_*^{-\frac{1}{2}} m_* \int_0^\infty \xi_*^2 H_{1b}(s_*, \xi_*)\, J_{-\frac{1}{2}}(x_*\xi_*)\, J_{\frac{1}{2}}(m_*\xi_*)\, d\xi_* \tag{4.28}$$

$$N_c(s_*, x_*, m_*) = m_* \int_0^\infty \xi_* H_{1b}(s_*, \xi_*)\, J_{\frac{1}{2}}(x_*\xi_*)\, J_{\frac{1}{2}}(m_*\xi_*)\, d\xi_* \tag{4.29}$$

$$N_d(s_*, x_*, m_*) = s_*^{-\frac{1}{2}} m_* \int_0^\infty \xi_*^2 H_{1b}(s_*, \xi_*)\, J_{\frac{1}{2}}(x_*\xi_*)\, J_{-\frac{1}{2}}(m_*\xi_*)\, d\xi_* \tag{4.30}$$

$$H_{1a}(s_*, \xi_*) = 1 + \frac{2\xi_*^2}{s_*}\left(\frac{\xi_*}{\sqrt{\xi_*^2 + s_*}} - 1\right) \tag{4.31}$$

$$H_{1b}(s_*, \xi_*) = 1 - \frac{\xi_*}{\sqrt{\xi_*^2 + s_*}} \tag{4.32}$$

Eqs. 4.23 and 4.24 show that $\theta_{1a}(s_*, x_*)$ and $\theta_{1b}(s_*, x_*)$ are influenced by the material properties through ω only.

4.3.2 Alternative Expression for $N_{a-d}(s_*, x_*, m_*)$

Prior to finding the solutions to the Fredholm integral equations, functions $N_{a-d}(s_*, x_*, m_*)$ need to be evaluated. The integral kernels in Eqs. 4.27-4.30 are highly oscillatory. However, we can again rewrite the integrals alternatively using two modified Struve functions of the second kind, $\mathrm{M}_0(\cdot)$ and $\mathrm{M}_1(\cdot)$, see Eqs. 2.44-2.49. For function $N_a(s_*, x_*, m_*)$,

$$\begin{aligned} N_a(s_*, x_*, m_*) = \sqrt{\frac{s_* m_*}{x_*}} \Bigg\{ &\left[\frac{2}{\pi} - \frac{\mathrm{M}_0(y_1)}{y_1} + \left(1 + \frac{2}{y_1^2}\right)\mathrm{M}_1(y_1)\right] \\ &+ \left[\frac{2}{\pi} - \frac{\mathrm{M}_0(y_2)}{y_2} + \left(1 + \frac{2}{y_2^2}\right)\mathrm{M}_1(y_2)\right]\Bigg\} \end{aligned} \tag{4.33}$$

where $y_1 = |x_* - m_*|\, s_*^{\frac{1}{2}}$ and $y_2 = (x_* + m_*)\, s_*^{\frac{1}{2}}$.

Asymptotes for $N_a(s_*, x_*, m_*)$ at the undrained and drained limits and in the far-field can

be obtained from the alternative expression,

$$\lim_{s_*\to\infty} N_a\left(s_*, x_*, m_*\right) = \delta\left(m_* - x_*\right) \tag{4.34}$$

$$\lim_{s_*\to 0} N_a\left(s_*, x_*, m_*\right) = 0 \tag{4.35}$$

$$\lim_{x_*\to\infty} N_a\left(s_*, x_*, m_*\right) = \frac{24}{\pi}\sqrt{\frac{m_*}{s_*^3 x_*^9}} \tag{4.36}$$

For function $N_b\left(s_*, x_*, m_*\right)$,

$$\begin{aligned} N_b\left(s_*, x_*, m_*\right) = &\sqrt{\frac{s_* m_*}{x_*}}\mathrm{Sign}\left(x_* - m_*\right)\left[\mathrm{M}_0\left(y_1\right) - \frac{\mathrm{M}_1\left(y_1\right)}{y_1}\right] \\ &-\sqrt{\frac{s_* m_*}{x_*}}\left[\mathrm{M}_0\left(y_2\right) - \frac{\mathrm{M}_1\left(y_2\right)}{y_2}\right] \end{aligned} \tag{4.37}$$

$$\lim_{s_*\to\infty} N_b\left(s_*, x_*, m_*\right) = \sqrt{\frac{4}{s_* x_*}}\frac{\partial}{\partial x_*}\left[x_*^{\frac{1}{2}}\delta\left(m_* - x_*\right)\right] \tag{4.38}$$

$$\lim_{s_*\to 0} N_b\left(s_*, x_*, m_*\right) = 0 \tag{4.39}$$

$$\lim_{x_*\to\infty} N_b\left(s_*, x_*, m_*\right) = -\frac{24}{\pi}\sqrt{\frac{m_*^3}{s_*^2 x_*^9}} \tag{4.40}$$

For function $N_c\left(s_*, x_*, m_*\right)$,

$$N_c\left(s_*, x_*, m_*\right) = \frac{1}{2}\sqrt{\frac{s_* m_*}{x_*}}\left[\mathrm{M}_1\left(y_1\right) - \mathrm{M}_1\left(y_2\right)\right] \tag{4.41}$$

$$\lim_{s_*\to\infty} N_c\left(s_*, x_*, m_*\right) = \delta\left(m_* - x_*\right) \tag{4.42}$$

$$\lim_{s_*\to 0} N_c\left(s_*, x_*, m_*\right) = 0 \tag{4.43}$$

$$\lim_{x_*\to\infty} N_c\left(s_*, x_*, m_*\right) = \frac{4}{\pi}\sqrt{\frac{m_*^3}{s_* x_*^7}} \tag{4.44}$$

For function $N_d(s_*, x_*, m_*)$,

$$\begin{aligned} N_d(s_*, x_*, m_*) = &-\frac{1}{2}\sqrt{\frac{s_* m_*}{x_*}}\text{Sign}(x_* - m_*)\left[\text{M}_0(y_1) - \frac{\text{M}_1(y_1)}{y_1}\right] \\ &-\frac{1}{2}\sqrt{\frac{s_* m_*}{x_*}}\left[\text{M}_0(y_2) - \frac{\text{M}_1(y_2)}{y_2}\right] \end{aligned} \tag{4.45}$$

$$\lim_{s_* \to \infty} N_d(s_*, x_*, m_*) = -\sqrt{\frac{1}{s_* x_*}}\frac{\partial}{\partial x_*}\left[x_*^{\frac{1}{2}}\delta(m_* - x_*)\right] \tag{4.46}$$

$$\lim_{s_* \to 0} N_d(s_*, x_*, m_*) = 0 \tag{4.47}$$

$$\lim_{x_* \to \infty} N_d(s_*, x_*, m_*) = \frac{4}{\pi}\sqrt{\frac{m_*}{s_*^2 x_*^7}} \tag{4.48}$$

4.3.3 Method of Successive Substitution

To solve for $\theta_{1a}(s_*, x_*)$ and $\theta_{1b}(s_*, x_*)$ in Eqs. 4.23 and 4.24, we adopt the method of successive substitution (Zemyan, 2012) by letting,

$$\theta_{1a}(s_*, x_*) = \sum_{n=0}^{\infty} a_n(s_*, x_*) \tag{4.49}$$

$$\theta_{1b}(s_*, x_*) = \sum_{n=0}^{\infty} b_n(s_*, x_*) \tag{4.50}$$

where,

$$a_0(s_*, x_*) = \omega M_a(s_*, x_*) \tag{4.51}$$

$$b_0(s_*, x_*) = M_b(s_*, x_*) \tag{4.52}$$

and,

$$a_n(s_*, x_*) = \begin{bmatrix} -\omega \int_1^{\infty} N_a(s_*, x_*, m_*)\, a_{n-1}(s_*, m_*)\, dm_* \\ -\omega \int_1^{\infty} N_b(s_*, x_*, m_*)\, b_{n-1}(s_*, m_*)\, dm_* \end{bmatrix}, \qquad n = 1, 2, 3... \tag{4.53}$$

$$b_n(s_*, x_*) = \begin{bmatrix} -\int_1^\infty N_d(s_*, x_*, m_*)\, a_{n-1}(s_*, m_*)\, dm_* \\ +\int_1^\infty N_c(s_*, x_*, m_*)\, b_{n-1}(s_*, m_*)\, dm_* \end{bmatrix}, \qquad n = 1, 2, 3... \tag{4.54}$$

Numerical integration for the improper integrals in Eqs. 4.53 and 4.54 is performed by substituting its infinite upper bound with a sufficiently large value (say, 100), and assigning adequate integration points in the vicinity of the peak or the discontinuity in N_a-N_d. Summation of the infinite series is replaced by a partial sum with 200 terms. Convergence is analyzed by truncating the series by different number of terms. For example, at $\omega = 0.25$, difference between the normalized force relaxation results of using 200 and 1000 terms is smaller than 5×10^{-5} at all time instances. Note that in cases I and II, when $\omega \leq 0.5$, the series in $\theta_1(s_*, x_*)$ converges rather fast and the partial sum with only 20 terms is sufficient to give a satisfactory approximation; when ω is close to 1, the convergence becomes slower but can be accelerated using Wynn's epsilon algorithm (Wynn, 1956) due to its effectiveness in dealing with alternating series. These results and techniques are however not applicable for case III, since ω does not exist in Eqs. 4.52 and 4.54 and the partial sum for $\sum_{n=0}^{\infty} b_n$ increases monotonically as the number of terms increases. As a result, a sufficient number of terms is needed to calculate $\theta_{1a}(s_*, x_*)$ and $\theta_{1b}(s_*, x_*)$ in order to reach convergence, even when ω is small.

By substituting Eqs. 4.36, 4.40, 4.44 and 4.48 into Eqs. 4.23-4.26, the asymptotes of $\theta_{1a,b}(s_*, x_*)$ and $M_{a,b}(s_*, x_*)$ at $x_* \to \infty$ can be expressed explicitly,

$$\lim_{x_* \to \infty} \log\left[\theta_{1a}(s_*, x_*)\right] = -\frac{9}{2}\log(x_*) + \log\left(\frac{16}{\pi}\omega s_*^{-\frac{3}{2}} - \frac{24}{\pi}\omega s_*^{-\frac{3}{2}}\Theta\right) \tag{4.55}$$

$$\lim_{x_* \to \infty} \log\left[\theta_{1b}(s_*, x_*)\right] = -\frac{7}{2}\log(x_*) + \log\left(\frac{8}{3\pi}s_*^{-1} - \frac{4}{\pi}s_*^{-1}\Theta\right) \tag{4.56}$$

$$\lim_{x_* \to \infty} \log\left[M_a(s_*, x_*)\right] = -\frac{9}{2}\log(x_*) + \log\left(\frac{16}{\pi}s_*^{-\frac{3}{2}}\right) \tag{4.57}$$

$$\lim_{x_* \to \infty} \log\left[M_b(s_*, x_*)\right] = -\frac{7}{2}\log(x_*) + \log\left(\frac{8}{3\pi}s_*^{-1}\right) \tag{4.58}$$

where,

$$\Theta = \int_1^{\infty} m_*^{\frac{1}{2}} \left[\theta_{1a}\left(s_*, m_*\right) - m_* s_*^{\frac{1}{2}} \theta_{1b}\left(s_*, m_*\right) \right] dm_*$$

Limits of $\theta_{1a}\left(s_*, x_*\right)$ and $\theta_{1b}\left(s_*, x_*\right)$ at $s_* \to 0$ and $s_* \to \infty$ can be determined after substituting the remaining asymptotic expressions for $N_{a-d}\left(s_*, x_*, m_*\right)$ into Eqs. 4.23 and 4.24. For $\theta_{1a}\left(s_*, x_*\right)$,

$$\lim_{s_* \to \infty} \theta_{1a}\left(s_*, x_*\right) = \begin{cases} \dfrac{\omega\left(1 - x_*^2\right)}{\sqrt{x_*}}, & 0 \le x_* \le 1 \\ 0, & x_* > 1 \end{cases} \tag{4.59}$$

$$\lim_{s_* \to 0} \theta_{1a}\left(s_*, x_*\right) = 0, \qquad x_* \ge 0 \tag{4.60}$$

For $\theta_{1b}\left(s_*, x_*\right)$,

$$\lim_{s_* \to \infty} s_*^{\frac{1}{2}} \theta_{1b}\left(s_*, x_*\right) = \begin{cases} 2\sqrt{x_*}, & 0 \le x_* \le 1 \\ 0, & x_* > 1 \end{cases} \tag{4.61}$$

$$\lim_{s_* \to 0} \theta_{1b}\left(s_*, x_*\right) = 0, \qquad x_* \ge 0 \tag{4.62}$$

4.4 Poroelastic Fields

Poroelastic fields on the surface and inside the half space can now be expressed in terms of $\theta_{1a}\left(s_*, x_*\right)$ and $\theta_{1b}\left(s_*, x_*\right)$ in the Laplace domain from direct substitution of the displacement functions $\overline{\mathcal{D}}$ and $\overline{\mathcal{F}}$ into Eqs. 2.9-2.16. However, these expressions from direct substitution all contain improper integrals with oscillatory kernels involving Bessel functions of the first kind $J_v\left(\cdot\right)$. Direct evaluation of these integrals could yield nonsmooth results at small depth. Oscillation in these integrals can however be removed with the aid of Abel transform (Bracewell, 1986; Poularikas, 2018), Sonine's integrals (Noble, 1963) and the use of integral representations of special functions with non-oscillatory kernels. These equations can be found from Eqs. 2.26, 2.27 and Section 2.5.

In the sections below, two sets of expressions, one from direct substitution and the other with the oscillatory kernels removed, are both presented for the pore pressure $\overline{p}$, vertical stress

$\overline{\sigma}_z$ and displacement $\overline{u}_z$. Details for the other non-trivial field variables are given in Appendix C.1. The undrained and drained asymptotes, which correspond to the undrained and drained responses of the Hertzian contact, are the same as those for case I and can be found in Appendix A.1.5.

Poroelastic fields in the time domain can then be computed using a numerical algorithm for inverse Lapalace transform. The Stehfest algorithm (Stehfest, 1970) with 6 expansion terms is again used here. Calculations are performed based on the material properties of the Gulf of Mexico shale (Cheng, 2016) as listed in Table 2.3. Viscosity of the saturating fluid is taken to be $\mu = 1$ cp. As a result, values of the drained and undrained Poisson's ratios are $\nu = 0.219$ and $\nu_u = 0.449$, which correspond to $\omega = 0.4174$. Given radius of the indenter $R = 50$ mm and the indentation depth $d = 0.1$ mm, the corresponding contact radius is $a = 2.23$ mm for this example case.

4.4.1 Pore Pressure

Expression 1 Substituting 4.1, 4.6, 4.17 and 4.22 into Eqs. 2.17 and 2.18 and then $\overline{\mathcal{D}}$ and $\overline{\mathcal{F}}$ into Eq. 2.11, we obtain,

$$\begin{aligned}\alpha\overline{p} = \frac{2G\left(2\eta-1\right)a^3}{cRs_*}\Bigg[&\omega\int_0^1\left(m_*^2-1\right)N_p\left(s_*,r_*,m_*,z_*\right)dm_* \\ &+\omega\int_1^\infty m_*^{\frac{1}{2}}\theta_{1a}\left(s_*,m_*\right)N_p\left(s_*,r_*,m_*,z_*\right)dm_* \\ &+\omega\int_1^\infty m_*^{\frac{1}{2}}s_*^{\frac{1}{2}}\theta_{1b}\left(s_*,m_*\right)\widetilde{N}_p\left(s_*,r_*,m_*,z_*\right)dm_*\Bigg]\end{aligned} \tag{4.63}$$

where,

$$\begin{aligned}N_p\left(s_*,r_*,m_*,z_*\right) = \frac{2}{\pi}\int_0^\infty\xi_*\Bigg[&\frac{\xi_*}{\sqrt{\xi_*^2+s_*}}\exp\left(-z_*\sqrt{\xi_*^2+s_*}\right) \\ &-\exp\left(-z_*\xi_*\right)\Bigg]\cos\left(m_*\xi_*\right)J_0\left(r_*\xi_*\right)d\xi_*\end{aligned} \tag{4.64}$$

and,

$$\widetilde{N}_p\left(s_*, r_*, m_*, z_*\right) = -\frac{2}{\pi}\int_0^\infty \frac{\xi_*}{\sqrt{\xi_*^2 + s_*}} \exp\left(-z_*\sqrt{\xi_*^2 + s_*}\right) \sin\left(m_*\xi_*\right) J_0\left(r_*\xi_*\right) d\xi_* \tag{4.65}$$

Along the contact axis, with $r_* = 0$ and $J_0\left(r_*\xi_*\right) = 1$, $N_p\left(s_*, 0, m_*, z_*\right)$ and $\widetilde{N}_p\left(s_*, 0, m_*, z_*\right)$ can be expressed explicitly since the first term in Eqs. 4.64 and 4.65 can be evaluated with the aid of the modified Bessel functions and the second term in Eq. 4.64 has an elementary antiderivative, i.e.,

$$\begin{aligned} N_p\left(s_*, 0, m_*, z_*\right) = &-\frac{2}{\pi} s_*^{\frac{1}{2}} \left[\frac{m_*^2 - z_*^2}{\left(m_*^2 + z_*^2\right)^{\frac{3}{2}}}\right] \mathrm{K}_1\left[\sqrt{s_*\left(m_*^2 + z_*^2\right)}\right] \\ &-\frac{2}{\pi} s_* \left(\frac{m_*^2}{m_*^2 + z_*^2}\right) \mathrm{K}_0\left[\sqrt{s_*\left(m_*^2 + z_*^2\right)}\right] + \frac{2}{\pi}\left[\frac{m_*^2 - z_*^2}{\left(m_*^2 + z_*^2\right)^2}\right] \end{aligned} \tag{4.66}$$

$$\widetilde{N}_p\left(s_*, 0, m_*, z_*\right) = -\frac{2}{\pi} s_*^{\frac{1}{2}} \frac{m_*}{\sqrt{m_*^2 + z_*^2}} \mathrm{K}_1\left[\sqrt{s_*\left(m_*^2 + z_*^2\right)}\right] \tag{4.67}$$

It is therefore convenient to use Eqs. 4.63, 4.66 and 4.67 to calculate the pore pressure along the contact axis. Note that for the sake of brevity, explicit expressions for similar integrals in the sections below will be omitted.

Expression 2 On the surface ($z_* = 0$), an alternative expression for the pore pressure field can be obtained by first applying Sonine's infinite integral in Eq. 2.27 to Eq. 4.63, and then the inverse Abel transform in Eq. 2.64 to the resulting equation, which gives,

$$\alpha\overline{p} = \frac{4G\left(2\eta - 1\right)a^3}{\pi c R s_*}\omega \int_{r_*}^1 \frac{x_*^{\frac{1}{2}} s_*^{\frac{1}{2}} \theta_{1b}\left(s_*, x_*\right) dx_*}{\sqrt{x_*^2 - r_*^2}} \tag{4.68}$$

Note that the pore pressure on the surface is continuous across $r_* = 1$ and is zero at $r_* \geq 1$.

Inside the half space ($z_* > 0$), the alternative expression for pore pressure can be derived by firstly applying Sonine's finite integral in Eq. 2.26 to Eq. 4.63, then multiplying both sides with $x_*^{\frac{1}{2}}$, taking derivative of the resulting equation with respect to x_*, and finally performing

the Abel transformation in Eq. 2.66. This gives,

$$\alpha\overline{p} = \frac{4G\left(2\eta-1\right)a^3}{\pi cRs_*}\int_0^{r_*}\frac{\theta_p\left(s_*,x_*,z_*\right)dx_*}{\sqrt{r_*^2-x_*^2}} \tag{4.69}$$

where $\theta_p\left(s_*,x_*,z_*\right)$ is,

$$\begin{aligned}\theta_p\left(s_*,x_*,z_*\right) &= \omega\int_0^1\left(m_*^2-1\right)N_{px,x}\left(s_*,x_*,m_*,z_*\right)dm_* \\ &+\omega\int_1^\infty m_*^{\frac{1}{2}}\theta_{1a}\left(s_*,m_*\right)N_{px,x}\left(s_*,x_*,m_*,z_*\right)dm_* \\ &+\omega\int_1^\infty m_*^{\frac{1}{2}}s_*^{\frac{1}{2}}\theta_{1b}\left(s_*,m_*\right)\widetilde{N}_{px,x}\left(s_*,x_*,m_*,z_*\right)dm_*\end{aligned} \tag{4.70}$$

and,

$$\begin{aligned}N_{px,x}\left(s_*,x_*,m_*,z_*\right) = \frac{2}{\pi}\int_0^\infty\xi_*\Bigg[&\frac{\xi_*}{\sqrt{\xi_*^2+s_*}}\exp\left(-z_*\sqrt{\xi_*^2+s_*}\right) \\ &-\exp\left(-z_*\xi_*\right)\Bigg]\cos\left(m_*\xi_*\right)\cos\left(x_*\xi_*\right)d\xi_*\end{aligned} \tag{4.71}$$

$$\widetilde{N}_{px,x}\left(s_*,x_*,m_*,z_*\right) = -\frac{2}{\pi}\int_0^\infty\frac{\xi_*}{\sqrt{\xi_*^2+s_*}}\exp\left(-z_*\sqrt{\xi_*^2+s_*}\right)\sin\left(m_*\xi_*\right)\cos\left(x_*\xi_*\right)d\xi_* \tag{4.72}$$

The oscillatory nature in $N_{px,x}$ and $\widetilde{N}_{px,x}$ can be removed with the aid of the modified Bessel functions.

Pore pressure in the time domain can be determined after taking the inverse Laplace transform to Eq. 4.69,

$$\alpha p = \frac{4G\left(2\eta-1\right)a}{\pi R}\int_0^{r_*}\frac{\mathcal{L}^{-1}\left[s_*^{-1}\theta_p\left(s_*,x_*,z_*\right)\right]dx_*}{\sqrt{r_*^2-x_*^2}} \tag{4.73}$$

Here $\mathcal{L}^{-1}$ denotes the inverse Laplace transform with respect to s_*, see Eq. 2.81.

Distribution of the pore pressure along the contact axis, calculated using Eqs. 4.63, 4.66 and 4.67, is shown in Fig. 4.1 for various dimensionless times. The pore pressure is the largest at the contact origin and decreases monotonically with depth. The Mandel-Cryer effect, where the pore pressure rises above the initial value at $t_* = 0$ before its dissipation, is observed at

early times (see the inset).

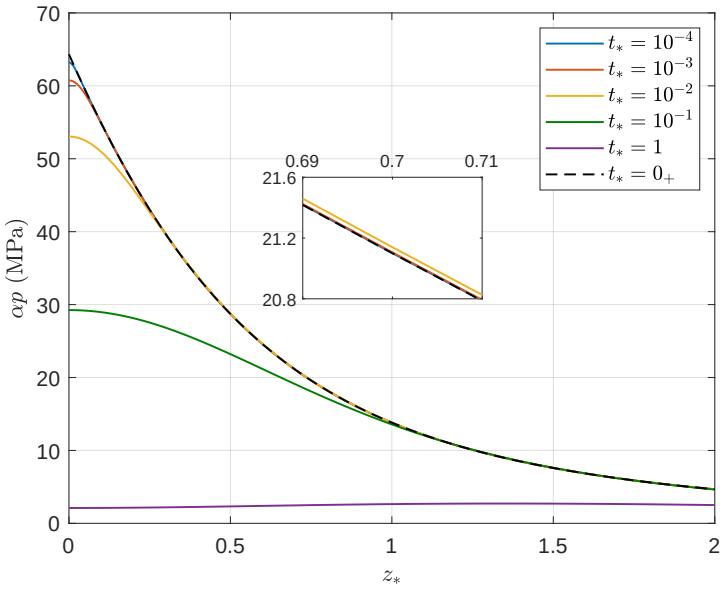

Figure 4.1: Distribution of the pore pressure along the contact axis.

4.4.2 Vertical Stress

Expression 1 The vertical stress field can be obtained after substituting $\overline{\mathcal{D}}$ and $\overline{\mathcal{F}}$ into into Eq. 2.12,

$$\begin{aligned}\overline{\sigma}_z = \frac{2Ga^3}{c\phi R s_*}\Bigg[&\int_0^1 \left(m_*^2 - 1\right) N_{sz}\left(s_*, r_*, m_*, z_*\right) dm_* \\ &+ \int_1^\infty m_*^{\frac{1}{2}} \theta_{1a}\left(s_*, m_*\right) N_{sz}\left(s_*, r_*, m_*, z_*\right) dm_* \\ &+ \int_1^\infty m_*^{\frac{1}{2}} s_*^{\frac{1}{2}} \theta_{1b}\left(s_*, m_*\right) \widetilde{N}_{sz}\left(s_*, r_*, m_*, z_*\right) dm_*\Bigg]\end{aligned} \tag{4.74}$$

where,

$$\begin{aligned}N_{sz}\left(s_*, r_*, m_*, z_*\right) = -\frac{2}{\pi}\int_0^\infty \xi_* \Bigg\{&\left(1 + z_*\xi_*\right)\exp\left(-z_*\xi_*\right) \\ &+ \frac{2\omega}{1+\omega}\left(\frac{\xi_*^2}{s_*}\right)\left[\frac{\xi_*}{\sqrt{\xi_*^2 + s_*}}\exp\left(-z_*\sqrt{\xi_*^2 + s_*}\right) - \exp\left(-z_*\xi_*\right)\right]\Bigg\}\cos\left(m_*\xi_*\right) J_0\left(r_*\xi_*\right) d\xi_*\end{aligned} \tag{4.75}$$

and,

$$\widetilde{N}_{sz}\left(s_*, r_*, m_*, z_*\right) = \frac{4\omega}{\pi\left(1+\omega\right)} \int_0^\infty \left(\frac{\xi_*^2}{s_*}\right) \left[\frac{\xi_*}{\sqrt{\xi_*^2 + s_*}} \exp\left(-z_* \sqrt{\xi_*^2 + s_*}\right) - \exp\left(-z_* \xi_*\right)\right] \sin\left(m_* \xi_*\right) J_0\left(r_* \xi_*\right) d\xi_* \tag{4.76}$$

Expression 2 On the surface ($z_* = 0$), expression of the normal stress in the second set can be obtained by applying Eqs. 2.27 and 2.65 successively to Eq. 4.74,

$$\overline{\sigma}_z = \frac{2G\left(2\eta - 1\right) a^3}{\pi c \eta R s_*} \begin{bmatrix} 2\sqrt{1 - r_*^2} + \dfrac{\theta_{1a}\left(s_*, 1\right)}{\sqrt{1 - r_*^2}} \\ -\displaystyle\int_{r_*}^1 \theta_3\left(s_*, x_*\right) \frac{dx_*}{\sqrt{x_*^2 - r_*^2}} \end{bmatrix}, \qquad r_* \leq 1 \tag{4.77}$$

where,

$$\theta_3\left(s_*, x_*\right) = \frac{\partial}{\partial x_*} \left[x_*^{\frac{1}{2}} \theta_{1a}\left(s_*, x_*\right)\right] \tag{4.78}$$

See Appendix C.2 for the expression of $\theta_3\left(s_*, x_*\right)$.

Inside the half space ($z_* > 0$), the vertical stress $\overline{\sigma}_z$ can be obtained by applying Eqs. 2.26 and 2.66 successively to Eq. 4.74,

$$\overline{\sigma}_z = \frac{4Ga^3}{\pi c \phi R s_*} \int_0^{r_*} \frac{\theta_{sz}\left(s_*, x_*, z_*\right) dx_*}{\sqrt{r_*^2 - x_*^2}} \tag{4.79}$$

where,

$$\begin{aligned} \theta_{sz}\left(s_*, x_*, z_*\right) = & \int_0^1 \left(m_*^2 - 1\right) N_{szx,x}\left(s_*, x_*, m_*, z_*\right) dm_* \\ & + \int_1^\infty m_*^{\frac{1}{2}} \theta_{1a}\left(s_*, m_*\right) N_{szx,x}\left(s_*, x_*, m_*, z_*\right) dm_* \\ & + \int_1^\infty m_*^{\frac{1}{2}} s_*^{\frac{1}{2}} \theta_{1b}\left(s_*, m_*\right) \widetilde{N}_{szx,x}\left(s_*, x_*, m_*, z_*\right) dm_* \end{aligned} \tag{4.80}$$

and,

$$N_{szx,x}\left(s_*, x_*, m_*, z_*\right) = -\frac{2}{\pi}\int_0^\infty \xi_* \left\{ \left(1 + z_*\xi_*\right)\exp\left(-z_*\xi_*\right) + \frac{2\omega}{1+\omega}\left(\frac{\xi_*^2}{s_*}\right)\left[\frac{\xi_*}{\sqrt{\xi_*^2 + s_*}}\exp\left(-z_*\sqrt{\xi_*^2 + s_*}\right) - \exp\left(-z_*\xi_*\right)\right]\right\}\cos\left(m_*\xi_*\right)\cos\left(x_*\xi_*\right)d\xi_* \tag{4.81}$$

$$\widetilde{N}_{szx,x}\left(s_*, x_*, m_*, z_*\right) = \frac{4\omega}{\pi\left(1+\omega\right)}\int_0^\infty \left(\frac{\xi_*^2}{s_*}\right)\left[\frac{\xi_*}{\sqrt{\xi_*^2 + s_*}}\exp\left(-z_*\sqrt{\xi_*^2 + s_*}\right) - \exp\left(-z_*\xi_*\right)\right]\sin\left(m_*\xi_*\right)\cos\left(x_*\xi_*\right)d\xi_* \tag{4.82}$$

Contact stress distributions at various times is shown in Fig. 4.2. Similar to the distributions in cases I and II, the contact stress from the full poroelastic solution reduces to the classical Hertzian solution at $t_* = 0$ and $t_* \to \infty$, while at intermediate times, the contact stress is bounded by the two limits within the contact region except near the contact edge around $r_* = 1$, where the contact stress is in fact singular. Such stress singularity can again be attributed to the assumption of a fixed contact radius a, which effectively allows a kink at $r_* = 1$ on the deformed surface to develop at intermediate times, see Fig. 4.3.

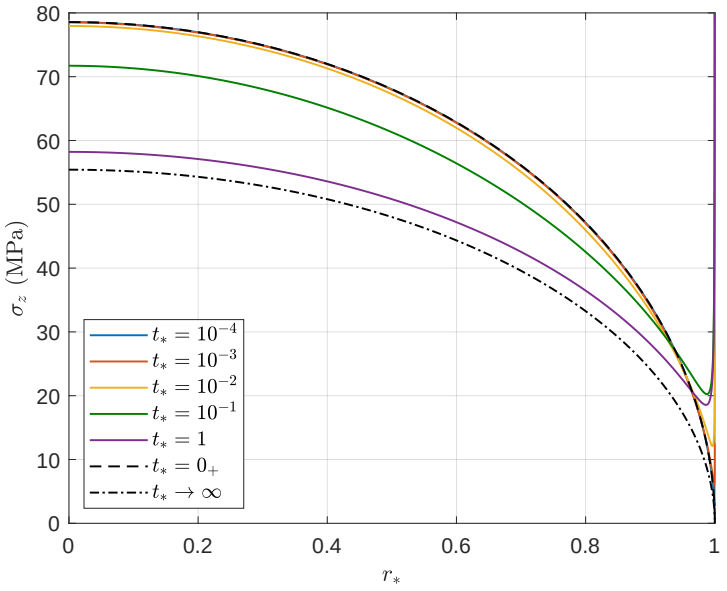

Figure 4.2: Distribution of the contact stress at various dimensionless times.

Instantaneously after indentation, the largest excess pore pressure is produced right beneath the contact surface. At early time, it is the drainage condition inside the contact area that controls the primary drainage path and therefore the poroelastic response. As a result, the isochrones of the contact stress at small times from case III is closer to that of case II. Difference of the stress distributions near the contact axis between cases II and III is insignificant at early times. However, the discrepancy at the contact edge is identifiable, compare Figs. 3.3 and 4.2. After all, the drainage condition right outside of the contact area are distinctly different between cases II and III.

At late time, the surface drainage conditions outside of the contact area becomes more critical in affecting the dissipation of excess pore pressure. At a given time (e.g., $t_* = 1$), the isochrone of contact stress from case III is closer to the drained asymptote than that of case II, but farther than that of case I.

4.4.3 Vertical Displacement

Expression 1 Vertical displacement $\overline{u}_z$ can be obtained after substituting $\overline{\mathcal{D}}$ and $\overline{\mathcal{F}}$ into Eq. 2.10,

$$\begin{aligned}\overline{u}_z = \frac{a^4}{c\phi R s_*}\Bigg[&\int_0^1 \left(m_*^2-1\right) N_{uz}\left(s_*, r_*, m_*, z_*\right) dm_* \\ &+ \int_1^\infty m_*^{\frac{1}{2}} \theta_{1a}\left(s_*, m_*\right) N_{uz}\left(s_*, r_*, m_*, z_*\right) dm_* \\ &+ \int_1^\infty m_*^{\frac{1}{2}} s_*^{\frac{1}{2}} \theta_{1b}\left(s_*, m_*\right) \widetilde{N}_{uz}\left(s_*, r_*, m_*, z_*\right) dm_*\Bigg]\end{aligned} \tag{4.83}$$

where,

$$\begin{aligned}N_{uz}\left(s_*, r_*, m_*, z_*\right) = -\frac{2}{\pi}\int_0^\infty \Bigg\{ &\left(\phi + z_*\xi_*\right)\exp\left(-z_*\xi_*\right) \\ +\frac{2\omega}{1+\omega}\left(\frac{\xi_*^2}{s_*}\right)&\left[\exp\left(-z_*\sqrt{\xi_*^2+s_*}\right) - \exp\left(-z_*\xi_*\right)\right]\Bigg\}\cos\left(m_*\xi_*\right) J_0\left(r_*\xi_*\right) d\xi_*\end{aligned} \tag{4.84}$$

and,

$$\begin{aligned}\widetilde{N}_{uz}\left(s_*, r_*, m_*, z_*\right) = \frac{4\omega}{\pi\left(1+\omega\right)}\int_0^\infty \left(\frac{\xi_*}{s_*}\right)&\left[\exp\left(-z_*\sqrt{\xi_*^2+s_*}\right)\right. \\ &\left. - \exp\left(-z_*\xi_*\right)\right]\sin\left(m_*\xi_*\right) J_0\left(r_*\xi_*\right) d\xi_*\end{aligned} \tag{4.85}$$

Expression 2 Inside the half space ($z_* > 0$), the vertical displacement $\overline{u}_z$ can be obtained in a similar way to the derivation for pore pressure and normal stress,

$$\overline{u}_z = \frac{2a^4}{\pi c\phi R s_*}\int_0^{r_*} \frac{\theta_{uz}\left(s_*, x_*, z_*\right) dx_*}{\sqrt{r_*^2 - x_*^2}} \tag{4.86}$$

where,

$$\begin{aligned}\theta_{uz}\left(s_*, x_*, z_*\right) = &\int_0^1 \left(m_*^2-1\right) N_{uzx,x}\left(s_*, x_*, m_*, z_*\right) dm_* \\ &+ \int_1^\infty m_*^{\frac{1}{2}} \theta_{1a}\left(s_*, m_*\right) N_{uzx,x}\left(s_*, x_*, m_*, z_*\right) dm_* \\ &+ \int_1^\infty m_*^{\frac{1}{2}} s_*^{\frac{1}{2}} \theta_{1b}\left(s_*, m_*\right) \widetilde{N}_{uzx,x}\left(s_*, x_*, m_*, z_*\right) dm_*\end{aligned} \tag{4.87}$$

and,

$$N_{uzx,x}\left(s_*, x_*, m_*, z_*\right) = -\frac{2}{\pi}\int_0^\infty \Bigg\{ \left(\phi + z_*\xi_*\right)\exp\left(-z_*\xi_*\right) + \frac{2\omega}{1+\omega}\left(\frac{\xi_*^2}{s_*}\right)\left[\exp\left(-z_*\sqrt{\xi_*^2+s_*}\right) - \exp\left(-z_*\xi_*\right)\right]\Bigg\}\cos\left(m_*\xi_*\right)\cos\left(x_*\xi_*\right)d\xi_* \tag{4.88}$$

$$\widetilde{N}_{uzx,x}\left(s_*, x_*, m_*, z_*\right) = \frac{4\omega}{\pi\left(1+\omega\right)}\int_0^\infty \left(\frac{\xi_*}{s_*}\right)\left[\exp\left(-z_*\sqrt{\xi_*^2+s_*}\right) - \exp\left(-z_*\xi_*\right)\right]\sin\left(m_*\xi_*\right)\cos\left(x_*\xi_*\right)d\xi_* \tag{4.89}$$

On the surface ($z_* = 0$), $\widetilde{N}_{uz}$ is zero and N_{uz} can be expressed in closed-form,

$$N_{uz}\left(s_*, x_*, m_*, 0\right) = -\frac{2\phi}{\pi\sqrt{r_*^2 - m_*^2}}\mathcal{H}\left(r_* - m_*\right) \tag{4.90}$$

Substituting Eq. 4.90 into Eq. 4.83 gives,

$$\overline{u}_z = \frac{a^4}{cRs_*}\left(1 - \frac{1}{2}r_*^2\right), \qquad r_* \le 1 \tag{4.91}$$

and,

$$\overline{u}_z = \frac{a^4}{\pi cRs_*}\left[\begin{array}{l} \sqrt{r_*^2-1} + \left(2 - r_*^2\right)\arcsin\left(\dfrac{1}{r_*}\right) \\ -2\displaystyle\int_1^{r_*} m_*^{\frac{1}{2}}\theta_{1a}\left(s_*, m_*\right)\frac{dm_*}{\sqrt{r_*^2 - m_*^2}} \end{array}\right], \qquad r_* \ge 1 \tag{4.92}$$

Vertical and radial displacement expressions in Eqs. 4.91-4.92 and Eqs. C.19-C.20 allow us to examine how the surface displacement evolves with time and differs from that of the case if the frictionless contact with a rigid sphere were to be modeled. Surface profile distributions for case III are shown in Fig. 4.3, which are very similar to the distributions in cases I and II. At a given transient time, the surface profile from case III is bounded by the curves from cases I and II.

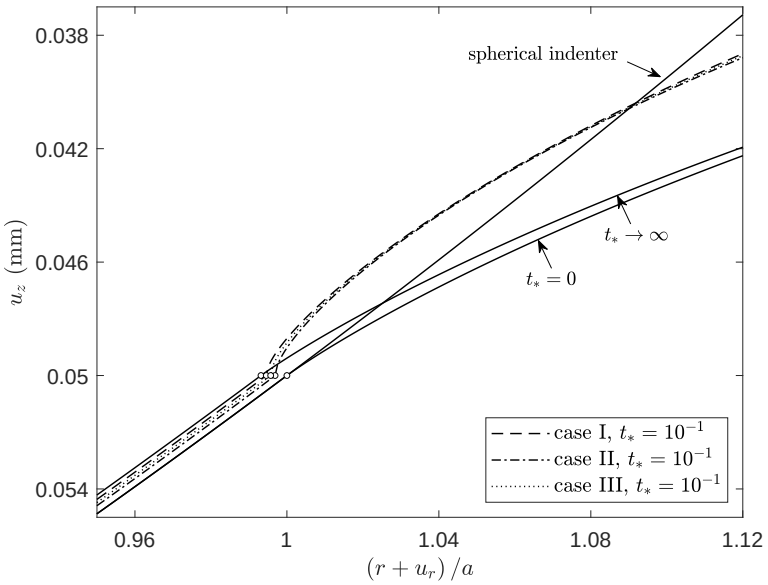

(a) incompressible constituents, $\nu = 0.219$ and $\nu_u = 0.5$

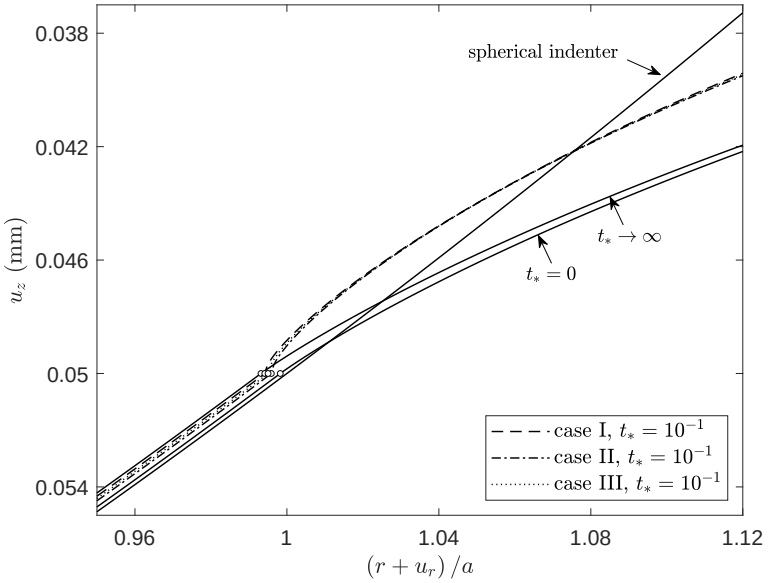

(b) compressible constituents, $\nu = 0.219$ and $\nu_u = 0.449$

Figure 4.3: Comparison of surface displacement profiles at the undrained and drained limits ($t_* = 0_+$, $t_* \to \infty$) and at $t_* = 0.1$ from cases I-III; the material point at the contact edge is marked by the empty circle.

4.5 Incipient Failure

Incipient failure in form of tensile fracturing and plastic deformation could take place in spherical indentation. It is therefore of interest to examine how poroelasticity could affect potential development of the indentation crack system and plastic failure.

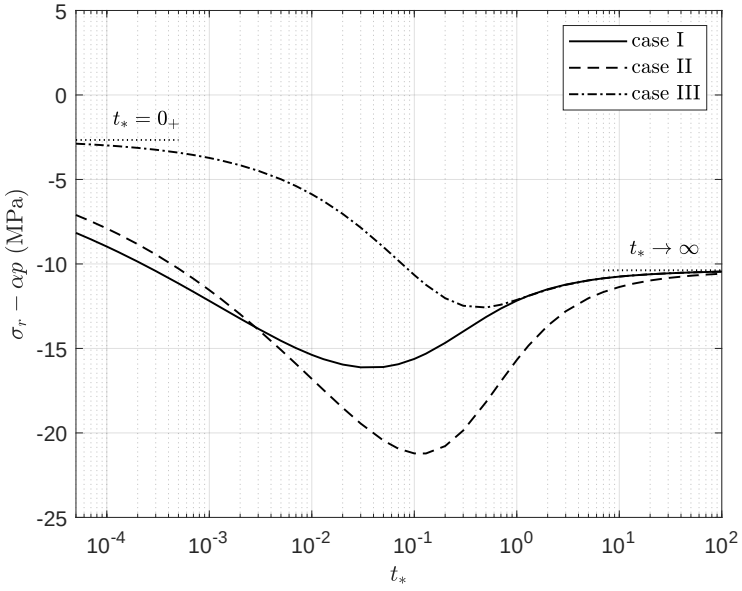

Figure 4.4: Variation of the effective radial stress with the dimensionless time at $r_* = 1_+$ on the surface (right outside of the contact area).

The classical Hertzian cone crack initiates on the surface as a ring crack slightly outside of the contact area and propagates stably downwards to form a cone (Lawn, 1998). Fig. 4.4 shows a comparison of the effective radial stress at the contact edge ($r_* = 1_+$) between three cases. In all of them, magnitude of the effective radial stress in tension first increases from the early time asymptote to a peak value, and then decreases and finally approaches to the drained asymptote. The peak values for cases I, II and III are -16.12, -21.22 and -12.58 MPa, respectively. This indicates that if the tensile strength is relatively large ($\gtrsim$ 10 MPa), then the ring/cone crack system is more likely to occur in case II, less likely in case I and least likely in case III.

At a given depth along the contact axis, the effective radial stress, $\sigma_r - \alpha p$, and the maximum

shear stress, $(\sigma_z - \sigma_r)/2$, can be used to infer the possibility of median crack nucleation and incipient plastic yielding, respectively. Variation of these two variables along the contact axis with the dimensionless time is very similar to those in case II except that at late time, the isochrones in case III are closer to the drained asymptote. These results are not shown here for the sake of brevity.

4.6 Indentation Force Relaxation

4.6.1 Master Curves

Following the normalization method in Section 2.7.1, explicit expression of the normalized indentation force $F_n(t_*)$ can be derived from Eq. 4.77,

$$F_n(t_*) = \frac{3}{2\omega}\mathcal{L}^{-1}\left[s_*^{-1}\int_0^1 x_*^{\frac{1}{2}}\theta_{1a}(s_*, x_*)\,dx_*\right] \tag{4.93}$$

The force relaxation behaviors at $\omega = 0,\ 0.5,\ 1$ are plotted for the three cases in Fig. 4.5. As expected, the normalized force relaxation response is the fastest in case I and slowest in case II, with case III being in the middle and bounded by cases II and I at early and late times, respectively. This can be explained by the fact that the drainage path and the corresponding relaxation time are the shortest when the surface is fully permeable, and the longest when the surface is fully impermeable. Fig. 4.5 also shows that dependence of the normalized force relaxation response on constant ω is rather weak for all three cases. In other words, uncertainty in ω is not likely to have a significant effect on the normalized force relaxation response.

The force relaxation response from our theoretical solution for case II can be fitted using a four-parameter function, see Eq. 2.111. The fitting parameters a_1, b_1, a_2, b_2 are listed in Table 4.2. Indeed, this elementary function gives an excellent approximation and the coefficient of determination for all ω is $R^2 = 1$. In addition, the expression of $t_{*0.5}$ with respect to ω is $t_{*0.5} = 0.333 - 0.0942\omega + 0.0649\omega^2 - 0.0176\omega^3$, where $t_{*0.5}$ denotes the dimensionless time where $F_n(t_*) = 0.5$.

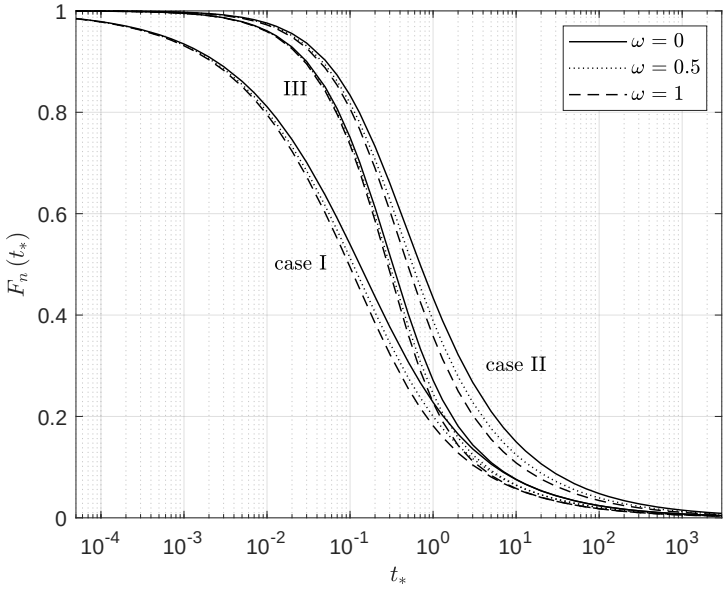

Figure 4.5: Relaxation of the normalized indentation force with the dimensionless time - comparison of cases I-III surface drainage conditions.

ω	a_1	b_1	a_2	b_2
0	1.4	0.634	6.56	1.3
0.1	1.45	0.639	6.72	1.313
0.3	1.55	0.647	7	1.336
0.44	1.62	0.651	7.16	1.348
0.5	1.65	0.655	7.23	1.355
0.7	1.73	0.662	7.42	1.37
0.9	1.82	0.669	7.57	1.383
1	1.86	0.671	7.68	1.391

Table 4.2: Values of the fitting parameters for the force relaxation curves.

A comparison is also made between this study (case III) and the fitting function from (Hu et al., 2010) based on their numerical simulations, where,

$$f_n(t_*) = 0.491 \exp\left(-0.908\sqrt{t_*}\right) + 0.509 \exp\left(-1.679 t_*\right) \tag{4.94}$$

The numerical analysis in Hu et al. (2010) assumes a case III surface drainage condition and step displacement loading. A domain size 20 times larger than the contact size is used. The

value of ω for the fully saturated hydrogel they studied is $\omega = 0.44$.

It can be seen from Fig. 4.6 that the theoretical and numerical result agree quite well overall. But there is some slight difference. Details of the numerical simulations, e.g., realization of the step displacement loading, finite size of the numerical domain with fully drained lateral boundaries, etc. are perhaps the reasons for the discrepancy, especially the faster relaxation response at late time from the numerical result.

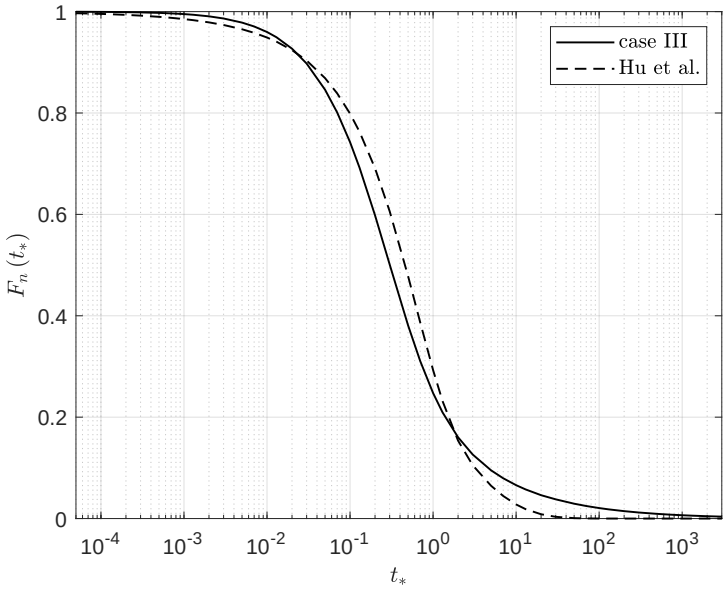

Figure 4.6: Comparison of the force relaxation curves between this study (case III) and Hu et al. (2010); $\omega = 0.44$.

4.6.2 Asymptotic Behaviors

At $\omega = 0$, the normalized indentation force $F_n(t_*)$ becomes indefinite, since the indentation force remains constant. However, mathematically, the limit of $F_n(t_*)$ at $\omega = 0$ exists and can be derived based on our solution scheme by taking Eq. 4.49 into Eq. 4.93 and setting $\omega = 0$. After some manipulations, the normalized indentation force can be expressed as,

$$F_n(t_*) = \frac{3}{2}\mathcal{L}^{-1}\left[s_*^{-1}\int_0^1 x_*^{\frac{1}{2}} M_a(s_*, x_*)\, dx_* + 2s_*^{-\frac{3}{2}}\left[M_b(s_*, 1) - \theta_{1c}(s_*, 1)\right]\right] \tag{4.95}$$

where $\theta_{1c}(s_*, 1)$ can be determined from,

$$\theta_{1c}(s_*, x_*) - \int_1^\infty N_c(s_*, x_*, m_*)\,\theta_{1c}(s_*, m_*)\,dm_* = M_b(s_*, x_*) \tag{4.96}$$

Solution for the Fredholm integral equation above is given by,

$$\theta_{1c}(s_*, x_*) = \sum_{n=0}^{\infty} c_n(s_*, x_*) \tag{4.97}$$

where,

$$c_0(s_*, x_*) = M_b(s_*, x_*) \tag{4.98}$$

$$c_n(s_*, x_*) = \int_1^\infty N_c(s_*, x_*, m_*)\,c_{n-1}(s_*, m_*)\,dm_*, \qquad n = 1, 2, 3... \tag{4.99}$$

Unlike cases I and II, in case III, we are unable to derive a closed-form expression for the force relaxation behavior at $\omega = 0$. However, a few interesting observations can be made based on the comparison of the full solutions plotted in a log-log scale for all three cases, see Fig. 4.7.

At early time, the curves of $1 - F_n(t_*)$ from different values of ω for case III appear to be indistinguishable from each other. A single curve parallel to those from case II seems to be adequate in describing the early time behavior. By fitting the full solution of case III at $\omega = 0$ for $t_* \leq 10^{-4}$, we obtain,

$$\lim_{t_* \to 0} F_n(t_*) = 1 - 5.5t_* \tag{4.100}$$

At late time, the force relaxation responses from case III become identical to those from case I at $t_* > 10$. Therefore, for case III, at $\omega = 0$,

$$\lim_{t_* \to \infty} F_n(t_*) = \frac{4}{3\pi^2}\left(\frac{t_*}{\pi}\right)^{-\frac{1}{2}} \tag{4.101}$$

At $\omega > 0$, the relaxation behaviors follow $t_*^{-\frac{1}{2}}$.

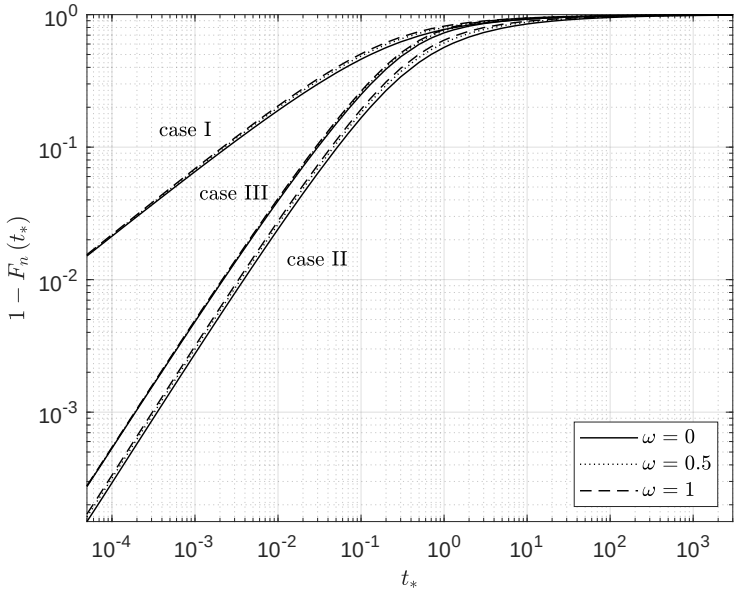

(a) early time behaviors

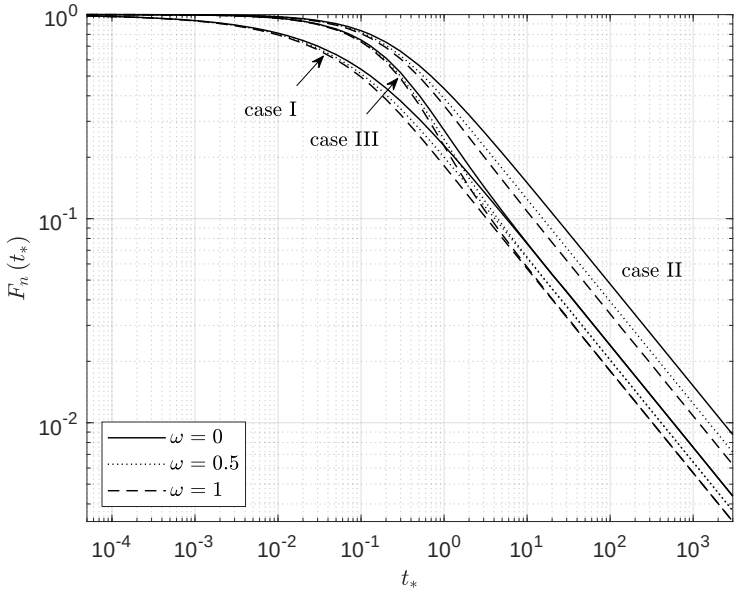

(a) late time behaviors

Figure 4.7: Asymptotic behaviors of the normalized indentation force at $\omega = 0$, 0.5 and 1 for cases I-III.

5 FINITE ELEMENT MODELING OF SPHERICAL INDENTATION IN A PORO-ELASTO-PLASTIC MEDIUM VIA STEP DISPLACEMENT LOADING

5.1 Introduction

Poroelastic spherical indentation via step displacement or step force loading has been developed as an experimental technique to characterize poroelasticity for fully saturated soft and biological materials such as polymeric gels and hydrated bones at both micro- and macro-scale (Galli and Oyen, 2008; Oyen, 2008; Hu et al., 2010; Kalcioglu et al., 2012). In theory, for a fully saturated porous medium consisting of incompressible constituents, if the indenter is subjected to either step displacement or step force loading, elastic constants can be determined from the undrained and drained responses according to the Hertzian contact solution (Hertz, 1881), while hydraulic diffusivity or the coefficient of consolidation can be obtained from the transient response by matching the measured indentation force or displacement as a function of time against a master curve. Such master curves for various indenter shapes under step displacement loading have been previously constructed through finite element simulations (Hu et al., 2010) and also semi-analytically for spherical indentation with step force loading (Agbezuge and Deresiewicz, 1974; Oyen, 2008). A unique feature of such a testing method is that the test duration scales with the contact area. As such, significant time saving can be achieved if the size of the spherical indenter and the depth of penetration are chosen appropriately (Kalcioglu et al., 2012).

Theoretical basis for generalizing the testing methodology to include geomaterials, where compressibility of the constituents is no longer negligible, has been established in our recent works (Liu and Huang, 2018, 2019a,b, 2021). Fully coupled theoretical solutions, derived within the framework of Biot's theory (Biot, 1941), have been obtained for poroelastic spherical indentation via step displacement loading for three distinct types of surface drainage conditions: case I − a fully permeable surface, case II − a fully impermeable surface and case III − a mixed drainage condition where the surface is impermeable in the contact region, but perme-

able everywhere else. However, for geomaterials, yielding and tensile fracturing may occur if the indentation depth exceeds a threshold. Understanding how plastic deformation and tensile failure affect the spherical indentation process is therefore crucial to establishing spherical indentation as an experimental technique for poroelasticity characterization of geomaterials.

In this work, we focus on numerically modeling the poroelastic and poro-elasto-plastic spherical indentation processes with step displacement loading in order to compare the numerical results with our theoretical solutions and to investigate the effect of plastic deformation on the indentation process with the ultimate goal of understanding the parameter space where our poroelastic solutions are applicable even when the medium is poro-elasto-plastic.

We implement a fully coupled finite element method (FEM) algorithm for poro-elasto-plasticity for both plane strain and cylindrically axisymmetric problems using MATLAB following the mixed continuous Galerkin formulation for displacement and pore pressure (Borja, 1986; Lewis and Schrefler, 1998; White and Borja, 2008; Verruijt, 2013). The FEM algorithm assumes that the porous medium is isotropic and elasto-perfectly plastic, following a Drucker-Prager yield criterion with an associative or non-associative flow rule. The Newton-Raphson method with the tangent stiffness scheme is adopted to deal with plasticity in the solid skeleton. A stabilization scheme (White and Borja, 2008), which permits equal-order spatial interpolation for the displacement and pore pressure fields and suppresses pore pressure oscillation in the incompressible or nearly incompressible limit, is incorporated in this FEM algorithm. We extensively benchmark the algorithm with not only analytical solutions to classical poroelastic problems (Terzaghi, 1943; Mandel, 1953; Cryer, 1963; De Leeuw, 1965; Verruijt, 2013) but also an analytical solution for one dimensional consolidation with plasticity incorporated, which we rederive based on an early work by Pariseau (Pariseau, 1999) for clarity in physical parameters and unifying the cases for the Drucker-Prager and Mohr-Coulomb failure criteria.

The paper is organized as follows. FEM formulation for linear poroelasticity and poro-elasto-plasticity is first introduced. The analytical solution for poro-elasto-plastic consolidation is derived next. After the numerical algorithm is validated for the effectiveness of the stabilization scheme and the accuracy against benchmark solutions, this fully coupled FEM

algorithm is applied to model the spherical indentation process in a poroelastic as well as a poro-elasto-plastic medium.

5.2 Numerical Formulation

5.2.1 Governing Equations

The equilibrium and storage equations for a fully coupled linear poroelasticity problem in a saturated isotropic porous medium can be written as (Biot, 1941; Detournay and Cheng, 1993; Wang, 2000; Verruijt, 2013; Cheng, 2016),

$$\nabla \cdot \left(\boldsymbol{\sigma}' - \alpha p \mathbf{I}\right) + \rho \mathbf{g} = \mathbf{0} \tag{5.1}$$

$$S\dot{p} + \alpha \nabla \cdot \dot{\mathbf{u}} - \frac{\kappa}{\mu}\left(\nabla^2 p\right) = 0 \tag{5.2}$$

where $\boldsymbol{\sigma}'$ is the effective stress tensor; p is the pore pressure; $\mathbf{u}$ is the displacement vector; $\mathbf{I}$ is the identity matrix; ρ and $\mathbf{g}$ are the bulk density and gravitational acceleration; μ and κ are the dynamic fluid viscosity and the intrinsic permeability; and α and S are Biot's coefficient and the storage coefficient, which can be related to the skeleton bulk modulus and porosity, K and n, and the fluid and solid phase bulk modulus, K_f and K_s, through,

$$\alpha = 1 - \frac{K}{K_s} \tag{5.3}$$

$$S = \frac{\alpha - n}{K_s} + \frac{n}{K_f} \tag{5.4}$$

Tension positive is adopted here and in Chapter 6 as the sign convention. Darcy's law for fluid flow in porous media is reflected in Eq. 5.2.

Constitutive relationship can be expressed in an incremental form,

$$\Delta\boldsymbol{\sigma}' = \mathbf{D}\Delta\boldsymbol{\varepsilon} \tag{5.5}$$

where $\boldsymbol{\varepsilon}$ is the strain tensor, $\boldsymbol{\varepsilon} = \frac{1}{2}\left(\nabla + \nabla^T\right)\mathbf{u}$, and $\mathbf{D}$ is the fourth-order tensor of tangent moduli, which allows for either an elastic or elasto-plastic material model. We assume that the porous medium obeys a Drucker-Prager yield criterion with an associative or non-associative flow rule. The failure criterion can be written as,

$$f\left(\boldsymbol{\sigma}'\right) = \sqrt{J_2} + bI_1 - s \tag{5.6}$$

where b and s are material constants; I_1 is the first stress invariant, $I_1 = tr\left(\boldsymbol{\sigma}'\right)$; and J_2 is the second deviatoric stress invariant. Denote $\boldsymbol{s}'$ as the deviatoric effective stress tensor, $\boldsymbol{s}' = \boldsymbol{\sigma}' - (I_1/3)\,\mathbf{I}$; J_2 can be determined from $J_2 = \frac{1}{2}tr\left(\boldsymbol{s}'\boldsymbol{s}'\right)$.

The Drucker-Prager failure criterion can also be expressed using the material parameters for a Mohr-Coulomb criterion (Chen, 2013). If we set,

$$b = \frac{2\sin\varphi}{\sqrt{3}\,(3-\sin\varphi)},\ s = \frac{6c_0\cos\varphi}{\sqrt{3}\,(3-\sin\varphi)} \tag{5.7}$$

with c_0 and φ being the cohesion and internal friction angle for a Mohr-Coulomb criterion, the Drucker-Prager failure envelope then intersects the outer edges of the Mohr-Coulomb failure criterion on the $\pi-$ plane, i.e., the triaxial compression state. The Drucker-Prager criterion inscribes the Mohr-Coulomb yield surface if,

$$b = \frac{2\sin\varphi}{\sqrt{3}\,(3+\sin\varphi)},\ s = \frac{6c_0\cos\varphi}{\sqrt{3}\,(3+\sin\varphi)} \tag{5.8}$$

In this study, we choose to set c_0 and φ as the input parameters with the Drucker-Prager material constants determined from Eq. 5.7.

The corresponding plastic potential can be written as,

$$g\left(\boldsymbol{\sigma}'\right) = \sqrt{J_2} + \bar{b}I_1 \tag{5.9}$$

where material parameter $\bar{b}$ is obtained by replacing φ with the dilatancy angle ψ in the

definition of b in Eq. 5.7. The flow rule is associative if $\varphi = \psi$ and non-associative if $\varphi > \psi \geqslant 0$.

Note here we extend the linear poroelasticity formulation to the realm of poro-elasto-plasticity by assuming the incremental form of the constitutive relationship in Eq. 5.5 with the yield criterion and flow rule expressed using Biot's effective stress definition. Implicitly, we assume that stress partitioning between the solid and fluid phases is still based on the initial poroelastic estimate of Biot's coefficient (Pariseau, 1999; Khalili and Loret, 2001; Selvadurai and Suvorov, 2012, 2014). While it is a fundamental concept in soil plasticity to express a yield criterion using Terzaghi's effective stress ($\alpha = 1$) due to the assumption of solid incompressibility, constitutive formulation for poro-elasto-plasticity with a compressible solid phase is an open question (Coussy, 1995; De Buhan and Dormieux, 1996; Xie and Shao, 2012). As defined in Eq. 5.3, Biot's coefficient α is pertinent to the ratio between the bulk moduli of the skeleton and the solid constituent. As plastic deformation accumulates, since the tangent bulk modulus of the skeleton decreases, α associated with the tangent modulus increases from the initial poroelastic value to approaching $\alpha = 1$ (Suvorov and Selvadurai, 2019). Evidences from laboratory experiments on chalk (Xie and Shao, 2012) and Berea sandstone (Makhnenko and Labuz, 2016) support an earlier suggestion (Rice, 1977) that it would be more appropriate to use Terzaghi's effective stress to calculate the incremental plastic strain. A recent work (Zhao and Borja, 2020) based on continuum thermodynamics shows that it is necessary to introduce two effective stresses, $\boldsymbol{\sigma}' = \boldsymbol{\sigma} + \boldsymbol{\alpha} p$ and $\boldsymbol{\sigma}'' = \boldsymbol{\sigma} + p\mathbf{I}$, where $\boldsymbol{\alpha}$ is the anisotropic Biot tensor and $\boldsymbol{\sigma}'$ and $\boldsymbol{\sigma}''$ are energy-conjugate to elastic and plastic strains, respectively.

In these contexts, we may therefore argue that a yield criterion expressed with Biot's effective stress definition is only admissible when plastic deformation is small and Biot's coefficient α is only slightly smaller than 1 prior to the onset of plastic flow. As shown in Section 5.7.1, plastic deformation is more severe if constituents of the porous medium are assumed to be incompressible. Since our interest here is in identifying the parameter space where our poroelastic spherical indentation solutions are still applicable, other than the simulations for numerical validation in Section 5.4.2 and those in Section 5.7.1, our numerical analyses are conducted assuming the worst case scenario of plastic deformation with $\alpha = 1$.

5.2.2 Poroelasticity Formulation

Following earlier work in the literature (Lewis and Schrefler, 1998; White and Borja, 2008; Verruijt, 2013), we establish the finite element equations for poroelasticity based on the mixed continuous Galerkin method with displacement $\mathbf{u}$ and pore pressure $\mathbf{p}$ as the basic variables. For an incremental loading/time step,

$$\begin{bmatrix} \mathbf{K} & -\mathbf{Q} \\ -\mathbf{Q}^T & -(\mathbf{Stab} + \mathbf{S} + \theta \Delta t \mathbf{H}) \end{bmatrix} \begin{Bmatrix} \mathbf{u}_{n+1} - \mathbf{u}_n \\ \mathbf{p}_{n+1} - \mathbf{p}_n \end{Bmatrix} = \begin{Bmatrix} \Delta \mathbf{f}_u \\ \mathbf{f}_p + \Delta t \mathbf{H} \mathbf{p}_n \end{Bmatrix} \tag{5.10}$$

where $\mathbf{u}_{n+1}$, $\mathbf{p}_{n+1}$ and $\mathbf{u}_n$, $\mathbf{p}_n$ are displacement and pore pressure at times t_{n+1} and t_n and Δt is the time step, $\Delta t = t_{n+1} - t_n$. Here θ is an integration parameter, $0 \leq \theta \leq 1$. We choose $\theta = 0.5$ in this study to give a second-order convergence in time. Note that Voigt notation is adopted for the FEM formulation and its implementation.

Submatrices on the left hand side of Eq. 5.10 can be expressed as,

$$\mathbf{K} = \int_\Omega \mathbf{B}_u^T \, \mathbf{D}^e \, \mathbf{B}_u \, d\Omega \tag{5.11}$$

$$\mathbf{Q} = \alpha \int_\Omega \mathbf{B}_u^T \, \mathbf{I} \, \mathbf{N}_p \, d\Omega \tag{5.12}$$

$$\mathbf{S} = S \int_\Omega \mathbf{N}_p^T \, \mathbf{N}_p \, d\Omega \tag{5.13}$$

$$\mathbf{H} = \frac{\kappa}{\mu} \int_\Omega (\nabla \mathbf{N}_p)^T \, \nabla \mathbf{N}_p \, d\Omega \tag{5.14}$$

where Ω denotes the spatial domain; $\mathbf{B}_u$ is the strain operator, $\boldsymbol{\varepsilon} = \mathbf{B}_u \mathbf{u}$ and $\mathbf{N}_u$ and $\mathbf{N}_p$ are shape functions for displacement and pore pressure, respectively. It should be noted that **Stab** is a submatrix that adds an additional term in the mass balance equation so that the incompressibility constraint can be modified to avoid spurious pressure oscillation at early time for low-order finite elements which use equal-order displacement and pore pressure interpolation and do not meet the Ladyzhenskaya–Babuška–Brezzi (LBB) stability condition (Babuška, 1971;

Brezzi, 1974; Murad and Loula, 1994; White and Borja, 2008). Details of the stabilization scheme are explained further in Section 5.2.4.

Vector $\mathbf{f}$ on the right hand side of Eq. 5.10 represents the applied external load and flux within a single time step,

$$\Delta \mathbf{f}_u = \int_\Gamma \mathbf{N}_u^T \left(\mathbf{T}_{n+1} - \mathbf{T}_n \right) d\Gamma \tag{5.15}$$

$$\mathbf{f}_p = \Delta t \left[(1-\theta) \int_\Gamma \mathbf{N}_p^T q_n d\Gamma + \theta \int_\Gamma \mathbf{N}_p^T q_{n+1} d\Gamma \right] \tag{5.16}$$

where Γ denotes the boundary of domain Ω; $\mathbf{T}$ is the applied traction and q is the imposed fluid flux normal to boundary Γ.

5.2.3 Poro-elasto-plasticity Formulation

Implementation of the elasto-plastic constitutive relations in a finite element context requires consideration at two different levels, namely, the global level for equilibrium and the local level for material behaviors. A global iterative procedure is required so that the out-of-balance force, or residual, vanishes. Meanwhile, at the local level, the failure criterion needs to be satisfied. Equations at these two levels for computation of a load step constitute a nonlinear system. An iterative procedure based on the full Newton-Raphson method with the stress return scheme is adopted here to solve the system of equations (Čermák et al., 2019; De Souza Neto et al., 2011).

To advance from load step n to $n+1$, the iteration scheme starts by calculating the displacement and pressure increments, $\Delta \mathbf{u}$ and $\Delta \mathbf{p}$, resulted from an external load $\mathbf{f}$ using the poroelastic formulation in Eq. 5.10. Displacement and pore pressure fields at step $n+1$ are initialized according to,

$$\begin{Bmatrix} \mathbf{u}_{n+1} \\ \mathbf{p}_{n+1} \end{Bmatrix} = \begin{Bmatrix} \mathbf{u}^{(0)} \\ \mathbf{p}^{(0)} \end{Bmatrix} = \begin{Bmatrix} \mathbf{u}_n \\ \mathbf{p}_n \end{Bmatrix} + \begin{Bmatrix} \Delta \mathbf{u} \\ \Delta \mathbf{p} \end{Bmatrix} \tag{5.17}$$

In the $\ell-$th iteration cycle ($\ell = 1, 2, 3...$), with displacement $\mathbf{u}^{(\ell-1)}$ known, a local material level

correction is first executed to find the stress state $\boldsymbol{\sigma}'^{(\ell)}$, which is then followed by a global level correction to determine the displacement and pore pressure field, $\mathbf{u}^{(\ell)}$ and $\mathbf{p}^{(\ell)}$. The iteration terminates if $\left|\mathbf{u}^{(\ell)} - \mathbf{u}^{(\ell-1)}\right| < \epsilon$, where ϵ is the tolerance. Field variables at load step $n+1$ are updated according to: $\mathbf{u}_{n+1} = \mathbf{u}^{(\ell)}$, $\mathbf{p}_{n+1} = \mathbf{p}^{(\ell)}$, $\boldsymbol{\sigma}'_{n+1} = \boldsymbol{\sigma}'^{(\ell)}$, and $\boldsymbol{\varepsilon}_{n+1} = \boldsymbol{\varepsilon}^{(\ell)}$.

Total strain associated with the displacement at all integration points in iteration cycle ℓ is determined from,

$$\boldsymbol{\varepsilon}^{(\ell)} = \mathbf{B}_u \mathbf{u}^{(\ell-1)} \tag{5.18}$$

We first assume that the strain increment $\boldsymbol{\varepsilon}^{(\ell)} - \boldsymbol{\varepsilon}_n$ is purely elastic. Here $\boldsymbol{\varepsilon}_n$ is the total strain at step n, $\boldsymbol{\varepsilon}_n = \boldsymbol{\varepsilon}_n^e + \boldsymbol{\varepsilon}_n^p$. It follows from Hooke's law that the "elastic predictor stress" can be calculated from,

$$\boldsymbol{\sigma}^e = \mathbf{D}^e \left(\boldsymbol{\varepsilon}^{(\ell)} - \boldsymbol{\varepsilon}_n^p\right) \tag{5.19}$$

If $f\left(\boldsymbol{\sigma}^e\right) \leq 0$, such an elastic trial stress state is admissible,

$$\boldsymbol{\sigma}'^{(\ell)} = \boldsymbol{\sigma}^e, \quad \mathbf{D}^{(\ell)ep} = \mathbf{D}^e, \quad \boldsymbol{\varepsilon}^{(\ell)p} = \boldsymbol{\varepsilon}_n^p \tag{5.20}$$

However, if $f\left(\boldsymbol{\sigma}^e\right) > 0$, this trial stress state is not admissible and needs to be corrected to ensure that the yield condition is met at each integration point. Two stress return mapping strategies are employed for the Drucker-Prager model. If $bI_1^e - 9Kb\bar{b}\sqrt{J_2^e}/G - s < 0$, where I_1^e and J_2^e are the corresponding stress invariants for $\boldsymbol{\sigma}^e$ and $\boldsymbol{s}^e$, the stress state is returned to the smooth portion of the yield surface according to,

$$\boldsymbol{\sigma}'^{(\ell)} = \boldsymbol{\sigma}^e - \frac{f\left(\boldsymbol{\sigma}^e\right)}{G + 9Kb\bar{b}} \left(\sqrt{2}G\mathbf{n} + 3K\bar{b}\mathbf{I}\right) \tag{5.21}$$

where $\mathbf{n} = \boldsymbol{s}^e/\sqrt{2J_2^e}$. The corresponding matrix of tangent moduli and total strain can be

expressed as,

$$\mathbf{D}^{(\ell)ep} = \mathbf{D}^{e} - \frac{1}{G + 9Kb\bar{b}} \begin{bmatrix} \dfrac{2G^2 f\left(\boldsymbol{\sigma}^{e}\right)}{\sqrt{J_2^e}} \left(\mathbf{I}_d - \mathbf{n} \otimes \mathbf{n}\right) \\ + \left(\sqrt{2}G\mathbf{n} + 3K\bar{b}\mathbf{I}\right) \otimes \left(\sqrt{2}G\mathbf{n} + 3Kb\mathbf{I}\right) \end{bmatrix} \tag{5.22}$$

$$\boldsymbol{\varepsilon}^{(\ell)p} = \boldsymbol{\varepsilon}_n^{p} + \frac{f\left(\boldsymbol{\sigma}^{e}\right)}{G + 9Kb\bar{b}} \left(\frac{\sqrt{2}}{2}\mathbf{n} + \bar{b}\mathbf{I}\right) \tag{5.23}$$

where $\mathbf{I}_d$ is the deviatoric projection tensor (Čermák et al., 2019; De Souza Neto et al., 2011).

On the other hand, if $bI_1^e - 9Kb\bar{b}\sqrt{J_2^e}/G - s \geqslant 0$, the stress state is returned to the apex of the yield surface,

$$\boldsymbol{\sigma}'^{(\ell)} = \frac{s}{3b}\mathbf{I}, \quad \mathbf{D}^{(\ell)ep} = \mathbf{O}, \quad \boldsymbol{\varepsilon}^{(\ell)p} = \boldsymbol{\varepsilon}^{(\ell)} - \frac{s}{9Kb}\mathbf{I} \tag{5.24}$$

where $\mathbf{O}$ is a zero fourth-order tensor.

After the stress state correction, the residual between the internal force/flux and the external load/flux at the ℓ-th iteration is,

$$\mathbf{r}^{(\ell)} = \begin{Bmatrix} \int_\Omega \mathbf{B}_u^T \left(\boldsymbol{\sigma}'^{(\ell)} - \boldsymbol{\sigma}'_n\right) d\Omega - \mathbf{Q}\left(\mathbf{p}^{(\ell-1)} - \mathbf{p}_n\right) \\ -\mathbf{Q}^T\left(\mathbf{u}^{(\ell-1)} - \mathbf{u}_n\right) - \left(\mathbf{Stab} + \mathbf{S} + \theta\Delta t\mathbf{H}\right)\left(\mathbf{p}^{(\ell-1)} - \mathbf{p}_n\right) \end{Bmatrix} - \begin{Bmatrix} \Delta\mathbf{f}_u \\ \mathbf{f}_p + \Delta t\mathbf{H}\mathbf{p}_n \end{Bmatrix} \tag{5.25}$$

In general, $\mathbf{r}^{(\ell)}$ may be nonzero since the corrected stress tensor $\boldsymbol{\sigma}'^{(\ell)}$ could be away from the equilibrium state. Displacement and pore pressure at nodal points need to be updated in order to eliminate the residual,

$$\begin{bmatrix} \mathbf{K}_t^{(\ell)} & -\mathbf{Q} \\ -\mathbf{Q}^T & -\left(\mathbf{Stab} + \mathbf{S} + \Delta t\theta\mathbf{H}\right) \end{bmatrix} \begin{Bmatrix} \mathbf{u}^{(\ell)} - \mathbf{u}^{(\ell-1)} \\ \mathbf{p}^{(\ell)} - \mathbf{p}^{(\ell-1)} \end{Bmatrix} = -\mathbf{r}^{(\ell)} \tag{5.26}$$

where the matrix of tangent moduli $\mathbf{K}_t^{(\ell)}$ is constructed using $\mathbf{D}^{(\ell)ep}$,

$$\mathbf{K}_t^{(\ell)} = \int_\Omega \mathbf{B}_u^T \, \mathbf{D}^{(\ell)ep} \, \mathbf{B}_u \, d\Omega \tag{5.27}$$

Note that since the matrix on the left hand side of Eq. 5.26 equals to the gradient of the residual $\mathbf{r}^{(\ell)}$ with respect to $\mathbf{u}^{(\ell-1)}$ and $\mathbf{p}^{(\ell-1)}$, convergence of this procedure is expected to be quadratic.

5.2.4 Stabilization Scheme

Numerical issues resulted from the incompressibility constraint for hydromechanically coupled problems at the undrained limit have long been noted (Vermeer and Verruijt, 1981; Zienkiewicz et al., 1990; Murad and Loula, 1992, 1994). Finite elements that employ equal-order spatial interpolation for displacement and pore pressure fields for a mixed formulation are numerically unstable as the shape functions do not satisfy the LBB condition (Zienkiewicz et al., 1990; Murad and Loula, 1992, 1994). In addition to sub-optimal convergence issue, the resulting pore pressure field could exhibit spurious oscillations. Nevertheless, low-order elements such as bilinear-displacement/bilinear-pressure quadrilateral elements (Q4P4) have computational advantages with fewer degrees of freedom, fewer Gauss points, and simpler data structures. Computational efficiency is especially important when we deal with an elasto-plastic material since significant computational effort is devoted to the iteration at the material level at each Gauss point; for example, Q9P4 elements, though stable in the LBB sense, would typically require 3×3 Gauss-quadrature, whereas only 2×2 is needed for Q4P4 elements.

It has been shown that for finite elements such as Q4P4, incorporating a stabilization scheme could produce numerically stable results (White and Borja, 2008; Bouklas et al., 2015). Here we adopt the stabilization formulation of White and Borja (2008) by adding an additional term in the mass balance equation, which is reflected by the sub-matrix **Stab** in Eqs. 5.10 and 5.26. With the addition of the **Stab** sub-matrix, the (2,2) sub-block of the coefficient matrix is no longer trivial at the undrained limit. For plane strain or cylindrical axisymmetric problems

with Q4P4 elements,

$$\mathbf{Stab} = \frac{\chi}{2G} \int_{\Omega} \left(\mathbf{N}_p^T - \frac{1}{4} \right) \left(\mathbf{N}_p - \frac{1}{4} \right) d\Omega \tag{5.28}$$

where χ is a multiplier, typically $O(1)$, for adjusting the level of stabilization.

5.3 Analytical Solution for Poro-elasto-plastic Consolidation

One-dimensional consolidation in a semi-infinite poro-elasto-plastic medium with either a Drucker-Prager or a Mohr-Coulomb yield criterion can be solved analytically. For a consolidation problem, a uniform mechanical load is applied instantaneously on the surface and held constant afterwards. Since the total stress field is independent of time, diffusion equations for the pore pressure become decoupled from solid deformation. In other words, the hydromechanical coupling is loosely one-way as the pore pressure is only affected by mechanical deformation through the change of the coefficient of consolidation when the material yields. For a semi-infinite domain or a laterally constrained one-dimensional column, the effective stresses resulted from the surface load are in triaxial compression states. Yielding according to a Drucker-Prager or a Mohr-Coulomb criterion can therefore be made equivalent if the material constants are expressed according to Eq. 5.7. As recognized by Pariseau (Pariseau, 1999), poro-elasto-plastic consolidation is analogous to a Stefan problem (Carslaw and Jaeger, 1992) and is a rare case where the analytical solution can be obtained to serve as a benchmark for poro-elasto-plastic numerical development. Below we present the derivation revised from the work by Pariseau (Pariseau, 1999) for clarity in physical parameters and with the Drucker-Prager and Mohr-Coulomb criteria unified.

5.3.1 Governing Equations

Initial and boundary conditions for the problem we deal with can be described as follows: at $z = 0$, $\sigma_z = \sigma_0$ for $t \geqslant 0$ and $p = 0$ for $t > 0$. Extent of the domain is $z \geqslant 0$. Since the problem

is one dimensional, $\varepsilon_x = \varepsilon_y = 0$, the storage equation takes the form (Verruijt, 2013),

$$\alpha \frac{\partial \varepsilon_z}{\partial t} + S \frac{\partial p}{\partial t} = \frac{\kappa}{\mu} \frac{\partial^2 p}{\partial z^2} \tag{5.29}$$

Assuming an incremental linear material response,

$$\Delta \sigma_z' = M \Delta \varepsilon_z \tag{5.30}$$

where M is the confined modulus, we obtain,

$$\frac{\alpha}{M} \frac{\partial \sigma_z'}{\partial t} + S \frac{\partial p}{\partial t} = \frac{\kappa}{\mu} \frac{\partial^2 p}{\partial z^2} \tag{5.31}$$

Substituting Biot's effective stress definition, $\sigma_z' = \sigma_0 + \alpha p$, into the above equation yields a diffusion equation for pore pressure,

$$\frac{\partial p}{\partial t} = c_v \frac{\partial^2 p}{\partial z^2} \tag{5.32}$$

where c_v is the coefficient of consolidation or hydraulic diffusivity,

$$c_v = \frac{\kappa M}{\mu \left(\alpha^2 + SM\right)} \tag{5.33}$$

The form of the diffusion equation in Eq. 5.32 remains the same regardless of plastic yielding.

Constitutive behaviors are reflected through the confined modulus M. Denote M_e as the confined modulus for linear poroelasticity,

$$M_e = K + \frac{4}{3} G = \frac{3K\left(1 - \nu\right)}{1 + \nu} \tag{5.34}$$

The corresponding diffusivity c_{ve} can be determined with $M = M_e$ from Eq. 5.33. At the undrained limit ($t = 0$), since there has not yet been any fluid loss from the domain, $\partial^2 p / \partial^2 z = 0$. The initial pore pressure induced by the sudden loading on the surface is thus uniform along

the depth. For linear poroelasticity, the initial pore pressure is,

$$p_{0e} = -\frac{\alpha}{\alpha^2 + SM_e}\sigma_0 \tag{5.35}$$

Denote M_p as the confined modulus of the plastic zone. Diffusivity of the plastic zone c_{vp} can be determined with $M = M_p$ from Eq. 5.33. Next we show that modulus M_p is constant for poro-elasto-plasticity with a Drucker-Prager or Mohr-Coulomb failure criterion. Since the load is applied in the $z-$direction, σ'_z is more compressive than the lateral effective stress $\sigma'_x = \sigma'_y = \sigma'_h$. The Drucker-Prager failure criterion can be written as,

$$\sigma'_z - \frac{1 + 2\sqrt{3}b}{1 - \sqrt{3}b}\sigma'_h + \frac{\sqrt{3}s}{1 - \sqrt{3}b} = 0 \tag{5.36}$$

A Mohr-Coulomb criterion can be made equivalent to the Drucker-Prager criterion in this particular case if the cohesion and internal friction angle are chosen according to Eq. 5.7. Indeed, substituting Eq. 5.7 into Eq. 5.36, we recover the Mohr-Coulomb criterion with,

$$K_p = \frac{1 + 2\sqrt{3}b}{1 - \sqrt{3}b} = \frac{1 + \sin\varphi}{1 - \sin\varphi} \qquad \sigma_c = \frac{\sqrt{3}s}{1 - \sqrt{3}b} = \frac{2c_0\cos\varphi}{1 - \sin\varphi} \tag{5.37}$$

where K_p and σ_c are the passive failure coefficient and uniaxial compressive strength, respectively. Given the plastic potential in Eq. 5.9, the flow rule can be expressed as,

$$\Delta\varepsilon_h^p = \lambda\frac{\partial g}{\partial\sigma'_h} = \lambda\left(\frac{\sqrt{3}}{6} + \bar{b}\right) \tag{5.38}$$

$$\Delta\varepsilon_z^p = \lambda\frac{\partial g}{\partial\sigma'_z} = \lambda\left(-\frac{\sqrt{3}}{3} + \bar{b}\right) \tag{5.39}$$

where λ is a plastic multiplier. Eqs. 5.36-5.39 in conjunction with Hooke's law and the strain

decomposition rule, e.g., $\Delta\varepsilon_z = \Delta\varepsilon_z^e + \Delta\varepsilon_z^p$, yield,

$$M_p = \frac{3K\left(1-2\nu\right)}{1+\dfrac{2\left(1-\nu\right)}{K_pK_d}-2\nu\left(\dfrac{1}{K_d}+\dfrac{1}{K_p}\right)} \tag{5.40}$$

where K_d is the dilatancy coefficient characterizing the plastic strain ratio between the lateral and the axial directions,

$$K_d = -\frac{2\Delta\varepsilon_h^p}{\Delta\varepsilon_z^p} = \frac{1+\sin\psi}{1-\sin\psi} \tag{5.41}$$

5.3.2 Pore Pressure Field

Depending on the magnitude of the applied load, the consolidation response could be purely poroelastic, poro-elasto-plastic or fully plastic. If the material response is poroelastic, we have $\sigma_h' = \nu/\left(1-\nu\right)\left(\sigma_0+\alpha p\right)$. At the undrained limit ($t = 0$), the pore pressure drops instantaneously from $p = p_{0e}$ to $p = 0$ on the surface. Onset of plastic yielding occurs if the stress state with $p = 0$ meets the failure criterion, whereas full plasticity takes place if the stress state with $p = p_{0e}$ does. Denote σ_{ep} and σ_{fp} as the threshold applied loads. Poro-elasto-plastic consolidation occurs only when $\sigma_{fp} < \sigma_0 < \sigma_{ep}$,

$$\sigma_{ep} = \frac{\sqrt{3}s\left(1-\nu\right)}{\sqrt{3}b\left(1+\nu\right)-1+2\nu} \tag{5.42}$$

$$\sigma_{fp} = \sigma_{ep}\left(1+\frac{\alpha^2}{SM_e}\right) \tag{5.43}$$

Note that a necessary condition for any plastic yielding to occur is $\sqrt{3}b\left(1+\nu\right)-1+2\nu < 0$, i.e., $K_p < \left(1-\nu\right)/\nu$ so that $\sigma_{ep} < 0$. Therefore, certain parameter combinations never result in plastic yielding, e.g., $\varphi = 30^\circ$ and $\nu = 0.25$. In addition, if both the solid and fluid phases are incompressible, $S = 0$, full plasticity never occurs.

For the case of poroelasticity ($\sigma_0 \geqslant \sigma_{ep}$) or full plasticity ($\sigma_0 \leqslant \sigma_{fp}$), the pore pressure field

is given by the classical solution to one dimensional diffusion (Carslaw and Jaeger, 1992),

$$p = p_0 \left[1 - \text{erfc}\left(z/2\sqrt{c_v t}\right)\right] \tag{5.44}$$

where $c_v = c_{ve}$ and $p_0 = p_{0e}$ for poroelasticity and $c_v = c_{vp}$ and $p_0 = p_{0p}$ for full plasticity,

$$p_{0p} = -\frac{\alpha}{\alpha^2 + SM_e}\sigma_{fp} - \frac{\alpha}{\alpha^2 + SM_p}\left(\sigma_0 - \sigma_{fp}\right) \tag{5.45}$$

The threshold pore pressure when $\sigma_0 = \sigma_{fp}$ is,

$$p_{fp} = -\frac{\alpha\sigma_{fp}}{\alpha^2 + SM_e} = -\frac{\alpha\sigma_{ep}}{SM_e} \tag{5.46}$$

The coupled problem for poro-elasto-plastic consolidation when $\sigma_{fp} < \sigma_0 < \sigma_{ep}$ can be formulated as follows,

$$\frac{\partial p}{\partial t} = c_{vp}\frac{\partial^2 p}{\partial z^2}, \quad 0 < z < \overline{z},\ t > 0 \tag{5.47}$$

$$\frac{\partial p}{\partial t} = c_{ve}\frac{\partial^2 p}{\partial z^2}, \quad \overline{z} \leqslant z < \infty,\ t > 0 \tag{5.48}$$

$$p = p_{0e}, \quad t = 0; \qquad p = 0, \quad z = 0, \quad t > 0 \tag{5.49}$$

where depth of the elasto-plastic interface $\overline{z}$ is a function of time. At $z = \overline{z}$, the effective normal stress and pore pressure are constant,

$$\overline{\sigma}'_z = \sigma_{ep} \qquad \overline{p} = -\frac{1}{\alpha}\left(\sigma_0 - \sigma_{ep}\right) \tag{5.50}$$

The continuity condition at the elasto-plastic interface requires,

$$\left(\frac{\partial p}{\partial z}\right)_{z=\overline{z}_+} = \left(\frac{\partial p}{\partial z}\right)_{z=\overline{z}_-} \tag{5.51}$$

The problem so defined is analogous to a Stefan problem (Pariseau, 1999) and the solution for

the pore pressure field is (Carslaw and Jaeger, 1992),

$$p = \frac{\overline{p}}{\operatorname{erf}\left(\sqrt{\beta/c_{vp}}\right)} \operatorname{erf}\left(\frac{z}{\overline{z}}\sqrt{\frac{\beta}{c_{vp}}}\right), \quad z \leq \overline{z} \tag{5.52}$$

$$p = p_{0e} + \frac{\overline{p} - p_{0e}}{\operatorname{erfc}\left(\sqrt{\beta/c_{ve}}\right)} \operatorname{erfc}\left(\frac{z}{\overline{z}}\sqrt{\frac{\beta}{c_{ve}}}\right), \quad z > \overline{z} \tag{5.53}$$

where $\overline{z}$ extends from the surface into the interior of the domain according to,

$$\overline{z}\,(t) = 2\sqrt{\beta t} \tag{5.54}$$

and constant β satisfies the transcendental equation,

$$\exp\left(\frac{\beta}{c_{ve}} - \frac{\beta}{c_{vp}}\right) \frac{\operatorname{erfc}\left(\sqrt{\beta/c_{ve}}\right)}{\operatorname{erf}\left(\sqrt{\beta/c_{vp}}\right)} = \left(\frac{p_{0e}}{\overline{p}} - 1\right)\sqrt{\frac{c_{vp}}{c_{ve}}} \tag{5.55}$$

In this regard, poro-elasto-plastic consolidation in a semi-infinite domain is self-similar with respect to $z/2\sqrt{\beta t}$. After the pore pressure field is known, strain and displacement fields can be readily derived, see Appendix D.2.

To what a degree the pore pressure field is affected by plastic deformation is dictated by c_{vp}/c_{ve}, or M_p/M_e when $\alpha = 1$ and $S = 0$. Depending on the parameter combinations of ν, φ and ψ, the influence could be negligible, e.g. $\nu = 0.22$, $\varphi = \psi = 30°$, $M_p/M_e = 0.995$, or appreciable, e.g. $\nu = 0$, $\varphi = 20°$, $\psi = 0°$, $M_p/M_e = 0.505$. Given φ and ψ, M_p/M_e decreases monotonically with ν.

5.4 Numerical Validation

5.4.1 Indentation Model Setup and Numerical Stability

We implement the finite element algorithm outlined in Section 5.2 in MATLAB. Effectiveness of the stabilization scheme is first tested by modeling poroelastic spherical indentation at the undrained limit. Here the indentation problem is chosen over classical poroelasticity benchmark

problems for its more complex stress field.

The numerical model consists of a cylindrical sample of radius $r_s = 40$ mm and height $r_h = 50$ mm. A roller boundary condition is applied at the bottom while the lateral boundary is traction free. A step displacement load is applied on the top surface within $0 \leq r \leq 1$ mm with $u_z = \left(d - r^2/2R\right)\mathcal{H}(t)$, where $\mathcal{H}(t)$ is a Heaviside function; d denotes the depth of penetration; and R is the radius of the spherical indenter, $d = 0.1$ mm and $R = 10$ mm. Radial displacement u_r is not constrained on the surface. At $r > 1$ mm, the surface is traction free. Boundary conditions so defined on the surface are consistent with the Hertzian assumption for the contact radius, $a = \sqrt{Rd}$. Case III drainage condition is prescribed on the surface while zero pore pressure is imposed on the lateral boundary. Gravity is ignored in this model. Axisymmetric quadrilateral (Q4P4) mesh is used and refined near the contact region.

Unless otherwise noted, material properties and simulation parameters listed in Table 5.1 are used as the default for parameters in this study. The properties are chosen based on those of the Gulf of Mexico shale in Cheng (2016). This set of parameters corresponds to $\alpha = 0.968$, $S = 0.153$ 1/GPa and $\omega = 0.416$. It should be noted that if K_s and K_f are finite, the porous medium as a whole is compressible even near the undrained limit. As such, the stabilization scheme is not necessarily needed. Therefore, for the purpose of validation simulations, both the solid and fluid phases are assumed to be incompressible, i.e., $K_s \to \infty$ and $K_f \to \infty$. The undrained limit is achieved by setting $\Delta t = 0$ in the numerical calculation.

It should be mentioned that shale is known to exhibit viscous behaviors (Chang and Zoback, 2009; Bennett et al., 2015; Borja et al., 2020). For a fluid-filled porous medium, both viscoelasticity and poroelasticity can result in indentation force relaxation. These two relaxation mechanisms are, however, distinct and can be distinguished from each other by their respective time scaling. Viscoelastic relaxation time is associated with the viscosity and elastic modulus of the material and is therefore independent of any length scale. This is in contrast to the quadratic relation between the relaxation time and the contact radius or indentation depth in poroelastic indentation (Hu et al., 2010; Kalcioglu et al., 2012), where the dimensionless time can be defined according to $t_* = tc_v/a^2$. Viscous effect is assumed to be negligible here.

Contours of the normalized pore pressure field from simulations with or without the stabilization scheme are shown in Fig. 5.1. Here the stabilization multiplier is set to be $\chi = 1$. The pore pressure is normalized according to $p_n = (p - p_{\min}) / (p_{\max} - p_{\min})$. Evidence of numerical oscillation is rather obvious when the numerical algorithm is unstabilized. However, the spurious oscillations are effectively suppressed and the pore pressure field becomes well behaved when the stabilization scheme is incorporated. Fig. 5.1(a) shows that right underneath the indenter, positive pore pressure is generated and along the contact axis, the pore pressure decreases gradually with depth. Pore pressure at the origin and the indentation force are $p = 193.079$ MPa and $F(0) = 406.6$ N from the simulation with the stabilized scheme, which are in excellent agreement with the analytical predictions of $p = 193.386$ MPa and $F(0) = 405$ N.

Additional simulations with $\chi = 0.1$, 10 and 100 are conducted to analyze the effect of the stabilization multiplier χ. The corresponding pore pressure at the origin and the indentation force for these three cases are $p = 208.260$, 178.661, 143.219 MPa, and $F(0) = 407.972$, 406.150, 392.109 N, respectively. With $\chi = 0.1$, the stabilization scheme is not effective and there are still moderate oscillations beneath the contact area. On the other hand, with $\chi = 10$ and 100, the pore pressure field is overly diffused. Therefore, the case with $\chi = 1$ is our baseline simulation for poroelastic indentation.

Skeleton Young's modulus, E	1.853 GPa
Skeleton Poisson's ratio, ν	0.22
Solid bulk modulus, K_s	34 GPa
Fluid bulk modulus, K_f	2.25 GPa
Porosity, n	0.3
Permeability, κ	$1 \times 10^{-19}\,\mathrm{m}^2$
Viscosity, μ	$1 \times 10^{-3}\,\mathrm{Pa} \cdot \mathrm{s}$
Stabilization multiplier, χ	1

Table 5.1: Baseline parameters for numerical simulations.

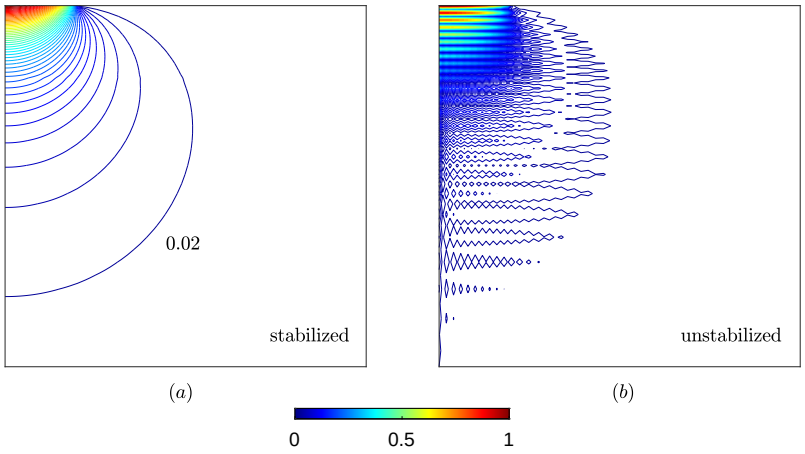

Figure 5.1: Contours of the normalized pore pressure field at the undrained limit, $p_n = (p - p_{\min}) / (p_{\max} - p_{\min})$; (a) with the stabilization scheme, $p_{\min} = -0.0309$ MPa, $p_{\max} = 193$ MPa; (b) without the stabilization scheme, $p_{\min} = -1.11$ MPa, $p_{\max} = 329$ MPa; contour interval: 0.02, plot window size: 5×5 mm.

5.4.2 Numerical Accuracy

Accuracy of the FEM algorithm is scrutinized by extensively benchmarking it against analytical solutions. Comparison is first made between the numerical results and poroelastic solutions to the problems of Terzaghi, Mandel, Cryer and De Leeuw (Terzaghi, 1943; Mandel, 1953; Cryer, 1963; De Leeuw, 1965; Verruijt, 2013). We observe that the stabilized Q4P4 scheme performs well and can model poroelasticity problems to a high degree of accuracy, see Appendix D.1. Though sharp pressure gradient near the drainage boundary still leads to some minor oscillations at early time, see Figs. D.1, D.2 and D.4, as discussed in White and Borja (2008), such oscillations cannot be completely avoided even with stable elements such as Q9P4 and these oscillations do not propagate to the rest of the domain.

Poro-elasto-plastic consolidation is then modeled as the second series of benchmark. The numerical model is setup with $\nu = 0$, $c_0 = 5$ MPa and $\varphi = \psi = 20^\circ$ in a domain of width 1 m and depth 300 m, which correspond to $\alpha = 0.982$ and $S = 0.153$ 1/GPa. The corresponding threshold loads for plastic yielding are $\sigma_{ep} = -14.28$ MPa and $\sigma_{fp} = -62.72$ MPa. A case with an applied load $\sigma_0 = -30$ MPa is first considered. Plastic yielding is expected to initiate

from the surface and extend into the domain with time. Comparisons between the numerical and analytical results show excellent agreements on the evolution of the elasto-plastic interface with time and distributions of the vertical strain along the depth at various times, see Fig. 5.2. It should be noted that at the end of this simulation ($t = 10^9$ s), change in pore pressure at $z \geqslant 100$ m is less than 0.1% of the initial value, which verifies that the numerical model is sufficiently large for simulating the consolidation problem in a semi-infinite domain.

Instantaneous pore pressure response at the undrained limit is further examined with $-150 < \sigma_0 < 0$ MPa. According to Eqs. 5.35 and 5.45, initial excess pore pressure p_0 as a function of σ_0 is a bilinear relationship. The rate of change is $\partial p_0/\partial |\sigma_0| = 0.787$ when $-62.72 \leqslant \sigma_0 < 0$ MPa. When $\sigma_0 \leqslant -62.72$ MPa, $\partial p_0/\partial |\sigma_0| = 0.887$ and 0.849 for $\psi = 0^\circ$ and 20°, respectively. Results from the numerical simulations confirm such a bilinear relationship, see Fig. 5.3. When there is plastic yielding, the rate of increase is higher than that of the purely poroelastic case since when $K_p < (1-\nu)/\nu$, $M_p < M_e$ (or $c_{vp} < c_{ve}$). Furthermore, M_p increases with K_d at a given K_p. Therefore, p_0 is smaller at $\psi = 20^\circ$ than $\psi = 0^\circ$ due to shear induced dilatancy.

5.5 Spherical Indentation

Theoretical solutions for poroelastic spherical indentation via step displacement loading with three distinct surface drainage conditions, namely, a fully permeable surface (case I), a fully impermeable surface (case II), or a mixed surface drainage condition, impermeable within the contact region but fully permeable everywhere else (case III), have been obtained in Chapters 2, 3 and 4. Denote t_* as the dimensionless time, $t_* = tc_v/a^2$. It follows from the Hertzian solution that at the undrained and drained limits, the indentation force can be determined from,

$$F(0) = \frac{16Ga^3}{3\phi R}, \qquad F(\infty) = \frac{8G(2\eta - 1)a^3}{3\eta R} \tag{5.56}$$

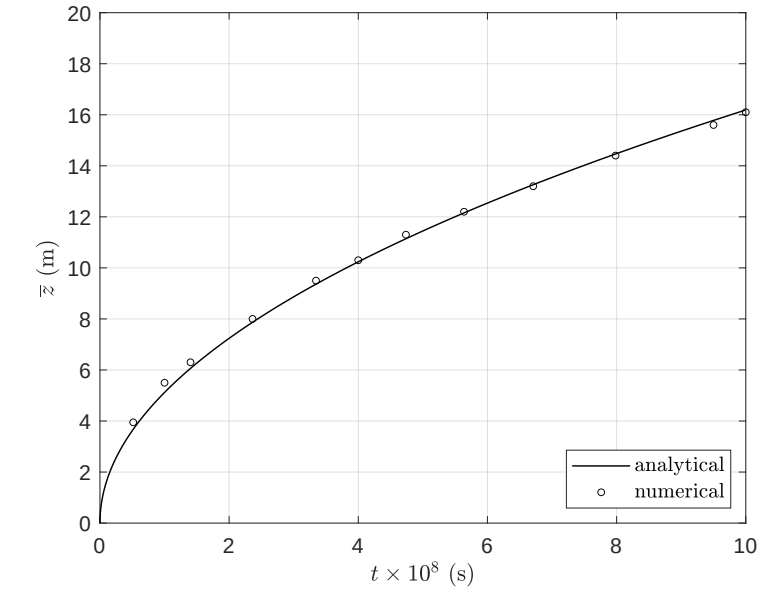

(a)

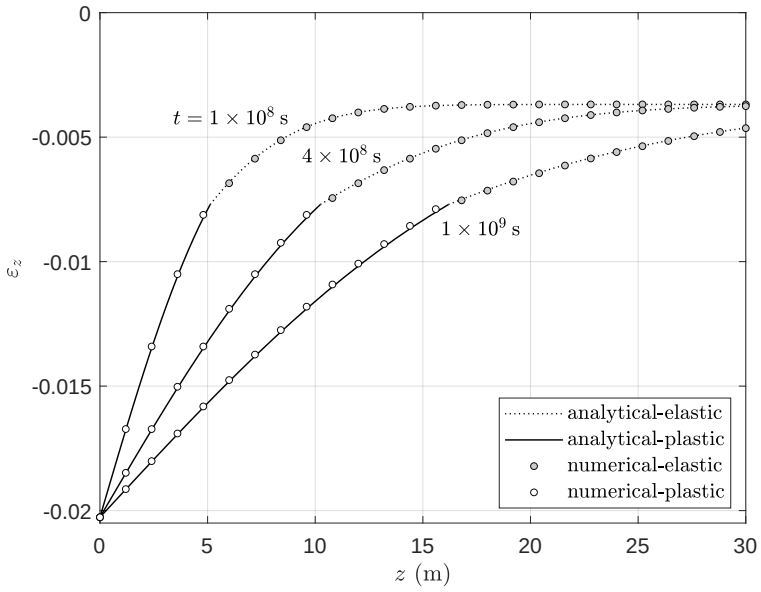

(b)

Figure 5.2: (a) Depth of the elasto-plastic interface $\overline{z}$ as a function of time; (b) Distributions of the vertical strain along the depth at $t_* = 1 \times 10^8$, 4×10^8, 1×10^9 s; theoretical predictions in lines.

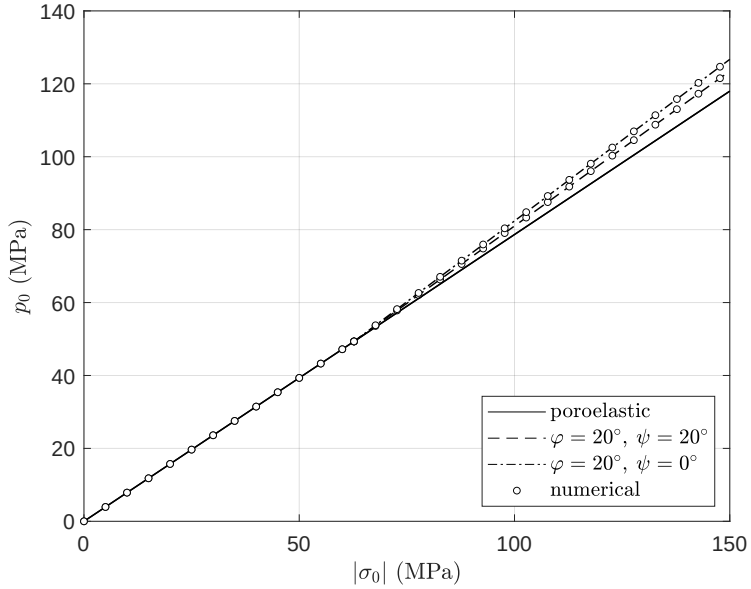

Figure 5.3: Instanenous excess pore pressure p_0 as a function of the applied load $|\sigma_0|$; theoretical solutions in lines.

where η and ϕ are two derived material constants,

$$\eta = \frac{K}{2G} + \frac{2}{3}, \qquad \phi = \frac{\alpha^2 + S\left(K + \frac{4}{3}G\right)}{\alpha^2 + S\left(K + \frac{1}{3}G\right)} \tag{5.57}$$

The ratio between the two force asymptotes gives,

$$\eta_f = \frac{F(0)}{F(\infty)} = 1 + \omega \tag{5.58}$$

where,

$$\omega = \frac{\phi + 2\eta(1 - \phi)}{\phi(2\eta - 1)} \tag{5.59}$$

The theoretical range of ω is $0 \leq \omega \leq 1$. If both the solid and fluid phases are incompressible ($\alpha = 1$, $S = 0$), we have $\phi = 1$ and $\omega = 1 - 2\nu$.

A normalized indentation force $F_n(t_*)$ can be defined according to,

$$F_n(t_*) = \frac{F(t_*) - F(\infty)}{F(0) - F(\infty)} \tag{5.60}$$

An important finding from the theoretical analysis is that mastercurves can be constructed for the normalized indentation force $F_n(t_*)$ as a function of dimensionless time t_* and they have weak dependence on ω only. For each case of surface drainage condition, $F_n(t_*)$ can be expressed explicitly in the Laplace domain. For example, for case I,

$$F_n(t_*) = \frac{3}{2\omega}\int_0^1 x_*^{\frac{1}{2}}\mathcal{L}^{-1}\left[s_*^{-1}\theta_1(s_*, x_*)\right]dx_* \tag{5.61}$$

where s_* is a Laplace variable for t_*; $\theta_1(s_*, x_*)$ is the solution to a Fredholm integral equation of the second kind, dependent on material properties through ω only and Laplace inversion $\mathcal{L}^{-1}[\cdot]$ is defined as,

$$\mathcal{L}^{-1}[f(s_*)] = \frac{1}{2\pi i}\int_{\gamma-i\infty}^{\gamma+i\infty} f(s_*)\exp(s_* t_*)\,ds_* \tag{5.62}$$

Function $F_n(t_*)$ for case I can be actually fitted by an elementary function with four parameters a_1, b_1, a_2, b_2 with the coefficient of determination $R^2 = 1$ for all ω,

$$f_n(t_*) = \frac{1}{2}\left(\frac{1}{1+a_1 t_*^{b_1}} + \frac{1}{1+a_2 t_*^{b_2}}\right) \tag{5.63}$$

If the bulk and shear modulus, K and G, Biot's coefficient α and storage coefficient S are known, ω is fully determined. An important implication of Eqs. 5.61-5.63 is that given ω, the corresponding master curve can be used to determine the hydraulic diffusivity c_v if the transient indentation force is measured in a poroelastic spherical indentation experiment.

If the porous medium obeys a Drucker-Prager or Mohr-Coulomb yield criterion, we now have three additional material constants, e.g., cohesion c_0, friction angle φ and dilatancy angle ψ. If we consider $\{t,\ a,\ R,\ \alpha,\ S,\ c_v,\ K,\ G\}$ as the governing parameters for poroelastic indentation, with the addition of the plasticity parameters, it follows from the Buckingham $\Pi-$theorem, the transient indentation force can be expressed as,

$$F(t) = \left(\frac{Ga^3}{R}\right) f\left(\frac{c_v t}{a^2}, \frac{a}{R}, \alpha, SK, \frac{K}{G}, \frac{c_0}{G}, \varphi, \psi\right) \tag{5.64}$$

If both the solid and fluid phases are incompressible, Eq. 5.64 can be rewritten as,

$$F(t) = \left(\frac{Ga^3}{R}\right) f\left(\frac{c_v t}{a^2}, \frac{a}{R}, \omega, \frac{c_0}{G}, \varphi, \psi\right) \tag{5.65}$$

Without additional insights from theoretical analysis, the list of dimensionless groups in Eqs. 5.64-5.65 cannot be further reduced in general for the normalized force $F_n(t_*)$ in poro-elasto-plastic indentation.

In this work, numerical analysis for poroelastic indentation therefore aims at investigating the role of ω as the sole parameter that influences the normalized indentation force relaxation curves. For poro-elasto-plastic indentation, the questions we intend to address are how c_0/G, φ and ψ affect the indentation process and whether the constituent compressibility of the Gulf of Mexico Shale has a strong effect when plasticity is considered. It should be noted that ratio a/R or d/R does affect development of plastic deformation.

5.6 Poroelastic Indentation

5.6.1 The Role of ω

Dependence of $F_n(t_*)$ on ω is first examined with four simulations cases, each having a distinct set of material and simulation parameters. Setup of the numerical model is the same as that in Section 5.4.1. The mixed surface drainage condition (case III) is applied. Parameters different from Table 5.1 for each set are:

- set i (baseline): $\nu = 0.22$, $K_s \to \infty$, $K_f \to \infty$
- set ii: $E = 18.53$ GPa, $\nu = 0.22$, $K_s \to \infty$, $K_f \to \infty$
- set iii: $\nu = 0.22$, $K_s \to \infty$, $K_f \to \infty$, $d = 0.233$ mm ($a = 1.526$ mm)
- set iv: $\nu = 0$, $K_s = 3$ GPa, $K_f = 3$ GPa

In these four sets, d/R (a/R), α, SK and K/G have all varied, but ω remains constant, $\omega = 0.56$. The simulation results show that the transient force responses from the four cases

differ significantly. Nevertheless, their force asymptotes at the undrained and drained limits are in good agreement with those predicted by the Hertzian solutions, see Table 5.2. Here the indentation force at the end of the simulation is taken as the drained asymptote. Now after the indentation force is normalized and plotted versus the dimensionless time t_*, the four force relaxation curves collapse into one mastercurve with only slight discrepancy at late time, see Fig. 5.4. Furthermore, the normalized curves from the simulations are in excellent agreement with the theoretical solution except for again some minor discrepancy at $t_* > 1$. Among them, transient force relaxation is the fastest in set iii with a larger contact radius.

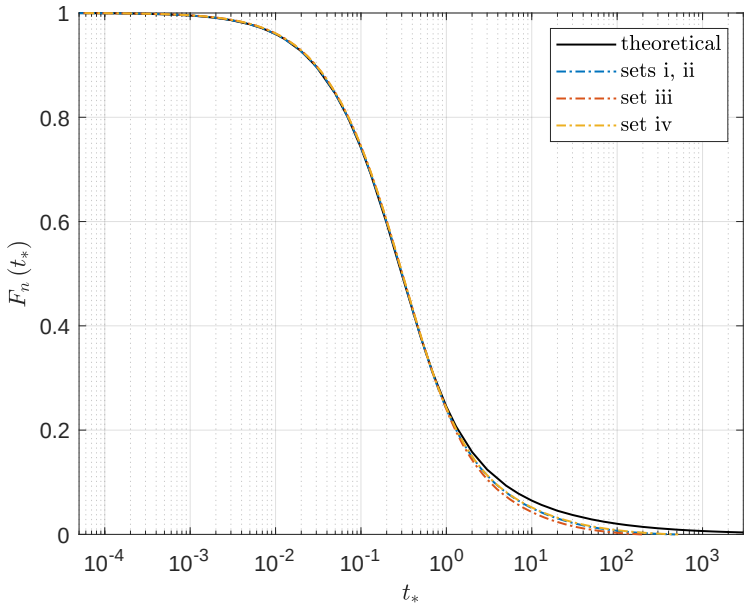

Figure 5.4: Comparison of the force relaxation curves between the poroelastic theoretical solution and numerical simulations conducted with sets i - iv parameters; $\omega = 0.56$.

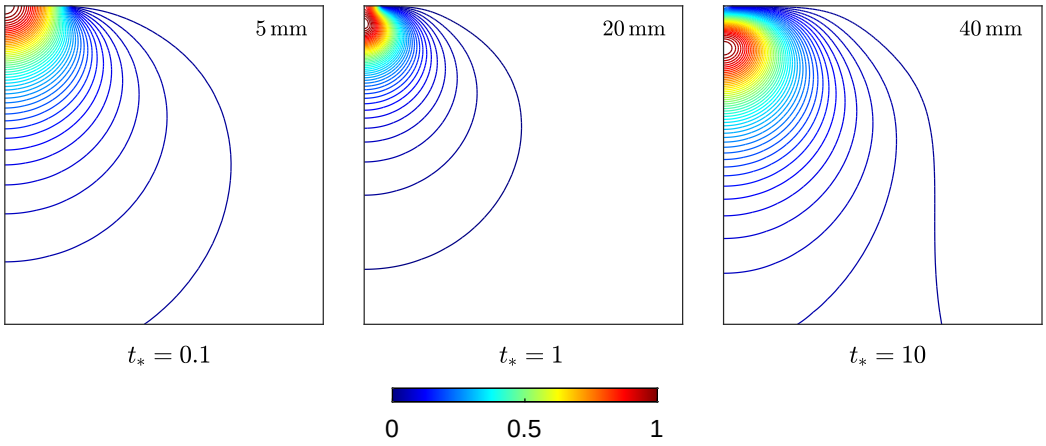

Figure 5.5: Contours of the normalized pore pressure p_n at $t_* = 0.1$, 1 and 10 from the baseline simulation; contour interval: 0.02; plot window size as marked.

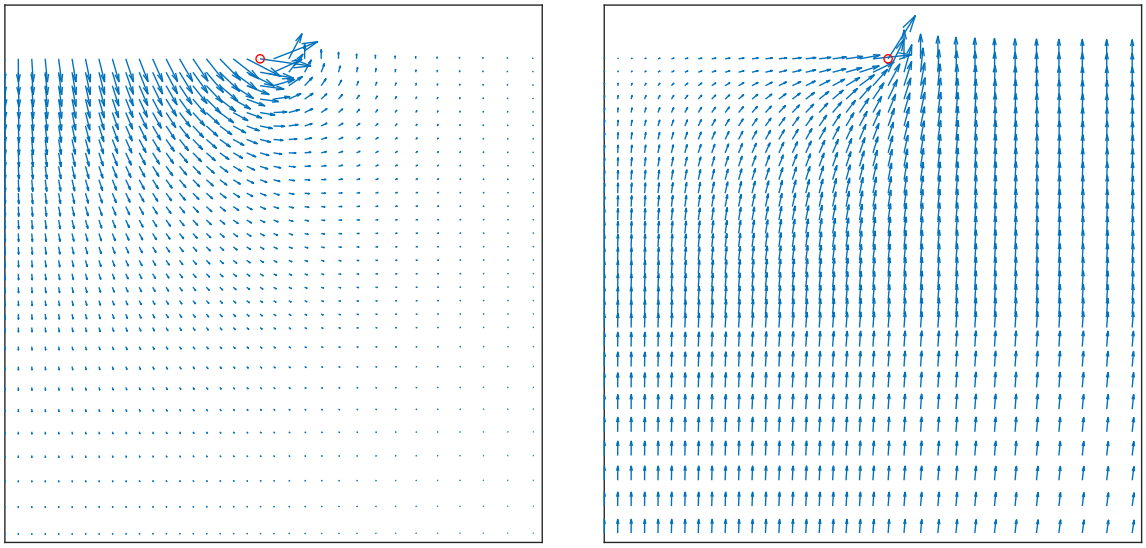

Figure 5.6: Flux field at $t_* = 0$ and 10 from the baseline simulation; plot window size: 2×2 mm; the maximum vector as marked by the red dot is $q_{\max} = 6.5214 \times 10^{-5}$ m/s and 6.4226×10^{-8} m/s at $t_* = 0$ and 10.

Discrepancies in the force relaxation curves at late time can be attributed to the boundary effect. Pore pressure field at various times for this baseline simulation is shown in Fig. 5.1(a) and 5.5. While the area of positive pore pressure grows with time, the maximum pore pressure $p_{\max}$

decreases and its location gradually moves downwards along the contact axis. The minimum and maximum pore pressures at $t_* = 0.1$, 1 and 10 are $p_{\min} = -0.0176$, -0.0099, -0.0039 MPa and $p_{\max} = 95$, 9.35, 0.672 MPa. At $t_* = 10$, the contour for $p_n = 0.02$ becomes nearly parallel to the lateral boundary, indicating the diffusion process is now affected by the drainage condition on the side.

Fluid flux field near the contact area at $t_* = 0$ and 10 is shown in Fig. 5.6. At $t_* = 0$, the sudden loading drives the fluid to flow downwards and around the contact edge. At $t_* = 10$, since the location of the maximum pore pressure is already inside the domain, fluid flows upwards towards the contact edge and the free surface. At both $t_* = 0$ and 10, the maximum flux vector is located at $r = 1$ owing to the discontinuity in the drainage boundary condition, and $q_{\max} = 6.52 \times 10^{-2}$, 6.42×10^{-5} mm/s, respectively.

Effect of parameter ω on the normalized indentation force $F_n(t_*)$ is examined further with $K_s \to \infty$, $K_f \to \infty$ and $\nu = 0$, 0.45. These parameters correspond to $\omega = 1$, 0.1. All three cases of surface drainage conditions are analyzed. For cases I and II, the simulations are carried out by setting the entire top surface as fully drained ($p = 0$) or undrained ($q_z = 0$), respectively. In all three surface drainage cases, the numerical results are in excellent agreement with the theoretical solutions. A comparison of the force asymptotes at the undrained and drained limits is given in Table 5.3. The discrepancy is the largest at 1.35% for $F(\infty)$ at $\omega = 1$ and is smaller than 1% for the rest. A comparison of the force relaxation at transient times in terms of ΔF_n is shown in Fig. 5.8. Here ΔF_n denotes the difference in the normalized indentation force $F_n(t_*)$ between the numerical and theoretical solutions. Overall, the transient results agree very well with the theoretical solutions. The relatively large discrepancy at large time is again attributed to the finite sample size and far field drainage boundary conditions.

Both the finite element simulations and theoretical solutions show that relaxation of the normalized indentation force is the slowest when the top surface is impermeable and the fastest when it is fully permeable, see Fig. 5.7. The mixed surface drainage cases behave asymptotically as the impermeable cases at early time, but as the permeable cases at late time. This can be explained by the fact that excess pore pressure is mostly being generated in the region

underneath the contact. Among the three surface drainage conditions, characteristic drainage paths for this excess pore pressure region are the shortest in case I and the longest in case II.

Simulations in this section illustrate the unique role of ω for poroelastic spherical indentation. Furthermore, the narrow bandwidth between the force relaxation curves at $\omega = 0.1$ and 1 suggests that dependence of $F_n(t_*)$ on ω is relatively weak. Among the three types of surface drainage conditions, case III seems to be the least affected by ω. It should be noted that though the theoretical range of ω is [0, 1], the values for sixteen saturated poroelastic geomaterials, based on the material constants listed in Cheng (2016), fall within the range between 0 and 0.5 (Liu and Huang, 2019b). This means dependence of the force relaxation curve on ω could be even weaker from a practical standpoint. In other words, these normalized force relaxation curves as mastercurves for poroelasticity characterization could be quite reliable as they are not strongly affected by the uncertainties in material properties.

	Theoretical				Numerical			
set	i	ii	iii	iv	i	ii	iii	iv
$F(0)$ (N)	405	4050	1447.5	386.1	406.6	4066	1462.6	387.1
$F(\infty)$ (N)	259.6	2596	927.9	247.1	261.9	2619	937.5	249.2

Table 5.2: Force asymptotes at early and late times for cases with parameters from sets i - iv.

	Theoretical		Numerical	
ω	0.1	1	0.1	1
$F(0)$ (N)	340.8	494.1	343.3	497.5
$F(\infty)$ (N)	309.8	247.1	312.7	250.3

Table 5.3: Force asymptotes at early and late times for $\omega = 0.1$ and 1 with case III surface drainage condition.

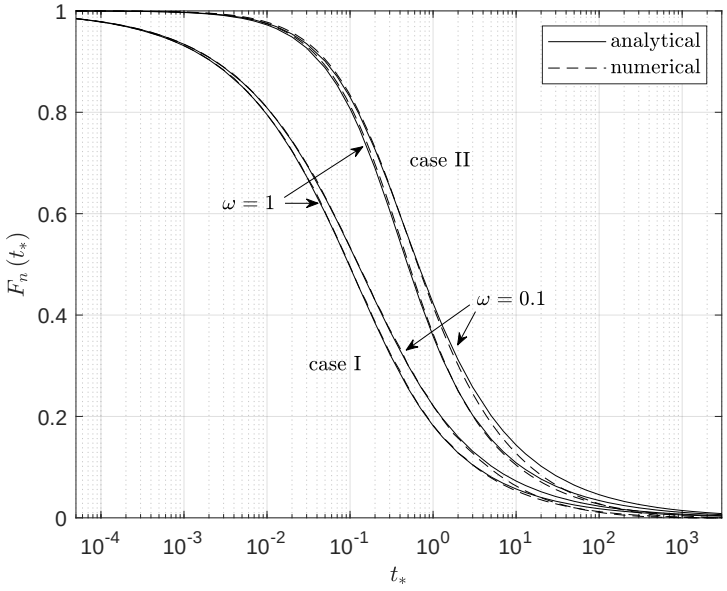

(a) case I and II surface drainage conditions

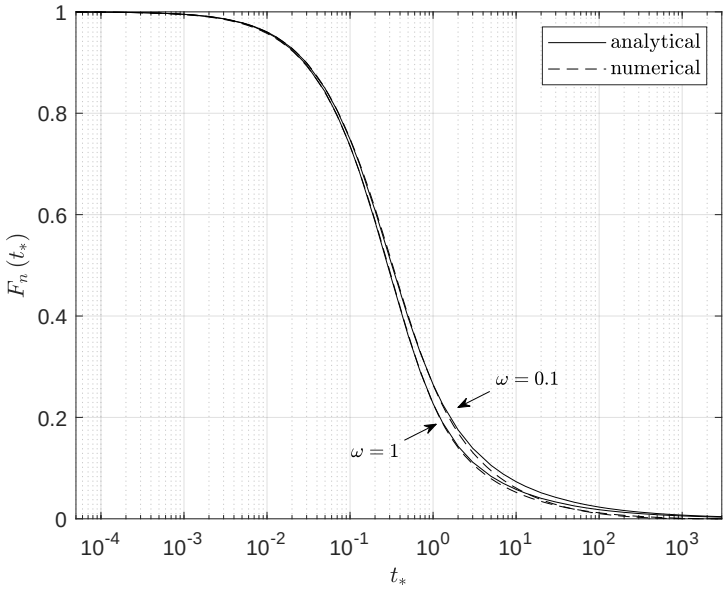

(b) case III surface drainage condition

Figure 5.7: Comparison of the poroelastic force relaxation responses between the numerical and theoretical solutions for (a) cases I & II and (b) case III surface drainage conditions; $\omega = 0.1$ and 1.

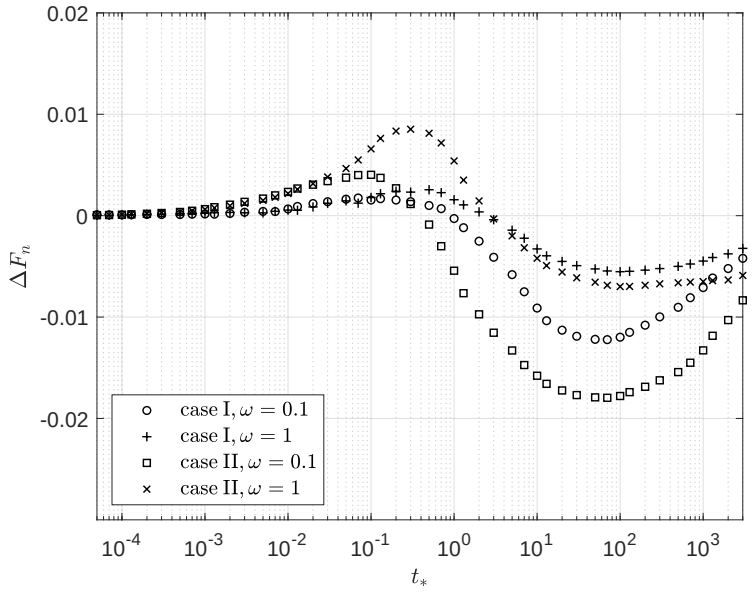

(a) case I and II surface drainage conditions

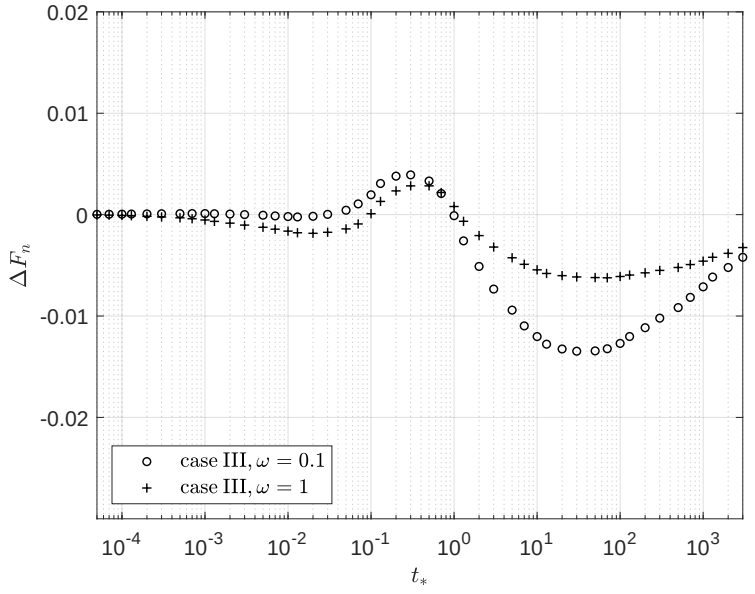

(b) case III surface drainage condition

Figure 5.8: Differences between the numerical and theoretical solutions in the normalized indentation force as a function of time at $\omega = 0.1$ and 1.

5.6.2 Onset of Plasticity

Poroelastic stress fields can be analyzed to understand onset of plasticity. Consider the baseline simulation case with $K_s \to \infty$, $K_f \to \infty$, $\nu = 0.22$ and case III drainage condition. Denote $\varrho = \sqrt{J_2} + bI_1$ as the Drucker-Prager stress. At the undrained limit, the maximum Drucker-Prager stress is $\varrho_{1\,\max} = 57.5$ MPa at $r = 0$, $z/a = 0.55$. Meanwhile, at the drained limit, there are two local maxima, $\varrho_{2\max} = 28.7$ MPa at $r = 0$, $z/a = 0.65$ and $\varrho_{3\,\max} = 23.1$ MPa at $r/a = 1$, $z = 0$. This means the corresponding cohesion to initiate plasticity is $c_0 = 46.9$ MPa ($c_0/G = 0.0618$) at the undrained state and $c_0 = 23.4$ and 18.8 MPa ($c_0 = 0.0308$, 0.0248) at the drained state, respectively. Therefore, if $c_0 \geqslant 46.9$ MPa, the indentation process will always be poroelastic.

5.7 Poro-elasto-plastic Indentation

5.7.1 Effect of Constituent Compressibility

Now we consider the material to be poro-elasto-plastic. Effect of constituent compressibility is first examined. Two series of numerical simulations with case III surface drainage condition are conducted. In the first series, properties of the Gulf of Mexico shale as listed in Table 5.1, $K_s = 34$ GPa and $K_f = 2.25$ GPa, are used. Poroelastic constants for this series are: $\alpha = 0.968$, $S = 0.153$ 1/GPa and $\omega = 0.416$. In the second series, we assume incompressibility for the solid and fluid phases, i.e., $K_s \to \infty$ and $K_f \to \infty$, which corresponds to $\alpha = 1$, $S = 0$ and $\omega = 0.56$.

In both series, we set $\varphi = \psi = 20^\circ$, $c_0 = 15.18$ and 32.45 MPa ($c_0/G = 0.02$ and 0.043). The cohesion values are chosen based on the empirical correlation in Horsrud (2001). For highly porous and unconsolidated shales from North Sea, which are similar to Gulf of Mexico shales, the uniaxial compressive strength (UCS, in MPa) can be correlated to the Young's modulus E (in GPa) derived from geophysical logs of velocity and density according to UCS $= 7.97E^{0.91}$. As an order of magnitude estimate, assuming a friction angle $\varphi = 20^\circ$, $\nu = 0.22$ and a ratio of $4-8$ between laboratory measured and log-derived Young's moduli, we have $c_0/G = 0.02-0.043$

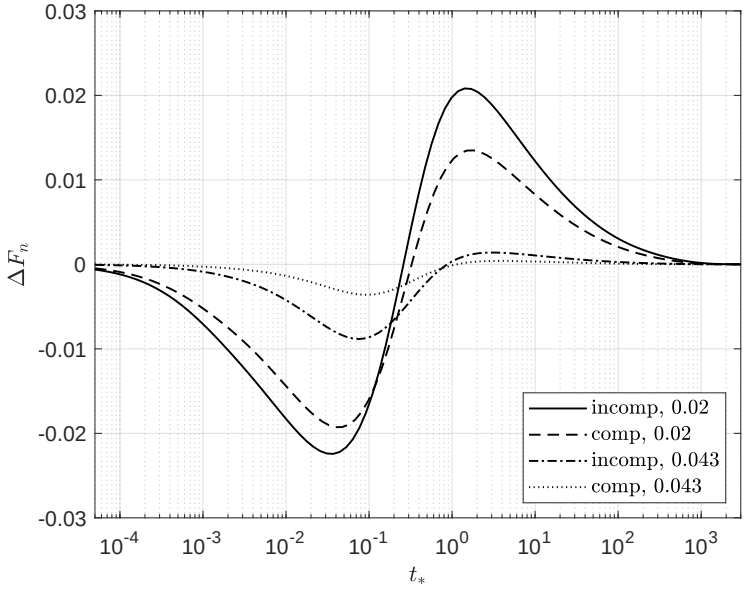

Figure 5.9: Effect of constituent compressibility on the normalized force relaxation behaviors; $c_0/G = 0.02$ and 0.043.

for this type of shales.

Denote ΔF_n as the difference in the normalized indentation force F_n between the numerical and the theoretical poroelasticity solutions. Variation of ΔF_n with the dimensionless time t_* is shown in Fig. 5.9. At $c_0/G = 0.02$ and 0.043, effect of compressibility on $|\Delta F_n|$ is relatively small and the differences between the two series are less than 0.73% and 0.52%, respectively.

Denote an equivalent plastic strain according to,

$$\varepsilon^p = \sqrt{\left(\varepsilon_r^p\right)^2 + \left(\varepsilon_z^p\right)^2 + \left(\varepsilon_\theta^p\right)^2 + 2\left(\varepsilon_{rz}^p\right)^2} \tag{5.66}$$

In all these cases, plastic deformation occurs immediately at the undrained state. The maximum plastic strain $\varepsilon_{\max}^p$ at a given time remains constant during the transient phase since there is no additional plastic strain accumulation as the excess pore pressure dissipates. For $c_0/G = 0.02$ and 0.043, $\varepsilon_{\max}^p = 0.0347$ and 0.0127 in the compressible cases and $\varepsilon_{\max}^p = 0.0394$ and 0.0195 in the incompressible cases, suggesting that plastic deformation is more severe when the constituents are incompressible. As a result, the two incompressible cases actually deviate

further from the poroelasticity solutions as shown in Figure 5.9. Therefore, in the subsequent sections, we set $K_s \to \infty$ and $K_f \to \infty$ to stay on the less conservative side as we systematically explore the effect of plastic deformation.

5.7.2 Effect of Cohesion - Associative Cases

In order to investigate the effect of plastic deformation on the coupled indentation process via cohesion, friction and dilatancy angles, we conduct four series of numerical simulations with case III surface drainage condition, assuming incompressibility in the constituents. According to the poroelasticity analysis in Section 5.6.2, since plastic deformation occurs only if $c_0 \leqslant 46.9$ MPa, cohesion is chosen from $c_0 = 0.05 - 46$ MPa, which covers the range of $c_0/G = 0.0001 - 0.06$. Friction and dilatancy angles for each series are taken as follows,

- series $\nmid$: $\varphi = \psi = 20^\circ$
- series $\nparallel$: $\varphi = \psi = 30^\circ$
- series $\nmid$: $\varphi = 20^\circ$, $\psi = 0^\circ$
- series $\nparallel$: $\varphi = 30^\circ$, $\psi = 0^\circ$

In addition, for each poro-elasto-plastic case, an elasto-plastic simulation is conducted as a reference for results at the drained limit.

The hydromechanically coupled responses are analyzed based on the plastic deformation mechanisms in terms of the plastic zone development and equivalent plastic strain, the force asymptotes at the undrained and drained limits, pore pressure and flux fields, and the transient force relaxation behaviors. Denote $\eta_\varepsilon = \varepsilon^p_{\max}(0)/\varepsilon^p_{\max}(\infty)$ as the ratio of the maximum equivalent plastic strains at the undrained and drained limits, $\eta_f = F(0)/F(\infty)$ as the ratio between the undrained and drained force asymptotes, and $\eta_* = F(0)/F_*$ as the ratio of the undrained force asymptote over the indentation force F_* from the elasto-plastic simulation. These ratios are to be used as quantitative measures for the effect of plastic deformation.

After synthesizing the simulation results from all four series, we find that given φ and ψ, as the cohesion varies, four distinct types of responses emerge as a result of juxtaposition of plastic deformation mechanisms and hydromechanical coupling. There are qualitatively differences between the associative ($\varphi = \psi$) and non-associative ($\psi = 0°$) cases. However, between Series ⅂ and ⅄, and Series ⅁ and ⅃, they differ only quantitatively in the critical cohesion values for transitions from one type of behaviors to another. Therefore, in the discussion below, we focus primarily on the results from Series ⅂ and ⅁ with $\varphi = 20°$.

For Series ⅂, the range of cohesion for each type of behaviors is,

- Type I: $29 \leqslant c_0 \leqslant 46.9$ MPa ($0.038 \leqslant c_0/G \leqslant 0.062$)
- Type II: $15 \leqslant c_0 < 29$ MPa ($0.020 \leqslant c_0/G < 0.038$)
- Type III: $3 \leqslant c_0 < 15$ MPa ($0.004 \leqslant c_0/G < 0.020$)
- Type IV: $c_0 < 3$ MPa ($c_0/G < 0.004$)

Characteristics of each type of behaviors can be described as follows. When $c_0 > 46.9$ MPa, there is no plastic deformation at all in the domain. The response is purely poroelastic. The drained force asymptote $F(\infty)$ is therefore identical to the indentation force F_* from the elasto-plastic simulation, $\eta_f = \eta_*$.

When $29 \leqslant c_0 \leqslant 46.9$ MPa, $\eta_\varepsilon = 1$ and $\eta_f \backsimeq \eta_* = 1.55$. In this regime, indentation induced plastic deformation is fully contained in a region at a distance beneath the contact surface. Plastic deformation occurs immediately at the undrained state. However, during the transient period, the plastic zone does not grow in size and there is no additional plastic strain accumulation. The maximum plastic strain $\varepsilon^p_{\max}$ remains constant at $z/a = 0.55$ and $r = 0$ and thus $\eta_\varepsilon = 1$ as the excess pore pressure dissipates, see Figs. 5.10 and 5.11. Furthermore, since plastic deformation induced by poro-plastic coupling is still relatively small, the drained force asymptote $F(\infty)$ remains almost the same as F_*, $\eta_f \backsimeq \eta_*$. If there is no presence of pore fluid, the indentation process is elastic.

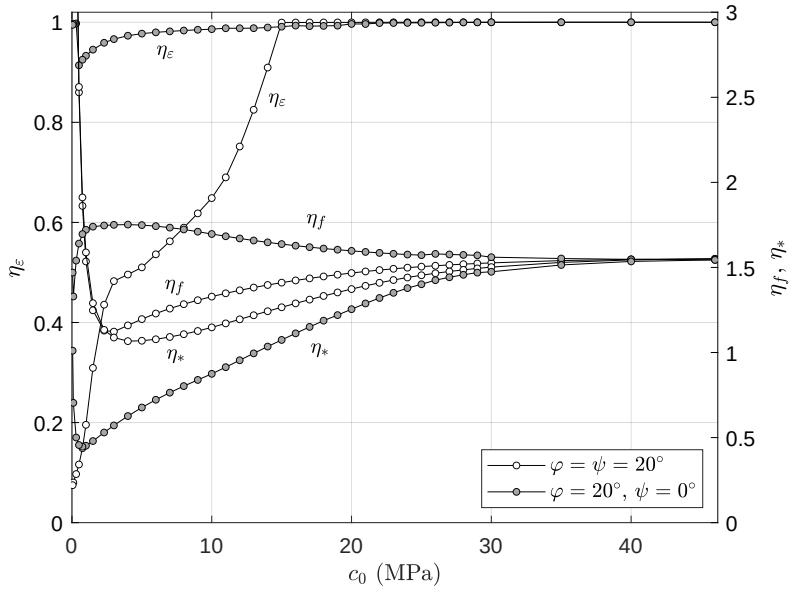

Figure 5.10: Series ⊦: $\varphi = \psi = 20°$, series ⊬: $\varphi = 20°$, $\psi = 0°$; Effect of cohesion on the ratios of the equivalent plastic strain η_ε and force asymptotes η_f and η_*.

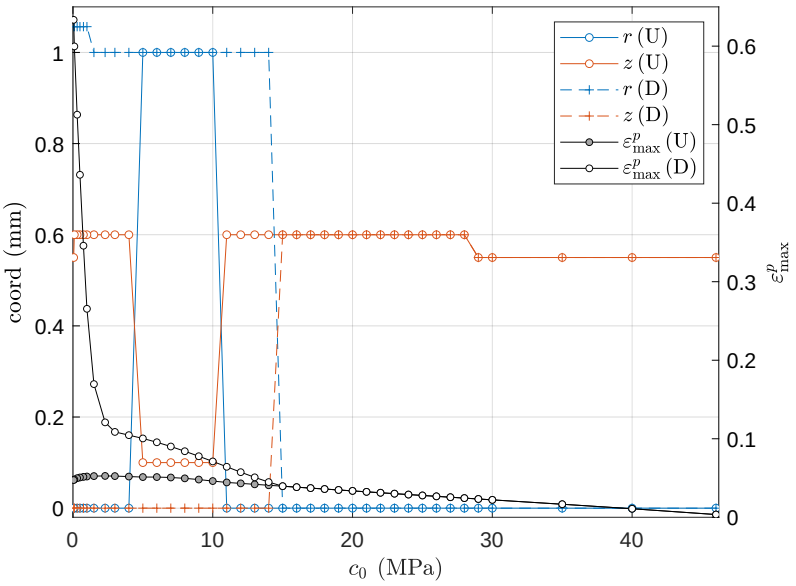

Figure 5.11: Series ⊦: Effect of cohesion on the location and magnitude of the maximum equivalent plastic strain $\varepsilon^p_{\max}$; U - undrained limit, D - drained limit.

When $15 \leqslant c_0 < 29$ MPa, $\eta_\varepsilon = 1$ and $\eta_f > \eta_*$. The main difference between behaviors in this cohesion range and Type I is that poro-plastic coupling has resulted in more extensive plastic deformation. As a result, the indentation force at the drained limit becomes smaller than that without the presence of pore fluid, i.e., $F(\infty) < F_*$. Magnitude of $\varepsilon^p_{\max}$ still remains the same throughout the indentation process, $\eta_\varepsilon = 1$, but the location is now at $z/a = 0.60$ and $r = 0$.

Results from a representative case with $c_0 = 25$ MPa at four dimensionless times, $t_* = 0$, 0.1, 1 and 10, are illustrated in Fig. 5.12. From top to bottom, they are contour plots of the normalized equivalent plastic strain, i.e., $\varepsilon^p_n = \varepsilon^p/\varepsilon^p_{\max}$, pore pressure and the vector plot of the normalized flux field. Unless otherwise noted, the plot window size is 5×5 mm for ε^p_n and p_n and 2×2 mm for the flux field. The contour interval is 0.05. Contours for $\varepsilon^p = 0$ and $p = 0$ as marked by the black lines are added. Location of the maximum flux vector is marked by a red dot.

At these four times, the maximum plastic strain remains constant at $\varepsilon^p_{\max} = 0.0278$. As can be seen from the contour plots of ε^p_n, plastic deformation is fully contained and the plastic zone does not grow in size over the transient period. The pore pressure and flux fields are very similar to the poroelastic case. The excess pore pressure being induced is mostly positive, indicating that shear induced dilatancy is not yet sufficient to counter volume compression due to elasticity. At the undrained state, there is a very small area right beneath the surface outside of the plastic zone, where the pore pressure is negative. The tensile stress field outside of the contact edge is responsible for this negative pore pressure development. At $t_* = 0$, the excess pore pressure at the origin is the largest and fluid flows mostly downwards. However, over time as fluid is being drained via the free surface, location of the largest pore pressure moves downwards and is already inside the domain at $t_* = 1$.

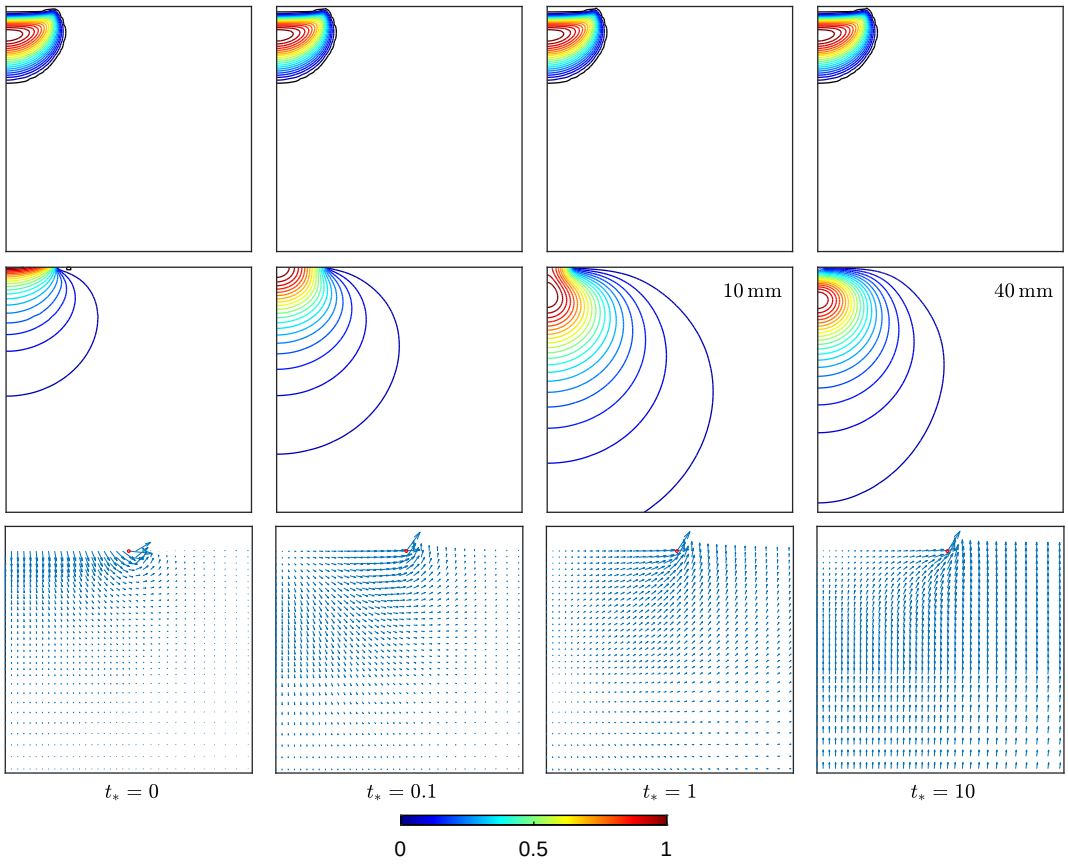

Figure 5.12: Series ϟ, $c_0 = 25$ MPa; from top to bottom - normalized equivalent plastic strain ε_n^p, pore pressure p_n and fluid flux at $t_* = 0$, 0.1, 1 and 10; at these four times, $\varepsilon_{\max}^p = 0.0278$, $p_{\min} = -0.0788$, -0.0163, -0.0093, -0.0038 MPa, $p_{\max} = 154.61$, 75.5, 8.105, 0.621 MPa and $q_{\max} = 7.0 \times 10^{-2}$, 2.48×10^{-2}, 2.86×10^{-3}, 5.90×10^{-5} mm/s; top and middle - contour interval: 0.05, plot window size: 5×5 mm if not otherwise marked; contours of $\varepsilon^p = 0$ and $p = 0$ marked by black lines are added; bottom: plot window size: 2×2 mm.

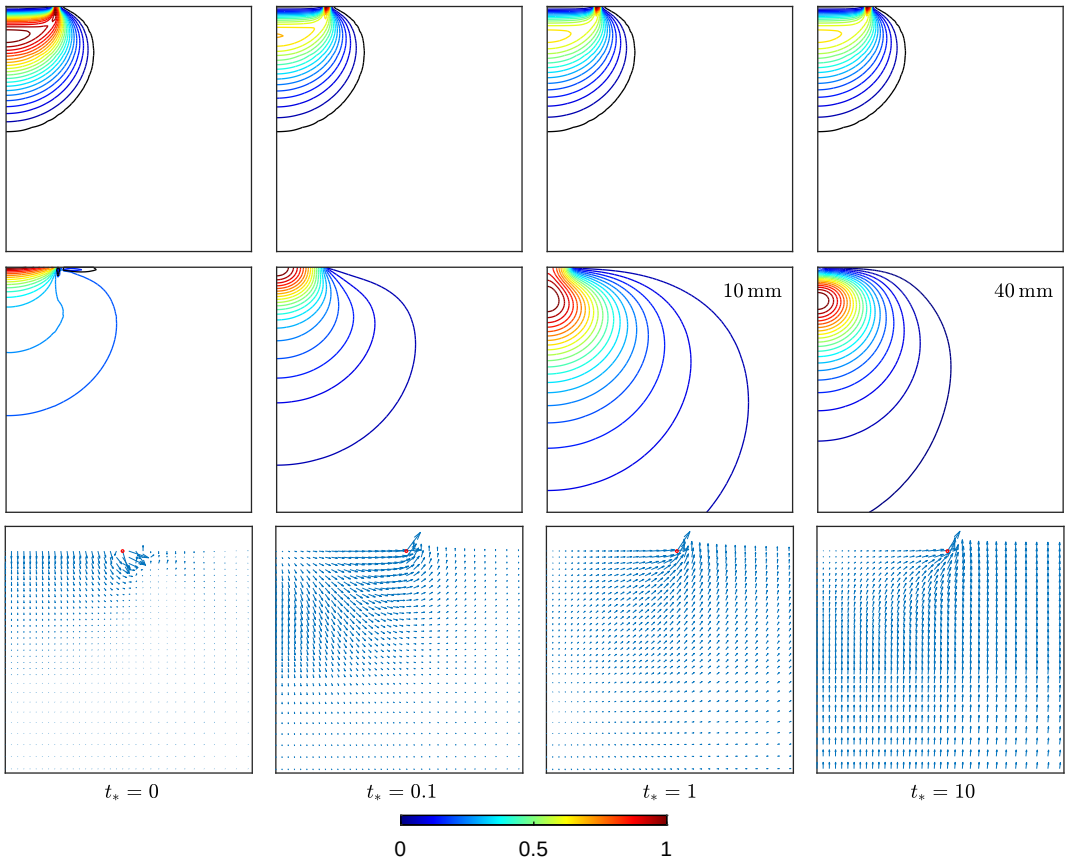

Figure 5.13: Series ϟ, $c_0 = 10$ MPa; from top to bottom - normalized equivalent plastic strain ε_n^p, pore pressure p_n and fluid flux at $t_* = 0$, 0.1, 1 and 10; at these times, $\varepsilon^p_{\max} = 0.0461$, 0.0682, 0.0711, 0.0711, $p_{\min} = -27.23$, -0.0121, -0.0074, -0.0031 MPa, $p_{\max} = 101.103$, 41.241, 4.372, 0.441 MPa, and $q_{\max} = 8.82 \times 10^{-2}$, 1.15×10^{-2}, 1.49×10^{-3}, 4.09×10^{-5} mm/s.

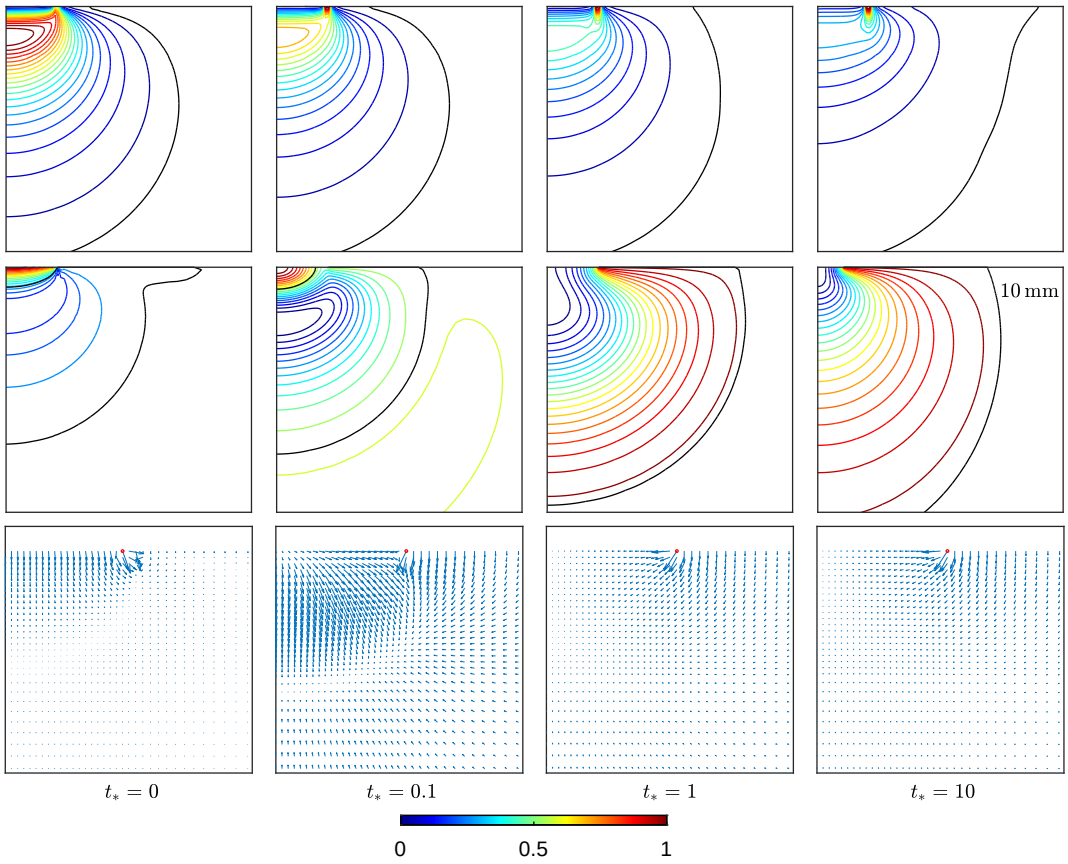

Figure 5.14: Series ϟ, $c_0 = 1$ MPa; from top to bottom - normalized equivalent plastic strain ε_n^p, pore pressure p_n and fluid flux at $t_* = 0$, 0.1, 1 and 10; for these times, $\varepsilon^p_{\max} = 0.0519$, 0.0729, 0.110, 0.205, $p_{\min} = -26.195$, -10.051, -5.041, -1.149 MPa, $p_{\max} = 56.032$, 8.034, 0.186, 0.0356 MPa, and $q_{\max} = 6.211 \times 10^{-2}$, 4.321×10^{-3}, 2.734×10^{-3}, 6.167×10^{-4} mm/s.

When $3 < c_0 \leqslant 15$ MPa, $\eta_\varepsilon < 1$, $\eta_f > \eta_*$. Though plastic flow is still contained beneath the surface, now there is moderate plastic strain accumulation in the transient phase. The maximum plastic strain increases with time. Though at the undrained state, location of the maximum plastic strain moves in the area between $z/a = 0.6$, $r = 0$ and $z = 0$, $r/a = 1$, see Fig. 5.11, with time, plastic deformation becomes fairly concentrated at the contact edge. For all cases with $c_0 \geqslant 3$, displacement on the surface exhibits the sink-in type behavior, indicating the process is not yet plasticity dominated (Taljat and Pharr, 2004).

Results from the case of $c_0 = 10$ MPa are shown in Fig. 5.13. The maximum plastic strain in this case increases from $\varepsilon^p_{\max} = 0.0461$ at $t_* = 0$ and stabilizes at $\varepsilon^p_{\max} = 0.0711$ at $t_* = 1$ and 10. The negative pore pressure at $t_* = 0$ is of appreciable magnitude, but is still limited to a very small area near the contact edge. Overall, the pore pressure and flux fields are very similar to those with $c_0 = 25$ MPa. As a result of the contained plastic deformation, the top surface sinks in immediately at $t_* = 0$ and the displacement profile barely changes over time, see Fig. 5.15.

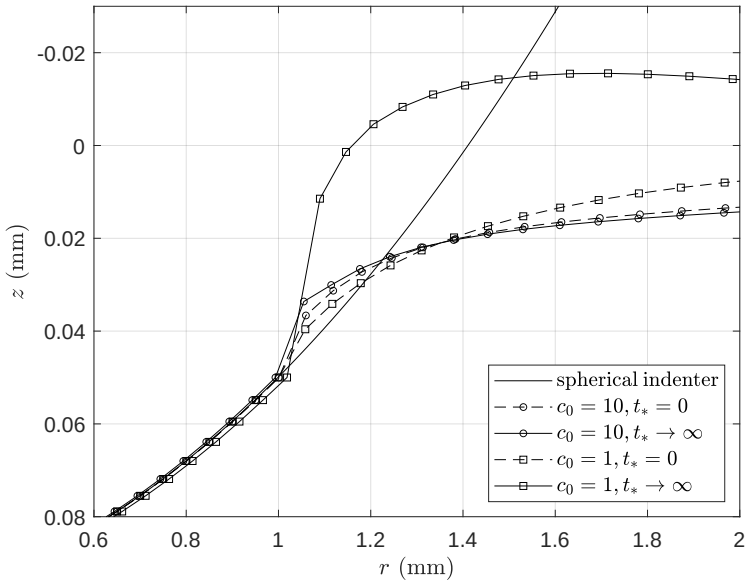

Figure 5.15: Series ϟ: Surface displacement profiles at the undrained and drained states with $c_0 = 1$ and 10 MPa.

When $c_0 \leqslant 3$ MPa, $\eta_\varepsilon < 1$ and $\eta_f \backsimeq \eta_*$. A distinct characteristic of this regime is that the plastic flow becomes uncontained. On the surface, the plastic zone has extended beyond the confinement of the contact area. The responses become plasticity dominated as surface displacement exhibits the pile-up type of behaviors at the drained state. Full associativity results in significant shear induced dilation, which in turn gives rise to a negative pore pressure zone inside the domain immediately at the undrained state.

As shown in Fig. 5.14 for the case of $c_0 = 1$ MPa, substantial negative pore pressure develops inside the domain. The areas enclosed by the black lines in the pore pressure contour plots are the negative pore pressure zones, which serve to shield the material from plastic deformation and also as sinks to attract fluid flow. As a result, plastic strain induced by hydromechanical coupling at the undrained state is a less significant portion of the total accumulated. The maximum plastic strain increases from $\varepsilon^p_{\max} = 0.0519$ at $t_* = 0$ to 0.266 at $t_* \to \infty$. The substantial increase in $\varepsilon^p_{\max}$ over time suggests that yielding occurs primarily over the transient phase as the excess pore pressure dissipates. As plastic flow becomes uncontained over time, the surface displacement profile also evolves from the sink-in type to the pile-up type, see Fig. 5.15. A manifestation of such hydromechanical coupling is that responses at the drained limit, e.g. the force asymptote $F(\infty)$, magnitude and location of the plastic strain $\varepsilon^p_{\max}$ and the plastic zone size, are nearly identical to their elasto-plastic counterparts.

These four distinct types of behaviors are reflected in the indentation force relaxation curves. When $c_0 \geqslant 29$ MPa, they are nearly identical to the poroelastic solution. For $15 \leqslant c_0 < 29$ MPa, the poro-elasto-plastic cases deviate only slightly, see Figs. 5.16 and 5.18. Compared with the poroelastic case, the poro-elasto-plastic cases relaxes slightly faster at early time, but slower at late time. At $c_0 = 15$ MPa, $\Delta F_n \leqslant 2.13\%$, see Fig. 5.18. This means even though plasticity occurs immediately at the undrained limit in these cohesion ranges, the normalized transient force relaxation behavior can be treated as approximately poroelastic.

As cohesion decreases to $c_0 = 3$ MPa, the curves gradually shift to the left at early time, but shift to the right at late time. This is reflected by the change in the maximum flux magnitude at the contact edge. For $c_0 = 25$ MPa, $q_{\max} = 0.07$ and 0.059 mm/s at $t_* = 0$ and 10; and for

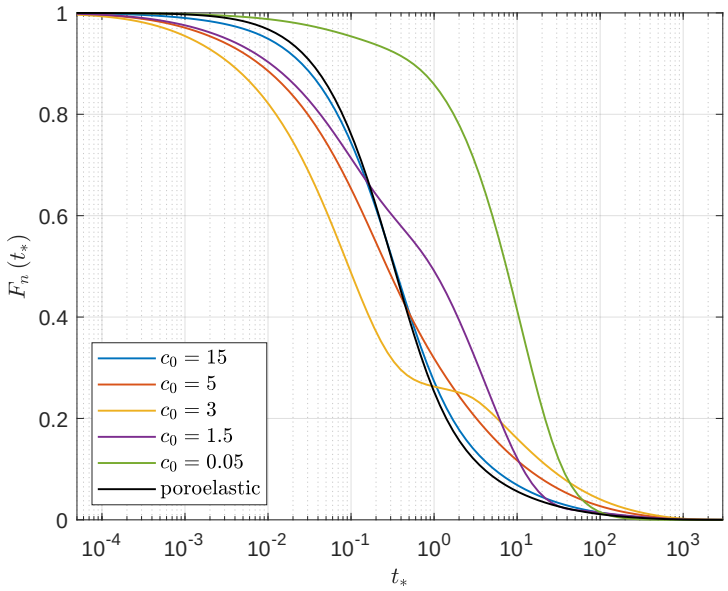

Figure 5.16: Series ϟ: Comparison of the force relaxation curves between the poroelastic case ($\omega = 0.56$) and the cases of $c_0 = 0.05$, 1.5, 3, 5 and 15 MPa.

$c_0 = 10$ MPa, $q_{\max} = 0.088$ and 0.041 mm/s at the same time instances. At $c_0 = 3$ MPa, the force relaxation curve exhibits a plateau-like transition region at $0.5 \lesssim t_* \lesssim 3$, suggesting that there are two distinct drainage mechanisms at play. Note that $c_0 = 3$ MPa is the threshold below which plastic deformation becomes uncontained. As cohesion decreases further from $c_0 = 3$ MPa, the force relaxation curves now shift to the right of $c_0 = 3$ MPa at early time, but to the left at late time. In the extreme case of $c_0 = 0.05$ MPa, the indentation force relaxes even slower than the poroelastic case most of the time.

Dependence of such transient responses on cohesion can be attributed to weakening of the material due to plastic deformation as well as the competition between promotion of drainage through the contact edge and impedance due to plastic deformation inside the domain. Drainage near the contact edge is facilitated by the tensile stress field right outside of the contact edge as well as shear induced dilation when yielding occurs in this region. Inside the domain, drainage is however hindered by the development of a plastic zone as shear induced dilation reduces the pore pressure to the extent that the negative pore pressure zone acts like

a sink that attracts fluid flow. As cohesion becomes small, such a mechanism clearly becomes dominant, see the flux field at $c_0 = 1$ MPa in Fig. 5.14.

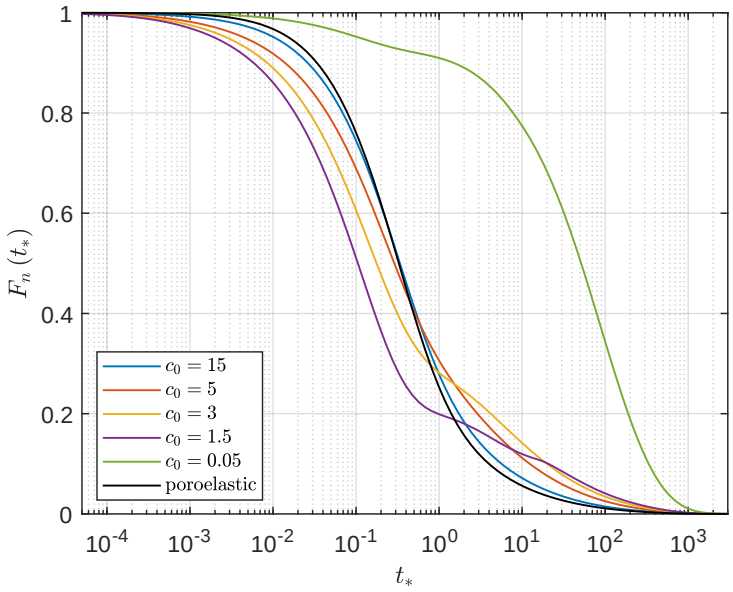

Figure 5.17: Series ⫽: Comparison of the force relaxation curves between the poroelastic case ($\omega = 0.56$) and the cases of $c_0 = 0.05$, 1.5, 3, 5 and 15 MPa.

When the friction and dilatancy angles are changed to $\varphi = \psi = 30°$ in Series ⫽, based on the criteria established above for η_ε, η_f and η_*, we can again identify the same four types of poro-elasto-plastic responses. Compared with Series ⫞, the threshold cohesion values in this series are smaller, $c_0 = 46.9$, 21, 8, and 1.5 MPa ($c_0/G = 0.062$, 0.027, 0.011, 0.002). For $c_0 \geqslant 8$ MPa, plastic deformation only occurs at the undrained state and does not accumulate in the transient phase. Difference in F_n between the case of $c_0 = 8$ MPa and the poroelastic case is $|\Delta F_n| \leqslant 0.0549$, see Fig. 5.18. Overall, the behaviors differ from those in Series ⫞ only quantitatively.

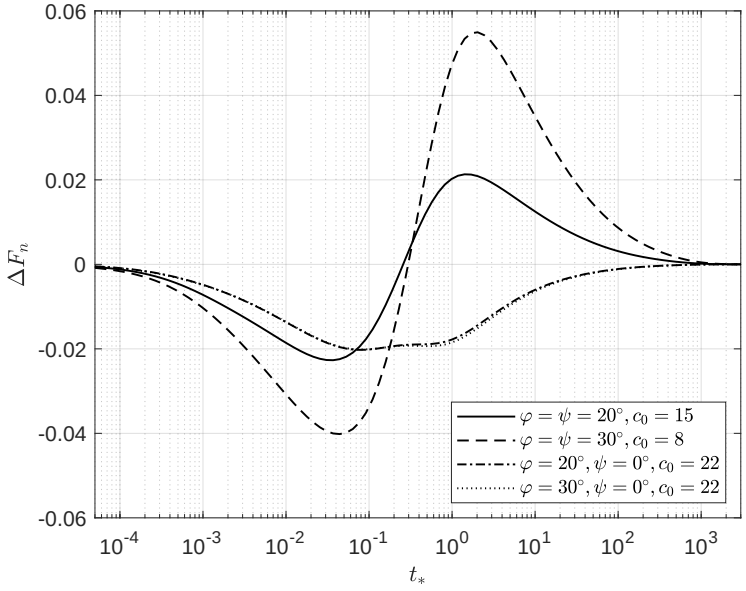

Figure 5.18: Variations of ΔF_n with time for four threshold cohesions in Series ⅂, ⅄, ⅃, ⅁; cohesion unit in MPa.

It should be noted that numerical analysis in this work is conducted within the framework of small strain. Therefore, large strain behaviors in the cases with very small cohesion values may not be accurately modeled. Furthermore, in reality, large negative pore pressure may result in fluid cavitation. This aspect is however not considered in this numerical analysis either.

5.7.3 Effect of Cohesion - Non-associative Cases

Four distinct types of behaviors can also be identified when the material is non-associative. For Series ⅃ with $\varphi = 20°$ and $\psi = 0°$, the threshold cohesion values are $c_0 = 46.9$, 40, 22, and 4 MPa ($c_0/G = 0.062$, 0.053, 0.029, 0.005). For Series ⅁ with $\varphi = 30°$ and $\psi = 0°$, we have $c_0 = 46.9$, 40, 22, and 6 MPa ($c_0/G = 0.062$, 0.053, 0.029, 0.008).

Between the associative and non-associative cases, characteristics of Types I and II behaviors are the same as the effect of plastic deformation is relatively small and there is no plastic strain accumulation over time. In Type I, $\eta_\varepsilon = 1$ and $\eta_f = \eta_*$, and in Type II, $\eta_\varepsilon = 1$ and $\eta_f > \eta_*$.

The primary differences are in Types III and IV behaviors when $\eta_\varepsilon < 1$. Given $\psi = 0°$,

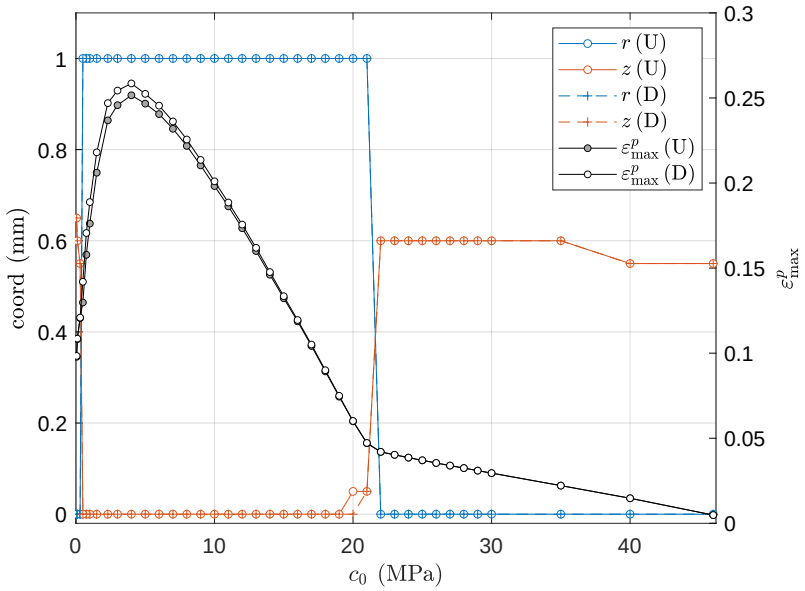

Figure 5.19: Series ɾ: Effect of cohesion on the location and magnitude of the maximum equivalent plastic strain $\varepsilon^p_{\max}$; U - undrained limit, D - drained limit.

though there is plastic strain accumulation over time in Types III and IV, plastic strain occurs mostly at early time and the increment over time is rather small. The equivalent strain ratio η_ε remains very close to 1, see Figs. 5.10 and 5.19. Variation of the maximum plastic strain $\varepsilon^p_{\max}$ with cohesion reaches a peak at $c_0 = 4$ MPa in series ɾ and $c_0 = 6$ MPa in series ʜ at both the undrained and drained states. For Type IV, the maximum plastic strain $\varepsilon^p_{\max}$ decreases as the cohesion decreases and $F_n(\infty) < F_n(0) < F_*$ or $\eta_* < 1 < \eta_f$ as the plastic deformation becomes uncontained.

Such differences between the associative and non-associative cases can be attributed to the lack of shear induced dilatancy when $\psi = 0°$. Note that shear induced dilatancy occurs only if the stress state is at the apex of the yield surface and is zero everywhere else in this FEM model when $\psi = 0°$. Without the shielding effect from the negative pore pressure due to shear induced dilatancy, plastic deformation causes the medium to be much weaker than the purely elasto-plastic case even at the undrained state in Type IV. The force asymptote at the undrained state is now smaller than the elasto-plastic case, $F(0) < F_*$ ($\eta_* < 1$).

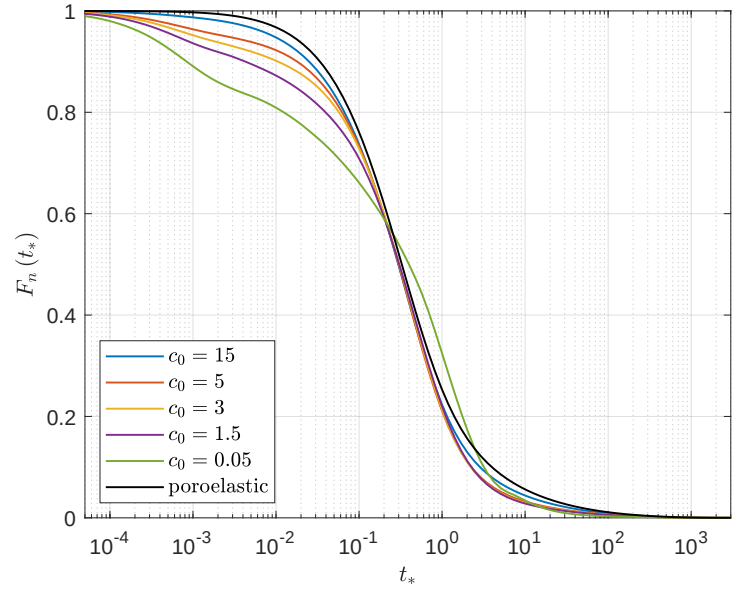

Figure 5.20: Series *r*: Comparison of the force relaxation curves between the poroelastic case ($\omega = 0.56$) and the cases of $c_0 = 0.05$, 1.5, 3, 5 and 15 MPa.

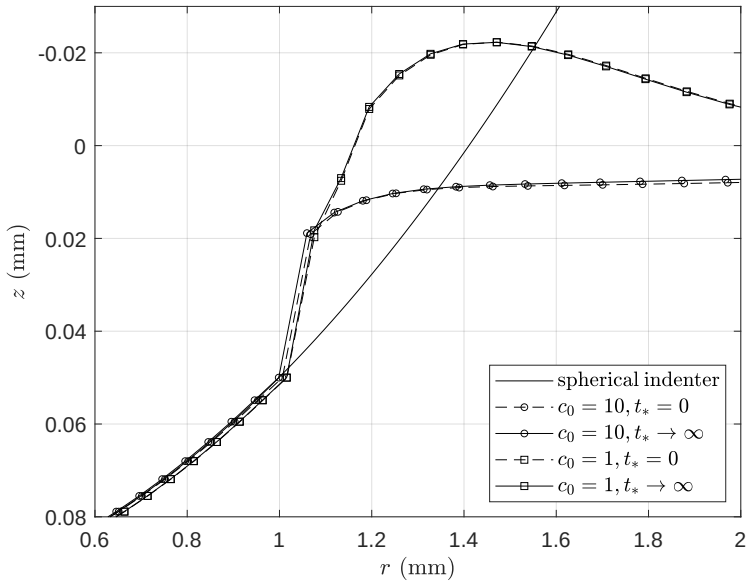

Figure 5.21: Series *r*: Surface displacement profiles at the undrained and drained states with $c_0 = 1$ and 10 MPa.

The fact that plastic deformation occurs mostly in early time when $\psi = 0^\circ$ is reflected in the force relaxation curves. Fig. 5.20 shows that deviation from the poroelasticity solution is more pronounced in early time. At $t_* > 0.1$, even the cases with rather small cohesion, e.g., $c_0 = 1.5$ MPa, are not very far from the poroelastic solution. Note that all cases except $c_0 = 0.05$ MPa in Fig. 5.20 relax faster than the poroelastic case at all time. This is in accordance with the argument that for the associative cases, dissipation of pore pressure is retarded in late time due to shear induced dilatancy. At $c_0 = 22$ MPa, which is the lower bound of Type II response in Series ɾ and ꟻ, $|\Delta F_n| < 0.020$ with $\varphi = 20^\circ$ and $\varphi = 30^\circ$, see Fig. 5.18. We may therefore conclude that from a practical standpoint, the normalized force relaxation behavior is approximately poroelastic if the cohesion value is such that it gives rise to Type I or II response.

Variation of ΔF_n over time for the non-associative cases in Fig. 5.18 also suggests that increase in the friction angle from $\varphi = 20^\circ$ to $\varphi = 30^\circ$ has little influence on the normalized indentation force response. The force asymptotes decrease slightly, $F(0) = 347.029$ N and $F(\infty) = 218.872$ N for $\varphi = 20^\circ$ and $F(0) = 341.923$ N and $F(\infty) = 213.345$ N for $\varphi = 30^\circ$. The decrease in the force asymptotes is because the tensile strength actually decreases in the Drucker-Prager criterion when c_0 is fixed, but φ increases.

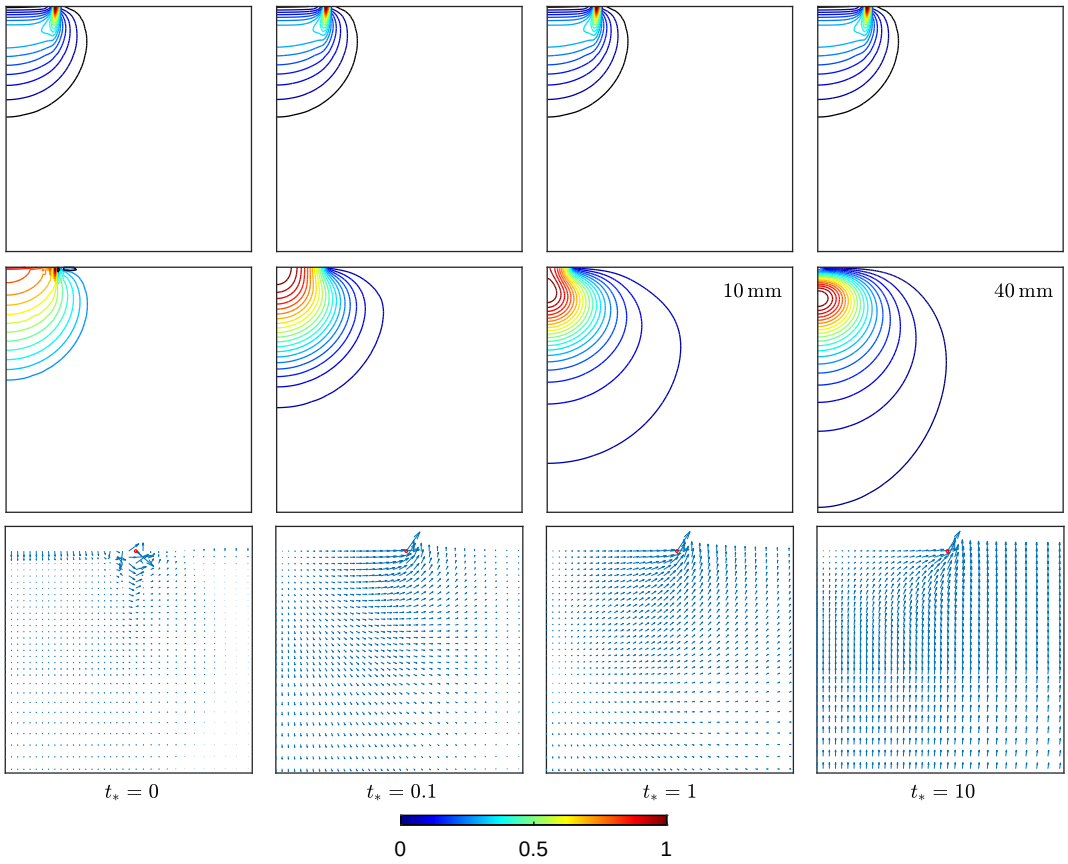

Figure 5.22: Series ɾ, $c_0 = 10$ MPa; from top to bottom - normalized equivalent plastic strain ε_n^p, pore pressure p_n and fluid flux at $t_* = 0$, 0.1, 1 and 10; at these times, $\varepsilon^p_{\max} = 0.202$, 0.205, 0.205, 0.205, $p_{\min} = -22.749$, -0.0092, -0.0042, -0.0017 MPa, $p_{\max} = 70.915$, 51.831, 5.588, 0.262 MPa, and $q_{\max} = 6.985 \times 10^{-2}$, 1.658×10^{-2}, 2.009×10^{-3}, 2.621×10^{-5} mm/s.

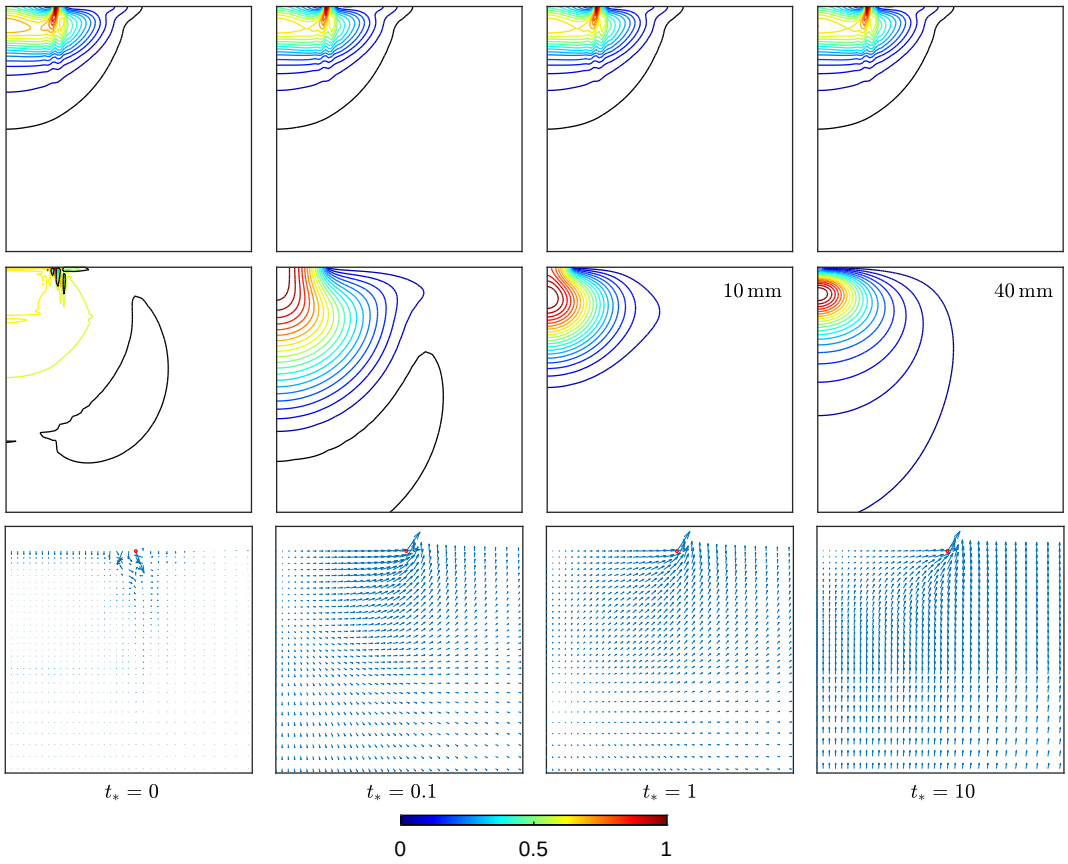

Figure 5.23: Series ɾ, $c_0 = 1$ MPa; from top to bottom - normalized equivalent plastic strain ε_n^p, pore pressure p_n and fluid flux at $t_* = 0$, 0.1, 1 and 10; at these times, $\varepsilon^p_{\max} = 0.176$, 0.189, 0.189, 0.189, $p_{\min} = -33.791$, -1.0496, -6.563×10^{-4}, -2.663×10^{-4} MPa, $p_{\max} = 28.850$, 5.889, 1.043, 0.0316 MPa, and $q_{\max} = 7.223 \times 10^{-2}$, 1.585×10^{-3}, 3.535×10^{-4}, 3.618×10^{-6} mm/s.

Contour plots of ε_n^p and p_n and the flux field from $c_0 = 10$ and 1 MPa in Series $\prime$ are shown in Figs. 5.22 and 5.23. Plastic deformation is contained at $c_0 = 10$ MPa, but becomes uncontained at $c_0 = 1$ MPa. Magnitude of $\varepsilon_{\max}^p$ and the plastic zone size and shape change very little over time. As a result, the surface displacement profiles at $t_* = 0$ and $t_* \to \infty$ are nearly identical in these two cases, even though the displacement responses have changed from the sink-in type at $c_0 = 10$ MPa to the pile-up type at $c_0 = 1$ MPa, see Fig. 5.21. In both cases, plastic strain is most concentrated at the contact edge, $r/a = 1$. However, gradient of the plastic strain at this location is lowered at $c_0 = 1$ MPa. This means though $\varepsilon_{\max}^p$ at $r/a = 1$ decreases as c_0 decreases in Type IV, see Fig. 5.19, plastic deformation is more severe in larger area when $c_0 = 1$ MPa.

Due to strong non-associativity, multiple bands of strain localization can be observed at the contact edge at $c_0 = 1$ MPa, which then result in large oscillatory distribution of pore pressure at the undrained limit around $r/a = 1$. Inside the domain, pore pressure variation is however quite small. Though a negative pore pressure zone grows right outside of the plastic zone, magnitude of the negative pore pressure in this zone is very small and the location suggests that it is associated with the tensile stress generated by the development of the plastic zone. At $t_* > 0.1$, the flux fields in both $c_0 = 1$ and 10 MPa are very similar to the poroelastic field in Fig. 5.6. It should be noted that strong non-associativity does present challenges in numerical computation. Convergence at the undrained limit has to be carefully dealt with by applying the Hertzian displacement boundary condition in small increments.

6 FINITE ELEMENT MODELING OF SPHERICAL INDENTATION IN A PORO-ELASTO-PLASTIC MEDIUM VIA A PENALTY-BASED CONTACT SCHEME

6.1 Introduction

In Chapter 5, a hydromechanically coupled finite element (FEM) algorithm following a mixed continuous Galerkin formulation for displacement and pore pressure is employed to model spherical indentation by prescribing the normal displacement over the contact area according to the Hertzian solution. For indentation in a poroelastic medium, numerical results confirm our previous theoretical findings that the normalized indentation force as a function of dimensionless time has a relatively weak dependence on the derived material parameter ω. For indentation in a poro-elasto-plastic medium, it is shown that hydromechanical coupling gives rise to four distinct types of poro-elasto-plastic responses. The normalized force relaxation behavior could be approximated as poroelastic if the cohesion value is such that yielding occurs only at the undrain limit and there is no accumulation of plastic strain during the transient phase.

Theoretical analyses in Chapters 2-4 have shown that the displaced surface profile resulted from such a type of step displacement loading does not conform to the spherical shape if $\nu \neq 0.5$ and $\nu_u \neq 0.5$. A kink develops at the contact edge, and stresses there become unbounded during the transient phase. In addition, the theoretical solution suggests that if frictionless contact with a rigid sphere were to be modeled, the contact radius would vary with time. In other words, poroelastic spherical indentation with a rigid sphere should be treated as a moving boundary problem.

It is therefore necessary to understand to what a degree our theoretical solutions and numerical results from step displacement loading differ from the cases where the frictionless contact between a rigid sphere and a fully saturated half space is fully modeled. Here we make a distinction between the two types of boundary conditions by referring step displacement loading to the case where only normal displacement is prescribed according to the Hertzian solution, and

rigid sphere loading to the case where a frictionless contact scheme is employed to model the indentation action. Objective of this chapter is to conduct finite element analysis to investigate how the indentation response is affected by the two different ways of modeling the spherical indentation action.

Numerical formulations for the contact scheme and its coupling with our previous finite element algorithm are first described. Results from numerical simulations via rigid sphere loading are then analyzed and compared with those from the theoretical and numerical results with step displacement loading.

6.2 Contact Scheme

6.2.1 General Formulation

Finite element formulations for contact problems in the literature are based on either the classical Lagrange multiplier method or the penalty-function method (Wriggers, 2006). Within the framework of the Lagrange multiplier method, the contact condition is exactly satisfied by transforming the constrained problem into an unconstrained one with the introduction of Lagrange multipliers. These extra variables add computational cost to the solution process which often requires special procedures to handle the presence of zero diagonal terms. Penalty method, on the other hand, enables one to transform the constrained problem into an unconstrained one without introducing additional variables. Though this method does not lead to an exact fulfillment of the contact conditions, it is computationally advantageous since no additional variables are introduced.

In this study, we adopt the penalty method (Wriggers, 2006) to solve for the cylindrically axisymmetric problems and consider a particular case where the contact is between a rigid sphere and a poro-elasto-plastic half space. Different from those studies that establish the contact conditions on nodal basis, the penalty-based scheme in this work is constructed on the basis of Gauss quadrature points as first proposed in Wriggers and Imhof (1993). With the global tangent stiffness constructed through variation and subsequent linearization on the

penalty energy term, this approach can be conveniently incorporated into the poro-elasto-plastic finite element algorithm outlined in Chapter 5.

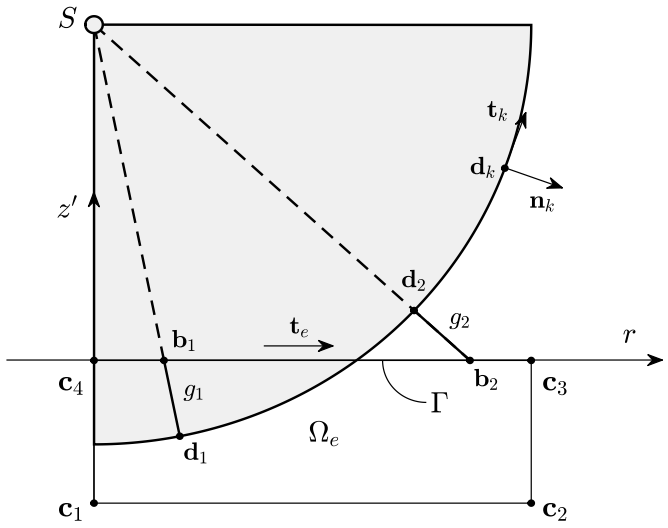

Figure 6.1: Schematic of the contact scheme with a rigid sphere.

Fig. 6.1 shows the schematic of the frictionless contact between a rigid sphere and a discretized half space. Only the first element in contact with the indenter is shown for the sake of simplicity and clarity. The subsequent derivation is given at the element level.

We introduce the nodal displacement vector $\mathbf{u}$ between the deformed state $\mathbf{c}$ and undeformed state $\mathbf{C}$,

$$\mathbf{c} = \mathbf{C} + \mathbf{u} \tag{6.1}$$

where,

$$\mathbf{u} = \begin{bmatrix} u_{1r} & u_{1z} & u_{2r} & u_{2z} & u_{3r} & u_{3z} & u_{4r} & u_{4z} \end{bmatrix}^T \tag{6.2}$$

$$\mathbf{c} = \begin{bmatrix} c_{1r} & c_{1z} & c_{2r} & c_{2z} & c_{3r} & c_{3z} & c_{4r} & c_{4z} \end{bmatrix}^T \tag{6.3}$$

The problem can be formulated by minimizing the sum of the strain and penalty energy,

$$\mathbf{\Pi}_p(\mathbf{u}) = \mathbf{\Pi}(\mathbf{u}) + \frac{\zeta}{2}\int_\Gamma g^2(\mathbf{u})\, d\Gamma \rightarrow \min \tag{6.4}$$

where Γ is the contact surface; $\mathbf{\Pi}(\mathbf{u})$ is the strain energy stored in Ω; g is the penetration distance; ζ is the penalty parameter; and

$$\frac{\zeta}{2}\int_\Gamma g^2(\mathbf{u})\, d\Gamma \tag{6.5}$$

represents the penalty energy from the contact. The penalty parameter ζ needs to be large in order to minimize penetration distances. If there is contact at the Gauss quadrature points, ζ can be interpreted as the stiffness of linear springs which support the body in the contact area, and ζg can be viewed as the contact stress. The penalty term then describes the total energy of all springs.

Before moving forward to construct the equilibrium equation by minimizing $\mathbf{\Pi}_p(\mathbf{u})$, we first discuss the special geometrical relations needed to set up the contact constraints at the contact interface. Consider an surface element, whose surface Γ is in contact with a rigid sphere. g_k is the distance between the Gauss points on the element surface and the rigid surface. Gauss points of Γ are represented by the isoparametric shape functions,

$$\mathbf{b}_k = \mathbf{N}(\xi_k)\,\mathbf{c}, \quad \xi_k \in [-1, 1] \tag{6.6}$$

where ξ_k is the Gaussian abscissas. $\mathbf{N}$ is,

$$\mathbf{N} = \begin{bmatrix} N_1 & 0 & N_2 & 0 & N_3 & 0 & N_4 & 0 \\ 0 & N_1 & 0 & N_2 & 0 & N_3 & 0 & N_4 \end{bmatrix} \tag{6.7}$$

and N_1-N_4 are shape functions, for example, $N_1 = (1-\xi)(1-\eta)/4$, with $-1 \leq \xi, \eta \leq 1$ being the local coordinate system.

Eq. 6.5 can be numerically integrated using the Gaussian quadrature rule,

$$\int_{\Gamma} g^2 (\mathbf{u})\, d\Gamma = \sum_{k=1}^{10} \omega_k g_k^2 \left|\mathbf{N}_* (\xi_k)\, \mathbf{c}\right| \left|\mathbf{N}_{,\xi} (\xi_k)\, \mathbf{c}\right| \tag{6.8}$$

where ω_k is the weight; $\mathbf{N}_{,\xi}$ is the derivative of $\mathbf{N}$ with respect to ξ and,

$$\mathbf{N}_* = \begin{bmatrix} N_1 & 0 & N_2 & 0 & N_3 & 0 & N_4 & 0 \\ 0 & 0 & 0 & 0 & 0 & 0 & 0 & 0 \end{bmatrix} \tag{6.9}$$

In this study, the number of the integration points is taken to be 10.

At a Gauss point, a penetration can be identified if the following condition holds,

$$\mathbf{n}_k \cdot (\mathbf{b}_k - \mathbf{d}_k) \leq 0 \tag{6.10}$$

where $\mathbf{d}_k$ is the projection points on the rigid surface from $\mathbf{b}_k$. If we denote d_k as the r-coordinate of $\mathbf{d}_k$, then $\mathbf{d}_k$ can be characterized by,

$$\mathbf{d}_k = \begin{bmatrix} d_k \\ f(d_k) \end{bmatrix} = \begin{bmatrix} d_k \\ z_S - \sqrt{R^2 - d_k^2} \end{bmatrix} \tag{6.11}$$

with z_S being the z'-coordinate of the center of the rigid sphere. $\mathbf{n}_k$ and $\mathbf{t}_k$ are the outward normal and tangential of the rigid sphere from the point $\mathbf{d}_k$ ($\mathbf{t}_k$ will appear in subsequent derivations). According to Fig. 6.1, they are given by,

$$\mathbf{n}_k = \frac{1}{R} \begin{bmatrix} d_k \\ -\sqrt{R^2 - d_k^2} \end{bmatrix}, \quad \mathbf{t}_k = \frac{1}{R} \begin{bmatrix} \sqrt{R^2 - d_k^2} \\ d_k \end{bmatrix} \tag{6.12}$$

The distance function g_k is positive only in the case of penetration, and is zero otherwise,

$$g_k = \begin{cases} |\mathbf{b}_k - \mathbf{d}_k|, \text{ if contact} \\ 0, \text{ otherwise} \end{cases} \tag{6.13}$$

The discretized version of the original problem therefore becomes,

$$\mathbf{\Pi}^h(\mathbf{u}) + \frac{\zeta}{2}\sum_{k=1}^{10}\left[\omega_k \left|\mathbf{N}(\xi_k)\,\mathbf{c} - \mathbf{d}_k\right|^2 \left|\mathbf{N}_*(\xi_k)\,\mathbf{c}\right| \left|\mathbf{N}_{,\xi}(\xi_k)\,\mathbf{c}\right|\right] \rightarrow \min \tag{6.14}$$

where $\mathbf{\Pi}^h(\mathbf{u})$ is discretized in Ω by standard finite element procedures.

The problem will be solved via Newton's method by applying variation and linearization to the discretized contact penalty term in Eq. 6.14.

6.2.2 Variation and Linearization

We can compute the minimum of Eq. 6.14 by variation,

$$\delta\mathbf{\Pi}^h(\mathbf{u}) + \delta\left[\frac{\zeta}{2}\sum_{k=1}^{10}\omega_k \left|\mathbf{N}(\xi_k)\,\mathbf{c} - \mathbf{d}_k\right|^2 \left|\mathbf{N}_{,\xi}(\xi_k)\,\mathbf{c}\right| \left|\mathbf{N}_*(\xi_k)\,\mathbf{c}\right|\right] = 0 \tag{6.15}$$

where δ is the variational operator.

The equation above also represents the weak form of the equilibrium which the displacement field has to fulfill. The variation of the first term follows the standard procedure. For linear elastic material,

$$\delta\mathbf{\Pi}^h(\mathbf{u}) = \delta\mathbf{u}^T\,\mathbf{K}\,\mathbf{u} \tag{6.16}$$

where,

$$\mathbf{K} = \int_\Omega \mathbf{B}_u^T\,\mathbf{D}^e\,\mathbf{B}_u\,d\Omega \tag{6.17}$$

Note that in this problem since there is no traction applied, the traction term is not seen in Eq. 6.16. The body force is also neglected in the formulation.

After applying the product rule to the second term in Eq. 6.15, we obtain,

$$\sum_{k=1}^{10}\frac{\zeta\omega_k}{2}\begin{bmatrix}\delta\left|\mathbf{N}(\xi_k)\,\mathbf{c} - \mathbf{d}_k\right|^2 \left|\mathbf{N}_{,\xi}(\xi_k)\,\mathbf{c}\right| \left|\mathbf{N}_*(\xi_k)\,\mathbf{c}\right| \\ +\left|\mathbf{N}(\xi_k)\,\mathbf{c} - \mathbf{d}_k\right|^2 \delta\left|\mathbf{N}_{,\xi}(\xi_k)\,\mathbf{c}\right| \left|\mathbf{N}_*(\xi_k)\,\mathbf{c}\right| \\ +\left|\mathbf{N}(\xi_k)\,\mathbf{c} - \mathbf{d}_k\right|^2 \left|\mathbf{N}_{,\xi}(\xi_k)\,\mathbf{c}\right| \delta\left|\mathbf{N}_*(\xi_k)\,\mathbf{c}\right|\end{bmatrix} \tag{6.18}$$

The three variations in the equation above could be further manipulated as follows,

$$\begin{aligned}\delta\left|\mathbf{N}\left(\xi_k\right)\mathbf{c}-\mathbf{d}_k\right|^2 &= 2\left[\mathbf{N}\left(\xi_k\right)\mathbf{c}-\mathbf{d}_k\right]\cdot\left[\mathbf{N}\left(\xi_k\right)\delta\mathbf{c}-\delta\mathbf{d}_k\right] \\ &= -2g_k\mathbf{n}_k\cdot\left[\mathbf{N}\left(\xi_k\right)\delta\mathbf{u}-\delta\mathbf{d}_k\right] \\ &= -2g_k\mathbf{n}_k\cdot\left[\mathbf{N}\left(\xi_k\right)\delta\mathbf{u}\right]\end{aligned} \tag{6.19}$$

$$\begin{aligned}\delta\left|\mathbf{N}_{,\xi}\left(\xi_k\right)\mathbf{c}\right| &= \frac{\mathbf{N}_{,\xi}\left(\xi_k\right)\mathbf{c}}{\left|\mathbf{N}_{,\xi}\left(\xi_k\right)\mathbf{c}\right|}\cdot\left[\mathbf{N}_{,\xi}\left(\xi_k\right)\delta\mathbf{c}\right] \\ &= \mathbf{t}_e\cdot\left[\mathbf{N}_{,\xi}\left(\xi_k\right)\delta\mathbf{u}\right]\end{aligned} \tag{6.20}$$

$$\begin{aligned}\delta\left|\mathbf{N}_{*}\left(\xi_k\right)\mathbf{c}\right| &= \frac{\mathbf{N}_{*}\left(\xi_k\right)\mathbf{c}}{\left|\mathbf{N}_{*}\left(\xi_k\right)\mathbf{c}\right|}\cdot\left[\mathbf{N}_{*}\left(\xi_k\right)\delta\mathbf{c}\right] \\ &= \mathbf{t}_*\cdot\left[\mathbf{N}_{*}\left(\xi_k\right)\delta\mathbf{u}\right]\end{aligned} \tag{6.21}$$

In the derivation for Eqs. 6.19-6.21, we set $\delta\mathbf{c}=\delta\mathbf{u}$ and $\mathbf{n}_k\cdot\delta\mathbf{d}_k=0$, which can be obtained from Eqs. 6.1 and 6.23, respectively. Since $\mathbf{d}_k$ also depends on the displacement field, we have to compute its variation as well,

$$\delta d_k = \nabla d_k\cdot\left[\mathbf{N}\left(\xi_k\right)\delta\mathbf{u}\right] \tag{6.22}$$

$$\delta\mathbf{d}_k = c_k\left(\mathbf{t}_k\otimes\mathbf{t}_k\right)\cdot\left[\mathbf{N}\left(\xi_k\right)\delta\mathbf{u}\right] \tag{6.23}$$

where,

$$\nabla d_k = \frac{h_k}{\sqrt{1+f'^2\left(d_k\right)}}\mathbf{t}_k = \frac{h_k}{1+f'^2\left(d_k\right)}\begin{bmatrix}1\\ f'\left(d_k\right)\end{bmatrix} \tag{6.24}$$

$$h_k = \frac{1+f'^2\left(d_k\right)}{1-f''\left(d_k\right)\left[z_k-f\left(d_k\right)\right]+f'^2\left(d_k\right)} \tag{6.25}$$

Now the problem in Eq. 6.15 becomes,

$$\mathbf{K}\mathbf{u}-\mathbf{f}_o=0 \tag{6.26}$$

where,

$$\mathbf{f}_o = \sum_{k=1}^{10} \zeta \omega_k g_k \left\{ \begin{array}{c} |\mathbf{N}_* (\xi_k)\, \mathbf{c}| \left[\begin{array}{c} -\dfrac{g_k}{2} \mathbf{N}_{,\xi}^T (\xi_k)\, \mathbf{t}_e \\ |\mathbf{N}_{,\xi} (\xi_k)\, \mathbf{c}|\, \mathbf{N}^T (\xi_k)\, \mathbf{n}_k \end{array} \right] \\ -\dfrac{g_k}{2} |\mathbf{N}_{,\xi} (\xi_k)\, \mathbf{c}|\, \mathbf{N}_*^T (\xi_k)\, \mathbf{t}_* \end{array} \right\} \tag{6.27}$$

$\mathbf{Ku}$ could be viewed as the internal force vector and $\mathbf{f}_o$ the external load from the indenter. Though the first term in Eq. 6.26 is linearly dependent on $\mathbf{u}$, the second term is not. Subsequent linearization is needed to determine the tangent matrix for the application of Newton's method. Here we start directly from Eq. 6.14 and derive the results for the penalty term,

$$\begin{aligned} &\Delta\delta \left[\frac{\zeta}{2} \sum_{k=1}^{10} \omega_k |\mathbf{N} (\xi_k)\, \mathbf{c} - \mathbf{d}_k|^2 |\mathbf{N}_{,\xi} (\xi_k)\, \mathbf{c}|\, |\mathbf{N}_* (\xi_k)\, \mathbf{c}| \right] = \\ &\frac{\zeta}{2} \sum_{k=1}^{10} \omega_k |\mathbf{N}_* (\xi_k)\, \mathbf{c}| \Big[\Delta\delta |\mathbf{N} (\xi_k)\, \mathbf{c} - \mathbf{d}_k|^2 |\mathbf{N}_{,\xi} (\xi_k)\, \mathbf{c}| \\ &+ |\mathbf{N} (\xi_k)\, \mathbf{c} - \mathbf{d}_k|^2 \Delta\delta |\mathbf{N}_{,\xi} (\xi_k)\, \mathbf{c}| \\ &+\delta |\mathbf{N} (\xi_k)\, \mathbf{c} - \mathbf{d}_k|^2 \Delta |\mathbf{N}_{,\xi} (\xi_k)\, \mathbf{c}| + \Delta |\mathbf{N} (\xi_k)\, \mathbf{c} - \mathbf{d}_k|^2 \delta |\mathbf{N}_{,\xi} (\xi_k)\, \mathbf{c}| \Big] \end{aligned} \tag{6.28}$$

where Δ is also a variational operator.

In the equation above, explicit expressions for the terms with only one operator (either Δ or δ) can be obtained following an analogous way to Eqs. 6.19 and 6.20. Explicit expressions of the terms with both operators are given as,

$$\Delta\delta |\mathbf{N} (\xi_k)\, \mathbf{c} - \mathbf{d}_k|^2 = 2 [\mathbf{N} (\xi_k)\, \delta\mathbf{u}]^T (\mathbf{I} - c_k \mathbf{t}_k \otimes \mathbf{t}_k) [\mathbf{N} (\xi_k)\, \Delta\mathbf{u}] \tag{6.29}$$

$$\Delta\delta |\mathbf{N}_{,\xi} (\xi_k)\, \mathbf{c}| = |\mathbf{N}_{,\xi} (\xi_k)\, \mathbf{c}|^{-1} [\mathbf{N}_{,\xi} (\xi_k)\, \delta\mathbf{u}]^T (\mathbf{I} - \mathbf{t}_e \otimes \mathbf{t}_e) [\mathbf{N}_{,\xi} (\xi_k)\, \Delta\mathbf{u}] \tag{6.30}$$

where $\mathbf{I}$ is the indentity matrix.

We then have,

$$\Delta\delta \left[\frac{\zeta}{2} \sum_{k=1}^{10} \omega_k |\mathbf{N} (\xi_k)\, \mathbf{c} - \mathbf{d}_k|^2 |\mathbf{N}_{,\xi} (\xi_k)\, \mathbf{c}|\, |\mathbf{N}_* (\xi_k)\, \mathbf{c}| \right] = \delta\mathbf{u}^T \mathbf{K}_c \Delta\mathbf{u} \tag{6.31}$$

where the tangent matrix $\mathbf{K}_c$ is,

$$\begin{aligned}\sum_{k=1}^{10} \zeta\omega_k \left|\mathbf{N}_*\left(\xi_k\right)\mathbf{c}\right| \Big\{ & \left|\mathbf{N}_{,\xi}\left(\xi_k\right)\mathbf{c}\right| \mathbf{N}^T\left(\xi_k\right)\left(\mathbf{I}-c_k\mathbf{t}_k\otimes\mathbf{t}_k\right)\mathbf{N}\left(\xi_k\right) \\ & - g_k\mathbf{N}^T\left(\xi_k\right)\left(\mathbf{n}_k\otimes\mathbf{t}_e\right)\mathbf{N}_{,\xi}\left(\xi_k\right) - g_k\mathbf{N}_{,\xi}^T\left(\xi_k\right)\left(\mathbf{t}_e\otimes\mathbf{n}_k\right)\mathbf{N}\left(\xi_k\right) \\ & + \frac{g_k^2}{2}\left|\mathbf{N}_{,\xi}\left(\xi_k\right)\mathbf{c}_I\right|^{-1}\mathbf{N}_{,\xi}^T\left(\xi_k\right)\left(\mathbf{I}-\mathbf{t}_e\otimes\mathbf{t}_e\right)\mathbf{N}_{,\xi}\left(\xi_k\right)\Big\}\end{aligned} \tag{6.32}$$

Now an iteration procedure can be established to solve Eq. 6.26. To advance from load step n to $n+1$, where an incremental displacement Δd is applied, the iteration scheme starts by calculating an initial value for $\mathbf{K}\mathbf{u}^{(0)}$ and $\mathbf{f}_o^{(0)}$ based on the displacement field at load step n and the current indentation depth, respectively. In the $\ell-$th iteration cycle ($\ell = 1, 2, 3\ldots$), with displacement $\mathbf{u}^{(\ell-1)}$ known, a residual between the external and internal force vectors can be determined,

$$\mathbf{r}^{(\ell)} = \mathbf{K}\mathbf{u}^{(\ell-1)} - \mathbf{f}_o^{(\ell-1)} \tag{6.33}$$

which must vanish in order to meet the equilibrium condition. Displacement at nodal points needs to be updated in order to eliminate the residual,

$$\left[\mathbf{K}+\mathbf{K}_c^{(\ell)}\right]\left\{\mathbf{u}^{(\ell)}-\mathbf{u}^{(\ell-1)}\right\} = -\mathbf{r}^{(\ell)} \tag{6.34}$$

Calculation is terminated when $\left|\mathbf{u}^{(\ell)}-\mathbf{u}^{(\ell-1)}\right| < \epsilon$, where ϵ is the tolerance.

It should be mentioned that though the term $\left|\mathbf{N}_*\left(\xi_k\right)\mathbf{c}\right|$ in Eq. 6.28, which actually represents the radial coordinate of the material point k, is not involved in the linearization process, the tangent stiffness $\mathbf{K}_c$ still works relatively well and the convergence speed is relatively fast. This could be explained by the fact that radial displacement is relatively small during the spherical indentation process, so the linearization on $\left|\mathbf{N}_*\left(\xi_k\right)\mathbf{c}\right|$ could be neglected.

6.2.3 Coupling with Poro-elasto-plasticity

Since the structure of Eq. 6.34 is analogous to the FEM formulation for poro-elasto-plasticity in Chapter 5, coupling between the two can be realized as follows,

$$\begin{bmatrix} \mathbf{K}_t^{(\ell)} + \mathbf{K}_c^{(\ell)} & -\mathbf{Q} \\ -\mathbf{Q}^T & -(\mathbf{Stab} + \mathbf{S} + \theta \Delta t \mathbf{H}) \end{bmatrix} \begin{Bmatrix} \mathbf{u}^{(\ell)} - \mathbf{u}^{(\ell-1)} \\ \mathbf{p}^{(\ell)} - \mathbf{p}^{(\ell-1)} \end{Bmatrix} = -\mathbf{r}^{(\ell)} \tag{6.35}$$

where the residual is given by,

$$\mathbf{r}^{(\ell)} = \mathbf{f}_{in}^{(\ell)} - \mathbf{f} - \begin{Bmatrix} \mathbf{f}_o^{(\ell-1)} - \mathbf{f}_{o,n} \\ \mathbf{0} \end{Bmatrix} \tag{6.36}$$

Residual in this case consists of three terms, i.e., an external incremental force vector due to the indentation action, $\mathbf{f}_o^{(\ell-1)} - \mathbf{f}_{o,n}$, an external incremental force/flux vector $\mathbf{f}$ due to Neumann boundaries and $\Delta t \mathbf{H} \mathbf{p}_n$, and an internal incremental force/flux vector $\mathbf{f}_{in}^{(\ell)}$. Detailed expressions for $\mathbf{f}_{in}^{(\ell)}$ and $\mathbf{f}$ and the submatrices in Eq. 6.35 can be found in Eqs. 5.10 and 5.25.

6.3 Validation of the Contact Scheme

Validity of the contact scheme is examined with an example case of poroelastic indentation. The indentation action at the undrained limit is realized by setting the time increment to zero in the finite element equations while ramping the indentation depth up to the prescribed value in small increments. In order to maximize the discrepancy caused by the radial displacement on the surface between the two modeling approaches, we set $\nu = 0$ and $\nu_u = 0.5$ ($K_s \to \infty$ and $K_f \to \infty$) while keeping the other material properties the same as those in Table 5.1 and the geometry of the numerical model the same as in Section 5.4.1.

The penalty stiffness ζ is first set to be 200 times of the Young's modulus of the domain, i.e., $\zeta = 370.6$ GPa. Denote δ_d as the ratio between the penetration distance of the material point originally at the contact origin and the prescribed indentation depth at the end of the ramping up stage. At this ζ value, $\delta_d = 0.31\%$ and the indentation force is $F(0) = 492.8$ N,

very close to the analytical prediction, $F(0) = 494.1$ N.

Additional simulations with $\zeta = 37$, 555.9 and 741.2 GPa are conducted to analyze the effect of the penalty stiffness. Significant convergence issues occur when $\zeta = 741.2$ GPa. We may attribute this to the fact that increase in ζ has led to an ill-conditioned equation system. When $\zeta = 37$ and 555.9 GPa, we have $\delta_d = 5.1\%$, 0.23% and $F(0) = 461$, 493.3 N, respectively. As δ_d with $\zeta = 370.6$ or 555.9 GPa is an order smaller than that with $\zeta = 37$ GPa, both $\zeta = 370.6$ and 555.9 GPa can be viewed as suitable choices for our particular problem. Subsequent numerical calculations are conducted with $\zeta = 370.6$ GPa.

Displacements of the nodal points on the surface during both the ramping up stage and the transient consolidating phase are tracked. For the surface drainage conditions, while there is no ambiguity in modeling the fully permeable or impermeable surface, the mixed case III surface drainage condition can be treated in different ways. Here we choose to set the nodes on the initially free surface as impermeable once a contact is detected; otherwise, they are permeable.

An example with case III surface drainage condition is shown in Fig. 6.2. The displaced surface profiles are constructed by updating coordinates of the nodal points with their displacements, namely, $z_* + u_z/a \to z_*$ and $r_* + u_r/a \to r_*$, where $a = \sqrt{Rd}$ denotes the nominal contact radius. We can observe that material points over the contact area now conform to the shape of the spherical indenter during not only the ramping up stage ($d = 0.02$, 0.04, 0.06, 0.08, 0.1 mm) but also the transient consolidation phase when the indenter is held at $d = 0.1$ mm. Within the contact region, there is negligible overlap and no vertical separation between the surface of the half-space and the rigid sphere. During the ramping up stage, since $\nu_u = 0.5$, radial displacement is zero everywhere on the surface. However, during the transient phase, all the material points do move radially inwards. Difference in their trajectories according to the Hertzian solution and from the numerical simulation with the contact scheme incorporated can be clearly identified, see inset in Fig. 6.2 showing the comparison for a material point initially at $r_* = 0.95$ and $z_* = 0$. Outside of the contact area, trajectories of the material points marked by the green dots indicate that the free surface rises and subsides during the transient phase. Consequently, the contact radius actually varies over time.

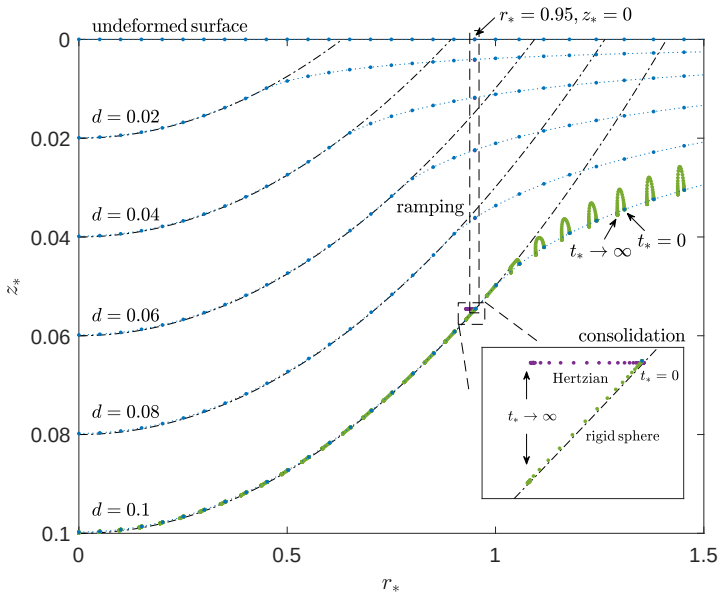

Figure 6.2: Displaced surface profiles and movement of the material points on the surface during the ramping up stage from $d = 0$ mm to $d = 0.02$, 0.04, 0.06, 0.08, 0.1 mm and the transient consolidation phase at $d = 0.1$ mm from numerical simulations with $\nu = 0$. The indenter profile is marked by the dash-dot black lines; profile of the surface is marked by the blue dotted lines. During the transient phase, trajectories of the material points are marked as green. The inset shows a comparison of the trajectories of a material point, initially at $r_* = 0.95$ and $z_* = 0$, according to the Hertzian solution and from the numerical simulation with the contact scheme during the transient phase.

6.4 Poroelastic Indentation

6.4.1 Undrained and Drained Limits

To examine how the indentation force is affected by the incorporation of the contact scheme, we first look at the indentation force at the undrained and drained limits. Denote δ_{f0} and $\delta_{f\infty}$ as the relative error between the theoretical and numerical solutions at the two limits,

$$\delta_{f0} = \frac{F_{\text{num}} - F(0)}{F(0)} \tag{6.37}$$

$$\delta_{f\infty} = \frac{F_{\text{num}} - F(\infty)}{F(\infty)} \tag{6.38}$$

where F_{num} is the indentation force at the undrained or drained limit from the numerical simulation with the contact scheme. $F(0)$ and $F(\infty)$ are the undrained and drained force asymptotes from the theoretical solution, see Eq. 5.56.

It can be shown that δ_{f0} and $\delta_{f\infty}$ are affected by the indentation strain d/R and the Poisson's ratios, ν_u for δ_{f0} and ν for $\delta_{f\infty}$, respectively, see Fig. 6.3. Change in the undrained Poisson's ratio in Fig. 6.3(a) is realized by varying K_s and K_f. With those listed in Table 5.1, $K_s = 34$ GPa and $K_f = 2.25$ GPa, give $\nu_u = 0.449$ and $\omega = 0.417$; $K_s = K_f = 2.28$ GPa gives $\nu_u = 0.35$ and $\omega = 0.2$; and $K_s = K_f = 1.26$ GPa gives $\nu_u = 0.25$ and $\omega = 0.039$.

At the undrained limit, Fig. 6.3(a) shows when ν_u is relatively small (e.g., $\nu_u = 0.25$), the discrepancy between the numerical and theoretical solution increases with d/R; now $F_{\text{num}} > F(0)$. At $\nu_u = 0.5$, magnitude of δ_{f0} still increases with the depth, but $F_{\text{num}} < F(0)$ at all depth. Meanwhile, at $\nu_u = 0.35$ and 0.449, variation of δ_{f0} with depth is non-monotonic. Similar trends can also be observed at the drained limit in Fig. 6.3(b).

Dependence of δ_{f0} and $\delta_{f\infty}$ on d/R and the Poisson's ratios highlights the two underlying reasons for the discrepancy between the numerical and theoretical solutions. One is the Hertzian assumption of using a parabola to approximate the spherical shape. Fig. 6.4 shows the surface displacement profiles at the undrained/drained limits with three different Poisson's ratios at $d/R = 0.01$ and 0.2, plotted according to our theoretical solution and compared with the

spherical shape. When $\nu_u = 0.5$ or $\nu = 0.5$, the radial displacement on the surface is zero, and there is a gap between the deformed surface and the sphere in the outer part of the contact region. While the gap may be negligible at $d/R = 0.01$, it becomes appreciable at $d/R = 0.2$. As a result, F_{num} is consistently smaller than the theoretical value and the discrepancy increases with the indentation strain. The other reason is that when the Poisson's ratio becomes small, the deformed surface actually penetrates the hypothetical sphere. Additional force would therefore be needed in rigid sphere loading in order to enforce the contact area to conform to the spherical shape, which explains $F_{\text{num}} > F(0)$. This effect is maximized when ν_u or $\nu = 0$. Combination of these two reasons gives rise to the non-monotonic trends at the intermediate Poisson's ratios. At a given indentation strain, the fact that the absolute magnitudes of δ_{f0} and $\delta_{f\infty}$ at $\nu_u = 0$ or $\nu = 0$ are larger than those at $\nu_u = 0.5$ or $\nu = 0.5$ suggests that the discrepancy caused by the inward radial displacement is relatively more pronounced.

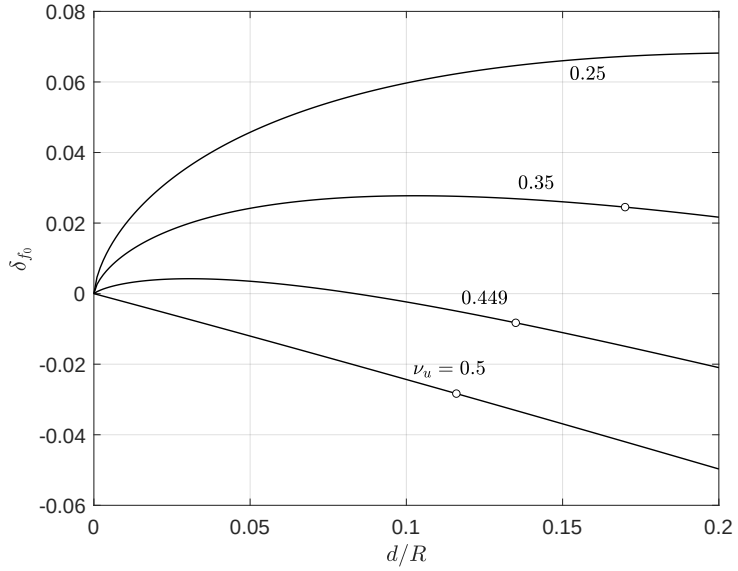

(a) undrained limit

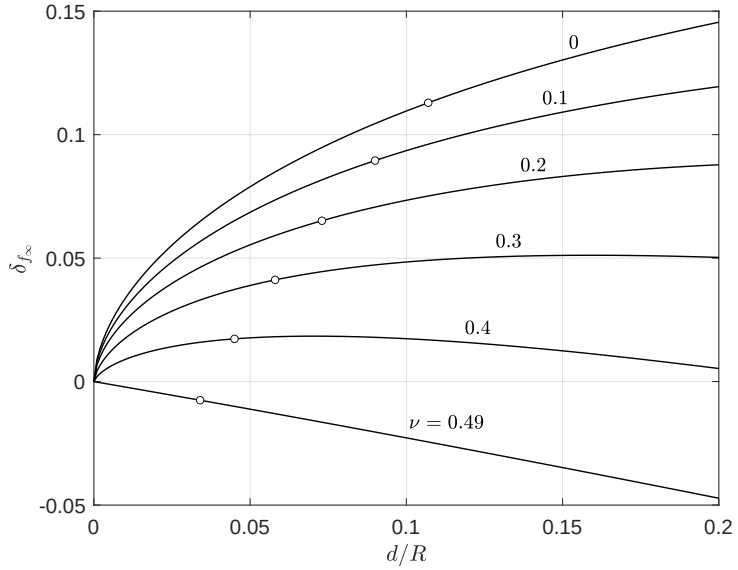

(b) drained limit

Figure 6.3: Variation of δ_{f0} and $\delta_{f\infty}$ as a function of d/R and ν_u or ν. The dots mark the indentation depth below which strain components are smaller than 0.1.

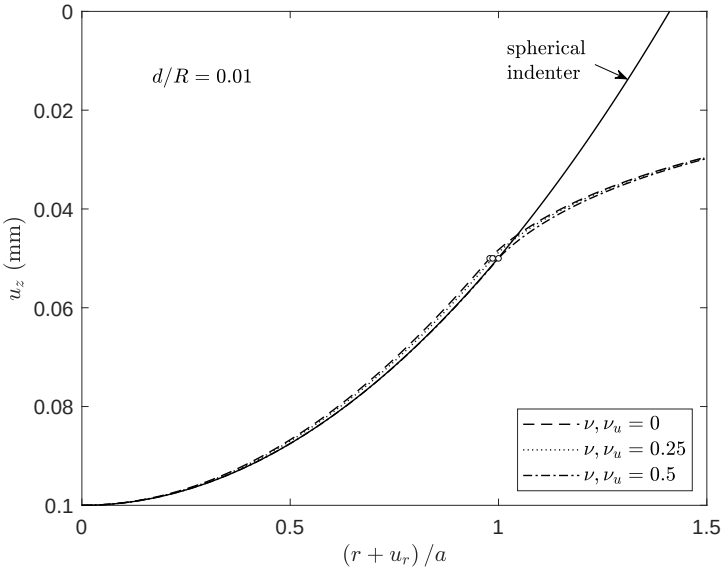

(a) $d/R = 0.01$

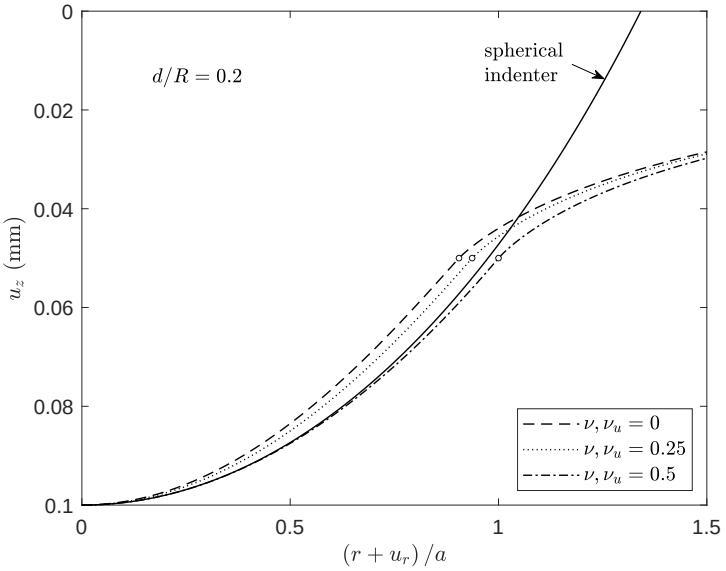

(b) $d/R = 0.2$

Figure 6.4: Surface displacement profiles at the undrained/drained limits with three different Poisson's ratios. Profile of the rigid sphere is marked by the solid line and the material point at the contact edge by the empty circles.

6.4.2 Transient Response

Incorporating the frictionless contact scheme to replace the boundary condition of step displacement loading has not introduced any additional physical parameter into the problem. It therefore follows from dimensional analysis that ω remains the sole material parameter affecting the normalized transient force response. For step displacement loading, the governing role of ω has been verified by the numerical simulations with material properties in sets i - iv ($\omega = 0.56$) in Section 5.6.1, $d/R = 0.01$ and case III surface drainage condition. Note that in set iv, both the solid and fluid phases are compressible. For rigid sphere loading, the critical role of ω is once again shown with these four sets at $d/R = 0.01$ and case III drainage condition, see Fig. 6.5 showing a comparison of the normalized transient force responses from the simulations with the theoretical results at $\omega = 0$ and 0.56. Though the undrained and drained force asymptotes differ among these four simulations, the normalized force relaxation curves collapse into one with only some discrepancies at large time, likely due to the drainage boundary effect as shown in Section 5.6.1.

Denote $\delta_{t_*0.5}$ as a measure for the degree of discrepancy between a numerical solution and the theoretical solution at a particular ω ,

$$\delta_{t_*0.5} = \frac{t_{*0.5\text{num}} - t_{*0.5\text{theo}}}{t_{*0.5\text{theo}}}$$

where $t_{*0.5}$ is the dimensionless time at which $F_n = 0.5$. For these four simulations, if compared with $t_{*0.5\text{theo}} = 0.333$ at $\omega = 0$, we have $\delta_{t_*0.5} = -2.16\%$, -2.16%, -1.51% and -1.29%, respectively. However, if compared with $t_{*0.5\text{theo}} = 0.298$ at $\omega = 0.56$, $\delta_{t_*0.5} = 9.3\%$, 9.3%, 10.1% and 10.3%. This means that the numerical results are in fact closer to the theoretical solution at $\omega = 0$ than that at $\omega = 0.56$.

To investigate the effect of ω on the transient force relaxation response in general, we conduct the numerical simulations with incompressible constituents ($\nu_u = 0.5$) and a small indentation strain ($d/R = 0.01$) at $\omega = 0.02$, 0.5, 1 ($\nu = 0.49$, 0.25, 0). Note that transient behavior at $\omega = 0$ is only meaningful mathematically as a limit. That is why the lower bound of ω is

chosen to be $\omega = 0.02$ in the numerical simulation. With the choice of $\nu_u = 0.5$, discrepancy between the numerical and theoretical solutions can therefore be attributed primarily to the drained Poisson's ratio ν. Fig. 6.7 shows a comparison of numerical results with cases I, II and III surface drainage condition and the theoretical solutions at $\omega = 0$ and 1. Overall, the three series of numerical simulations are in rather good agreement with the theoretical solutions. This indicates that the assumption of a fixed contact radius when deriving our theoretical solution is valid, provided that the indentation strain is small. We can also draw a few interesting observations. First of all, the numerical results appear to show an even weaker dependence on ω than the theoretical solutions. Secondly, the numerical results are rather close to the theoretical curve of $\omega = 0$. At $t_* > 1$, the numerical results relax slightly faster than the theoretical case of $\omega = 0$.

Variation of $\delta_{t_*0.5}$ with d/R with the theoretical solution from $\omega = 0$, 0.5 and 1 chosen as the reference is shown in Fig. 6.6. The results clearly indicate that at $d/R \leq 0.01$, where the Hertzian assumption is applicable, $\delta_{t_*0.5}$ determined according to $t_{*0.5\text{theo}}$ at $\omega = 0$, 0.5 and 1 remains nearly constant at about -2.5%, 10% and 17%, respectively. Fig. 6.6 gives further evidences that the force relaxation curves from rigid sphere loading are relatively insensitive to ω and among the three theoretical references ($\omega = 0$, 0.5 and 1), the solution with $\omega = 0$ gives the best approximation when d/R is relatively small.

Meanwhile, at small indentation strain, $\delta_{t_*0.5}$ being positive with $t_{*0.5\text{theo}}$ at $\omega = 0.5$ and 1 as the reference suggests that the force relaxation response as measured at $t_{*0.5}$ is slightly slower in the numerical model with $\omega = 0.5$ and 1 as a result of rigid sphere loading. This could be explained by the fact that at these ω values, the surface material points from rigid sphere loading undergo a downward movement during the transient stage (see Fig. 6.2), additional excess pore pressure is generated as a result, which could slow down the relaxation process. At $\omega \backsimeq 0$, since the radial displacement is close to zero during both the ramping up and consolidation stages, the poroelastic responses resulting from the rigid sphere and step displacement loadings are almost identical. Consequently, the force relaxation curves at $\omega \backsimeq 0$ between the two loading methods agree well.

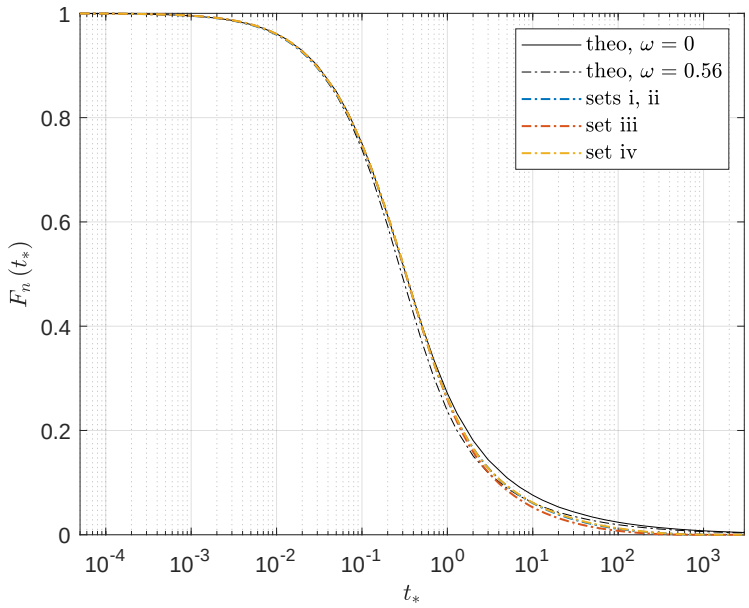

Figure 6.5: Comparison of the force relaxation curves between the poroelastic theoretical solution ($\omega = 0$, 0.56, marked with "theo") and numerical simulations conducted with sets i - iv parameters ($\omega = 0.56$); $d/R = 0.01$ and case III drainage condition.

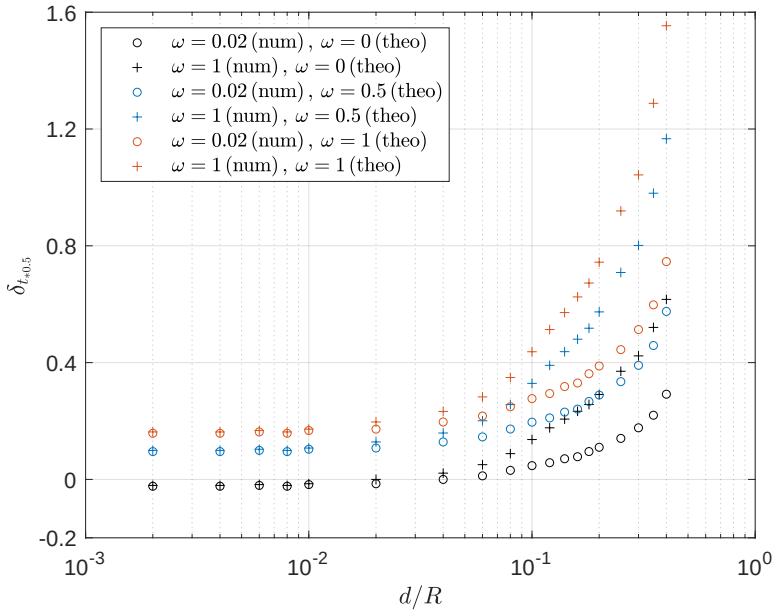

Figure 6.6: Variation of $\delta_{t_*0.5}$ with the indentation strain d/R.

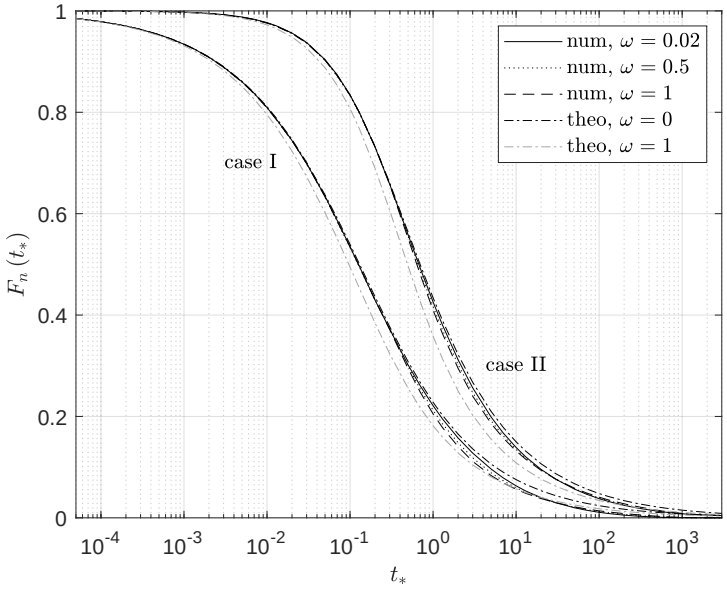

(a) case I and II surface drainage conditions

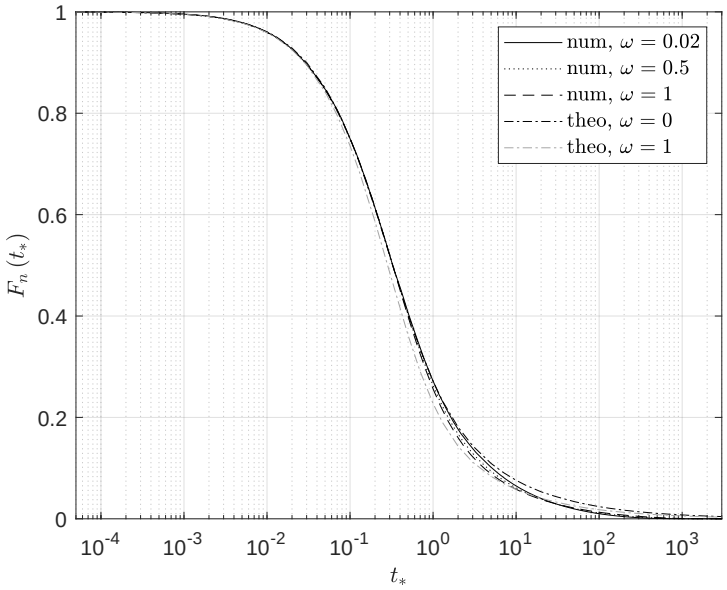

(b) case III surface drainage conditions

Figure 6.7: Relaxation of the normalized indentation force with case I, II and III surface drainage conditions: comparison between the numerical results with rigid sphere loading ("num") and the theoretical solution.

Further increase of d/R leads to significant increase in $\delta_{t_*0.5}$, suggesting that the theoretical solutions are no longer applicable. This could be attributed to the fact that the Hertzian assumption in approximating the spherical shape by a parabola is no longer valid at large indentation strain.

From a practical stand point, we may conclude that the theoretical force relaxation curve at $\omega = 0$ could be a suitable master curve for the entire range of ω in rigid sphere loading as long as the indentation strain is relatively small, e.g., $d/R \leq 0.05$. Similar conclusions can also be drawn for cases I and II surface drainage conditions.

6.5 Poro-elasto-plastic Indentation

Effect of plasticity on the spherical indentation process is now reanalyzed by modeling the indentation action using the frictionless contact scheme outlined in Section 6.2. We aim to examine: 1) how the elasto-plastic response changes when the load is applied via a rigid sphere since the removal of the stress singularity at the contact edge is likely to have an impact on the plastic deformation; 2) whether the criteria to define the four types of behaviors are still applicable. Numerical simulations will be carried out with case III surface drainage condition and two different Poisson's ratios; one is $\nu = 0.22$, as previously used in Section 5.7 for the simulations with step displacement loading, and the other is $\nu = 0.45$. The other properties are chosen based on those of the Gulf of Mexico shale in Table 5.1. We assume incompressibility in the constituents, which allows us to stay on the less conservative side as far as yielding is concerned. Geometry of the numerical model and boundary conditions, except for the indentation action, remain the same as described in Section 5.4.1.

6.5.1 Numerical Results with $\nu = 0.22$

Two series of numerical simulations are performed with $d = 0.1$ mm and $R = 10$ mm. Cohesion of the porous medium is chosen from $c_0 = 0.05 - 46$ MPa, which covers the range of $c_0/G = 0.0001 - 0.06$. Friction and dilatancy angles for each series are taken as follows,

- series $\dagger$: $\varphi = \psi = 20^\circ$
- series $\ddagger$: $\varphi = 20^\circ, \psi = 0^\circ$

In addition, for each poro-elasto-plastic case, an elasto-plastic simulation is conducted as a reference for results at the drained limit. To facilitate analysis, we denote $\eta_\varepsilon = \varepsilon^p_{\max}(0)/\varepsilon^p_{\max}(\infty)$ as the ratio of the maximum equivalent plastic strains at the undrained and drained limits, $\eta_f = F(0)/F(\infty)$ as the ratio between the undrained and drained force asymptotes, and $\eta_* = F(0)/F_*$ as the ratio of the undrained force asymptote over the indentation force F_* from the elasto-plastic simulation.

Figs. 6.8-6.11 show the simulation results for Series $\dagger$ with the surface being loaded by a rigid sphere via the contact scheme. There are several notable differences if we compare these results with those from step displacement loading in Section 5.7.2. Firstly, with the removal of the kink in the surface displacement profile, the ratio of the maximum plastic strain remains $\eta_\varepsilon = 1$ at $c_0 \geq 3$ MPa, instead of $c_0 \geq 15$ MPa. Secondly, at $3 \leq c_0 < 11$ MPa, though $\eta_\varepsilon = 1$, the location of $\varepsilon^p_{\max}$ at the undrained state at the prescribed indentation depth is no longer at $r = 0$ and $z/a \backsimeq 0.55$ as predicted by the poroelastic solution. Note that here $a = \sqrt{Rd}$ denotes the nominal contact radius. Denote P_0 as the point where onset of plasticity occurs according to the poroelastic solution and P as the location of $\varepsilon^p_{\max}$ at the undrained state from the numerical simulation. At $3 \leq c_0 < 11$ MPa, point P has moved away from point P_0, but remains inside of the half-space and no longer reaches to the contact edge, see Figs. 6.12 and 6.13. Finally, removal of the kink in the surface displacement profile has also affected the plastic accumulation and pore pressure dissipation characteristics as the force relaxation curves are now mostly to the right of the theoretical curve at $\omega = 0$ except at the early time.

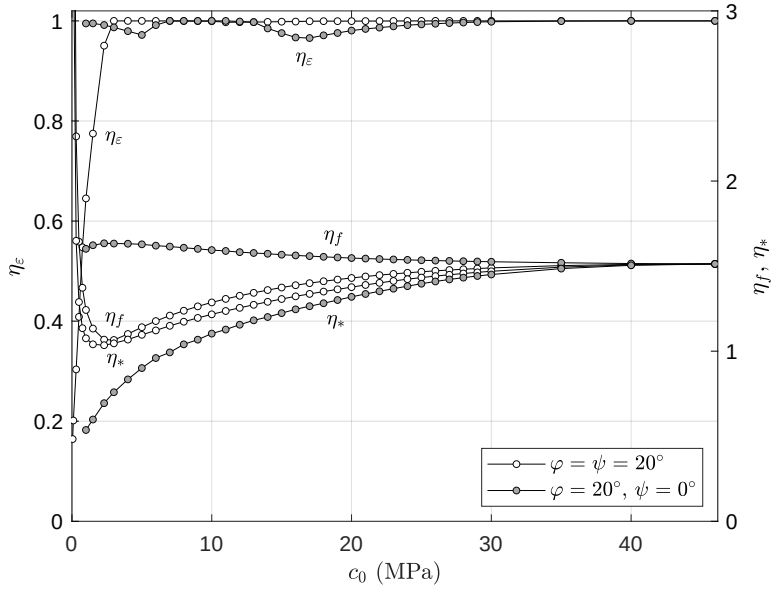

Figure 6.8: Series ⊦: $\varphi = \psi = 20°$, series ⊧: $\varphi = 20°$, $\psi = 0°$; Effect of cohesion on the ratios of the equivalent plastic strain η_ε and force asymptotes η_f and η_*.

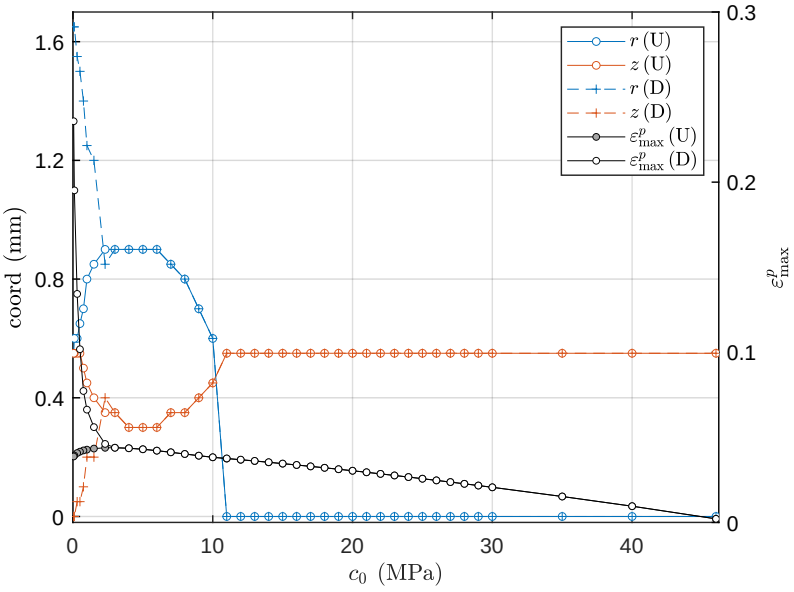

Figure 6.9: Series ⊦: Effect of cohesion on the location and magnitude of the maximum equivalent plastic strain $\varepsilon^p_{\max}$; U - undrained limit, D - drained limit.

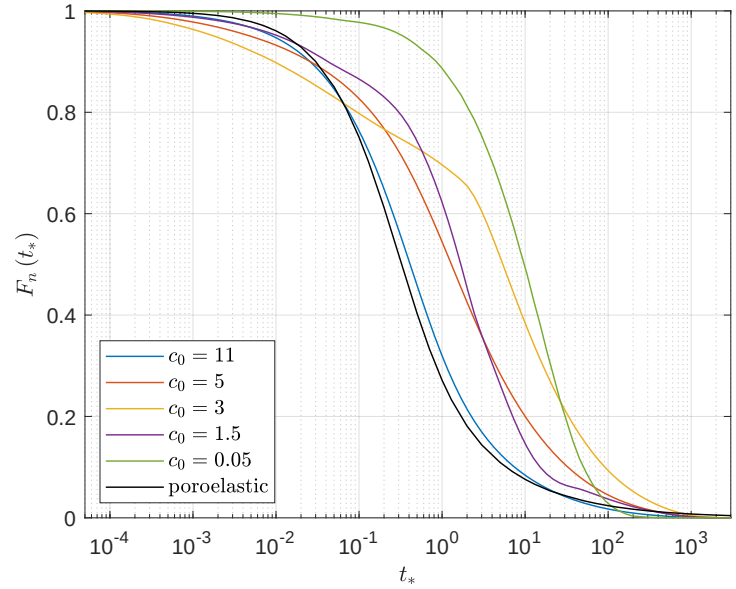

Figure 6.10: Series ϟ: Comparison of the force relaxation curves between the theoretical solution at $\omega = 0$ and the numerical results with $c_0 = 0.05$, 1.5, 3, 5 and 11 MPa.

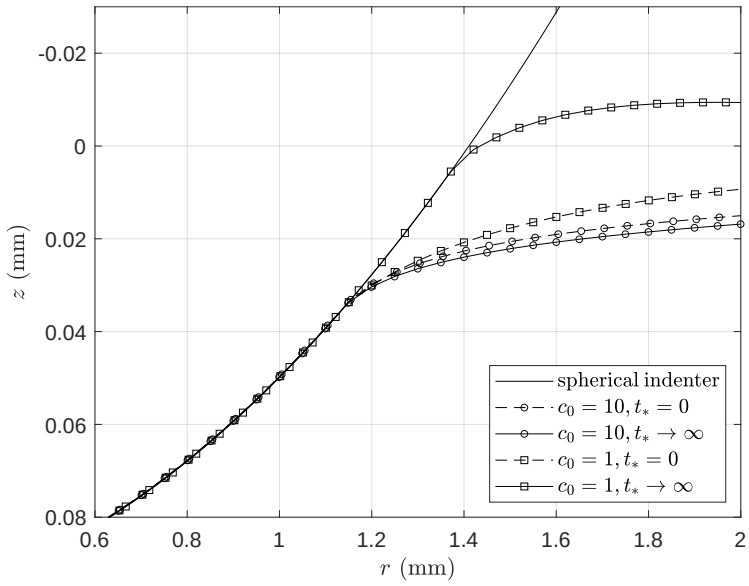

Figure 6.11: Series ϟ: Surface displacement profiles at the undrained and drained states with $c_0 = 1$ and 10 MPa.

Observations above allow us to still apply the same principles we used in Section 5.7.2 to classify the four types of indentation responses. However, we can no longer use $\eta_\varepsilon = 1$ alone to indicate that the normalized transient force response can be approximated as poroelastic. Instead, we need to include $P = P_0$ as part of the criterion. Consequently, for Series ǂ, the ranges of cohesion for the four types of indentation responses are,

- Type I: $29 \leqslant c_0 \leqslant 46.9$ MPa ($0.038 \leqslant c_0/G \leqslant 0.062$)
- Type II: $11 \leqslant c_0 < 29$ MPa ($0.014 \leqslant c_0/G < 0.038$)
- Type III: $3 \leqslant c_0 < 11$ MPa ($0.004 \leqslant c_0/G < 0.014$)
- Type IV: $c_0 < 3$ MPa ($c_0/G < 0.004$)

When $29 \leqslant c_0 \leqslant 46.9$ MPa, $\eta_f \simeq \eta_*$, $\eta_\varepsilon = 1$ and $P = P_0$. In this regime, plastic yielding has little influence on the overall indentation response. Both the force asymptotes at the undrained and drained limits and the transient response are not much affected.

When $11 \leqslant c_0 < 29$ MPa, $\eta_f > \eta_*$, $\eta_\varepsilon = 1$ and $P = P_0$. Plastic deformation has caused the force asymptotes to be smaller than those from the poroelastic solutions. Nevertheless, as can be see from Fig. 6.10, at $c_0 = 11$ MPa, which is the lower bound of Type II, the force relaxation curve is still rather close to the theoretical solution with $\omega = 0$. In both Types I and II, the plastic zone develops immediately at the undrained limit, but remains contained inside the half-space, and there is no additional plastic strain accumulation during the transient phase. Therefore, from a practical stand point, the normalized force relaxation response in both Types I and II can be approximated as poroelastic.

When $3 \leqslant c_0 < 11$ MPa, $\eta_f > \eta_*$, $\eta_\varepsilon = 1$ and $P \neq P_0$. Results from a representative case with $c_0 = 10$ MPa at four dimensionless times, $t_* = 0$, 0.1, 1 and 10, are shown in Fig. 6.12. From top to bottom, they are contour plots of the normalized equivalent plastic strain and pore pressure and the vector plot of the normalized flux field, e.g., $p_n = (p - p_{\min}) \,/\, (p_{\max} - p_{\min})$ and $\varepsilon^p_n = \varepsilon^p / \varepsilon^p_{\max}$. Unless otherwise noted, the plot window size is 5×5 mm for ε^p_n and p_n and 2×2 mm for the flux field. The contour interval is 0.05. Contours for $\varepsilon^p = 0$ and $p = 0$ as marked

by the black lines are added. Location of the maximum flux vector is marked by a red dot. Compared with the results from step displacement loading, see Fig. 5.13, the maximum plastic strain $\varepsilon^p_{\max}$ remains constant instead of increasing with time. With the plastic deformation being contained, the surface displacement exhibits a sink-in type of behaviors, see Fig. 6.11. The surface subsides slightly as pore pressure dissipates with time. At $t_* = 0$, because $\varepsilon^p_{\max}$ is smaller with rigid sphere loading, magnitude of negative pore pressure is also smaller. The maximum flux still occurs at the contact edge. However, the edge of the contact has increased from $r_* = 1$ to around $r_* = 1.15$. In addition, $q_{\max}$ at $t_* = 0$ and 0.1 is slightly smaller than those with step displacement loading. The reasons for the slower dissipation process after the early time as shown in Fig. 6.10 can be attributed to the combination of a few factors, namely, no additional material weakening from plastic strain accumulation, increase in the impermeable contact area with time, and the decrease in the flux magnitude near the contact edge.

When $c_0 < 3$ MPa, $\eta_f > \eta_*$, $\eta_\varepsilon < 1$ and $P \neq P_0$. In this regime, plastic deformation becomes uncontained, see the equivalent plastic strain contour plot in Fig. 6.13 with $c_0 = 1$ MPa. Dominance of plastic deformation is reflected by the "pile-up" behavior in the surface displacement profile shown in Fig. 6.11. As plastic strain accumulates with time, the free surface rises up substaintially, resulting in rather significant increase in the contact radius. However, since the surface profile is now smooth with the frictionless contact scheme, $\varepsilon^p_{\max}$ in this case is much smaller than their counterpart with step displacement loading.

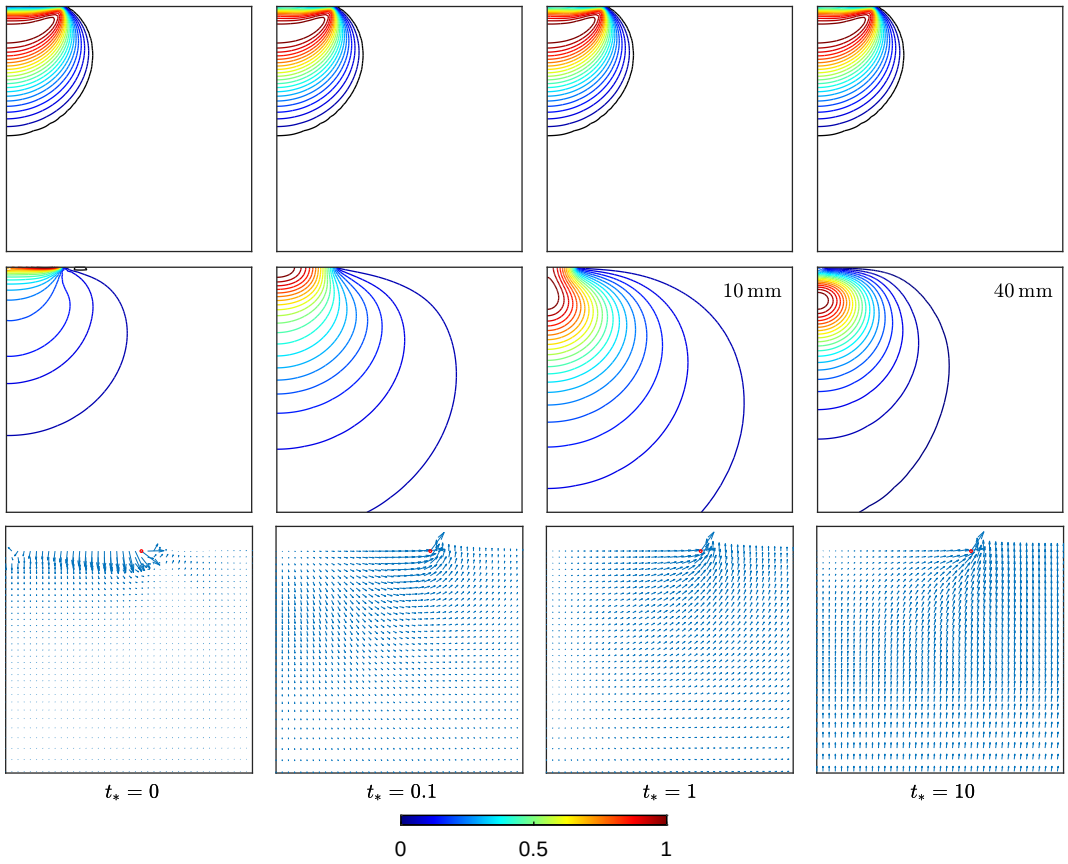

Figure 6.12: Series ϟ, $c_0 = 10$ MPa; from top to bottom - normalized equivalent plastic strain ε_n^p, pore pressure p_n and fluid flux at $t_* = 0$, 0.1, 1 and 10; at these times, $\varepsilon^p_{\max} = 0.0382$, 0.0382, 0.0382, 0.0382, $p_{\min} = -0.491$, -0.0126, -0.0092, -0.0034 MPa, $p_{\max} = 74.7706$, 28.243, 5.251, 0.513 MPa, and $q_{\max} = 6.11 \times 10^{-2}$, 9.31×10^{-3}, 1.83×10^{-3}, 5.53×10^{-5} mm/s; top and middle - contour interval: 0.05, plot window size: 5×5 mm unless otherwise noted; contours of $\varepsilon^p = 0$ and $p = 0$ marked by black lines; bottom: plot window size: 2×2 mm. Location of the maximum flux vector is marked by a red dot.

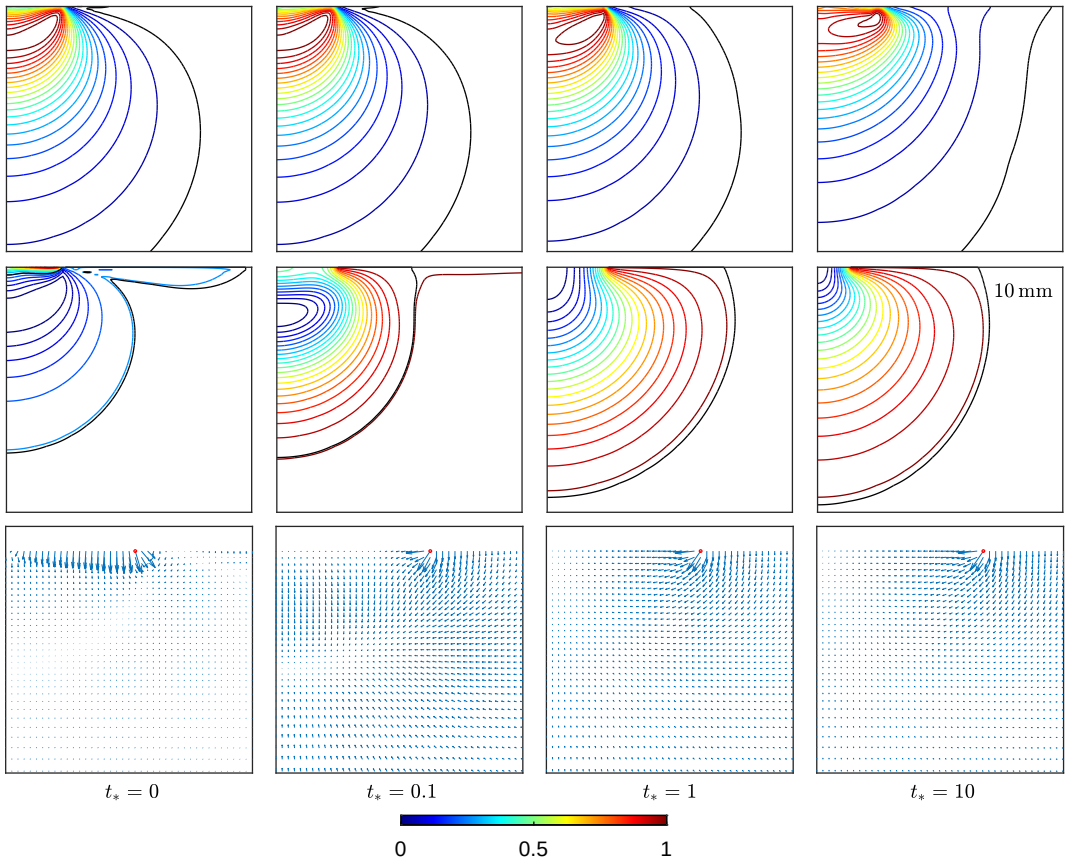

Figure 6.13: Series ϟ, $c_0 = 1$ MPa; from top to bottom - normalized equivalent plastic strain ε_n^p, pore pressure p_n and fluid flux at $t_* = 0$, 0.1, 1 and 10; for these times, $\varepsilon^p_{\max} = 0.0427$, 0.0427, 0.0451, 0.0617, $p_{\min} = -12.639$, -10.551, -6.656, -1.127 MPa, $p_{\max} = 31.35$, 0.557, 0.261, 0.048 MPa, and $q_{\max} = 4.694 \times 10^{-2}$, 4.522×10^{-3}, 2.856×10^{-3}, 4.695×10^{-4} mm/s; contours of $\varepsilon^p = 0$ and $p = 0$ marked by black lines.

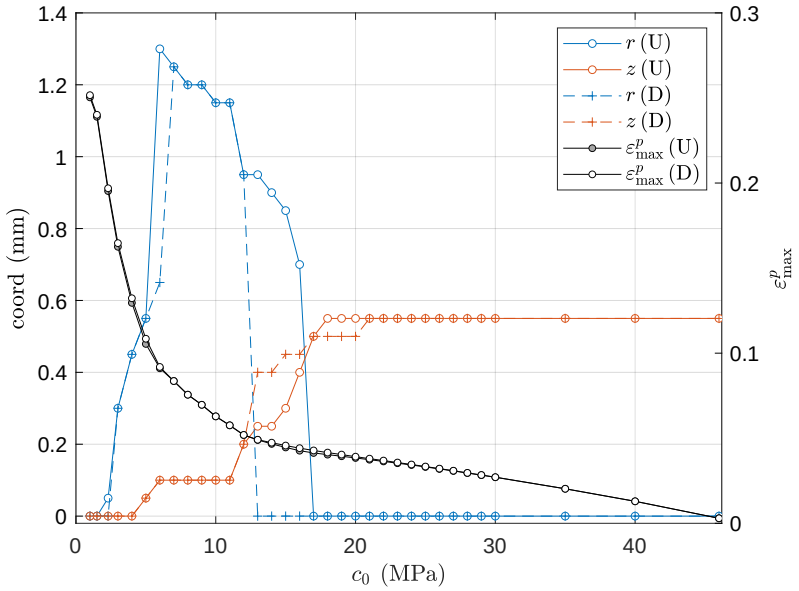

Figure 6.14: Series ɾ: Effect of cohesion on the location and magnitude of the maximum equivalent plastic strain $\varepsilon^p_{\max}$; U - undrained limit, D - drained limit.

For a non-associative material (Series ɾ), the poro-elasto-plastic response to spherical indentation can still be distinguished based on the criteria outlined above. The corresponding threshold cohesion values are now $c_0 = 46.9$, 40, 18 and 4 MPa ($c_0/G = 0.062$, 0.053, 0.024 and 0.005), see Figs. 6.14-6.15. Most characteristics of the poro-elasto-plastic behaviors in this series are similar to the non-associative cases with step displacement loading except those in Type IV. When $c_0 \leq 4$ MPa, with rigid sphere loading, $\varepsilon^p_{\max}$ increases instead of decreases with the decrease in cohesion. In addition, when the plastic deformation becomes uncontained, the maximum equivalent shear strain $\varepsilon^p_{\max}$ occurs right beneath the contact area instead of near the contact edge. Overall, even at very low cohesion values, yielding occurs mostly at the undrained state and there is little plastic strain accumulation during the transient phase. As such, in this series, the surface displacement profiles barely change over time and the normalized force relaxation curves compare relatively well with the poroelastic solution at $\omega = 0$ even when the cohesion is small.

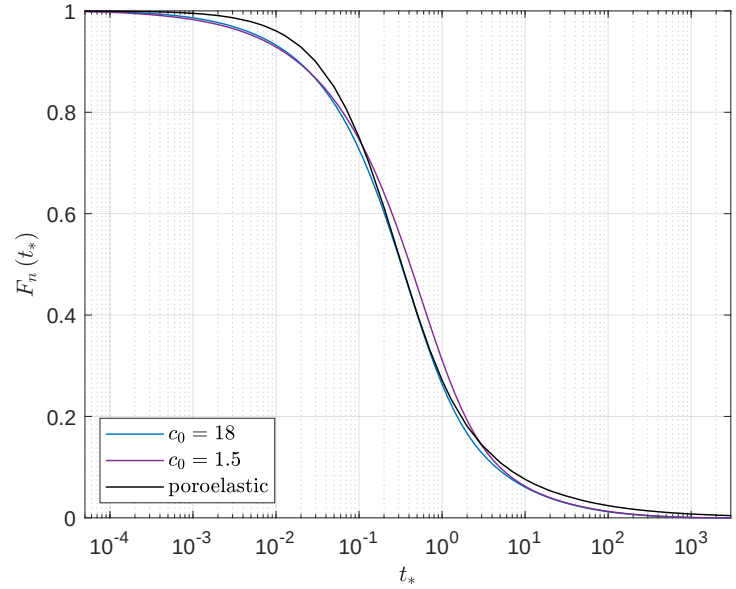

Figure 6.15: Series *r*: Comparison of the force relaxation curves between the theoretical solution at $\omega = 0$ and the numerical results with $c_0 = 1.5$ and 18 MPa.

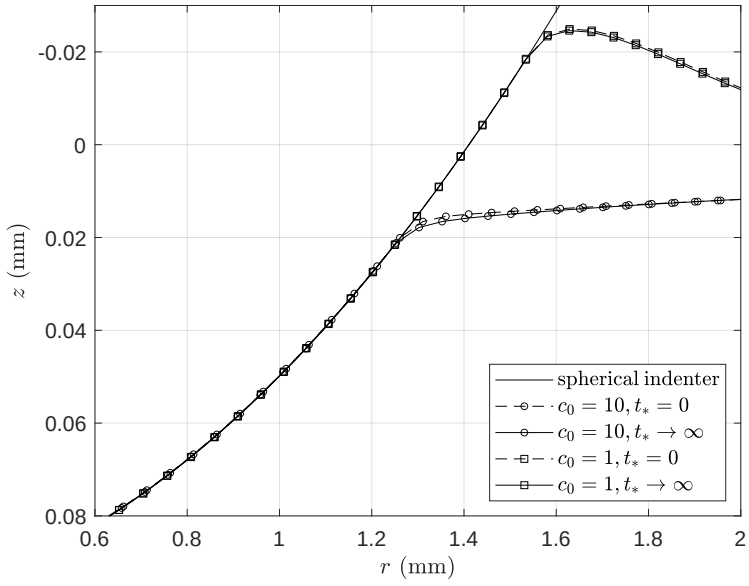

Figure 6.16: Series *r*: Surface displacement profiles at the undrained and drained states with $c_0 = 1$ and 10 MPa.

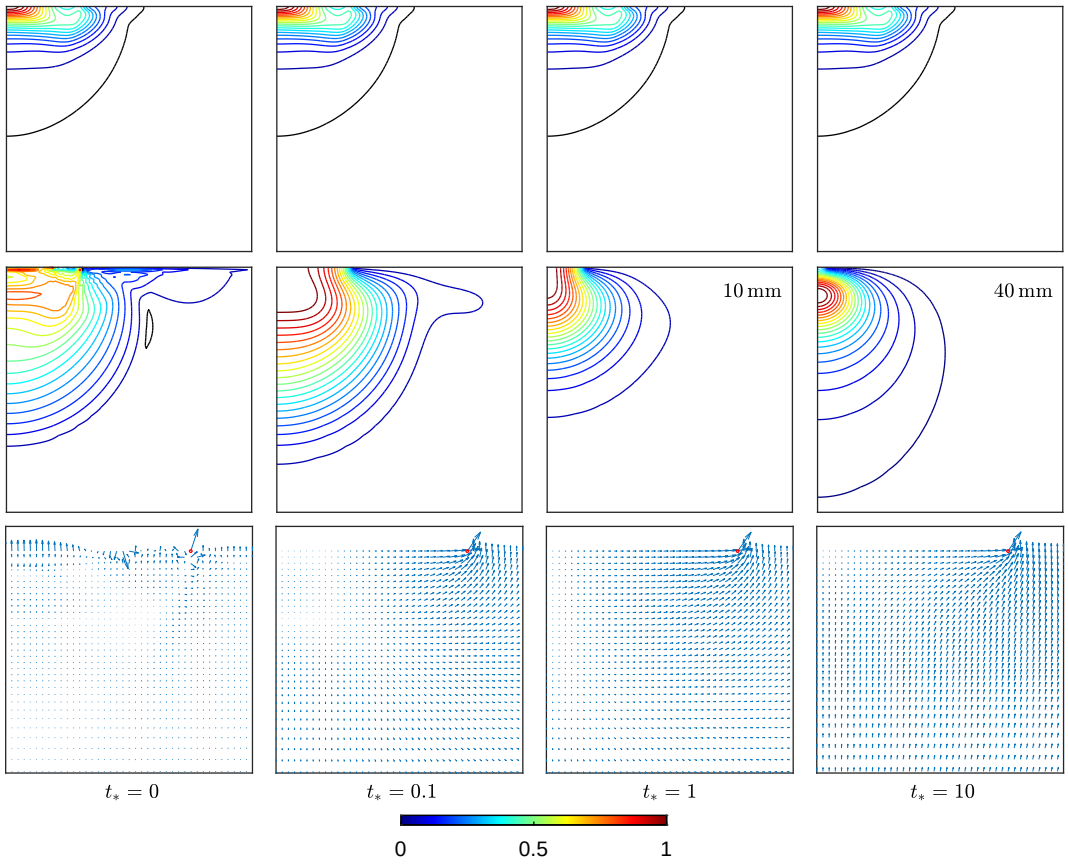

Figure 6.17: Series ϟ, $c_0 = 1$ MPa; from top to bottom - normalized equivalent plastic strain ε_n^p, pore pressure p_n and fluid flux at $t_* = 0$, 0.1, 1 and 10; for these times, $\varepsilon^p_{\max} = 0.2506$, 0.2513, 0.2513, 0.2513, $p_{\min} = -0.385$, -1.8×10^{-3}, -1.2×10^{-3}, 4.365×10^{-4} MPa, $p_{\max} = 6.26$, 4.12, 1.65, 0.066 MPa, and $q_{\max} = 1.206 \times 10^{-2}$, 1.822×10^{-3}, 5.22×10^{-4}, 9.416×10^{-6} mm/s; contours of $\varepsilon^p = 0$ and $p = 0$ marked by black lines.

6.5.2 Numerical Results with $\nu = 0.45$

In the poro-elasto-plastic analysis so far, the drained Poisson's ratio is set to $\nu = 0.22$. Effect of the negative pore pressure is prominent only in the Type IV response of Series ϟ when the material is associative and the cohesion is small. However, if the Poisson's ratio increases, at the undrained limit, negative pore pressure can be easily induced by plastic deformation since shear induced dilatancy could become dominant over the elastic volumetric compressive strain. Subsequent plastic accumulation may then be strongly affected by the presence of negative pore pressure throughout the transient phase even when the cohesion is relatively large. Consequently, Types I and II behaviors may no longer exist even at large c_0.

Such an effect of the Poisson's ratio can be observed from a comparison of four simulation cases with $c_0 = 13$ MPa and $\phi = 20°$. The dilatancy angle and the Poisson's ratio of each case are: 1) $\psi = \phi$, $\nu = 0.22$; 2) $\psi = 0°$, $\nu = 0.22$; 3) $\psi = \phi$, $\nu = 0.45$ and 4) $\psi = 0°$, $\nu = 0.45$. In these four simulations, the shear modulus and the undrained Poisson's ratio are kept the same, $G = 759.4$ MPa and $\nu_u = 0.5$. Therefore, at the undrained limit, if there is no plastic deformation, the pore pressure distribution is the same across the four cases, which can be seen from the pore pressure expression in Table A.1. However, if there is plastic deformation, the differences in the pore pressure development can be attributed to ν and ψ only. Fig. 6.18 shows the contour plots of the normalized equivalent plastic strain and the pore pressure at the undrained limit for the four simulation cases. Among them, substantial development of negative pore pressure occurs when $\phi = \psi$ and $\nu = 0.45$. In this case, the corresponding $\varepsilon^p_{\max}$ is the smallest of the four as a result of shielding effect from the negative pore pressure. However, as the pore pressure dissipates, plastic strain accumulates over time ($\eta_\varepsilon < 1$).

Two series of simulations are now conducted with $\nu = 0.45$, Series ⫴: $\psi = \phi = 20°$ and Series ⫲: $\phi = 20°$, $\psi = 0°$. Figs. 6.19 and 6.20 show that $\eta_\varepsilon < 1$ even at large c_0 when the plastic strain is rather small. For Series ⫴, what we identify as Types I & II responses no longer exists. Therefore, we make no further attempt to determine a lower bound for cohesion above which the force relaxation curves may be approximated as poroelastic. When the material

is non-associative (Series ϟ), $\eta_\varepsilon = 1$ and η_f remain constant for nearly the whole range of cohesion values in this series. Similar to the observation from Series ϟ (see Fig. 6.15), the force relaxation curves are relatively close to the theoretical solution even at small c_0. Here the threshold between Types II and III is at $c_0 = 18$ MPa, see Fig. 6.19 and 6.21.

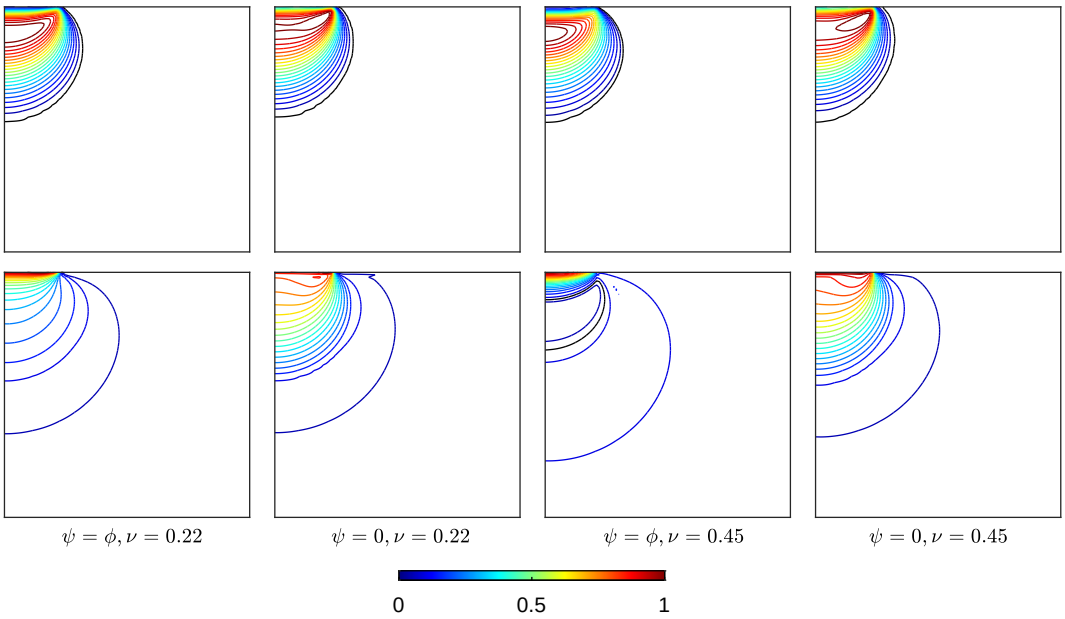

Figure 6.18: From top to bottom - normalized equivalent plastic strain ε_n^p and pore pressure p_n at the undrained limit; from left to right: 1) $\psi = \phi$, $\nu = 0.22$; 2) $\psi = 0$, $\nu = 0.22$; 3) $\psi = \phi$, $\nu = 0.45$; 4) $\psi = 0$, $\nu = 0.45$; from left to right, $\varepsilon^p_{\max} = 0.0361$, 0.049, 0.0151, 0.049, $p_{\min} = -0.0191$, -0.0158, -9.481, -0.0126 MPa, $p_{\max} = 87.615$, 70.88, 158.269, 65.05 MPa; contours of $\varepsilon^p = 0$ and $p = 0$ marked by black lines.

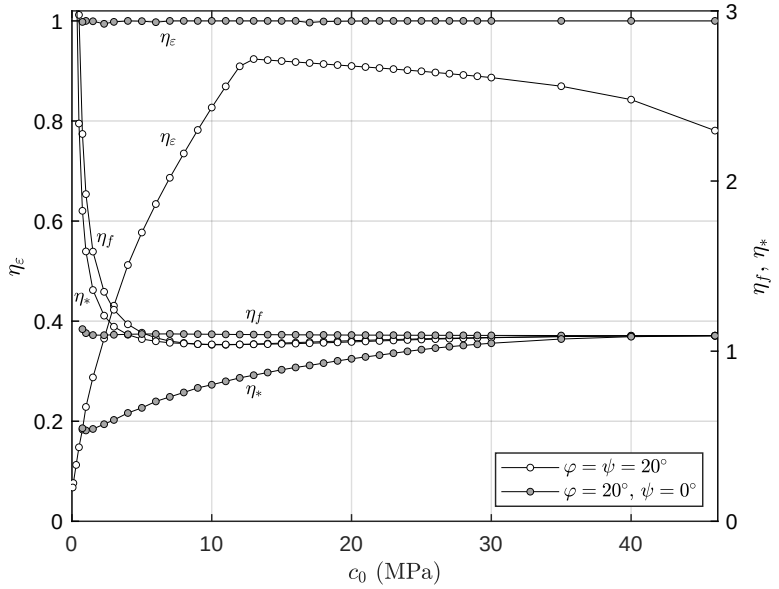

Figure 6.19: Series ⫲, $\nu = 0.45$; series ⫲, $\nu = 0.45$; Effect of cohesion on the ratios of the equivalent plastic strain η_ε and force asymptotes η_f and η_*.

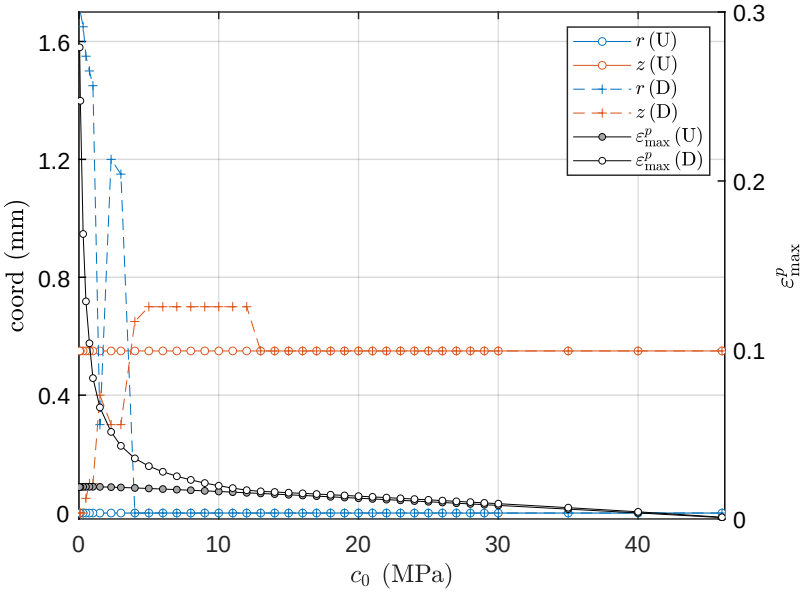

Figure 6.20: Series ⫲, $\nu = 0.45$: Effect of cohesion on the location and magnitude of the maximum equivalent plastic strain $\varepsilon^p_{\max}$; U - undrained limit, D - drained limit.

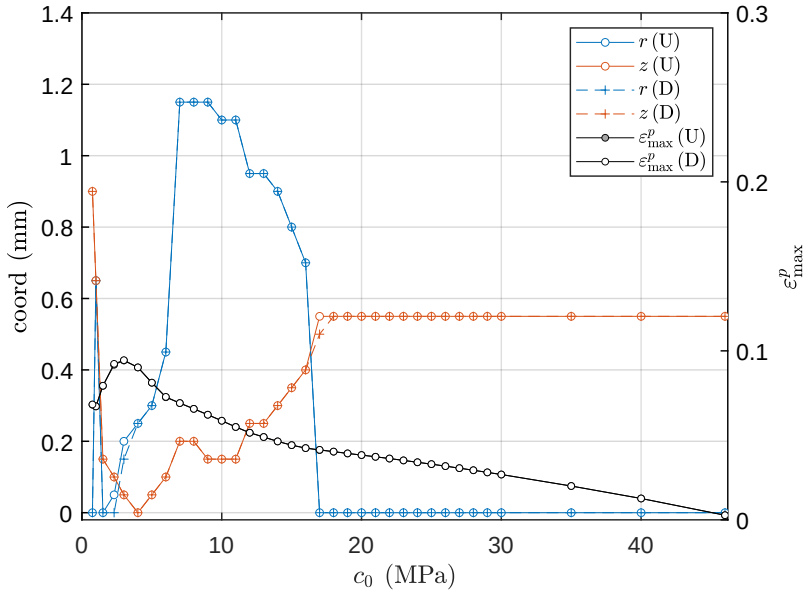

Figure 6.21: Series ⋔, $\nu = 0.45$: Effect of cohesion on the location and magnitude of the maximum equivalent plastic strain $\varepsilon^p_{\max}$; U - undrained limit, D - drained limit.

6.6 Parameter Space

6.6.1 Incipient Failure Consideration

Some useful information can be extracted from the undrained and drained asymptotes of the theoretical solution for poroelastic spherical indentation (see Appendix A.1.5), which will be used to construct the parameter space. It follows from the Hertzian solution that at the undrained limit, the non-zero poroelastic fields along the contact axis can be expressed as,

$$\alpha p = \frac{16\eta\omega G}{\pi\phi\,(1+\omega)}\sqrt{\frac{d}{R}}\left[1 - z_* \arctan\left(z_*^{-1}\right)\right] \tag{6.39}$$

$$\sigma_z = -\frac{8G}{\pi\phi}\sqrt{\frac{d}{R}}\left(1+z_*^2\right)^{-1} \tag{6.40}$$

$$\sigma_r = \sigma_\theta = -\frac{8G}{\pi\phi}\sqrt{\frac{d}{R}}\left[\left(2-\frac{1}{2}\phi\right)\left[1 - z_* \arctan\left(z_*^{-1}\right)\right] - \frac{1}{2}\left(1+z_*^2\right)^{-1}\right] \tag{6.41}$$

where $r_* = r/a$, $z_* = z/a$ and $a = \sqrt{Rd}$. The corresponding Drucker-Prager stress along depth is therefore,

$$\varrho = \frac{8G}{\pi\phi}\sqrt{\frac{d}{R}}\left[\begin{array}{l} \dfrac{\sqrt{3}}{2}\left(1+z_*^2\right)^{-1} - \dfrac{\sqrt{3}}{2}\left[1 - z_* \arctan\left(z_*^{-1}\right)\right] \\ + \left(\dfrac{3bK}{G} - \dfrac{\sqrt{3}}{6}\right)(1-\phi)\left[1 - z_* \arctan\left(z_*^{-1}\right)\right] \end{array}\right] \tag{6.42}$$

It can be seen from Eq. 6.42 that at a given depth, ϱ in the incompressible case ($\phi = 1$) is always larger than the compressible case ($\phi > 1$), which suggests that the plastic deformation is likely to be more severe when the constituents are incompressible. This purely poroelastic analysis is consistent with the poro-elasto-plastic analysis in Section 5.7.1. As a result, when constructing the parameter space, we will only focus on the responses with $\phi = 1$ to stay on the less conservative side.

Setting $\phi = 1$, Eq. 6.42 becomes,

$$\varrho = \frac{4\sqrt{3}G}{\pi}\sqrt{\frac{d}{R}}\left[\frac{1}{1+z_*^2} + z_* \arctan\left(\frac{1}{z_*}\right) - 1\right] \tag{6.43}$$

In this case, ϱ reaches its maximum at $z_* \backsimeq 0.55$, with a magnitude being $\varrho_{\max} \backsimeq 0.783G\sqrt{d/R}$. As a result, from the Drucker-Prager failure criterion, we could derive an equation that marks the onset of plastic yielding at the undrained limit,

$$\sqrt{\frac{d}{R}} = \frac{c_0}{G}\frac{\cos\varphi}{0.226\left(3 - \sin\varphi\right)} \tag{6.44}$$

At the drained limit, the non-zero fields along the contact axis can be expressed as,

$$\sigma_z = -\frac{2E}{\pi\left(1-\nu^2\right)}\sqrt{\frac{d}{R}}\left(1+z_*^2\right)^{-1} \tag{6.45}$$

$$\sigma_r = \sigma_\theta = -\frac{2E}{\pi\left(1-\nu^2\right)}\sqrt{\frac{d}{R}}\left[(1+\nu)\left[1 - z_* \arctan\left(z_*^{-1}\right)\right] - \frac{1}{2}\left(1+z_*^2\right)^{-1}\right] \tag{6.46}$$

The corresponding Drucker-Prager stress along depth is therefore,

$$\varrho = \frac{2E}{\pi\left(1-\nu^2\right)}\sqrt{\frac{d}{R}}\left[\frac{\sqrt{3}}{2}\left(1+z_*^2\right)^{-1} - \left(\frac{\sqrt{3}}{3}+2b\right)(1+\nu)\left[1 - z_* \arctan\left(z_*^{-1}\right)\right]\right] \tag{6.47}$$

It can be shown from Eqs. 6.43 and 6.47 that $\varrho_{\max}$ at the undrained and drained limits equals to each other only when $\nu = 0.5$ and $b = 0$. For all other scenarios, $\varrho_{\max}$ is larger at the undrained limit. This gives support to the observation from the numerical simulations that if the cohesion is above a threshold, plastic strain occurs only at the undrained limit.

6.6.2 Parameter Space Construction

For spherical indentation, plastic deformation is affected by the indentation strain d/R. The threshold cohesion values for the four different types of poro-elasto-plastic reponses are therefore also dependent on d/R. As our interest is on the parameter space where the force relaxation response can be approximated as poroelastic, we limit our focus on identifying the lower bound cohesion value for the Type II response at a given d/R. Fig. 6.22 shows such a parameter space for $\nu = 0.22$, $\nu_u = 0.5$ and both the associative and non-associative cases with $\phi = 20°$. The condition for onset of plasticity at the undrained state can be determined from Eq. 6.44. The lowerbound of Type II response is determined based on the criteria of $\eta_\varepsilon = 1$ and $P = P_0$. The results show that when indentation strain is small ($d/R < 0.01$), the two lower bounds for Type II response are nearly linear in the log-log plot. As d/R increases, the boundary curves up and intersects Eq. 6.44 at $d/R = 0.08$ and $c_0/G = 0.18$. For extreme cases at $d/R > 0.08$, Types I and II responses no longer occur since now the Hertzian assumption is no longer valid. The location for the onset of plasticity at the undrained limit is no longer at P_0. Essentially, Fig. 6.22 gives us a practical guidance to determine a suitable range of indentation strain for poroelasticity characterization in the laboratory if material properties such as cohesion and shear modulus are known.

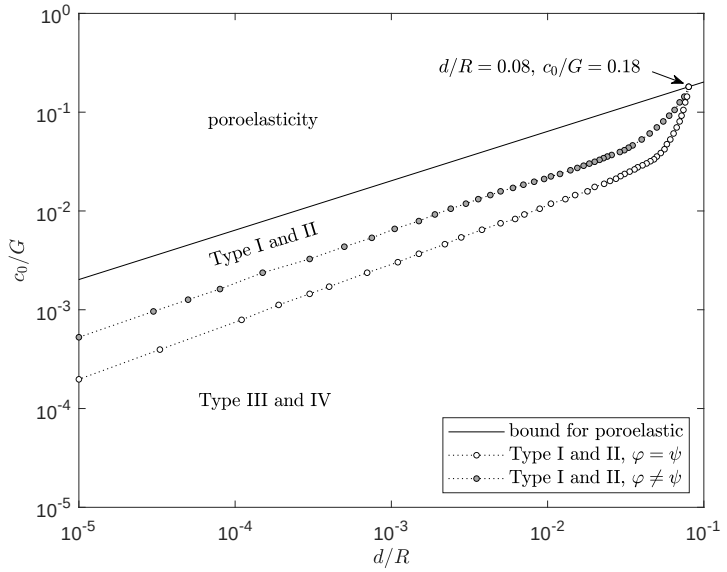

Figure 6.22: Parameter space for spherical indentation into a poro-elasto-plastic material, showing different regimes of response; associative case: $\varphi = \psi = 20°$, $\nu = 0.22$; non-associative case: $\varphi = 20°$, $\psi = 0°$, $\nu = 0.22$.

6.6.3 Effect of Loading Rate and Testing Duration

In a physical experiment, step displacement loading can only be realized by ramping up the displacement over a fixed time period t_r. Therefore, effect of the loading rate on the transient indentation relaxation behavior is examined here. In the numerical simulation, instead of ramping up to the prescribed depth incrementally all at $t_* = 0$, the depth of penetration is reached by a linear ramping of the indentation displacement in time. In Fig. 6.23, the force relaxation response is plotted for three different dimensionless ramping times ($t_r = 10^{-3}$, 10^{-2} and 10^{-1}), in comparison with the result for instantaneous loading ($t_r = 0$). These poroelastic simulations are conducted with case III drainage condition, $d = 0.1$ mm and $R = 10$ mm. The setup is the same as those described in Section 6.3. The material properties are based on those of the Gulf of Mexico shale except that the consituents are set as incompressible and $\nu = 0$. The simulation is terminated at $t_* = 10^6$ as the indentation force now barely changes with time.

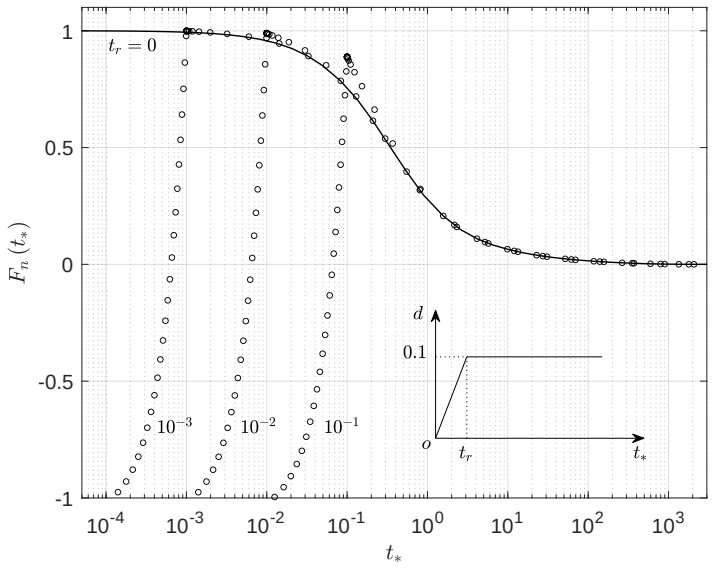

Figure 6.23: Effect of the loading rate on the force relaxation behavior. The inset shows that during the ramping stage the indentation displacement increases linearly with time until reaching the prescribed depth at $d = 0.1$ mm; the dimensionless ramping times are $t_r = 10^{-3}$, 10^{-2}, and 10^{-1}.

The earliest and latest forces from $t_r = 0$ are used to normalize the force-time data at different ramping times. For the case of high loading rate ($t_r = 10^{-3}$), the peak force is close to the undrained force asymptote and the subsequent relaxation closely follows the curve for instantaneous loading. For a relatively low loading rate ($t_r = 10^{-1}$), however, the peak force is lower than the instantaneous limit but higher than the force corresponding to the same time from the curve at $t_r = 0$. In other words, the indentation force overshoots from the reference curve for zero ramping time. Fig. 6.23 shows that the transient indentation relaxation response depends on the loading rate. In order to have a force relaxation curve that can be well represented by the curve with $t_r = 0$, a sufficiently high loading rate should be imposed, e.g., $t_r < 10^{-2}$. In addition, in order to ensure that the late time force relaxation response can be well captured, the dimensionless testing duration t_d should be larger than 1000, at which $F_n \approx 0.001$.

7 POROELATIC SPHERICAL INDENTATION UNDER STEP FORCE

7.1 Introduction

Poroelastic spherical indentation via step force loading is analyzed in this chapter. Step force loading was first examined theoretically by Agbezuge and Deresiewicz (1974) for the three distinct cases of surface drainage conditions. Master curves used in the experimental work of Oyen (2008) was constructed by fitting the solution of Agbezuge and Deresiewicz (1974), see details in Section 1.2.2.

When a spherical indenter is pressed into a poroelastic half space with compressible constituents by a constant step force $F\mathcal{H}(t)$, the instantaneous contact radius and indentation displacement can be determined from the Hertzian solution,

$$a(0) = \left(\frac{3\phi FR}{16G}\right)^{\frac{1}{3}}, \qquad d(0) = \left(\frac{3\phi F}{16G\sqrt{R}}\right)^{\frac{2}{3}} \tag{7.1}$$

As the pore pressure dissipates, the depth of indentation increases with time. To formulate this problem theoretically, two approaches can be employed to approximate the contact radius response. One is to assume that the contact radius remains constant $a(t) = a(0)$, and the other is to assume $a(t) = \sqrt{Rd(t)}$. The first corresponds to a particular case where the indenter has a fixed radius spherical tip, which is in complete contact with the surface of the half space at any time, but does not get in contact with the initially free surface at $r > a(0)$. Such a problem is mathematically amenable and can be solved theoretically via the McNamee-Gibson displacement function method. The second approach, which is more appropriate for a spherical indenter, involves a moving boundary condition and cannot be solved theoretically. However, we can still formulate the problem to gain insights about how the transient response is affected by the material properties. These insights combined with limited number of finite element simulations with the frictionless contact scheme incorporated then allow us to obtain the solution for the transient displacement without having to make the assumption about

contact radius *a priori*.

7.2 Constant Contact Radius

7.2.1 Theoretical Formulation

Boundary conditions for the problem assuming a constant contact radius are given in Table 7.1 for case I surface drainage. Here $\mathcal{G}(t)$ is a function that describes the increase of indentation displacement with time, $d(t) = d(0)\,\mathcal{G}(t)$, and $g(s)$ is the Laplace tranform of $\mathcal{G}(t)$ with respect to t. These two functions are unknowns and need to be determined as part of the solution. The other two surface drainage conditions can be written as $z = 0$, $q_z = 0$ in case II and $q_z = 0$ within $0 \le r \le a(0)$ and $p = 0$ at $r \ge a(0)$ in case III.

	time domain	Laplace domain
$0 \le r \le a(0)$	$u_z = d(0)\,\mathcal{G}(t) - \dfrac{r^2}{2R}\mathcal{H}(t)$	$\overline{u}_z = d(0)\,g(s) - \dfrac{r^2}{2R}s^{-1}$
	$\sigma_{zr} = p = 0$	$\overline{\sigma}_{zr} = \overline{p} = 0$
$r \ge a(0)$	$\sigma_z = \sigma_{zr} = p = 0$	$\overline{\sigma}_z = \overline{\sigma}_{zr} = \overline{p} = 0$

Table 7.1: Boundary conditions for step force loading with case I surface drainage condition, assuming $a(t) = a(0)$.

For case I, matching the poroelastic fields (see Section 2.2) with the boundary conditions in the Laplace domain yields a set of dual integral equations. Using the method from Noble (1963), the pair of dual integral equations can be further reduced to a Fredholm integral equation of the second kind,

$$\theta_1(s_*, x_*) + \omega \int_1^\infty N(s_*, x_*, m_*)\,\theta_1(s_*, m_*)\,dm_* = \omega M(s_*, x_*) \tag{7.2}$$

where,

$$N\left(s_*, x_*, m_*\right) = m_* \int_0^\infty \xi_* H_1\left(s_*, \xi_*\right) J_{-\frac{1}{2}}\left(x_* \xi_*\right) J_{-\frac{1}{2}}\left(m_* \xi_*\right) d\xi_* \tag{7.3}$$

$$M\left(s_*, x_*\right) = \int_0^1 m_*^{-\frac{1}{2}} \left[g\left(s\right) s - m_*^2\right] N\left(s_*, x_*, m_*\right) dm_* \tag{7.4}$$

$$H_1\left(s_*, \xi_*\right) = 1 + \frac{2\xi_*^2}{s_*}\left(1 - \frac{\sqrt{\xi_*^2 + s_*}}{\xi_*}\right) \tag{7.5}$$

In the equations above, the dimensionless variables are defined as follows,

$$\begin{aligned} &x_* = x/a\left(0\right) \qquad m_* = m/a\left(0\right) \qquad r_* = r/a\left(0\right) \qquad z_* = z/a\left(0\right) \\ &\xi_* = \xi a\left(0\right) \qquad s_* = \lambda a^2\left(0\right) \qquad t_* = tc/a^2\left(0\right) \qquad u_* = uc/a^2\left(0\right) \end{aligned} \tag{7.6}$$

There are two unknowns in the Fredholm integral equation, i.e., $g\left(s\right) s$ and $\theta_1\left(s_*, x_*\right)$. An additional equation for them is therefore needed. This equation can be obtained by equating the resultant of the normal stress over the contact area to the applied force,

$$g\left(s\right) s = 1 + \frac{2}{3}\omega - \int_0^1 x_*^{\frac{1}{2}} \theta_1\left(s_*, x_*\right) dx_* \tag{7.7}$$

To solve for $g\left(s\right) s$ and $\theta_1\left(s_*, x_*\right)$ in Eqs. 7.2 and 7.7, an iteration procedure is adopted. Note that since Eq. 7.2 has a similar structure to the Fredholm equation for case I with step displacement loading, techniques we previously develop to overcome the mathematical difficulties associated with evaluating integrals with oscillatory kernels and solving the Fredholm integral equation can be directly used here. Once functions $g\left(s\right) s$ and $\theta_1\left(s_*, x_*\right)$ are obtained, $\mathcal{G}\left(t\right)$ can be determined by applying the inverse Laplace transformation to Eq. 7.7,

$$\mathcal{G}\left(t\right) = \mathcal{L}_s^{-1}\left[g\left(s\right)\right] = 1 + \frac{2}{3}\omega - \int_0^1 x_*^{\frac{1}{2}} \mathcal{L}^{-1}\left[s_*^{-1} \theta_1\left(s_*, x_*\right)\right] dx_* \tag{7.8}$$

where $\mathcal{L}_s^{-1}$ and $\mathcal{L}^{-1}$ denote the inverse Laplace transformation with respect to s and s_*, respectively.

For case II, equations to determine $\mathcal{G}\left(t\right)$ are the same as those in case I except that $H_1\left(s_*, \xi_*\right)$

is replaced with,

$$H_1(s_*, \xi_*) = 1 + \frac{2\xi_*^2}{s_*}\left(\frac{\xi_*}{\sqrt{\xi_*^2 + s_*}} - 1\right) \tag{7.9}$$

For case III, equations to determine $\mathcal{G}(t)$ involve a nonlinear relationship for $g(s)$ and $\theta_{1a}(s_*, x_*)$ and two coupled Fredholm integral equations of the second kind,

$$g(s)\, s = 1 + \frac{2}{3}\omega - \int_0^1 x_*^{\frac{1}{2}} \theta_{1a}(s_*, x_*)\, dx_* \tag{7.10}$$

and,

$$\begin{aligned} &\theta_{1a}(s_*, x_*) + \omega \int_1^\infty N_a(s_*, x_*, m_*)\, \theta_{1a}(s_*, m_*)\, dm_* \\ &+\omega \int_1^\infty N_b(s_*, x_*, m_*)\, \theta_{1b}(s_*, m_*)\, dm_* = \omega M_a(s_*, x_*) \end{aligned} \tag{7.11}$$

$$\begin{aligned} &\theta_{1b}(s_*, x_*) + \int_1^\infty N_d(s_*, x_*, m_*)\, \theta_{1a}(s_*, m_*)\, dm_* \\ &- \int_1^\infty N_c(s_*, x_*, m_*)\, \theta_{1b}(s_*, m_*)\, dm_* = M_b(s_*, x_*) \end{aligned} \tag{7.12}$$

where,

$$M_a(s_*, x_*) = \int_0^1 m_*^{-\frac{1}{2}} \left[g(s)\, s - m_*^2\right] N_a(s_*, x_*, m_*)\, dm_* \tag{7.13}$$

$$M_b(s_*, x_*) = \int_0^1 m_*^{-\frac{1}{2}} \left[g(s)\, s - m_*^2\right] N_d(s_*, x_*, m_*)\, dm_* \tag{7.14}$$

Expressions for $N_a(s_*, x_*, m_*)$-$N_d(s_*, x_*, m_*)$ and their alternative formulations can be found in Section 4.3.1. $\mathcal{G}(t)$ in case III can be determined by applying the inverse Laplace transformation to Eq. 7.10.

In these three cases, ω is the only material constant affecting $\theta_1(s_*, x_*)$ or $\theta_{1a}(s_*, x_*)$, and therefore both $g(s)\, s$ and $\mathcal{G}(t)$.

7.2.2 Results

Once $\mathcal{G}(t)$ is known, the time-dependent behavior of the indentation displacement $d(t_*)$ can be readily obtained since $d(t_*) = d(0)\, \mathcal{G}(t)$. With $\theta_{1,1a}(s_* \to \infty, x_* \leq 1) = \omega x_*^{-\frac{1}{2}}\left(1 - x_*^2\right)$ and $\theta_{1,1a}(s_* \to 0, x_*) = 0$, we have $\mathcal{G}(0) = 1$ and $\mathcal{G}(\infty) = 1 + 2\omega/3$. The indentation displacement

at $t_* \to \infty$ can therefore be related to the indentation force through,

$$d(\infty) = \left(1 + \frac{2\omega}{3}\right)\left(\frac{3\phi F}{16G\sqrt{R}}\right)^{\frac{2}{3}} \tag{7.15}$$

A normalized indentation displacement $d_n(t_*)$ can be defined as follows,

$$d_n(t_*) = \frac{d(\infty) - d(t_*)}{d(\infty) - d(0)} \tag{7.16}$$

and therefore,

$$d_n(t_*) = \frac{\mathcal{G}(\infty) - \mathcal{G}(t)}{\mathcal{G}(\infty) - \mathcal{G}(0)} \tag{7.17}$$

where $d_n(0) = 1$ and $d_n(\infty) = 0$, and $d_n(t_*)$ depends on material properties through ω only.

Transient behaviors of the normalized indentation displacement at $\omega = 0, 0.5, 1$ are plotted for cases I, II and III drainage conditions in Fig. 7.1. When $\omega = 0$, the problem is no longer time-depedent and $d_n(t_*)$ becomes indefinite according to Eq. 7.17. Nevertheless, mathematical limit of $d_n(t_*)$ still exists and simply equals to the normalized force relaxation $F_n(t_*)$ at $\omega = 0$.

Similar to the concept of step displacement loading test, in principle, the step force loading test can also be used for poroelasticity characterization. The two displacement asymptotes can be used to determine material constants G/ϕ and ω. Once ω is known, hydraulic diffusivity c can be determined by matching the transient displacement response from experiments with the master curves. However, compared with step displacement loading, the step force loading test may be less reliable as $d_n(t_*)$ appears to be more sensitive to ω. For example, the differences of $t_{*0.5}$ in $d_n(t_*)$ between $\omega = 0$ and 1 for cases I, II and III are 0.202, 1.26 and 0.183, respectively, while these numbers for $F_n(t_*)$ are 0.033, 0.204 and 0.047. Consequently, accuracy in determining the hydraulic diffusivity c from $d_n(t_*)$ has a stronger dependence on the accuracy of ω.

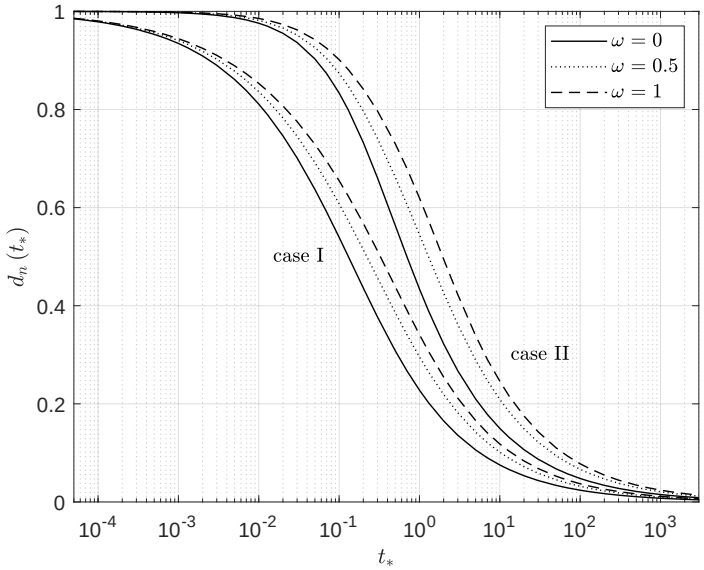

(a) cases I and II

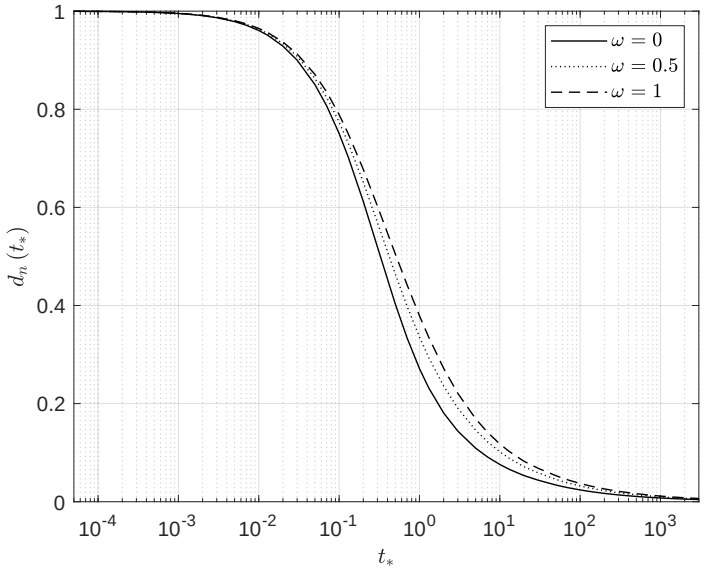

(b) case III

Figure 7.1: Theoretical solutions for the time-dependent behaviors of the normalized indentation displacement, assuming a constant contact radius.

7.3 Varying Contact Radius

If we assume that the contact radius obeys the Hertzian relationship, $a(t) = \sqrt{Rd(t)}$, the problem now involves a moving boundary. This problem was firstly attempted by Agbezuge and Deresiewicz (1974). Their derivation was facilitated by treating the contact pressure as a slowly varying function of time, which could then be taken out of the convolutional type of integral. It is unclear to us whether such an assumption is legitimate. However, without this assumption, theoretical solution cannot be obtained due to the high nonlinearity in the equation system. Meanwhile, with the frictionless contact scheme incorporated in our finite element algorithm, the assumption on the contact radius is no longer required *a priori*. Therefore, we revisit this problem via an integrated theoretical and numerical approach.

Boundary conditions for this problem can only be given in the time domain, since a varying contact radius is used. As an example, Table 7.2 gives the boundary conditions for case I drainage condition.

$0 \le r \le a(t)$	$u_z = d(t) - \dfrac{r^2}{2R}$
	$\sigma_{zr} = p = 0$
$r \ge a(t)$	$\sigma_z = \sigma_{zr} = p = 0$

Table 7.2: Boundary conditions for step force loading with case I surface drainage condition, assuming $a(t) = \sqrt{Rd(t)}$.

If we assume $a(t) = \sqrt{Rd(t)}$, both the initial and final indentation depth can be determined according to the Hertzian solution,

$$d(0) = \frac{a^2(0)}{R} = \left(\frac{3\phi F}{16G\sqrt{R}}\right)^{\frac{2}{3}} \tag{7.18}$$

$$d(\infty) = \frac{a^2(\infty)}{R} = \left[\frac{3\eta F}{8G(2\eta - 1)\sqrt{R}}\right]^{\frac{2}{3}} \tag{7.19}$$

Their ratio gives,

$$\frac{d\left(0\right)}{d\left(\infty\right)}=\frac{a^{2}\left(0\right)}{a^{2}\left(\infty\right)}=\left(1+\omega\right)^{-\frac{2}{3}} \tag{7.20}$$

Two approaches can be used for the scaling of the dimensionless time, namely, $t_{*}=tc/a^{2}\left(0\right)$ or $t_{*}=tc/a^{2}\left(t\right)$. We first prove through theoretical analysis that for both forms of dimensionless time, if the Hertzian relationship $a\left(t\right)=\sqrt{Rd\left(t\right)}$ is valid, then $d_{n}\left(t_{*}\right)$, as defined in Eq. 7.16, is affected by material constants through ω only. We then perform finite element simulations by first checking the validity of the Hertzian relationship and then investigating the behaviors of $d_{n}\left(t_{*}\right)$ at different ω.

7.3.1 Theoretical Analysis

According to the McNamee-Gibson displacement function method, see Section 2.2, field variables on the surface in the time domain can be expressed as,

$$u_{z}=\int_{0}^{\infty}\mathcal{L}_{s}^{-1}\left[A_{1}\xi+A_{2}\sqrt{\xi^{2}+\lambda}+\left(1-2\phi\right)B_{1}\right]J_{0}\left(r\xi\right)d\xi \tag{7.21}$$

$$\frac{\sigma_{z}}{2G}=\int_{0}^{\infty}\mathcal{L}_{s}^{-1}\left(A_{1}\xi^{2}+A_{2}\xi^{2}-\phi B_{1}\xi\right)J_{0}\left(r\xi\right)d\xi \tag{7.22}$$

$$\frac{\alpha p}{2G}=\int_{0}^{\infty}\mathcal{L}_{s}^{-1}\left\{-\eta A_{2}\lambda-\left[\phi+2\eta\left(1-\phi\right)\right]B_{1}\xi\right\}J_{0}\left(r\xi\right)d\xi \tag{7.23}$$

$$\frac{\sigma_{zr}}{2G}=\int_{0}^{\infty}\mathcal{L}_{s}^{-1}\left[A_{1}\xi^{2}+A_{2}\xi\sqrt{\xi^{2}+\lambda}+\left(1-\phi\right)B_{1}\xi\right]J_{1}\left(r\xi\right)d\xi \tag{7.24}$$

$$\frac{\alpha\mu q_{z}}{2G\kappa}=\int_{0}^{\infty}\mathcal{L}_{s}^{-1}\left\{-\eta A_{2}\lambda\sqrt{\xi^{2}+\lambda}-\left[\phi+2\eta\left(1-\phi\right)\right]B_{1}\xi^{2}\right\}J_{0}\left(r\xi\right)d\xi \tag{7.25}$$

Cases I and II Matching the poroelastic fields in the time domain with the boundary condition yields the following dual integral equations,

$$a^{3}\left(0\right)\int_{0}^{\infty}\chi_{a}\left(t,\xi\right)J_{0}\left(r\xi\right)d\xi=\frac{3}{16}\left[\frac{r^{2}}{2}-a^{2}\left(t\right)\right],\quad r\leq a\left(t\right) \tag{7.26}$$

$$\int_{0}^{\infty}\xi\left[c\xi^{2}\int_{0}^{t}K_{a}\left(u,\xi\right)\chi_{a}\left(t-u,\xi\right)du-\chi_{a}\left(t,\xi\right)\right]J_{0}\left(r\xi\right)d\xi=0,\quad r\geq a\left(t\right) \tag{7.27}$$

where,

$$\chi_a(t,\xi) = \mathcal{L}_s^{-1}\left(\frac{GB_1}{F}\right) \tag{7.28}$$

Expression of $K_a(t,\xi)$ for case I is,

$$K_a(t,\xi) = \frac{2\omega}{1+\omega}\left[\left(\pi ct\xi^2\right)^{-\frac{1}{2}}\exp\left(-ct\xi^2\right) + \operatorname{erf}\left(\sqrt{ct}\xi\right) - 1\right] \tag{7.29}$$

and for case II,

$$K_a(t,\xi) = \frac{2\omega}{1+\omega}\left[1 - \operatorname{erf}\left(\sqrt{ct}\xi\right)\right] \tag{7.30}$$

Integrating the normal stress over the contact area and setting the resultant to be equal to the indentation force F yields an additional equation,

$$\int_0^{a(t)} r\left\{\int_0^{\infty}\xi\left[c\xi^2\int_0^t K_a(u,\xi)\,\chi_a(t-u,\xi)\,du - \chi_a(t,\xi)\right]J_0(r\xi)\,d\xi\right\}dr = \frac{1}{4\pi} \tag{7.31}$$

The term $\int_0^t K_a(u,\xi)\,\chi_a(t-u,\xi)\,du$ is obtained based on the convolution theorem.

Here we adopt two methods to define the dimensionless variables. One is according to Eq. 7.6, where variables are scaled with respect to the initial contact radius $a(0)$, and the other is according to,

$$\begin{gathered} x_* = x/a(t) \qquad m_* = m/a(t) \qquad r_* = r/a(t) \\ z_* = z/a(t) \qquad \xi_* = \xi a(t) \qquad t_* = ct/a^2(t) \qquad u_* = cu/a^2(t) \end{gathered} \tag{7.32}$$

Of course, regardless of the scaling approach, the end results we obtain should be identical.

From the first method, Eqs. 7.26, 7.27 and 7.31 become,

$$\int_0^{\infty}\chi_1(t_*,\xi_*)\,J_0(r_*\xi_*)\,d\xi_* = \frac{3}{16}\left[\frac{r_*^2}{2} - \frac{a^2(t_*)}{a^2(0)}\right], \quad r_* \le \frac{a(t_*)}{a(0)} \tag{7.33}$$

$$\int_0^{\infty}\xi_*\psi(t_*,\xi_*)\,J_0(r_*\xi_*)\,d\xi_* = 0, \quad r_* \ge \frac{a(t_*)}{a(0)} \tag{7.34}$$

$$\int_0^{\frac{a(t_*)}{a(0)}} r_* \left[\int_0^{\infty} \xi_* \psi \left(t_*, \xi_* \right) J_0 \left(r_* \xi_* \right) d\xi_* \right] dr_* = \frac{1}{4\pi} \tag{7.35}$$

From the second method, Eqs. 7.26, 7.27 and 7.31 become,

$$\frac{a^3 \left(0 \right)}{a^3 \left(t_* \right)} \int_0^{\infty} \chi_1 \left(t_*, \xi_* \right) J_0 \left(r_* \xi_* \right) d\xi_* = \frac{3}{16} \left(\frac{r_*^2}{2} - 1 \right), \quad r_* \leq 1 \tag{7.36}$$

$$\int_0^{\infty} \xi_* \psi \left(t_*, \xi_* \right) J_0 \left(r_* \xi_* \right) d\xi_* = 0, \quad r_* \geq 1 \tag{7.37}$$

$$\int_0^{1} r_* \left[\int_0^{\infty} \xi_* \psi \left(t_*, \xi_* \right) J_0 \left(r_* \xi_* \right) d\xi_* \right] dr_* = \frac{1}{4\pi} \tag{7.38}$$

where $\chi_1 \left(t_*, \xi_* \right) = \chi \left(t, \xi \right)$. Expression of $\psi \left(t_*, \xi_* \right)$ is given as follow,

$$\psi \left(t_*, \xi_* \right) = \xi_*^2 \int_0^{t_*} K_1 \left(u_*, \xi_* \right) \chi_1 \left(t_* - u_*, \xi_* \right) du_* - \chi_1 \left(t_*, \xi_* \right)$$

$K_1 \left(t_*, \xi_* \right)$ for case I is,

$$K_1 \left(t_*, \xi_* \right) = \frac{2\omega}{1+\omega} \left[\left(\pi t_* \xi_*^2 \right)^{-\frac{1}{2}} \exp \left(-t_* \xi_*^2 \right) + \operatorname{erf} \left(\sqrt{t_*} \xi_* \right) - 1 \right] \tag{7.39}$$

and for case II,

$$K_1 \left(t_*, \xi_* \right) = \frac{2\omega}{1+\omega} \left[1 - \operatorname{erf} \left(\sqrt{t_*} \xi_* \right) \right] \tag{7.40}$$

It can be seen that for both scaling methods, $a \left(t_* \right) / a \left(0 \right)$ are influenced by material constants through ω only.

Case III Matching the displacement and normal stress with the mechanical boundary condition yields the first set of dual integral equations,

$$a^3 \left(0 \right) \int_0^{\infty} \chi_a \left(t, \xi \right) J_0 \left(r \xi \right) d\xi = \frac{3}{16} \left[\frac{r^2}{2} - a^2 \left(t \right) \right], \quad r \leq a \left(t \right) \tag{7.41}$$

$$\int_0^{\infty} \xi \left[c \xi^2 \int_0^{t} K_b \left(u, \xi \right) \chi_b \left(t - u, \xi \right) du - \chi_a \left(t, \xi \right) \right] J_0 \left(r \xi \right) d\xi = 0, \quad r \geq a \left(t \right) \tag{7.42}$$

Matching the pore pressure and normal flux with the drainage boundary conditions yields the other set of dual integral equations,

$$\int_0^\infty \xi^2 \left[\int_0^t K_c(u,\xi)\, \chi_b(t-u,\xi)\, du + \frac{2\omega}{1+\omega} \chi_a(t,\xi) \right] J_0(r\xi)\, d\xi = 0, \quad r \le a(t) \tag{7.43}$$

$$\int_0^\infty \xi \left[\chi_b(t,\xi) + \frac{2\omega}{1+\omega} \chi_a(t,\xi) \right] J_0(r\xi)\, d\xi = 0, \quad r \ge a(t) \tag{7.44}$$

Again an additional equation can be obtained from the force equilibrium condition for the indenter,

$$\int_0^{a(t)} r \left\{ \int_0^\infty \xi \left[c\xi^2 \int_0^t K_b(u,\xi)\, \chi_b(t-u,\xi)\, du - \chi_a(t,\xi) \right] J_0(r\xi)\, d\xi \right\} dr = \frac{1}{4\pi} \tag{7.45}$$

where,

$$\chi_b(t,\xi) = \mathcal{L}_s^{-1}\left(\frac{\lambda G A_2}{F\xi} \right) \tag{7.46}$$

$$K_b(t,\xi) = 1 - \left(\pi c t \xi^2\right)^{-\frac{1}{2}} \exp\left(-ct\xi^2\right) - \operatorname{erf}\left(\sqrt{ct}\xi\right) \tag{7.47}$$

$$K_c(t,\xi) = -\frac{1}{2}\left(\pi c t \xi^2\right)^{-\frac{1}{2}} t^{-1} \exp\left(-ct\xi^2\right) \tag{7.48}$$

After normalizing the variables into dimensionless form following either Eq. 7.6 or Eq. 7.32, we can show that $a(t_*)/a(0)$ in case III is also affected by material properties through ω only. Detailed equations are omitted here for the sake of brevity. Therefore, considering the fact that $a(\infty)/a(0) = (1+\omega)^{\frac{1}{3}}$, for both scaling methods, $d_n(t_*)$ can be proven to be solely dependent on ω once the assumption $a(t) = \sqrt{Rd(t)}$ is validated.

7.3.2 Numerical Results

Here finite element simulations are used to first examine the validity of the assumption on the contact radius, i.e., $a(t) = \sqrt{Rd(t)}$. The transient displacement behaviors of $d_n(t_*)$ at different ω are then explored. While the contact scheme in Section 6.2 provides a means to simulate spherical indentation with a given indentation depth, it does not illustrate how the

step force loading problem, where the indentation depth is not known *a priori*, can be solved.

Here a simple yet effective iteration procedure is added to model step force loading. To advance from loading step n to $n+1$, the scheme starts by calculating an initial indentation depth $d^{(0)}$. In the ramping up stage, this initial indentation depth is determined according to Eq. 7.18; in the transient stage, the initial depth is set to be equal to the indentation depth at step n. In the $\ell-$th iteration cycle ($\ell = 1, 2, 3, ...$), given $d^{(\ell-1)}$, an indentation force $F^{(\ell-1)}$ can be determined from the finite element simulation. The residual between the applied force F and the force corresponding to $d^{(\ell-1)}$ is therefore $\Delta F = F - F^{(\ell-1)}$. Such a residual is used to calculate an incremental displacement Δd according to $\Delta d = \phi \Delta F / 8G\sqrt{Rd^{(0)}}$, based on Eq. 7.18. The indentation depth for next iteration is therefore $d^{(\ell)} = d^{(\ell-1)} + \Delta d$. The iteration terminates if $|\Delta d| < \epsilon$, where ϵ is the tolerance. Field variables and indentation depth at loading step $n+1$ are then updated according to $\mathbf{u}_{n+1} = \mathbf{u}^{(\ell)}$, $\mathbf{p}_{n+1} = \mathbf{p}^{(\ell)}$ and $d_{n+1} = d^{(\ell)}$.

For each surface drainage condition, dependence of $d_n(t_*)$ on ω is examined with four distinct sets of material properties. For each set, the parameter values different from those of the Gulf of Mexico shale are as follows,

- set i: $\nu = 0$, $K_s \to \infty$, $K_f \to \infty$ ($\omega = 1$)
- set ii: $\nu = 0.25$, $K_s \to \infty$, $K_f \to \infty$ ($\omega = 0.5$)
- set iii: $\nu = 0.49$, $K_s \to \infty$, $K_f \to \infty$ ($\omega = 0.02$)
- set iv: $\nu = 0$, $K_s = 2.75$ GPa, $K_f = 2$ GPa ($\omega = 0.5$)

In the numerical simulations, the applied force for each set is determined according to Eq. 7.18 with $d(0) = 0.1$ mm. Simulation results suggest that the displacement asymptotes at the undrained and drained limits are consistent with the theoretical solution, see Table 7.3.

	Theoretical				Numerical			
set	i	ii	iii	iv	i	ii	iii	iv
$d(0)$ (mm)	0.1	0.1	0.1	0.1	0.0996	0.0993	0.0995	0.0993
$d(\infty)$ (mm)	0.101	0.131	0.159	0.131	0.101	0.128	0.153	0.128

Table 7.3: Indentation displacement asymptotes at the undrained and drained limits for sets i-iv.

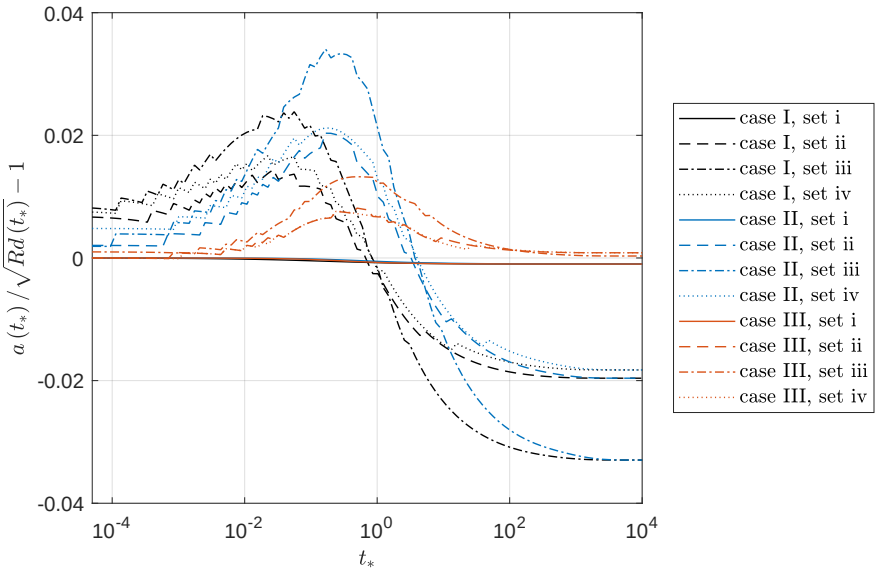

Figure 7.2: Evolution of $a(t_*)/\sqrt{Rd(t_*)} - 1$ with dimensionless time $t_* = tc/a^2(0)$.

It is interesting to observe that in all these simulations,

$$\left| \frac{a\left(t_*\right)}{\sqrt{Rd\left(t_*\right)}} - 1 \right| < 0.035$$

see Fig. 7.2. The values are even smaller for case III surface drainage condition. From a practical stand point, we may therefore consider that $a\left(t\right) = \sqrt{Rd\left(t\right)}$ is a valid assumption for step force loading. Note that in Fig. 7.2, the dimensionless time is scaled according to $t_* = tc/a^2\left(0\right)$, but the same conclusion still holds if $t_* = tc/a^2\left(t\right)$.

In the aforementioned theoretical analysis, it is shown that if $a\left(t\right) = \sqrt{Rd\left(t\right)}$ is valid, $d_n\left(t_*\right)$ is expected to be influenced by material constants through ω only. The governing role of ω is indeed confirmed by numerical simulations. As shown in Fig. 7.3, $d_n\left(t_*\right)$ from sets ii and iv are almost identical. In these two sets, the material properties are rather different, but ω is the same ($\omega = 0.5$). In this figure, behaviors of the normalized indentation displacement are plotted for the four sets of material properties with $t_* = tc/a^2\left(0\right)$. The differences of $t_{*0.5}$ in $d_n\left(t_*\right)$ between $\omega = 0.02$ and 1 are 0.206, 1.095 and 0.533 for cases I, II and III, respectively.

A comparison of the indentation displacment at transient times between the numerical simulation and the theoretical solution at $\omega = 0$ is shown in Fig. 7.4. Denote Δd_n as the difference in the normalized indentation displacement $d_n\left(t_*\right)$ between the numerical results at $\omega = 0.02$ and the theoretical solutions at $\omega = 0$. The latter simply equals to $F_n\left(t_*\right)$ at $\omega = 0$. As expected, the transient results agree very well with the theoretical solutions. The relatively large discrepancy at large time is attributed to the finite sample size and far field drainage boundary conditions imposed at the lateral surface.

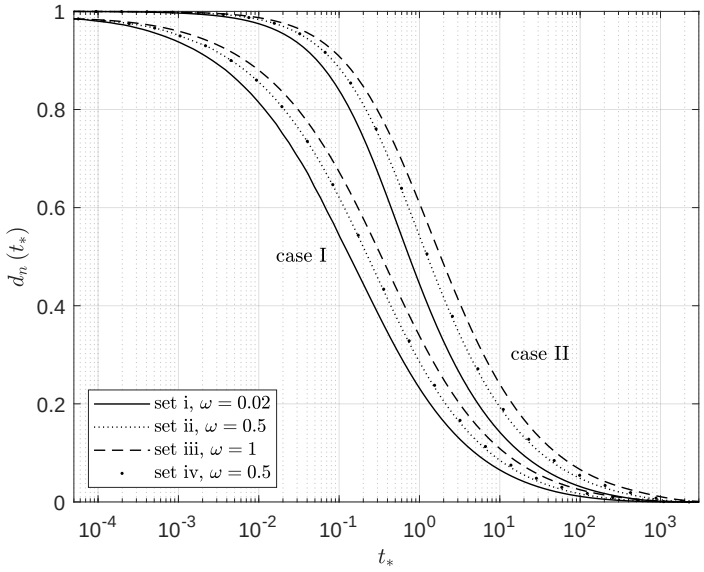

(a) cases I and II

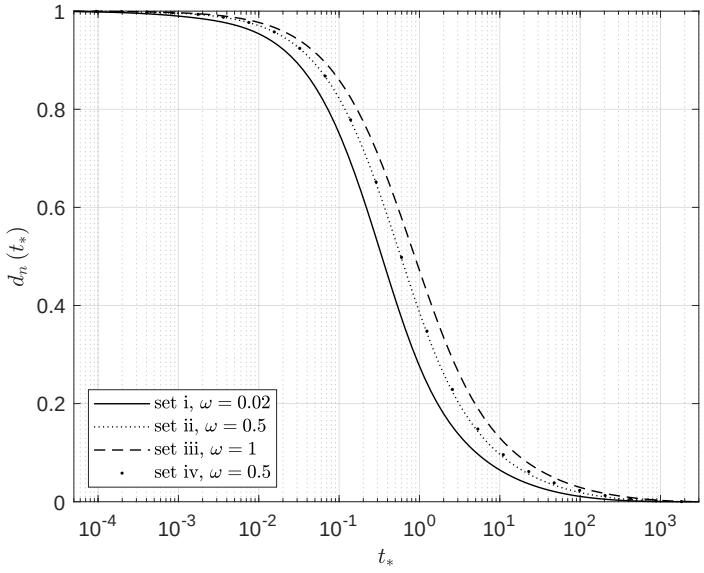

(b) case III

Figure 7.3: Time-dependent behaviors of the normalized indentation displacement, assuming a varying contact radius; $t_* = ct/a^2$ (0).

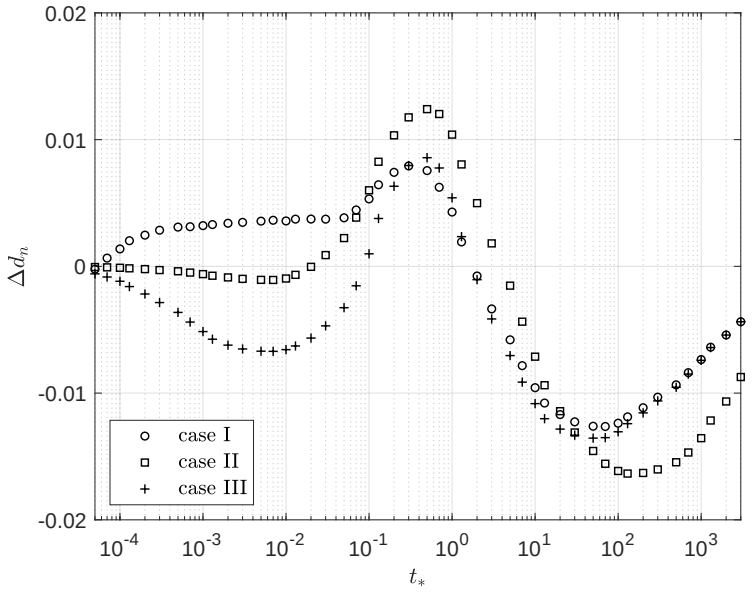

Figure 7.4: Difference between the numerical results at $\omega = 0.02$ and the theoretical solutions at $\omega = 0$ in the normalized indentation displacement as a function of time; $t_* = ct/a^2\,(0)$.

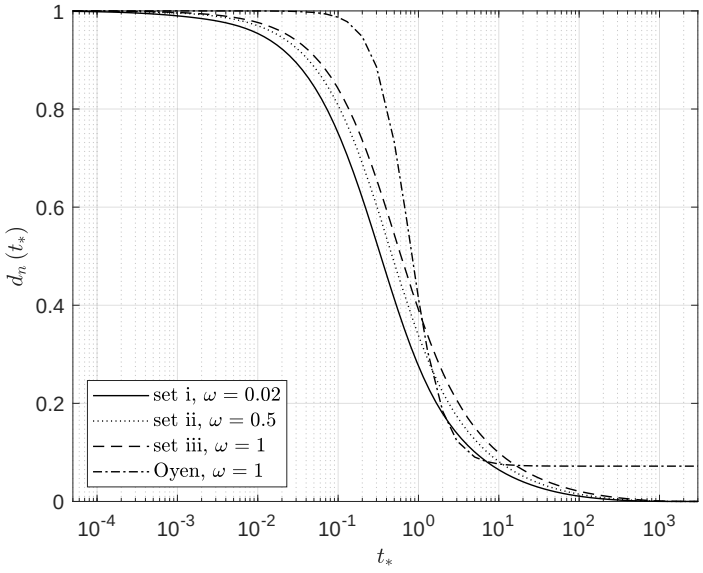

Figure 7.5: Time-dependent behaviors of the normalized indentation displacement for case III, assuming a varying contact radius; $t_* = ct/a^2\,(t)$. The master curve from Oyen (2008) is plotted for comparison.

In order to see whether the transient displacement response becomes less sensitive to ω if time is scaled according to $t_* = tc/a^2(t)$, we replot the simulation results from cases III with $\omega = 0.02$, 0.5 and 1 in Fig. 7.5 with time scaled against $a(t)$. Difference of $t_{*0.5}$ between $\omega = 0.02$ and 1 is now 0.27, still much larger than 0.047 for $F_n(t_*)$. This suggests that compared with step displacement loading, the step force loading test may be less reliable from the point of view of data interpretation.

A comparison is made between our numerical results for case III and the fitting function from Oyen (2008), contructed based on the semi-analytical results from Agbezuge and Deresiewicz (1974) assuming $\nu = 0$ and $t_* = ct/a^2(t)$, see Eq. 1.5. Agreement is however not satisfactory. The assumption in Agbezuge and Deresiewicz (1974) to treat the contact pressure as a slowly varing function of time is perhaps the reason for the discrepancy.

8 CONCLUSION AND FUTURE WORK

8.1 Conclusion

A set of fully coupled poroelastic solutions to the problems of spherical indentation in a semi-infinite domain with case I-III surface drainage conditions via step displacement loading or step force loading is derived based on the McNamee-Gibson displacement function method within the framework of Biot's theory. With the aid of a variety of mathematical techniques, effective solution schemes are constructed to overcome the difficulties generally associated with evaluating integrals with oscillatory kernels and solving the Fredholm integral equation of the second kind. Field variables on the surface as well as inside the domain are both derived.

For all these cases, the theoretical solutions show that the normalized transient force or displacement responses are affected by material properties through a single derived material constant ω only. Furthermore, such dependence on ω is relatively weak if the indentation process is displacement-controlled. Master curves for the force relaxation or transient displacement response can be constructed by fitting the full solutions using a four-parameter elementary function with a coefficient of determination $R^2 \backsimeq 1$.

For the particular case of $\omega = 0$, closed-form asymptotic expressions for the early and late time force relaxation responses from step displacement loading are derived for both cases I and II surface drainage conditions. Given a tolerance of 1%, a combination of these early and late time asymptotic expressions can approximate the full solution for the entire time range.

In principle, both the step displacement or step force loading test can be used for poroelasticity characterization in the laboratory. However, from the point of view of data interpretation, the relatively weak dependence on ω is an indication that the stepdisplacement test is likely more reliable than the stepforce test. For the step displacement test, the asymptotes of the indentation force at the undrained and drained limits can be used to determine G/φ and $G\left(2\eta - 1\right)/\eta$. The ratio between the two yields constant ω. Hydraulic diffusivity c can then be determined by matching the measured transient force response against the corresponding master curve.

A hydromechanically coupled finite element method (FEM) algorithm following a mixed continuous Galerkin formulation for displacement and pore pressure and incorporating a penalty-based frictionless contact scheme is constructed for modeling of spherical indentation in a poro-elasto-plastic medium in order to examine how factors such as plastic deformation, depth of penetration and loading rate affect the indentation response. The fully saturated porous medium is assumed to be isotropic and elasto-perfectly plastic, obeying a Drucker-Prager yield criterion with an associative or non-associated flow rule. The Newton-Raphson method with the tangent stiffness scheme is adopted to deal with plasticity in the solid skeleton. A stabilization scheme, which permits equal-order interpolation for the displacement and pore pressure fields and suppresses pore pressure oscillation in the incompressible or nearly incompressible limit is incorporated in this FEM algorithm.

Numerical simulations are first carried out for poroelastic spherical indentation via both step displacement and rigid sphere loadings and are compared with the theoretical solution. For step displacement loading, excellent agreement is achieved between the numerical and theoretical solutions. For rigid sphere loading, at the undrained and drained limits, depending on the magnitude of indentation strain and Poisson's ratio, the force asymptote from the numerical simulations could be either larger or smaller than their theoretical counterparts; at transient time, when the indentation strain is small, e.g., $d/R \leq 0.05$, the numerical results show an even weaker dependence on ω than that of the theoretical solutions. The numerical results with $\omega = 0.02$ and 1 agree very well with the theoretical curve at $\omega = 0$. This means that from a practical stand point, the theoretical force relaxation curve at $\omega = 0$ is a suitable master curve for the entire range of ω as long as the indentation strain is relatively small.

Numerical simulations are then performed for indentation in a poro-elasto-plastic medium. It is shown that hydromechanical coupling gives rise to four distinct types of poro-elasto-plastic responses, which can be distinguished based on the equivalent plastic strain ratio η_ε, the two force ratios η_f and η_* as well as the location of the maximum plastic strain $\varepsilon^p_{\max}$. Even though plasticity could occur immediately at the undrained limit, if the indentation strain and material strength are such that the maximum plastic strain at the undrained limit remains at

the location of onset of plasticity as predicted by the poroelastic solutions and plastic strain does not accumulate during the transient period, the normalized force relaxation behavior could still be approximated as poroelastic. A parameters space could be constructed to determine a suitable range of indentation strain for poroelasticity characterization of geomaterials if material properties such as cohesion and shear modulus are known. Effects of the loading rate and testing duration on the quality of relaxation curves are also investigated. In order to have a force relaxation curve that can be well characterized by the theoretical solution, a sufficiently high loading rate should be imposed, and a sufficiently long testing duration should be ensured.

8.2 Future Work

Future work can be built upon the theoretical and numerical approaches outlined in the present work. The mathematical techniques we developed in the theoretical analyses can be applied to solve other types of contact problems. Meanwhile, numerical development can be further extended to investigate other types of constitutive behaviors. Laboratory testing with poroelastic spherical indentation could also be improved with our findings.

References

Agbezuge, L. K. (1975). The consolidation settlement of a circular footing. *Israel Journal of Technology 13*, 264–269.

Agbezuge, L. K. (1976). Consolidation settlement of a permeable punch. In *17th US Rock Mechanics/Geomechanics Symposium*. American Rock Mechanics Association.

Agbezuge, L. K. and H. Deresiewicz (1974). On the indentation of a consolidating half-space. *Israel Journal of Technology 12*, 322–338.

Argatov, I. and G. Mishuris (2018). *Indentation testing of biological materials*. Springer.

Ateshian, G. A., W. M. Lai, W. B. Zhu, and V. C. Mow (1994). An asymptotic solution for the contact of two biphasic cartilage layers. *Journal of Biomechanics 27*(11), 1347–1360.

Babuška, I. (1971). Error-bounds for finite element method. *Numerische Mathematik 16*(4), 322–333.

Bateman, H. (1953). *Higher transcendental functions [Volumes I-III]*. McGraw-Hill, New York.

Bateman, H. (1954). *Tables of integral transforms*. McGraw-Hill, New York.

Bembey, A. K., A. J. Bushby, A. Boyde, V. L. Ferguson, and M. L. Oyen (2006). Hydration effects on the micro-mechanical properties of bone. *Journal of Materials Research 21*(8), 1962–1968.

Bennett, K. C., L. A. Berla, W. D. Nix, and R. I. Borja (2015). Instrumented nanoindentation and 3d mechanistic modeling of a shale at multiple scales. *Acta Geotechnica 10*(1), 1–14.

Biot, M. A. (1941). General theory of three-dimensional consolidation. *Journal of Applied Physics 12*(2), 155–164.

Biot, M. A. (1956). General solutions of the equations of elasticity and consolidation for a porous material. *Journal of Applied Mechanics 23*(1), 91–96.

Booker, J. R. and J. C. Small (1985). The consolidation of a deep clay stratum subject to an impermeable axisymmetric surface loading. *Computers and Geotechnics 1*(4), 245–261.

Borja, R. I. (1986). Finite element formulation for transient pore pressure dissipation: A variational approach. *International Journal of Solids and Structures 22*(11), 1201–1211.

Borja, R. I., Q. Yin, and Y. Zhao (2020). Cam-clay plasticity. part ix: On the anisotropy, heterogeneity, and viscoplasticity of shale. *Computer Methods in Applied Mechanics and Engineering 360*, 112695.

Bouklas, N., C. M. Landis, and R. Huang (2015). A nonlinear, transient finite element method for coupled solvent diffusion and large deformation of hydrogels. *Journal of the Mechanics and Physics of Solids 79*, 21–43.

Brace, W. F., J. B. Walsh, and W. T. Frangos (1968). Permeability of granite under high pressure. *Journal of Geophysical Research 73*(6), 2225–2236.

Bracewell, R. N. (1986). *The fourier transform and its applications*. McGraw-Hill, New York.

Brezzi, F. (1974). On the existence, uniqueness and approximation of saddle-point problems arising from Lagrangian multipliers. *Publications Mathématiques et Informatique de Rennes* (S4), 1–26.

Carslaw, H. S. and J. C. Jaeger (1992). *Conduction of heat in solids*. Clarendon Press, Oxford.

Čermák, M., S. Sysala, and J. Valdman (2019). Efficient and flexible matlab implementation of 2d and 3d elastoplastic problems. *Applied Mathematics and Computation 355*, 595–614.

Chan, E. P., Y. Hu, P. M. Johnson, Z. Suo, and C. M. Stafford (2012). Spherical indentation testing of poroelastic relaxations in thin hydrogel layers. *Soft Matter 8*(5), 1492–1498.

Chang, C. and M. D. Zoback (2009). Viscous creep in room-dried unconsolidated gulf of mexico shale (i): Experimental results. *Journal of Petroleum Science and Engineering 69*(3-4), 239–246.

Chen, S. L. and Y. Abousleiman (2010). Time-dependent behaviour of a rigid foundation on a transversely isotropic soil layer. *International Journal for Numerical and Analytical Methods in Geomechanics 34*(9), 937–952.

Chen, S. L., L. M. Zhang, and L. Z. Chen (2005a). The axisymmetric consolidation of a semi-infinite transversely isotropic saturated soil. *International Journal for Numerical and Analytical Methods in Geomechanics 29*(13), 1249–1270.

Chen, S. L., L. M. Zhang, and L. Z. Chen (2005b). Consolidation of a finite transversely isotropic soil layer on a rough impervious base. *Journal of Engineering Mechanics 131*(12), 1279–1290.

Chen, W. F. (2013). *Limit analysis and soil plasticity*. Elsevier.

Cheng, A. H.-D. (2016). *Poroelasticity*. Springer.

Chiarella, C. and J. R. Booker (1975). The time-settlement behaviour of a rigid die resting on a deep clay layer. *The Quarterly Journal of Mechanics and Applied Mathematics 28*(3), 317–328.

Cook, N. G. W., M. Hood, and F. Tsai (1984). Observations of crack growth in hard rock loaded by an indenter. *International Journal of Rock Mechanics and Mining Sciences & Geomechanics Abstracts 21*(2), 97–107.

Cook, R. F. and G. M. Pharr (1990). Direct observation and analysis of indentation cracking in glasses and ceramics. *Journal of the American Ceramic Society 73*(4), 787–817.

Coussy, O. (1995). *Mechanics of porous continua*. Wiley.

Cryer, C. W. (1963). A comparison of the three-dimensional consolidation theories of Biot and Terzaghi. *The Quarterly Journal of Mechanics and Applied Mathematics 16*(4), 401–412.

David, C., J. Wassermann, F. Amann, et al. (2018a). Kg^2b, a collaborative benchmarking exercise for estimating the permeability of the grimsel granodiorite - part 1: measurements,

pressure dependence and pore-fluid effects. *Geophysical Journal International 215*(2), 799–824.

David, C., J. Wassermann, F. Amann, et al. (2018b). Kg^2b, a collaborative benchmarking exercise for estimating the permeability of the grimsel granodiorite - part 2: modelling, microstructures and complementary data. *Geophysical Journal International 215*(2), 825–843.

De Buhan, P. and L. Dormieux (1996). On the validity of the effective stress concept for assessing the strength of saturated porous materials: a homogenization approach. *Journal of the Mechanics and Physics of Solids 44*(10), 1649–1667.

De Josselin De Jong, G. (1957). Application of stress functions to consolidation problems. In *Proceedings of the Fourth International Conference on Soil Mechanics and Foundation Engineering*, London, pp. 320–323.

De Leeuw, E. H. (1965). The theory of three-dimensional consolidation applied to cylindrical bodies. In *Proceedings of the Sixth International Conference on Soil Mechanics and Foundation Engineering*, Volume 1, Montreal, pp. 287–290.

De Souza Neto, E. A., D. Peric, and D. R. J. Owen (2011). *Computational methods for plasticity: theory and applications*. John Wiley & Sons.

Delavoipière, J., Y. Tran, E. Verneuil, and A. Chateauminois (2016). Poroelastic indentation of mechanically confined hydrogel layers. *Soft Matter 12*(38), 8049–8058.

Deresiewicz, H. (1979). Effects of restricted flow at the surface of saturated clay. *International Journal for Numerical and Analytical Methods in Geomechanics 3*(1), 1–11.

Detournay, E. and A. H.-D. Cheng (1993). *Comprehensive Rock Engineering*, Volume 2, Chapter Fundamentals of Poroelasticity, pp. 113–171. New York: Pergamon.

Esteki, M. H., A. A. Alemrajabi, C. Hall, G. K. Sheridan, M. Azadi, and E. Moeendarbary (2019). A new framework for characterization of poroelastic materials using indentation. *Acta Biomaterialia*.

Fowell, R. J. (1993). *Comprehensive Rock Engineering*, Volume 4, Chapter The Mechanics of Rock Cutting, pp. 155–176. Oxford: Pergamon.

Galli, M., K. S. Comley, T. A. Shean, and M. L. Oyen (2009). Viscoelastic and poroelastic mechanical characterization of hydrated gels. *Journal of Materials Research 24*(3), 973–979.

Galli, M. and M. L. Oyen (2008). Spherical indentation of a finite poroelastic coating. *Applied Physics Letters 93*(031911), 1–3.

Galli, M. and M. L. Oyen (2009). Fast identification of poroelastic parameters from indentation tests. *Cmes-Computer Modeling in Engineering & Sciences 48*(3), 241–269.

Gaszynski, J. and G. Szefer (1978). Axisymmetric problem of the punch for the consolidating semi-space with mixed boundary permeability conditions. *Archiwum Mechaniki Stosowanej 30*, 17–26.

Gibson, R. E. and J. Mcnamee (1963). A three-dimensional problem of the consolidation of a semi-infinite clay stratum. *The Quarterly Journal of Mechanics and Applied Mathematics 16*(1), 115–127.

Gibson, R. E., R. L. Schiffman, and S. L. Pu (1970). Plane strain and axially symmetric consolidation of a clay layer on a smooth impervious base. *The Quarterly Journal of Mechanics and Applied Mathematics 23*(4), 505–520.

Han, L., E. H. Frank, J. J. Greene, H. Y. Lee, H. H. K. Hung, A. J. Grodzinsky, and C. Ortiz (2011). Time-dependent nanomechanics of cartilage. *Biophysical Journal 100*(7), 1846–1854.

Harnpattanapanich, T. and I. Vardoulakis (1987). Numerical laplace–fourier transform inversion technique for layered soil consolidation problems; ii, gibson soil layer. *International Journal for Numerical and Analytical Methods in Geomechanics 11*(1), 103–112.

Hart, D. J. (2000). *Laboratory measurements of poroelastic constants and flow parameters and some associated phenomena*. Ph. D. thesis, University of Wisconsin–Madison.

Hart, D. J. and H. F. Wang (1995). Laboratory measurements of a complete set of poroelastic moduli for berea sandstone and indiana limestone. *Journal of Geophysical Research: Solid Earth 100*(B9), 17741–17751.

Hertz, H. (1881). On contact between elastic bodies. *Journal für die Reine und Angewandte Mathematik 92*, 156–171.

Horsrud, P. (2001). Estimating mechanical properties of shale from empirical correlations. *SPE Drill Completion 16*(02), 68–73.

Hu, Y., E. P. Chan, J. J. Vlassak, and Z. Suo (2011). Poroelastic relaxation indentation of thin layers of gels. *Journal of Applied Physics 110*(086103), 1–3.

Hu, Y., J. You, D. T. Auguste, Z. Suo, and J. J. Vlassak (2012). Indentation: A simple, nondestructive method for characterizing the mechanical and transport properties of ph-sensitive hydrogels. *Journal of Materials Research 27*(1), 152–160.

Hu, Y., X. Zhao, J. J. Vlassak, and Z. Suo (2010). Using indentation to characterize the poroelasticity of gels. *Applied Physics Letters 96*(121904), 1–3.

Islam, M. R. and M. L. Oyen (2021). A poroelastic master curve for time-dependent and multiscale mechanics of hydrogels. *Journal of Materials Research*.

Jana, R. N. (1965). Indentation of a semi-infinite fluid-saturated poroelastic medium by an undeformable porous punch. *Applied Scientific Research, Section A 14*(1), 361–378.

Johnson, K. L. (1987). *Contact mechanics*. Cambridge University Press.

Kalcioglu, Z. I., R. Mahmoodian, Y. Hu, Z. Suo, and K. J. Van V. (2012). From macro-to microscale poroelastic characterization of polymeric hydrogels via indentation. *Soft Matter 8*(12), 3393–3398.

Khalili, N. and B. Loret (2001). An elasto-plastic model for non-isothermal analysis of flow and deformation in unsaturated porous media: formulation. *International Journal of Solids and Structures 38*(46-47), 8305–8330.

Kim, J. and A. P. S. Selvadurai (2016). A note on the consolidation settlement of a rigid circular foundation on a poroelastic halfspace. *International Journal for Numerical and Analytical Methods in Geomechanics 40*(14), 2003–2016.

Kranz, R. L., J. S. Saltzman, and J. D. Blacic (1990). Hydraulic diffusivity measurements on laboratory rock samples using an oscillating pore pressure method. *International Journal of Rock Mechanics and Mining Sciences & Geomechanics Abstracts 27*(5), 345–352.

Lai, Y. and Y. Hu (2017). Unified solution for poroelastic oscillation indentation on gels for spherical, conical and cylindrical indenters. *Soft Matter 13*(4), 852–861.

Lai, Y. and Y. Hu (2018). Probing the swelling-dependent mechanical and transport properties of polyacrylamide hydrogels through afm-based dynamic nanoindentation. *Soft Matter 14*(14), 2619–2627.

Lan, Q. and A. P. S. Selvadurai (1996). Interacting indentors on a poroelastic half space. *Zeitschrift für angewandte Mathematik und Physik ZAMP 47*(5), 695–716.

Lawn, B. (1993). *Fracture of brittle solids*. Cambridge University Press.

Lawn, B. R. (1998). Indentation of ceramics with spheres: a century after Hertz. *Journal of the American Ceramic Society 81*(8), 1977–1994.

Lewis, R. W. and B. A. Schrefler (1998). *The finite element method in the static and dynamic deformation and consolidation of porous media*. John Wiley.

Liu, M. and H. Huang (2016). Sphere indentation-the hertzian stress field and the effect of far-field confining stress. In *50th US Rock Mechanics/Geomechanics Symposium*. American Rock Mechanics Association.

Liu, M. and H. Huang (2018). Poroelastic response of spherical-tip indentation. In *52nd US Rock Mechanics/Geomechanics Symposium*. American Rock Mechanics Association.

Liu, M. and H. Huang (2019a). Poroelastic response of spherical indentation - step displacement loading. In *53rd US Rock Mechanics/Geomechanics Symposium*. American Rock Mechanics Association.

Liu, M. and H. Huang (2019b). Poroelastic response of spherical indentation into a half space with a drained surface via step displacement. *International Journal of Solids and Structures 165*, 34–49.

Liu, M. and H. Huang (2021). Poroelastic response of spherical indentation into a half-space with an impermeable surface via step displacement, first-round revision. *Journal of the Mechanics and Physics of Solids*.

Love, A. E. H. (1929). Ix. the stress produced in a semi-infinite solid by pressure on part of the boundary. *Philosophical Transactions of the Royal Society of London. Series A, Containing Papers of a Mathematical or Physical Character 228*(659-669), 377–420.

Mak, A. F., W. M. Lai, and V. C. Mow (1987). Biphasic indentation of articular cartilage i: Theoretical analysis. *Journal of Biomechanics 20*(7), 703–714.

Makhnenko, R. Y. and J. F. Labuz (2016). Elastic and inelastic deformation of fluid-saturated rock. *Philosophical Transactions of the Royal Society A: Mathematical, Physical and Engineering Sciences 374*(2078).

Mandel, J. (1953). Consolidation des sols (étude mathématique). *Géotechnique 3*(7), 287–299.

Marshall, D. B., R. F. Cook, N. P. Padture, M. L. Oyen, A. Pajares, J. E. Bradby, I. E. Reimanis, R. Tandon, T. F. Page, G. M. Pharr, and B. R. Law (2015). The compelling case for indentation as a functional exploratory and characterization tool. *Journal of the American Ceramic Society 98*(9), 2671–2680.

Mattice, J. M., A. G. Lau, M. L. Oyen, and R. W. Kent (2006). Spherical indentation load-relaxation of soft biological tissues. *Journal of Materials Research 21*(8), 2003–2010.

McNamee, J. and R. E. Gibson (1960a). Displacement functions and linear transforms applied to diffusion through porous elastic media. *The Quarterly Journal of Mechanics and Applied Mathematics 13*(1), 98–111.

McNamee, J. and R. E. Gibson (1960b). Plane strain and axially symmetric problems of the consolidation of a semi-infinite clay stratum. *The Quarterly Journal of Mechanics and Applied Mathematics 13*(2), 210–227.

Moeendarbary, E., L. Valon, M. Fritzsche, A. R. Harris, D. A. Moulding, A. J. Thrasher, E. Stride, L. Mahadevan, and G. T. Charras (2013). The cytoplasm of living cells behaves as a poroelastic material. *Nature Materials 12*(3), 253.

Murad, M. A. and A. F. Loula (1992). Improved accuracy in finite element analysis of Biot's consolidation problem. *Computer Methods in Applied Mechanics and Engineering 95*(3), 359–382.

Murad, M. A. and A. F. Loula (1994). On stability and convergence of finite element approximations of Biot's consolidation problem. *International Journal for Numerical Methods in Engineering 37*(4), 645–667.

Noble, B. (1963). The solution of bessel function dual integral equations by a multiplying-factor method. *Mathematical Proceedings of the Cambridge Philosophical Society 59*(2), 351–362.

Olson, R. E. (1986). State of the art: consolidation testing. In *Consolidation of Soils: Testing and Evaluation*. ASTM International.

Olver, F. W. (2010). *NIST handbook of mathematical functions hardback and CD-ROM*. Cambridge University Press.

Oyen, M. L. (2008). Poroelastic nanoindentation responses of hydrated bone. *Journal of Materials Research 23*(5), 1307–1314.

Oyen, M. L. (2014). Mechanical characterisation of hydrogel materials. *International Materials Reviews 59*(1), 44–59.

Paria, G. (1957). Axisymmetric consolidation for a porous elastic material containing a fluid. *Journal of Mathematics and Physics 36*(1-4), 338–346.

Pariseau, W. G. (1999). Poroelastic-plastic consolidation-analytical solution. *International Journal for Numerical and Analytical Methods in Geomechanics 23*(7), 577–594.

Poularikas, A. D. (2018). *Transforms and applications handbook*. CRC press.

Rice, J. R. (1977). Pore pressure effects in inelastic constitutive formulations for fissured rock masses. In *ASCE Advances in Civil Engineering Through Engineering Mechanics*, pp. 295–297. New York: American Society of Civil Engineers.

Rowe, P. W. and L. Barden (1966). A new consolidation cell. *Geotechnique 16*(2), 162–170.

Sanyal, D. C. (1972). On the two-dimensional deformation of a semi-infinite porous elastic medium. *Applied Scientific Research 26*(1), 227–245.

Schiffman, R. L. and A. A. Fungaroli (1965). Consolidation due to tangential loads. In *Proceedings of the Sixth International Conference on Soil Mechanics and Foundation Engineering*, Volume 1, Montreal, pp. 188–192.

Schiffman, R. L. and A. A. Fungaroli (1973). Pore pressure and effective stress generation due to slowly moving loads. *Geotechnique 23*(2), 271–278.

Selvadurai, A. P. S. and P. Samea (2020). On the indentation of a poroelastic halfspace. *International Journal of Engineering Science 149*, 103246.

Selvadurai, A. P. S. and A. P. Suvorov (2012). Boundary heating of poro-elastic and poro-elasto-plastic spheres. *Proceedings of the Royal Society A: Mathematical, Physical and Engineering Sciences 468*(2145), 2779–2806.

Selvadurai, A. P. S. and A. P. Suvorov (2014). Thermo-poromechanics of a fluid-filled cavity in a fluid-saturated geomaterial. *Proceedings of the Royal Society A: Mathematical, Physical and Engineering Sciences 470*(2163), 20130634.

Selvadurai, A. P. S. and Z. Q. Yue (1994). On the indentation of a poroelastic layer. *International Journal for Numerical and Analytical Methods in Geomechanics 18*(3), 161–175.

Singh, S. J., R. Kumar, and S. Rani (2009). Consolidation of a poroelastic half-space with anisotropic permeability and compressible constituents by axisymmetric surface loading. *Journal of Earth System Science 118*(5), 563.

Singh, S. J. and S. Rani (2006). Plane strain deformation of a multi-layered poroelastic half-space by surface loads. *Journal of Earth System Science 115*(6), 685–694.

Singh, S. J., S. Rani, and R. Kumar (2007). Quasi-static deformation of a poroelastic half-space with anisotropic permeability by two-dimensional surface loads. *Geophysical Journal International 170*(3), 1311–1327.

Stehfest, H. (1970). Algorithm 368: Numerical inversion of laplace transforms [d5]. *Communications of the ACM 13*(1), 47–49.

Suarez-Rivera, R., M. Chertov, D. M. Willberg, S. J. Green, and J. Keller (2012). Understanding permeability measurements in tight shales promotes enhanced determination of reservoir quality. In *SPE Canadian Unconventional Resources Conference*. Society of Petroleum Engineers.

Suvorov, A. P. and A. P. S. Selvadurai (2019). The biot coefficient for an elasto-plastic material. *International Journal of Engineering Science 145*, 103166.

Taljat, B. and G. M. Pharr (2004). Development of pile-up during spherical indentation of elastic–plastic solids. *International Journal of Solids and Structures 41*(14), 3891–3904.

Terzaghi, K. (1943). *Theoretical soil mechanics*. John Wiley & Sons, Inc.

Tinni, A., E. Fathi, R. Agarwal, et al. (2012). Shale permeability measurements on plugs and crushed samples. In *SPE Canadian Unconventional Resources Conference*. Society of Petroleum Engineers.

Vardoulakis, I. and T. Harnpattanapanich (1986). Numerical laplace-fourier transform inversion technique for layered-soil consolidation problems: I. fundamental solutions and validation. *International Journal for Numerical and Analytical Methods in Geomechanics 10*(4), 347–365.

Vermeer, P. A. and A. Verruijt (1981). An accuracy condition for consolidation by finite elements. *International Journal for Numerical and Analytical Methods in Geomechanics 5*(1), 1–14.

Verruijt, A. (1971). Displacement functions in the theory of consolidation or in thermoelasticity. *Zeitschrift für angewandte Mathematik und Physik ZAMP 22*(5), 891–898.

Verruijt, A. (2013). *Theory and problems of poroelasticity*. Delft University of Technology.

Wahlquist, J. A., F. W. DelRio, M. A. Randolph, A. H. Aziz, C. M. Heveran, S. J. Bryant, C. P. Neu, and V. L. Ferguson (2017). Indentation mapping revealed poroelastic, but not viscoelastic, properties spanning native zonal articular cartilage. *Acta Biomaterialia 64*, 41–49.

Wang, H. F. (2000). *Theory of linear poroelasticity with applications to geomechanics and hydrogeology*. Princeton University Press.

White, J. A. and R. I. Borja (2008). Stabilized low-order finite elements for coupled solid-deformation/fluid-diffusion and their application to fault zone transients. *Computer Methods in Applied Mechanics and Engineering 197*(49-50), 4353–4366.

Wriggers, P. (2006). *Computational contact mechanics*. Springer.

Wriggers, P. and M. Imhof (1993). On the treatment of nonlinear unilateral contact problems. *Archive of Applied Mechanics 63*(2), 116–129.

Wynn, P. (1956). On a device for computing the $e_m(s_n)$ transformation. *Mathematical Tables and Other Aids to Computation*, 91–96.

Xie, S. Y. and J. F. Shao (2012). Experimental investigation and poroplastic modelling of saturated porous geomaterials. *International Journal of Plasticity 39*, 27–45.

Yue, Z. Q. and A. P. S. Selvadurai (1994). On the asymmetric indentation of a consolidating poroelastic half space. *Applied Mathematical Modelling 18*(4), 170–185.

Yue, Z. Q. and A. P. S. Selvadurai (1995). Contact problem for saturated poroelastic solid. *Journal of Engineering Mechanics 121*(4), 502–512.

Zemyan, S. M. (2012). Fredholm integral equations of the second kind (general kernel). In *The Classical Theory of Integral Equations*. Springer.

Zhao, Y. and R. I. Borja (2020). A continuum framework for coupled solid deformation–fluid flow through anisotropic elastoplastic porous media. *Computer Methods in Applied Mechanics and Engineering 369*, 113225.

Zienkiewicz, O. C., A. H. C. Chan, M. Pastor, D. K. Paul, and T. Shiomi (1990). Static and dynamic behaviour of soils: a rational approach to quantitative solutions. I. Fully saturated problems. *Proceedings of the Royal Society of London. Series A, Mathematical and Physical Sciences 429*(1877), 285–309.

A Additional Results for Chapter 2

A.1 Additional Stress and Displacement Fields

In addition to the pore pressure, vertical stress and displacement fields in Section 2.5, here we provide the expressions for the remaining non-trivial stress and displacement fields in the Laplace domain and their asymptotes at the undrained and drained limits in the time domain. Similar to Section 2.5, two sets of expressions are provided for the field quantities.

A.1.1 Radial Stress

Expression 1

$$\begin{aligned}\overline{\sigma}_r = \frac{2Ga^3}{c\phi R s_*}\Bigg\{&\int_0^1 \left(m_*^2-1\right)\begin{bmatrix} N_{sr1}\left(s_*,r_*,m_*,z_*\right) \\ +N_{sr2}\left(s_*,r_*,m_*,z_*\right)\end{bmatrix} dm_* \\ &+\int_1^\infty m_*^{\frac{1}{2}}\theta_1\left(s_*,m_*\right)\begin{bmatrix} N_{sr1}\left(s_*,r_*,m_*,z_*\right) \\ +N_{sr2}\left(s_*,r_*,m_*,z_*\right)\end{bmatrix} dm_*\Bigg\}\end{aligned} \tag{A.1}$$

where,

$$\begin{aligned}N_{sr1}\left(s_*,r_*,m_*,z_*\right) = \frac{2}{\pi}\int_0^\infty \xi_*\Bigg\{&\left(z_*\xi_*-1\right)\exp\left(-z_*\xi_*\right)+\frac{2\omega}{1+\omega}\exp\left(-z_*\sqrt{\xi_*^2+s_*}\right) \\ +\frac{2\omega}{1+\omega}\left(\frac{\xi_*^2}{s_*}\right)&\left[\exp\left(-z_*\sqrt{\xi_*^2+s_*}\right)-\frac{\sqrt{\xi_*^2+s_*}}{\xi_*}\exp\left(-z_*\xi_*\right)\right]\Bigg\}\cos\left(m_*\xi_*\right)J_0\left(r_*\xi_*\right)d\xi_*\end{aligned} \tag{A.2}$$

$$\begin{aligned}N_{sr2}\left(s_*,r_*,m_*,z_*\right) = -\frac{2}{\pi}\frac{1}{r_*}\int_0^\infty \Bigg\{&\left(1-\phi+z_*\xi_*\right)\exp\left(-z_*\xi_*\right) \\ +\frac{2\omega}{1+\omega}\left(\frac{\xi_*^2}{s_*}\right)&\left[\exp\left(-z_*\sqrt{\xi_*^2+s_*}\right)-\frac{\sqrt{\xi_*^2+s_*}}{\xi_*}\exp\left(-z_*\xi_*\right)\right]\Bigg\}\cos\left(m_*\xi_*\right)J_1\left(r_*\xi_*\right)d\xi_*\end{aligned} \tag{A.3}$$

Expression 2 The second expression for $\overline{\sigma}_r$ can be derived by decomposing $\overline{\sigma}_r$ into $\overline{\sigma}_r = \overline{\sigma}_{r1}+\overline{\sigma}_{r2}$, where $\overline{\sigma}_{r1}$ and $\overline{\sigma}_{r2}$ correspond to the parts of the equation containing N_{sr1} and N_{sr2}

in Eq. A.1, respectively. On the surface ($z_* = 0$), applying Eq. 2.27 to $\overline{\sigma}_{r1}$, we obtain,

$$\int_{x_*}^{\infty} \overline{\sigma}_{r1} \frac{r_* dr_*}{\sqrt{r_*^2 - x_*^2}} = \int_{x_*}^{\infty} \overline{\sigma}_z \frac{r_* dr_*}{\sqrt{r_*^2 - x_*^2}} + \frac{2G\left(1-2\eta\right) a^3}{c\eta R s_*} \theta_1\left(s_*, x_*\right) x_*^{\frac{1}{2}} \tag{A.4}$$

Applying the inverse Abel transform gives,

$$\overline{\sigma}_{r1} = \overline{\sigma}_z + \frac{2G\left(2\eta-1\right) a^3}{\pi c\eta R s_*} \int_{r_*}^{\infty} \frac{2\theta_3\left(s_*, x_*\right) dx_*}{\sqrt{x_*^2 - r_*^2}} \tag{A.5}$$

Similarly, $\overline{\sigma}_{r2}$ can be expressed as follows, at $r_* \leq 1$,

$$\begin{aligned} \overline{\sigma}_{r2} = -\frac{2G\left(2\eta-1\right) a^3}{\pi c\eta R s_*} \Bigg\{ & \int_{r_*}^{1} \left[\begin{array}{c} \theta_1\left(s_*, x_*\right) x_*^{-\frac{1}{2}} + \theta_2\left(s_*, x_*\right) x_*^{-2} \\ + \dfrac{1}{2\eta-1}\left(x_* - x_*^{-1}\right) \end{array} \right] \frac{dx_*}{\sqrt{x_*^2 - r_*^2}} \\ & + \int_{1}^{\infty} \left[\frac{2\eta}{2\eta-1} \theta_1\left(s_*, x_*\right) x_*^{-\frac{1}{2}} + \theta_2\left(s_*, x_*\right) x_*^{-2} \right] \frac{dx_*}{\sqrt{x_*^2 - r_*^2}} \Bigg\} \end{aligned} \tag{A.6}$$

and at $r_* \geq 1$,

$$\overline{\sigma}_{r2} = -\frac{2G\left(2\eta-1\right) a^3}{\pi c\eta R s_*} \int_{r_*}^{\infty} \left[\frac{2\eta}{2\eta-1} \theta_1\left(s_*, x_*\right) x_*^{-\frac{1}{2}} + \theta_2\left(s_*, x_*\right) x_*^{-2} \right] \frac{dx_*}{\sqrt{x_*^2 - r_*^2}} \tag{A.7}$$

Expressions for $\theta_2\left(s_*, x_*\right)$ and $\theta_3\left(s_*, x_*\right)$ are given in Appendix A.3.

Inside the half space ($z_* > 0$), the alternative expressions for $\overline{\sigma}_r$ and other poroelastic fields from the sections below can be determined using the similar procedures outlined in Section 2.5. They are therefore omitted here.

A.1.2 Tangential Stress

Expression 1

$$\begin{aligned}\overline{\sigma}_{\theta} = \frac{2Ga^3}{c\phi Rs_*}\Bigg\{&\int_0^1 \left(m_*^2-1\right)\begin{bmatrix} N_{s\theta 1}\left(s_*,r_*,m_*,z_*\right) \\ -N_{sr2}\left(s_*,r_*,m_*,z_*\right)\end{bmatrix} dm_* \\ &+\int_1^{\infty} m_*^{\frac{1}{2}}\theta_1\left(s_*,m_*\right)\begin{bmatrix} N_{s\theta 1}\left(s_*,r_*,m_*,z_*\right) \\ -N_{sr2}\left(s_*,r_*,m_*,z_*\right)\end{bmatrix} dm_*\Bigg\}\end{aligned} \tag{A.8}$$

where,

$$\begin{aligned}N_{s\theta 1}\left(s_*,r_*,m_*,z_*\right) = \frac{2}{\pi}\int_0^{\infty}\xi_*\Bigg[&\frac{2\omega}{1+\omega}\exp\left(-z_*\sqrt{\xi_*^2+s_*}\right) \\ &-\left(2-\phi\right)\exp\left(-z_*\xi_*\right)\Bigg]\cos\left(m_*\xi_*\right)J_0\left(r_*\xi_*\right)d\xi_*\end{aligned} \tag{A.9}$$

Expression 2 Let $\overline{\sigma}_{\theta} = \overline{\sigma}_{\theta 1}+\overline{\sigma}_{\theta 2}$, where $\overline{\sigma}_{\theta 1}$ and $\overline{\sigma}_{\theta 2}$ are the parts of the equations containing $N_{s\theta 1}$ and N_{sr2} in Eq. A.8, respectively. We have $\overline{\sigma}_{\theta 2} = -\overline{\sigma}_{r2}$. On the surface ($z_* = 0$), applying Eq. 2.27 to $\overline{\sigma}_{\theta 1}$ gives,

$$\int_{x_*}^{\infty}\overline{\sigma}_{\theta 1}\frac{r_*dr_*}{\sqrt{r_*^2-x_*^2}} = \frac{2-2\eta}{1-2\eta}\int_{x_*}^{\infty}\overline{\sigma}_z\frac{r_*dr_*}{\sqrt{r_*^2-x_*^2}} + \frac{2G\left(1-\eta\right)a^3}{c\eta Rs_*}\theta_1\left(s_*,x_*\right)x_*^{\frac{1}{2}} \tag{A.10}$$

Applying the inverse Abel transform gives,

$$\overline{\sigma}_{\theta 1} = \frac{2-2\eta}{1-2\eta}\overline{\sigma}_z + \frac{2G\left(\eta-1\right)a^3}{\pi c\eta Rs_*}\int_{r_*}^{\infty}\frac{2\theta_3\left(s_*,x_*\right)dx_*}{\sqrt{x_*^2-r_*^2}} \tag{A.11}$$

A.1.3 Shear Stress

Expression 1

$$\begin{aligned}\overline{\sigma}_{zr} = \frac{2Ga^3}{c\phi Rs_*}\Bigg[&\int_0^1\left(m_*^2-1\right)N_{szr}\left(s_*,r_*,m_*,z_*\right)dm_* \\ &+\int_1^{\infty}m_*^{\frac{1}{2}}\theta_1\left(s_*,m_*\right)N_{szr}\left(s_*,r_*,m_*,z_*\right)dm_*\Bigg]\end{aligned} \tag{A.12}$$

where,

$$N_{szr}\left(s_*, r_*, m_*, z_*\right) = -\frac{2}{\pi}\int_0^\infty \xi_* \left\{ z_*\xi_* \exp\left(-z_*\xi_*\right) + \frac{2\omega}{1+\omega}\frac{\xi_*\sqrt{\xi_*^2+s_*}}{s_*}\left[\exp\left(-z_*\sqrt{\xi_*^2+s_*}\right) - \exp\left(-z_*\xi_*\right)\right]\right\} \cos\left(m_*\xi_*\right) J_1\left(r_*\xi_*\right) d\xi_* \tag{A.13}$$

On the surface ($z_* = 0$), $\overline{\sigma}_{zr} = 0$. The second set expression for shear stress for $z_* > 0$ is omitted here.

A.1.4 Radial Displacement

Expression 1

$$\overline{u}_r = \frac{a^4}{c\phi R s_*}\left[\int_0^1 \left(m_*^2 - 1\right) N_{ur}\left(s_*, r_*, m_*, z_*\right) dm_* + \int_1^\infty m_*^{\frac{1}{2}} \theta_1\left(s_*, m_*\right) N_{ur}\left(s_*, r_*, m_*, z_*\right) dm_*\right] \tag{A.14}$$

where,

$$N_{ur}\left(s_*, r_*, m_*, z_*\right) = -\frac{2}{\pi}\int_0^\infty \left\{ \left(1 - \phi + z_*\xi_*\right) \exp\left(-z_*\xi_*\right) + \frac{2\omega}{1+\omega}\left(\frac{\xi_*^2}{s_*}\right)\left[\exp\left(-z_*\sqrt{\xi_*^2+s_*}\right) - \frac{\sqrt{\xi_*^2+s_*}}{\xi_*}\exp\left(-z_*\xi_*\right)\right]\right\} \cos\left(m_*\xi_*\right) J_1\left(r_*\xi_*\right) d\xi_* \tag{A.15}$$

Expression 2 Only the expression on the surface ($z_* = 0$) is given here. At $r_* \leq 1$,

$$\overline{u}_r = -\frac{\left(2\eta - 1\right) a^4 r_*}{\pi c \eta R s_*}\left\{\int_{r_*}^1 \left[\begin{array}{c}\theta_1\left(s_*, x_*\right) x_*^{-\frac{1}{2}} + \theta_2\left(s_*, x_*\right) x_*^{-2} \\ + \frac{1}{2\eta - 1}\left(x_* - x_*^{-1}\right)\end{array}\right] \frac{dx_*}{\sqrt{x_*^2 - r_*^2}} + \int_1^\infty \left[\frac{2\eta}{2\eta - 1}\theta_1\left(s_*, x_*\right) x_*^{-\frac{1}{2}} + \theta_2\left(s_*, x_*\right) x_*^{-2}\right] \frac{dx_*}{\sqrt{x_*^2 - r_*^2}}\right\} \tag{A.16}$$

and at $r_* \geq 1$,

$$\overline{u}_r = -\frac{(2\eta - 1)\, a^4 r_*}{\pi c \eta R s_*} \int_{r_*}^{\infty} \left[\frac{2\eta}{2\eta - 1} \theta_1 \left(s_*, x_* \right) x_*^{-\frac{1}{2}} + \theta_2 \left(s_*, x_* \right) x_*^{-2} \right] \frac{dx_*}{\sqrt{x_*^2 - r_*^2}} \tag{A.17}$$

A.1.5 Undrained and Drained Asymptotes

	undrained asymptotes ($t \to 0$)
αp	$\frac{4\eta\omega Ga}{\phi(1+\omega)R}\int_0^1 \left(1-m_*^2\right) I_2 dm_*$
σ_z	$\frac{2Ga}{\phi R}\int_0^1 \left(1-m_*^2\right)\left(I_2+z_* I_3\right) dm_*$
σ_r	$\frac{2Ga}{\phi R}\int_0^1 \left(1-m_*^2\right)\left[I_2 - z_* I_3 + (1-\phi) I_4 + z_* I_5\right] dm_*$
σ_θ	$-\frac{2Ga}{\phi R}\int_0^1 \left(1-m_*^2\right)\left[(\phi-2) I_2 + (1-\phi) I_4 + z_* I_5\right] dm_*$
σ_{zr}	$\frac{2Ga}{\phi R} r_* z_* \int_0^1 \left(1-m_*^2\right) I_6 dm_*$
u_z	$\frac{a^2}{\phi R}\int_0^1 \left(1-m_*^2\right)\left(\phi I_1 + z_* I_2\right) dm_*$
u_r	$\frac{a^2}{\phi R} r_* \int_0^1 \left(1-m_*^2\right)\left[(1-\phi) I_4 + z_* I_5\right] dm_*$

Table A.1: Undrained asymptotes of the poroelastic fields.

	drained asymptotes ($t \to \infty$)
αp	0
σ_z	$\dfrac{G\,(2\eta-1)\,a}{\eta R}\int_0^1 \left(1-m_*^2\right)\left(I_2+z_* I_3\right) dm_*$
σ_r	$\dfrac{G\,(2\eta-1)\,a}{\eta R}\int_0^1 \left(1-m_*^2\right)\left(I_2-z_* I_3+\dfrac{1}{1-2\eta} I_4+z_* I_5\right) dm_*$
σ_θ	$-\dfrac{Ga}{\eta R}\int_0^1 \left(1-m_*^2\right)\left[(2-2\eta)\,I_2-I_4+(2\eta-1)\,z_* I_5\right] dm_*$
σ_{zr}	$\dfrac{G\,(2\eta-1)\,a}{\eta R} r_* z_* \int_0^1 \left(1-m_*^2\right) I_6 dm_*$
u_z	$\dfrac{a^2}{R}\int_0^1 \left(1-m_*^2\right)\left[I_1-\left(\dfrac{1-2\eta}{2\eta}\right) z_* I_2\right] dm_*$
u_r	$-\dfrac{a^2}{2R} r_* \int_0^1 \left(1-m_*^2\right)\left[\dfrac{1}{\eta} I_4+\left(\dfrac{1-2\eta}{\eta}\right) z_* I_5\right] dm_*$

Table A.2: Drained asymptotes of the poroelastic fields.

I_1	$\frac{2}{\pi}\int_0^\infty \exp\left(-z_*\xi_*\right)\cos\left(m_*\xi_*\right)J_0\left(r_*\xi_*\right)d\xi_*$ $= \frac{2}{\pi}\mathrm{Re}\left\{\left[\left(z_*+im_*\right)^2+r_*^2\right]^{-\frac{1}{2}}\right\}$
I_2	$\frac{2}{\pi}\int_0^\infty \xi_*\exp\left(-z_*\xi_*\right)\cos\left(m_*\xi_*\right)J_0\left(r_*\xi_*\right)d\xi_*$ $= \frac{2}{\pi}\mathrm{Re}\left\{\left(z_*+im_*\right)\left[\left(z_*+im_*\right)^2+r_*^2\right]^{-\frac{3}{2}}\right\}$
I_3	$\frac{2}{\pi}\int_0^\infty \xi_*^2\exp\left(-z_*\xi_*\right)\cos\left(m_*\xi_*\right)J_0\left(r_*\xi_*\right)d\xi_*$ $= \frac{2}{\pi}\mathrm{Re}\left\{\begin{array}{c}3\left(z_*+im_*\right)^2\left[\left(z_*+im_*\right)^2+r_*^2\right]^{-\frac{5}{2}} \\ -\left[\left(z_*+im_*\right)^2+r_*^2\right]^{-\frac{3}{2}}\end{array}\right\}$
I_4	$\frac{2}{\pi r_*}\int_0^\infty \exp\left(-z_*\xi_*\right)\cos\left(m_*\xi_*\right)J_1\left(r_*\xi_*\right)d\xi_*$ $= \frac{2}{\pi r_*^2}\mathrm{Re}\left\{1-\left(z_*+im_*\right)\left[\left(z_*+im_*\right)^2+r_*^2\right]^{-\frac{1}{2}}\right\}$
I_5	$\frac{2}{\pi r_*}\int_0^\infty \xi_*\exp\left(-z_*\xi_*\right)\cos\left(m_*\xi_*\right)J_1\left(r_*\xi_*\right)d\xi_*$ $= \frac{2}{\pi}\mathrm{Re}\left\{\left[\left(z_*+im_*\right)^2+r_*^2\right]^{-\frac{3}{2}}\right\}$
I_6	$\frac{2}{\pi r_*}\int_0^\infty \xi_*^2\exp\left(-z_*\xi_*\right)\cos\left(m_*\xi_*\right)J_1\left(r_*\xi_*\right)d\xi_*$ $= \frac{2}{\pi}\mathrm{Re}\left\{3\left(z_*+im_*\right)\left[\left(z_*+im_*\right)^2+r_*^2\right]^{-\frac{5}{2}}\right\}$

Table A.3: Expressions of $I_1\left(z_*,m_*,r_*\right)-I_6\left(z_*,m_*,r_*\right)$.

A.2 Contour Integration

The application of the method of contour integration for rewriting an integral with an oscillatory kernel is illustrated here. For example, the last term in Eq. 2.88 can be written in form of,

$$\int_0^\infty \xi_*^2 \sqrt{\xi_*^2 + s_*} \exp\left(-z_* \xi_*\right) \sin\left(y \xi_*\right) d\xi_* \tag{A.18}$$

This is the imaginary part of,

$$\int_\infty^0 \xi_*^2 \sqrt{\xi_*^2 + s_*} \exp\left[-\left(z_* + iy\right) \xi_*\right] d\xi_* \tag{A.19}$$

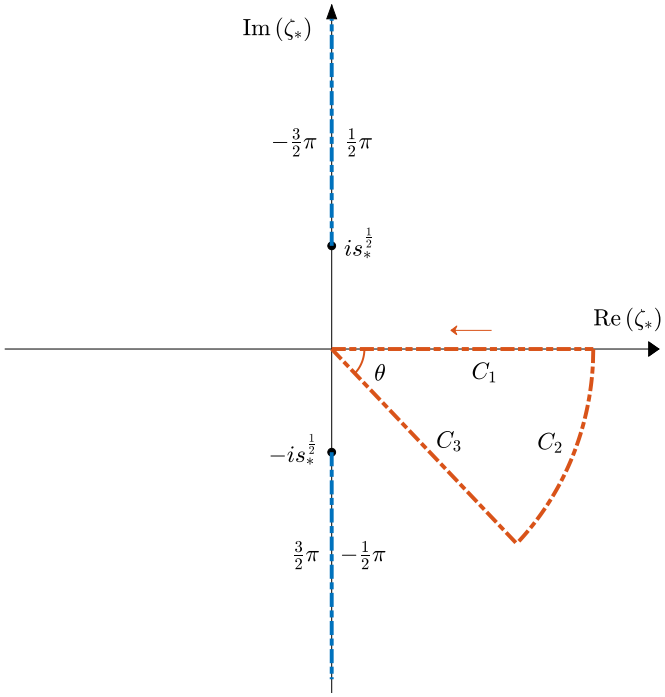

Figure A.1: Integration contour (red dashed lines) and branch cuts (blue dashed lines) in the complex plane. In the contour, $\theta = \arctan\left(y/z_*\right)$; C_1 is the path from ∞ to 0 in the negative direction of the real axis; C_3 is a ray with an angle of θ with respect to the horizontal axis; and C_2 is a circular arc connecting the end point of path C_3 to the stating point of path C_1.

Since the integrand in Eq. A.19 is analytical inside the domain enclosed by the contour $C_1 +$

C_2+C_3, see Fig. A.1, integration along the closed contour should be zero. In addition, according to Jordan's lemma, the integral over the circular arc C_2 does not contribute. Therefore, the integral along C_1 (Eq. A.19) equals to the negative value of the integral along path C_3,

$$-\int_{C_3} \zeta_*^2 \sqrt{\zeta_*^2 + s_*} \exp\left[-\left(z_* + iy\right)\zeta_*\right] d\zeta_* \tag{A.20}$$

Path C_3 can be parameterized as $\zeta_* = \left(z_* - iy\right)\xi_*$. Eq. A.20 then becomes,

$$\left(iy - z_*\right)^3 \int_0^\infty \xi_*^2 \sqrt{\left(z_* - iy\right)^2 \xi_*^2 + s_*} \exp\left[-\left(z_*^2 + y^2\right)\xi_*\right] d\xi_* \tag{A.21}$$

Thus, Eq. A.18 equals to the imaginary part of Eq. A.21, where the oscillatory nature is no longer present.

A.3 Expressions for $\theta_{2-3}\left(s, x\right)$

Functions $\theta_i\left(s, x\right)$, $i = 2, 3$, can be evaluated from direct integration of the following integrals,

$$\begin{aligned}\theta_i\left(s, x\right) = \omega \Bigg[&\int_0^1 \left(m^2 - 1\right) N_i\left(s, x, m\right) dm \\ &+ \int_1^\infty m^{\frac{1}{2}} \theta_1\left(s, m\right) N_i\left(s, x, m\right) dm \Bigg]\end{aligned} \tag{A.22}$$

where $N_i\left(s, x, m\right)$ can be calculated as follows,

$$N_2\left(s, x, m\right) = \mathrm{Sign}\left(x - m\right) \frac{\mathrm{M}_1\left(y_1\right)}{y_1} + \frac{\mathrm{M}_1\left(y_2\right)}{y_2} + \left(\frac{1+\omega}{\omega}\right)\left(1 - \phi\right)\mathcal{H}\left(x - m\right) \tag{A.23}$$

with $y_1 = \left|x - m\right| s^{\frac{1}{2}}$ and $y_2 = \left(x + m\right) s^{\frac{1}{2}}$.

$$\begin{aligned}N_3\left(s, x, m\right) = \mathrm{Sign}\left(x - m\right) s \Bigg\{ &-\frac{2}{\pi y_1} + \mathrm{M}_0\left(y_1\right)\frac{3}{y_1^2} - \mathrm{M}_1\left(y_1\right)\left(\frac{6}{y_1^3} + \frac{1}{y_1}\right)\Bigg\} \\ + s \Bigg\{ &-\frac{2}{\pi y_2} + \mathrm{M}_0\left(y_2\right)\frac{3}{y_2^2} - \mathrm{M}_1\left(y_2\right)\left(\frac{6}{y_2^3} + \frac{1}{y_2}\right)\Bigg\}\end{aligned} \tag{A.24}$$

A.4 Closed Form Expressions

The following equations are used to derive the closed form expressions for $M(s_*, x_*)$ and $\int_0^1 x_*^{\frac{1}{2}} M(s_*, x_*)\, dx_*$. Two recurrence relationships of the modified Struve functions of the second kind will be used,

$$\mathrm{M}_1(y) = \mathrm{M}_0'(y) - \frac{2}{\pi} \tag{A.25}$$

$$\mathrm{M}_0(y) = \frac{\mathrm{M}_1(y)}{y} + \mathrm{M}_1'(y) \tag{A.26}$$

An indefinite integral for $\mathrm{M}_0(y)$ will also be used,

$$\int \mathrm{M}_0(y)\, dy = \frac{1}{\pi} y^2 \mathrm{F}_{2,3}\left[\begin{array}{c}(1,1)\\(1.5,1.5,2)\end{array}, \frac{y^2}{4}\right] - y\mathrm{F}_{1,2}\left[\begin{array}{c}0.5\\(1,1.5)\end{array}, \frac{y^2}{4}\right] \tag{A.27}$$

where $\mathrm{F}_{1,2}[\cdot]$ and $\mathrm{F}_{2,3}[\cdot]$ are two generalized hypergeometric functions. Eq. A.27 is derived based on the fact that,

$$\mathrm{M}_0(y) = \mathrm{L}_0(y) - \mathrm{I}_0(y) \tag{A.28}$$

$$\int \mathrm{L}_0(y)\, dy = \frac{1}{\pi} y^2 \mathrm{F}_{2,3}\left[\begin{array}{c}(1,1)\\(1.5,1.5,2)\end{array}, \frac{y^2}{4}\right] \tag{A.29}$$

$$\int I_0(y)\, dy = y\mathrm{F}_{1,2}\left[\begin{array}{c}0.5\\(1,1.5)\end{array}, \frac{y^2}{4}\right] \tag{A.30}$$

where $\mathrm{L}_0(\cdot)$ is the modified Struve function of the first kind of order 0, and $\mathrm{I}_0(\cdot)$ the modified Bessel function of the first kind of order 0. All relations above can be found in Bateman (1953) and Olver (2010).

Case I Closed form expression of the integral in $M(s_*, x_*)$ in case I can be obtained based on its alternative expression for $N(s_*, x_*, m_*)$, see Eqs. 2.38 and 2.50. By rearranging its

integrand using Eqs. A.25 and A.26 and then applying Eq. A.27, we have, at $x_* \leq 1$,

$$\begin{aligned} x_*^{\frac{1}{2}} M\left(s_*, x_*\right) &= 1 - x_*^2 + \frac{2}{s_*}\left[2 + \mathrm{M}_0\left(y_{10}\right) + \mathrm{M}_0\left(y_{20}\right)\right] \\ &+ \frac{2}{\sqrt{s_*}}\left\{x_*\left[\mathrm{M}_1\left(y_{20}\right) + y_{20}\mathrm{F}\left(\frac{y_{20}^2}{4}\right)\right] - x_*\left[\mathrm{M}_1\left(y_{10}\right) + y_{10}\mathrm{F}\left(\frac{y_{10}^2}{4}\right)\right] - \frac{4}{\pi}\right\} \end{aligned} \tag{A.31}$$

and at $x_* \geq 1$,

$$\begin{aligned} x_*^{\frac{1}{2}} M\left(s_*, x_*\right) &= -\frac{2}{s_*}\left[\mathrm{M}_0\left(y_{10}\right) - \mathrm{M}_0\left(y_{20}\right)\right] \\ &\frac{2}{\sqrt{s_*}}\left\{x_*\left[\mathrm{M}_1\left(y_{20}\right) + y_{20}\mathrm{F}\left(\frac{y_{20}^2}{4}\right)\right] - x_*\left[\mathrm{M}_1\left(y_{10}\right) + y_{10}\mathrm{F}\left(\frac{y_{10}^2}{4}\right)\right] - \frac{4}{\pi}\right\} \end{aligned} \tag{A.32}$$

where $y_{10} = \left|1 - x_*\right| s_*^{\frac{1}{2}}$ and $y_{20} = \left(1 + x_*\right) s_*^{\frac{1}{2}}$ and,

$$\mathrm{F}\left(y\right) = \mathrm{F}_{1,2}\left[\begin{array}{c} 0.5 \\ (1, 1.5) \end{array}, y\right] - \frac{2}{\pi} y^{\frac{1}{2}} \mathrm{F}_{2,3}\left[\begin{array}{c} (1,1) \\ (1.5, 1.5, 2) \end{array}, y\right] \tag{A.33}$$

By again rearranging the integrand, explicit expression of the integral $\int_0^1 x_*^{\frac{1}{2}} M\left(s_*, x_*\right) dx_*$ can also be obtained,

$$\int_0^1 x_*^{\frac{1}{2}} M\left(s_*, x_*\right) dx_* = \frac{2}{3} - \frac{4}{\pi\sqrt{s_*}} + \frac{2}{s_*}\left[1 - \mathrm{F}\left(s_*\right)\right] \tag{A.34}$$

B Additional Results for Chapter 3

B.1 Additional Stress and Displacement Fields

In addition to the pore pressure and vertical stress and displacement fields in Section 3.4, here we provide the expressions for the remaining non-trivial stress and displacement fields in the Laplace domain. Asymptotes of the field variables at the undrained and drained states are the same with those in case I, so they will not be shown here. Similar to Section 3.4, two sets of expressions are provided for the field quantities.

B.1.1 Radial Stress

Expression 1

$$\overline{\sigma}_r = \frac{2Ga^3}{c\phi R s_*}\left\{\int_0^1 \left(m_*^2-1\right)\begin{bmatrix} N_{sr1}\left(s_*,r_*,m_*,z_*\right) \\ +N_{sr2}\left(s_*,r_*,m_*,z_*\right)\end{bmatrix} dm_* \right. \\ \left. + \int_1^\infty m_*^{\frac{1}{2}}\theta_1\left(s_*,m_*\right)\begin{bmatrix} N_{sr1}\left(s_*,r_*,m_*,z_*\right) \\ +N_{sr2}\left(s_*,r_*,m_*,z_*\right)\end{bmatrix} dm_*\right\} \tag{B.1}$$

where,

$$N_{sr1}\left(s_*,r_*,m_*,z_*\right) = \frac{2}{\pi}\int_0^\infty \xi_*\left\{\left(z_*\xi_*-1\right)\exp\left(-z_*\xi_*\right)\right. \\ \left. +\frac{2\omega}{1+\omega}\left(\frac{\xi_*^2}{s_*}\right)\left[\frac{\sqrt{\xi_*^2+s_*}}{\xi_*}\exp\left(-z_*\sqrt{\xi_*^2+s_*}\right)-\exp\left(-z_*\xi_*\right)\right]\right\}\cos\left(m_*\xi_*\right)J_0\left(r_*\xi_*\right)d\xi_* \tag{B.2}$$

$$N_{sr2}\left(s_*,r_*,m_*,z_*\right) = -\frac{2}{\pi}\frac{1}{r_*}\int_0^\infty \left\{\left(1-\phi+z_*\xi_*\right)\exp\left(-z_*\xi_*\right)\right. \\ \left. +\frac{2\omega}{1+\omega}\left(\frac{\xi_*^2}{s_*}\right)\left[\frac{\xi_*}{\sqrt{\xi_*^2+s_*}}\exp\left(-z_*\sqrt{\xi_*^2+s_*}\right)-\exp\left(-z_*\xi_*\right)\right]\right\}\cos\left(m_*\xi_*\right)J_1\left(r_*\xi_*\right)d\xi_* \tag{B.3}$$

Expression 2 The second expression for $\overline{\sigma}_r$ can be derived by decomposing $\overline{\sigma}_r$ into $\overline{\sigma}_r = \overline{\sigma}_{r1} + \overline{\sigma}_{r2}$, where $\overline{\sigma}_{r1}$ and $\overline{\sigma}_{r2}$ correspond to the parts containing N_{sr1} and N_{sr2} in Eq. B.1, respectively. On the surface ($z_* = 0$), applying Eq. 2.27 to $\overline{\sigma}_{r1}$ and then the inverse Abel transform gives,

$$\overline{\sigma}_{r1} = \overline{\sigma}_z + \frac{2G\left(2\eta - 1\right)a^3}{\pi c \eta R s_*} \int_{r_*}^{\infty} \left[2\theta_3\left(s_*, x_*\right) - s_* \theta_2\left(s_*, x_*\right)\right] \frac{dx_*}{\sqrt{x_*^2 - r_*^2}} \tag{B.4}$$

Applying Eq. 2.69 to $\overline{\sigma}_{r2}$ and then the inverse Abel transform gives, at $r_* \leq 1$,

$$\begin{aligned} \overline{\sigma}_{r2} = -\frac{2G\left(2\eta - 1\right)a^3}{\pi c \eta R s_*} \Bigg\{ & \int_{r_*}^{1} \left[\begin{array}{c} \theta_1\left(s_*, x_*\right) x_*^{-\frac{1}{2}} + \theta_4\left(s_*, x_*\right) x_*^{-2} \\ + \dfrac{1}{2\eta - 1}\left(x_* - x_*^{-1}\right) \end{array} \right] \frac{dx_*}{\sqrt{x_*^2 - r_*^2}} \\ & + \int_{1}^{\infty} \left[\frac{2\eta}{2\eta - 1} \theta_1\left(s_*, x_*\right) x_*^{-\frac{1}{2}} + \theta_4\left(s_*, x_*\right) x_*^{-2} \right] \frac{dx_*}{\sqrt{x_*^2 - r_*^2}} \Bigg\} \end{aligned} \tag{B.5}$$

and at $r_* \geq 1$,

$$\overline{\sigma}_{r2} = -\frac{2G\left(2\eta - 1\right)a^3}{\pi c \eta R s_*} \int_{r_*}^{\infty} \left[\frac{2\eta}{2\eta - 1} \theta_1\left(s_*, x_*\right) x_*^{-\frac{1}{2}} + \theta_4\left(s_*, x_*\right) x_*^{-2} \right] \frac{dx_*}{\sqrt{x_*^2 - r_*^2}} \tag{B.6}$$

Expressions for $\theta_2\left(s_*, x_*\right)$, $\theta_3\left(s_*, x_*\right)$ and $\theta_4\left(s_*, x_*\right)$ are given in Appendix B.2.

Inside the half space ($z_* > 0$), the alternative expressions for $\overline{\sigma}_r$ and other poroelastic fields from the sections below can be determined using the similar procedures outlined in Section 3.4. They are therefore omitted here.

B.1.2 Tangential Stress

Expression 1

$$\overline{\sigma}_{\theta} = \frac{2Ga^3}{c\phi R s_*} \left\{ \int_0^1 \left(m_*^2 - 1\right) \begin{bmatrix} N_{s\theta 1}\left(s_*, r_*, m_*, z_*\right) \\ -N_{sr2}\left(s_*, r_*, m_*, z_*\right) \end{bmatrix} dm_* \right. \\ \left. + \int_1^{\infty} m_*^{\frac{1}{2}} \theta_1\left(s_*, m_*\right) \begin{bmatrix} N_{s\theta 1}\left(s_*, r_*, m_*, z_*\right) \\ -N_{sr2}\left(s_*, r_*, m_*, z_*\right) \end{bmatrix} dm_* \right\} \tag{B.7}$$

where,

$$N_{s\theta 1}\left(s_*, r_*, m_*, z_*\right) = \frac{2}{\pi} \int_0^{\infty} \xi_* \left[\frac{2\omega}{1+\omega} \frac{\xi_*}{\sqrt{\xi_*^2 + s_*}} \exp\left(-z_* \sqrt{\xi_*^2 + s_*}\right) \right. \\ \left. - (2-\phi) \exp\left(-z_* \xi_*\right) \right] \cos\left(m_* \xi_*\right) J_0\left(r_* \xi_*\right) d\xi_* \tag{B.8}$$

Expression 2 Let $\overline{\sigma}_{\theta} = \overline{\sigma}_{\theta 1} + \overline{\sigma}_{\theta 2}$, where $\overline{\sigma}_{\theta 1}$ and $\overline{\sigma}_{\theta 2}$ are the parts of the equations containing $N_{s\theta 1}$ and N_{sr2} in Eq. B.7, respectively. We have $\overline{\sigma}_{\theta 2} = -\overline{\sigma}_{r2}$. On the surface ($z_* = 0$), applying Eq. 2.27 to $\overline{\sigma}_{\theta 1}$ and then the inverse Abel transform yield,

$$\overline{\sigma}_{\theta 1} = \left(\frac{2-2\eta}{1-2\eta}\right) \overline{\sigma}_z + \frac{2G\left(2\eta - 1\right) a^3}{\pi c \eta R s_*} \left[\left(\frac{2-2\eta}{1-2\eta}\right) \int_{r_*}^{\infty} \theta_3\left(s_*, x_*\right) \frac{dx_*}{\sqrt{x_*^2 - r_*^2}} \right. \\ \left. - \int_{r_*}^{\infty} s_* \theta_2\left(s_*, x_*\right) \frac{dx_*}{\sqrt{x_*^2 - r_*^2}} \right] \tag{B.9}$$

B.1.3 Shear Stress

$$\overline{\sigma}_{zr} = \frac{2Ga^3}{c\phi R s_*} \left[\int_0^1 \left(m_*^2 - 1\right) N_{szr}\left(s_*, r_*, m_*, z_*\right) dm_* \right. \\ \left. + \int_1^{\infty} m_*^{\frac{1}{2}} \theta_1\left(s_*, m_*\right) N_{szr}\left(s_*, r_*, m_*, z_*\right) dm_* \right] \tag{B.10}$$

where,

$$N_{szr}\left(s_*, r_*, m_*, z_*\right) = -\frac{2}{\pi} \int_0^{\infty} \xi_* \left\{ z_* \xi_* \exp\left(-z_* \xi_*\right) \right. \\ \left. + \frac{2\omega}{1+\omega} \left(\frac{\xi_*^2}{s_*}\right) \left[\exp\left(-z_* \sqrt{\xi_*^2 + s_*}\right) - \exp\left(-z_* \xi_*\right) \right] \right\} \cos\left(m_* \xi_*\right) J_1\left(r_* \xi_*\right) d\xi_* \tag{B.11}$$

On the surface ($z_* = 0$), $\overline{\sigma}_{zr} = 0$. The second set expression for shear stress for $z_* > 0$ is omitted here.

B.1.4 Radial Displacement

Expression 1

$$\begin{aligned}\overline{u}_r = \frac{a^4}{c\phi R s_*}\Bigg[&\int_0^1 \left(m_*^2 - 1\right) N_{ur}\left(s_*, r_*, m_*, z_*\right) dm_* \\ &+ \int_1^\infty m_*^{\frac{1}{2}} \theta_1\left(s_*, m_*\right) N_{ur}\left(s_*, r_*, m_*, z_*\right) dm_*\Bigg]\end{aligned} \tag{B.12}$$

where,

$$\begin{aligned}N_{ur}\left(s_*, r_*, m_*, z_*\right) = -\frac{2}{\pi}\int_0^\infty \Bigg\{&\left(1 - \phi + z_*\xi_*\right)\exp\left(-z_*\xi_*\right) \\ + \frac{2\omega}{1+\omega}\left(\frac{\xi_*^2}{s_*}\right)&\left[\frac{\xi_*}{\sqrt{\xi_*^2 + s_*}}\exp\left(-z_*\sqrt{\xi_*^2 + s_*}\right) - \exp\left(-z_*\xi_*\right)\right]\Bigg\}\cos\left(m_*\xi_*\right) J_1\left(r_*\xi_*\right) d\xi_*\end{aligned} \tag{B.13}$$

Expression 2 On the surface ($z_* = 0$), at $r_* \leq 1$,

$$\begin{aligned}\overline{u}_r = -\frac{\left(2\eta - 1\right) a^4 r_*}{\pi c\eta R s_*}\Bigg\{&\int_{r_*}^1 \left[\begin{array}{c}\theta_1\left(s_*, x_*\right) x_*^{-\frac{1}{2}} + \theta_4\left(s_*, x_*\right) x_*^{-2} \\ + \dfrac{1}{2\eta - 1}\left(x_* - x_*^{-1}\right)\end{array}\right]\frac{dx_*}{\sqrt{x_*^2 - r_*^2}} \\ &+ \int_1^\infty \left[\frac{2\eta}{2\eta - 1}\theta_1\left(s_*, x_*\right) x_*^{-\frac{1}{2}} + \theta_4\left(s_*, x_*\right) x_*^{-2}\right]\frac{dx_*}{\sqrt{x_*^2 - r_*^2}}\Bigg\}\end{aligned} \tag{B.14}$$

and at $r_* \geq 1$,

$$\overline{u}_r = -\frac{\left(2\eta - 1\right) a^4 r_*}{\pi c\eta R s_*}\int_{r_*}^\infty \left[\frac{2\eta}{2\eta - 1}\theta_1\left(s_*, x_*\right) x_*^{-\frac{1}{2}} + \theta_4\left(s_*, x_*\right) x_*^{-2}\right]\frac{dx_*}{\sqrt{x_*^2 - r_*^2}} \tag{B.15}$$

B.2 Expressions for $\theta_{2-4}(s,x)$

Functions $\theta_i(s,x)$, $i=2,3,4$, can be evaluated from direct integration of the following integrals,

$$\begin{aligned}\theta_i(s,x) = \omega \Bigg[& \int_0^1 \left(m^2-1\right) N_i(s,x,m)\, dm \\ & + \int_1^\infty m^{\frac{1}{2}} \theta_1(s,m)\, N_i(s,x,m)\, dm \Bigg]\end{aligned} \tag{B.16}$$

where $N_i(s,x,m)$ can be calculated as follows,

$$N_2(s,x,m) = \mathrm{Sign}(x-m)\left[\frac{\mathrm{M}_1(y_1)}{y_1} - \mathrm{M}_0(y_1)\right] + \left[\frac{\mathrm{M}_1(y_2)}{y_2} - \mathrm{M}_0(y_2)\right] \tag{B.17}$$

with $y_1 = |x-m|\, s^{\frac{1}{2}}$ and $y_2 = (x+m)\, s^{\frac{1}{2}}$.

$$\begin{aligned}N_3(s,x,m) = & \mathrm{Sign}(x-m)\, s \left[\frac{2}{\pi y_1} - \mathrm{M}_0(y_1)\left(1+\frac{3}{y_1^2}\right) + \mathrm{M}_1(y_1)\left(\frac{6}{y_1^3}+\frac{2}{y_1}\right)\right] \\ & + s\left[\frac{2}{\pi y_2} - \mathrm{M}_0(y_2)\left(1+\frac{3}{y_2^2}\right) + \mathrm{M}_1(y_2)\left(\frac{6}{y_2^3}+\frac{2}{y_2}\right)\right]\end{aligned} \tag{B.18}$$

$$N_4(s,x,m) = \frac{1+\omega}{\omega}(1-\phi)\,\mathcal{H}(x-m) - N_2(s,x,m) \tag{B.19}$$

B.3 Closed Form Expressions

Closed form expression of the integral in $M(s_*,x_*)$ in case II can be obtained in a similar approach to the derivation for case I, see Appendix A.4. At $x_* \le 1$,

$$x_*^{\frac{1}{2}} M(s_*,x_*) = \frac{2}{\sqrt{s_*}}\left[\mathrm{M}_1(y_{10}) + \mathrm{M}_1(y_{20}) + y_{10} + \frac{4}{\pi}\right] - \frac{2}{s_*}\left[\mathrm{M}_0(y_{10}) + \mathrm{M}_0(y_{20}) + \frac{y_{10}^2}{2} + 2\right] \tag{B.20}$$

and at $x_* \ge 1$,

$$x_*^{\frac{1}{2}} M(s_*,x_*) = \frac{2}{\sqrt{s_*}}\left[\mathrm{M}_1(y_{10}) + \mathrm{M}_1(y_{20}) + \frac{4}{\pi}\right] + \frac{2}{s_*}\left[\mathrm{M}_0(y_{10}) - \mathrm{M}_0(y_{20})\right] \tag{B.21}$$

with $y_{10} = |1 - x_*| \, s_*^{\frac{1}{2}}$ and $y_{20} = (1 + x_*) \, s_*^{\frac{1}{2}}$.

The integral is given by,

$$\int_0^1 x_*^{\frac{1}{2}} M(s_*, x_*) \, dx_* = \frac{2}{3} + \frac{2}{s_*} \left[-1 + \mathrm{M}_0 \left(2\sqrt{s_*} \right) + 2\mathrm{F}(s_*) \right] \tag{B.22}$$

C Additional Results for Chapter 4

C.1 Additional Stress and Displacement Fields

In addition to the pore pressure and vertical stress and displacement fields in Section 4.4, here we provide the expressions for the remaining non-trivial stress and displacement fields in the Laplace domain. Asymptotes of the field variables at the undrained and drained limits are the same with those in case I, so they will not be repeated here. Similar to Section 4.4, two sets of expressions are provided for the field quantities.

C.1.1 Radial Stress

Expression 1

$$\begin{aligned}\overline{\sigma}_r = \frac{2Ga^3}{c\phi R s_*}\Bigg\{ &\int_0^1 \left(m_*^2-1\right)\begin{bmatrix} N_{sr1}\left(s_*,r_*,m_*,z_*\right) \\ +N_{sr2}\left(s_*,r_*,m_*,z_*\right)\end{bmatrix} dm_* \\ &+\int_1^\infty m_*^{\frac{1}{2}}\theta_{1a}\left(s_*,m_*\right)\begin{bmatrix} N_{sr1}\left(s_*,r_*,m_*,z_*\right) \\ +N_{sr2}\left(s_*,r_*,m_*,z_*\right)\end{bmatrix} dm_* \\ &+\int_1^\infty m_*^{\frac{1}{2}} s_*^{\frac{1}{2}}\theta_{1b}\left(s_*,m_*\right)\begin{bmatrix} \widetilde{N}_{sr1}\left(s_*,r_*,m_*,z_*\right) \\ +\widetilde{N}_{sr2}\left(s_*,r_*,m_*,z_*\right)\end{bmatrix} dm_*\Bigg\}\end{aligned} \tag{C.1}$$

where,

$$\begin{aligned}N_{sr1}\left(s_*,r_*,m_*,z_*\right) = \frac{2}{\pi}\int_0^\infty \xi_*\Bigg\{ &\left(z_*\xi_*-1\right)\exp\left(-z_*\xi_*\right) \\ +\frac{2\omega}{1+\omega}\left(\frac{\xi_*^2}{s_*}\right)&\left[\frac{\sqrt{\xi_*^2+s_*}}{\xi_*}\exp\left(-z_*\sqrt{\xi_*^2+s_*}\right)-\exp\left(-z_*\xi_*\right)\right]\Bigg\}\cos\left(m_*\xi_*\right)J_0\left(r_*\xi_*\right)d\xi_*\end{aligned} \tag{C.2}$$

$$\begin{aligned}N_{sr2}\left(s_*,r_*,m_*,z_*\right) = -\frac{2}{\pi}\frac{1}{r_*}\int_0^\infty \Bigg\{ &\left(1-\phi+z_*\xi_*\right)\exp\left(-z_*\xi_*\right) \\ +\frac{2\omega}{1+\omega}\left(\frac{\xi_*^2}{s_*}\right)&\left[\frac{\xi_*}{\sqrt{\xi_*^2+s_*}}\exp\left(-z_*\sqrt{\xi_*^2+s_*}\right)-\exp\left(-z_*\xi_*\right)\right]\Bigg\}\cos\left(m_*\xi_*\right)J_1\left(r_*\xi_*\right)d\xi_*\end{aligned} \tag{C.3}$$

and,

$$\widetilde{N}_{sr1}\left(s_*, r_*, m_*, z_*\right) = -\frac{4\omega}{\pi\left(1+\omega\right)} \int_0^\infty \left(\frac{\xi_*^2}{s_*}\right) \left[\frac{\sqrt{\xi_*^2+s_*}}{\xi_*} \exp\left(-z_*\sqrt{\xi_*^2+s_*}\right) - \exp\left(-z_*\xi_*\right)\right] \sin\left(m_*\xi_*\right) J_0\left(r_*\xi_*\right) d\xi_* \tag{C.4}$$

$$\widetilde{N}_{sr2}\left(s_*, r_*, m_*, z_*\right) = \frac{4\omega}{\pi\left(1+\omega\right)} \frac{1}{r_*} \int_0^\infty \left(\frac{\xi_*}{s_*}\right) \left[\frac{\xi_*}{\sqrt{\xi_*^2+s_*}} \exp\left(-z_*\sqrt{\xi_*^2+s_*}\right) - \exp\left(-z_*\xi_*\right)\right] \sin\left(m_*\xi_*\right) J_1\left(r_*\xi_*\right) d\xi_* \tag{C.5}$$

Expression 2 The second expression for $\overline{\sigma}_r$ can be derived by decomposing $\overline{\sigma}_r$ into $\overline{\sigma}_r = \overline{\sigma}_{r1} + \overline{\sigma}_{r2}$, where $\overline{\sigma}_{r1}$ and $\overline{\sigma}_{r2}$ correspond to the parts containing N_{sr1}, $\widetilde{N}_{sr1}$ and N_{sr2}, $\widetilde{N}_{sr2}$ in Eq. C.1, respectively. On the surface ($z_* = 0$), applying Eq. 2.27 to $\overline{\sigma}_{r1}$ and then the inverse Abel transform gives,

$$\overline{\sigma}_{r1} = \overline{\sigma}_z + \frac{2G\left(2\eta-1\right)a^3}{\pi c\eta R s_*} \int_{r_*}^\infty \left[2\theta_3\left(s_*, x_*\right) - s_*\theta_2\left(s_*, x_*\right)\right] \frac{dx_*}{\sqrt{x_*^2 - r_*^2}} \tag{C.6}$$

Applying Eq. 2.69 to $\overline{\sigma}_{r2}$ and then the inverse Abel transform yields, at $r_* \leq 1$,

$$\overline{\sigma}_{r2} = -\frac{2G\left(2\eta-1\right)a^3}{\pi c\eta R s_*} \left\{ \int_{r_*}^1 \left[\begin{array}{c} \theta_{1a}\left(s_*, x_*\right) x_*^{-\frac{1}{2}} + \theta_4\left(s_*, x_*\right) x_*^{-2} \\ + \dfrac{1}{2\eta-1}\left(x_* - x_*^{-1}\right) \end{array}\right] \frac{dx_*}{\sqrt{x_*^2 - r_*^2}} + \int_1^\infty \left[\frac{2\eta}{2\eta-1}\theta_{1a}\left(s_*, x_*\right) x_*^{-\frac{1}{2}} + \theta_4\left(s_*, x_*\right) x_*^{-2}\right] \frac{dx_*}{\sqrt{x_*^2 - r_*^2}} \right\} \tag{C.7}$$

and at $r_* \geq 1$,

$$\overline{\sigma}_{r2} = -\frac{2G\left(2\eta-1\right)a^3}{\pi c\eta R s_*} \int_{r_*}^\infty \left[\frac{2\eta}{2\eta-1}\theta_{1a}\left(s_*, x_*\right) x_*^{-\frac{1}{2}} + \theta_4\left(s_*, x_*\right) x_*^{-2}\right] \frac{dx_*}{\sqrt{x_*^2 - r_*^2}} \tag{C.8}$$

See Appendix C.2 for the expressions of $\theta_2\left(s_*, x_*\right)$, $\theta_3\left(s_*, x_*\right)$ and $\theta_4\left(s_*, x_*\right)$.

Inside the half space ($z_* > 0$), the alternative expressions for $\overline{\sigma}_r$ and other poroelastic fields

from the sections below can be determined using the similar procedures outlined in Section 4.4. They are therefore omitted here.

C.1.2 Tangential Stress

$$\begin{aligned}\overline{\sigma}_{\theta} = \frac{2Ga^3}{c\phi R s_*}\Bigg\{ & \int_0^1 \left(m_*^2-1\right)\begin{bmatrix} N_{s\theta 1}\left(s_*, r_*, m_*, z_*\right) \\ -N_{sr2}\left(s_*, r_*, m_*, z_*\right)\end{bmatrix} dm_* \\ & + \int_1^{\infty} m_*^{\frac{1}{2}}\theta_{1a}\left(s_*, m_*\right)\begin{bmatrix} N_{s\theta 1}\left(s_*, r_*, m_*, z_*\right) \\ -N_{sr2}\left(s_*, r_*, m_*, z_*\right)\end{bmatrix} dm_* \\ & + \int_1^{\infty} m_*^{\frac{1}{2}} s_*^{\frac{1}{2}}\theta_{1b}\left(s_*, m_*\right)\begin{bmatrix} \widetilde{N}_{s\theta 1}\left(s_*, r_*, m_*, z_*\right) \\ -\widetilde{N}_{sr2}\left(s_*, r_*, m_*, z_*\right)\end{bmatrix} dm_* \Bigg\}\end{aligned} \tag{C.9}$$

where,

$$\begin{aligned}N_{s\theta 1}\left(s_*, r_*, m_*, z_*\right) = \frac{2}{\pi}\int_0^{\infty}\xi_*\Bigg[& \frac{2\omega}{1+\omega}\frac{\xi_*}{\sqrt{\xi_*^2+s_*}}\exp\left(-z_*\sqrt{\xi_*^2+s_*}\right) \\ & -\left(2-\phi\right)\exp\left(-z_*\xi_*\right)\Bigg]\cos\left(m_*\xi_*\right)J_0\left(r_*\xi_*\right)d\xi_*\end{aligned} \tag{C.10}$$

and,

$$\widetilde{N}_{s\theta 1}\left(s_*, r_*, m_*, z_*\right) = -\frac{4\omega}{\pi\left(1+\omega\right)}\int_0^{\infty}\frac{\xi_*}{\sqrt{\xi_*^2+s_*}}\exp\left(-z_*\sqrt{\xi_*^2+s_*}\right)\sin\left(m_*\xi_*\right)J_0\left(r_*\xi_*\right)d\xi_* \tag{C.11}$$

Expression 2 Let $\overline{\sigma}_{\theta} = \overline{\sigma}_{\theta 1} + \overline{\sigma}_{\theta 2}$, where $\overline{\sigma}_{\theta 1}$ and $\overline{\sigma}_{\theta 2}$ are the parts of the equations containing $N_{s\theta 1}$, $\widetilde{N}_{s\theta 1}$ and N_{sr2}, $\widetilde{N}_{sr2}$ in Eq. C.9, respectively. We have $\overline{\sigma}_{\theta 2} = -\overline{\sigma}_{r2}$. On the surface ($z_* = 0$), applying Eq. 2.27 to $\overline{\sigma}_{\theta 1}$ and then the inverse Abel transform yields,

$$\begin{aligned}\overline{\sigma}_{\theta 1} = \frac{2-2\eta}{1-2\eta}\overline{\sigma}_z + \frac{2G\left(2\eta-1\right)a^3}{\pi c\eta R s_*}\Bigg[& \frac{2-2\eta}{1-2\eta}\int_{r_*}^{\infty}\theta_3\left(s_*, x_*\right)\frac{dx_*}{\sqrt{x_*^2-r_*^2}} \\ & -\int_{r_*}^{\infty} s_*\theta_2\left(s_*, x_*\right)\frac{dx_*}{\sqrt{x_*^2-r_*^2}}\Bigg]\end{aligned} \tag{C.12}$$

C.1.3 Shear Stress

Expression 1

$$\begin{aligned}\overline{\sigma}_{zr} = \frac{2Ga^3}{c\phi Rs_*}\Bigg[&\int_0^1 \left(m_*^2-1\right) N_{szr}\left(s_*, r_*, m_*, z_*\right) dm_* \\ &+ \int_1^\infty m_*^{\frac{1}{2}} \theta_{1a}\left(s_*, m_*\right) N_{szr}\left(s_*, r_*, m_*, z_*\right) dm_* \\ &+ \int_1^\infty m_*^{\frac{1}{2}} s_*^{\frac{1}{2}} \theta_{1b}\left(s_*, m_*\right) \widetilde{N}_{szr}\left(s_*, r_*, m_*, z_*\right) dm_*\Bigg]\end{aligned} \tag{C.13}$$

where,

$$\begin{aligned}N_{szr}\left(s_*, r_*, m_*, z_*\right) = -\frac{2}{\pi}\int_0^\infty \xi_* \Bigg\{ &z_*\xi_* \exp\left(-z_*\xi_*\right) \\ +\frac{2\omega}{1+\omega}\left(\frac{\xi_*^2}{s_*}\right)&\left[\exp\left(-z_*\sqrt{\xi_*^2+s_*}\right) - \exp\left(-z_*\xi_*\right)\right]\Bigg\} \cos\left(m_*\xi_*\right) J_1\left(r_*\xi_*\right) d\xi_*\end{aligned} \tag{C.14}$$

and,

$$\begin{aligned}\widetilde{N}_{szr}\left(s_*, r_*, m_*, z_*\right) = \frac{4\omega}{\pi\left(1+\omega\right)}\int_0^\infty \left(\frac{\xi_*^2}{s_*}\right)&\left[\exp\left(-z_*\sqrt{\xi_*^2+s_*}\right)\right. \\ &\left. - \exp\left(-z_*\xi_*\right)\right] \sin\left(m_*\xi_*\right) J_1\left(r_*\xi_*\right) d\xi_*\end{aligned} \tag{C.15}$$

On the surface ($z_* = 0$), $\overline{\sigma}_{zr} = 0$.

C.1.4 Radial Displacement

Expression 1

$$\begin{aligned}\overline{u}_r = \frac{a^4}{c\phi Rs_*}\Bigg[&\int_0^1 \left(m_*^2-1\right) N_{ur}\left(s_*, r_*, m_*, z_*\right) dm_* \\ &+ \int_1^\infty m_*^{\frac{1}{2}} \theta_{1a}\left(s_*, m_*\right) N_{ur}\left(s_*, r_*, m_*, z_*\right) dm_* \\ &+ \int_1^\infty m_*^{\frac{1}{2}} s_*^{\frac{1}{2}} \theta_{1b}\left(s_*, m_*\right) \widetilde{N}_{ur}\left(s_*, r_*, m_*, z_*\right) dm_*\Bigg]\end{aligned} \tag{C.16}$$

where,

$$N_{ur}\left(s_*, r_*, m_*, z_*\right) = -\frac{2}{\pi}\int_0^\infty \left\{ \left(1-\phi+z_*\xi_*\right)\exp\left(-z_*\xi_*\right) \right.$$
$$\left. +\frac{2\omega}{1+\omega}\left(\frac{\xi_*^2}{s_*}\right)\left[\frac{\xi_*}{\sqrt{\xi_*^2+s_*}}\exp\left(-z_*\sqrt{\xi_*^2+s_*}\right)-\exp\left(-z_*\xi_*\right)\right]\right\}\cos\left(m_*\xi_*\right)J_1\left(r_*\xi_*\right)d\xi_* \tag{C.17}$$

and,

$$\widetilde{N}_{ur}\left(s_*, r_*, m_*, z_*\right) = \frac{4\omega}{\pi\left(1+\omega\right)}\int_0^\infty \left(\frac{\xi_*}{s_*}\right)\left[\frac{\xi_*}{\sqrt{\xi_*^2+s_*}}\exp\left(-z_*\sqrt{\xi_*^2+s_*}\right)\right.$$
$$\left. -\exp\left(-z_*\xi_*\right)\right]\sin\left(m_*\xi_*\right)J_1\left(r_*\xi_*\right)d\xi_* \tag{C.18}$$

Expression 2 On the surface ($z_* = 0$), at $r_* \leq 1$,

$$\overline{u}_r = -\frac{\left(2\eta-1\right)a^4 r_*}{\pi c\eta R s_*}\left\{\int_{r_*}^1 \left[\begin{array}{c}\theta_{1a}\left(s_*, x_*\right)x_*^{-\frac{1}{2}}+\theta_4\left(s_*, x_*\right)x_*^{-2}\\ +\frac{1}{2\eta-1}\left(x_*-x_*^{-1}\right)\end{array}\right]\frac{dx_*}{\sqrt{x_*^2-r_*^2}}\right.$$
$$\left. +\int_1^\infty\left[\frac{2\eta}{2\eta-1}\theta_{1a}\left(s_*, x_*\right)x_*^{-\frac{1}{2}}+\theta_4\left(s_*, x_*\right)x_*^{-2}\right]\frac{dx_*}{\sqrt{x_*^2-r_*^2}}\right\} \tag{C.19}$$

and at $r_* \geq 1$,

$$\overline{u}_r = -\frac{\left(2\eta-1\right)a^4 r_*}{\pi c\eta R s_*}\int_{r_*}^\infty\left[\frac{2\eta}{2\eta-1}\theta_{1a}\left(s_*, x_*\right)x_*^{-\frac{1}{2}}+\theta_4\left(s_*, x_*\right)x_*^{-2}\right]\frac{dx_*}{\sqrt{x_*^2-r_*^2}} \tag{C.20}$$

C.2 Expressions of $\theta_{2-4}\left(s, x\right)$

Functions $\theta_i\left(s, x\right)$, $i = 2, 3, 4$, can be evaluated from direct integration of the following integrals.

$$\theta_i\left(s, x\right) = \omega\left[\int_0^1\left(m^2-1\right)N_i\left(s, x, m\right)dm\right.$$
$$+\int_1^\infty m^{\frac{1}{2}}\theta_{1a}\left(s, m\right)N_i\left(s, x, m\right)dm \tag{C.21}$$
$$\left.+\int_1^\infty m^{\frac{1}{2}}\theta_{1b}\left(s, m\right)\widetilde{N}_i\left(s, x, m\right)dm\right]$$

where $N_i(s,x,m)$ and $\widetilde{N}_i(s,x,m)$ can be calculated as follows,

$$N_2(s,x,m) = \text{Sign}(x-m)\left[\frac{\text{M}_1(y_1)}{y_1} - \text{M}_0(y_1)\right] + \left[\frac{\text{M}_1(y_2)}{y_2} - \text{M}_0(y_2)\right] \tag{C.22}$$

$$\widetilde{N}_2(s,x,m) = -\left[\text{M}_1(y_1) - \text{M}_1(y_2)\right] + 2\sqrt{\frac{x_*}{m_* s_*}}\delta(m_* - x_*) \tag{C.23}$$

with $y_1 = |x-m|\, s^{\frac{1}{2}}$ and $y_2 = (x+m)\, s^{\frac{1}{2}}$.

$$\begin{aligned} N_3(s,x,m) = \text{Sign}(x-m)\, s &\left[\frac{2}{\pi y_1} - \text{M}_0(y_1)\left(1+\frac{3}{y_1^2}\right) + \text{M}_1(y_1)\left(\frac{6}{y_1^3}+\frac{2}{y_1}\right)\right] \\ +s &\left[\frac{2}{\pi y_2} - \text{M}_0(y_2)\left(1+\frac{3}{y_2^2}\right) + \text{M}_1(y_2)\left(\frac{6}{y_2^3}+\frac{2}{y_2}\right)\right] \end{aligned} \tag{C.24}$$

$$\begin{aligned} \widetilde{N}_3(s,x,m) = -s &\left[\frac{2}{\pi} - \frac{1}{y_1}\text{M}_0(y_1) + \left(1+\frac{2}{y_1^2}\right)\text{M}_1(y_1)\right] \\ +s &\left[\frac{2}{\pi} - \frac{1}{y_2}\text{M}_0(y_2) + \left(1+\frac{2}{y_2^2}\right)\text{M}_1(y_2)\right] \end{aligned} \tag{C.25}$$

$$N_4(s,x,m) = \frac{1+\omega}{\omega}(1-\phi)\,\mathcal{H}(x-m) - N_2(s,x,m) \tag{C.26}$$

$$\widetilde{N}_4(s,x,m) = \text{M}_1(y_1) - \text{M}_1(y_2) \tag{C.27}$$

D Additional Results for Chapter 5

D.1 Poroelasticity Benchmarks

The FEM algorithm is benchmarked with analytical solutions to the classical poroelasticity problems of Terzaghi, Mandel, Cryer and De Leeuw (Terzaghi, 1943; Mandel, 1953; Cryer, 1963; De Leeuw, 1965; Verruijt, 2013). Given a mechanical load σ and a characteristic dimension ℓ, the pore pressure and temporal and spatial coordinates are normalized according to: $p_* = p/\sigma$, $t_* = tc_v/\ell^2$, and $x_* = x/\ell$, $z_* = z/\ell$ for a rectilinear coordinate system or $r_* = r/\ell$ for a cylindrical or spherical coordinate system. Material properties in the numerical models are chosen to be the same as those in Table 5.1 except the Poisson's ratio; $v = 0$ in the problems of Mandel and De Leeuw and $\nu = 0$, 0.25, 0.45 in Cryer's problem. Poisson's ratio could be arbitrary in modeling Terzaghi's problem. Compressibility of the constituents is not considered in these benchmark comparisons.

D.1.1 Terzaghi's Problem

Terzaghi's 1D consolidation problem corresponds to a sample of thickness h ($\ell = h$), loaded by a constant vertical stress σ at $z = h$ (Terzaghi, 1943). The lower boundary ($z = 0$) is impermeable, while the upper boundary is fully permeable.

Analytical solution for the normalized pore pressure can be expressed as,

$$p_* = \frac{4}{\pi} \sum_{k=1}^{\infty} \frac{(-1)^{k-1}}{2k-1} \cos\left[\frac{\pi}{2}(2k-1)\, z_*\right] \exp\left[-\frac{\pi^2}{4}(2k-1)^2\, t_*\right] \tag{D.1}$$

Fig. D.1 presents the excess pore pressure profile along the depth at various dimensionless times, showing gradual dissipation of pressure as the drainage process proceeds. Numerical results are in excellent agreement with the analytical predictions except for the region near the surface ($z_* \approx 1$), where there is large pressure gradient at very early time ($t_* \approx 0$).

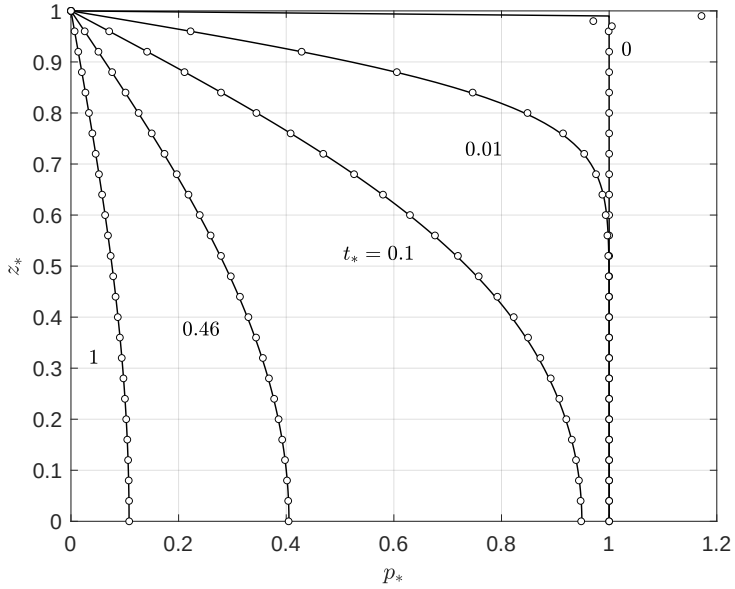

Figure D.1: Pore pressure distribution along the depth at various dimensionless times; comparison of the analytical (lines) and finite element solutions (circles) of Terzaghi's problem.

D.1.2 Mandel's Problem

In this plane strain problem, a rectangular sample is subjected to a constant vertical stress σ at its top, through a rigid and frictionless plate of width $2a$ ($\ell = a$). Drainage is only allowed in the lateral direction. Since both the top and bottom plates are impermeable and frictionless, pore pressure distribution from the center line ($x_* = 0$) to the side ($x_* = 1$) becomes independent of depth (Mandel, 1953; Verruijt, 2013),

$$p_* = \mathcal{L}^{-1}\left[\frac{2m}{s_*}\frac{\cosh\left(\sqrt{s_*}x_*\right) - \cosh\left(\sqrt{s_*}\right)}{\sinh\left(\sqrt{s_*}\right)/\sqrt{s_*} - 2m\cosh\left(\sqrt{s_*}\right)}\right] \tag{D.2}$$

where $m = (1-\nu)/(1-2\nu)$ and s_* is the Laplace variable for t_*.

Distributions of the pore pressure at various times with $\nu = 0$ are shown in Fig. D.2. At the center of the sample, the pore pressure exhibits the so-called Mandel-Cryer effect, where

the pore pressure rises above the initial value before its dissipation. Such an effect can also be observed in Cryer's and De Leeuw's problem shown next.

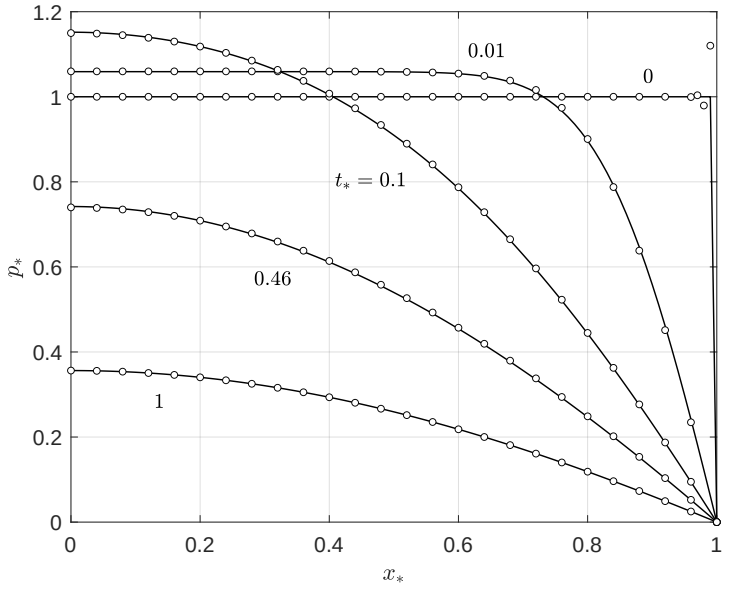

Figure D.2: Pore pressure distribution in the horizontal direction at various dimensionless times; comparison of the analytical (lines) and finite element solutions (circles) of Mandel's problem.

D.1.3 Cryer's Problem

Cryer's problem corresponds to a spherical sample of radius a ($\ell = a$) subjected to a uniform load σ at its fully permeable outer boundary. Immediately when the load is applied, a uniform pore pressure is generated inside the spherical body. After that, since the pore pressure at the outer boundary remains zero, fluid will be drained from the center radially outward to the outer surface. Transient pore pressure at the center can be written as (Cryer, 1963; Verruijt, 2013),

$$p_* = \mathcal{L}^{-1}\left[\frac{m}{2}\frac{\sinh\left(\sqrt{s_*}\right) - \sqrt{s_*}}{(1+ms_*/2)\sinh\left(\sqrt{s_*}\right) - \sqrt{s_*}\cosh\left(\sqrt{s_*}\right)}\right] \tag{D.3}$$

Fig. D.3 shows the comparison of the transient excess pressure at the center of the sphere

between the numerical and analytical solution. The initial pore pressure increase can be explained by noting that at early time, drainage at the outer boundary results in a sharp decrease in the pore pressure at the outer surface, shrinkage of which then leads to pore pressure increase in the core of the sample.

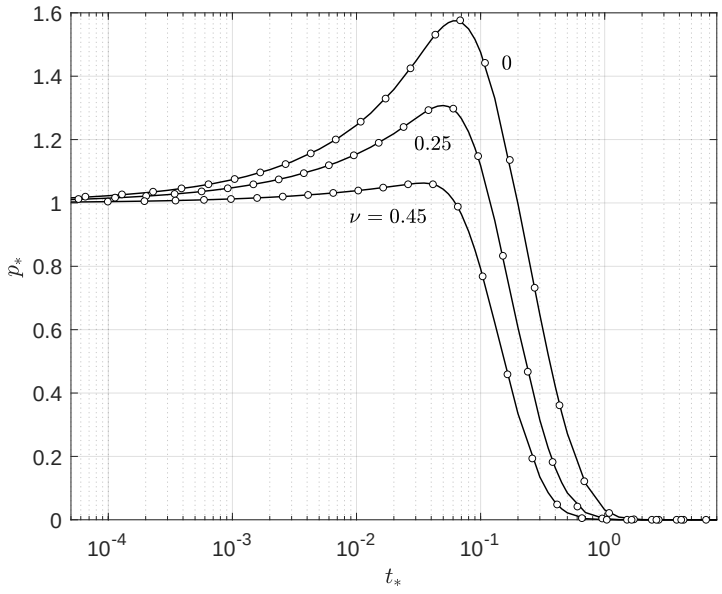

Figure D.3: Evolution of the pore pressure with time at the center of the spherical sample for different Poisson's ratios; comparison of the analytical (lines) and finite element solutions (circles) of Cryer's problem.

D.1.4 De Leeuw's Problem

De Leeuw's problem examines a cylindrical sample of radius a ($\ell = a$) bounded by two rigid, frictionless and impermeable plates. A uniform radial load σ is applied at its outer surface, which is fully drained. Analytical solution for the scaled pore pressure can be expressed as (De Leeuw, 1965; Verruijt, 2013),

$$p_* = \mathcal{L}^{-1}\left[\frac{m}{\sqrt{s_*}}\frac{\mathrm{I}_0\left(\sqrt{s_*}\right) - \mathrm{I}_0\left(\sqrt{s_*}r_*\right)}{m\sqrt{s_*}\mathrm{I}_0\left(\sqrt{s_*}\right) - \mathrm{I}_1\left(\sqrt{s_*}\right)}\right] \tag{D.4}$$

where $\mathrm{I}_n(\cdot)$ is the modified Bessel function of the first kind of order n. Distributions of the pore pressure at various dimensionless times with $\nu = 0$ are shown in Fig. D.4.

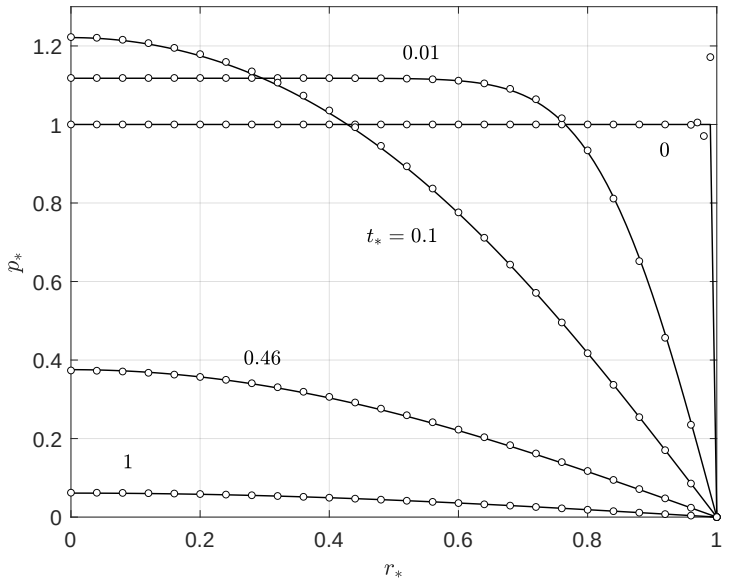

Figure D.4: Distributions of the pore pressure at various dimensionless times; comparison of analytical (lines) and finite element solutions (circles) of De Leeuw's problem.

D.2 Poro-elasto-plastic Consolidation - Strain and Displacement

For the one dimensional poro-elasto-plastic consolidation problem outlined in Section 5.3, after the pore pressure field is known, strain and displacement fields can be derived based on the constitutive and kinematic relations. It should be noted that since instantaneous loading results in a constant initial strain, under general circumstance, the displacement field in a semi-infinite domain is unbounded and not physically meaningful. However, the strain and displacement solutions can still be used for benchmark purposes since the relative displacement is definite for a numerical model of a finite size.

At $t = 0$, since there is not yet any fluid loss from the domain, it follows from Eq. 5.29

that,

$$\varepsilon_{z0} = -\frac{Sp_0}{\alpha} \tag{D.5}$$

For poroelastic consolidation ($\sigma_0 \geqslant \sigma_{ep}$),

$$\varepsilon_{z0e} = -\frac{Sp_{0e}}{\alpha} = \frac{S\sigma_0}{\alpha^2 + SM_e} \tag{D.6}$$

The total strain is,

$$\varepsilon_z = \varepsilon_{z0e} - \frac{\alpha p_{0e}}{M_e}\text{erfc}\left(\frac{z}{2\sqrt{c_{ve}t}}\right) \tag{D.7}$$

At $t \to \infty$, $\varepsilon_z = \sigma_0/M_e$. Displacement u_z can be expressed as,

$$u_z = \varepsilon_{z0e}z - \frac{\alpha p_{0e}u_{*e}}{M_e} + C_1 \tag{D.8}$$

$$u_{*e} = z\text{erfc}\left(\frac{z}{2\sqrt{c_{ve}t}}\right) - 2\sqrt{\frac{c_{ve}t}{\pi}}\exp\left(-\frac{z^2}{4c_{ve}t}\right) \tag{D.9}$$

where C_1 is an integration constant and u_{*e} is the normalized displacement when the constituents are incompressible ($\alpha = 1$, $S = 0$) and is finite.

For the fully plastic scenario ($\sigma_0 \leqslant \sigma_{fp}$), we may consider the instantaneous mechanical load and pore pressure follow the path of elastic loading from 0 to $\sigma_{fp}(p_{fp})$ and then plastic loading to reach $\sigma_0(p_{0p})$, or alternatively elastic loading from 0 to $\sigma_{ep}(0)$ and then plastic loading to reach $\sigma_0(p_{0p})$. These two paths yield identical results. Therefore,

$$\varepsilon_{z0p} = \frac{S}{\alpha^2 + SM_e}\sigma_{fp} + \frac{S}{\alpha^2 + SM_p}\left(\sigma_0 - \sigma_{fp}\right) \tag{D.10}$$

$$\varepsilon_z = \varepsilon_{z0p} - \frac{\alpha p_{0p}}{M_p}\text{erfc}\left(\frac{z}{2\sqrt{c_{vp}t}}\right) \tag{D.11}$$

Displacement u_z can be expressed as,

$$u_z = \varepsilon_{z0p} z - \frac{\alpha p_{0p} u_{*p}}{M_p} + C_2 \tag{D.12}$$

$$u_{*p} = z\text{erfc}\left(\frac{z}{2\sqrt{c_{vp}t}}\right) - 2\sqrt{\frac{c_{vp}t}{\pi}}\exp\left(-\frac{z^2}{4c_{vp}t}\right) \tag{D.13}$$

where C_2 is an integration constant.

For poro-elasto-plastic consolidation ($\sigma_{ep} > \sigma_0 > \sigma_{fp}$), in the plastic zone, instantaneously the pore pressure increases from 0 to p_{0e}. The total strain field can be expressed as,

$$\varepsilon_z = -\frac{Sp_{0e}}{\alpha} + \frac{\alpha\left(\overline{p} - p_{0e}\right)}{M_e} - \frac{\alpha\overline{p}}{M_p} + \left(\frac{\alpha\overline{p}}{M_p}\right)\frac{\text{erf}\left(\dfrac{z}{2\sqrt{c_{vp}t}}\right)}{\text{erf}\left(\sqrt{\beta/c_{vp}}\right)}, \quad z \leqslant \overline{z} \tag{D.14}$$

$$\varepsilon_z = -\frac{Sp_{0e}}{\alpha} + \alpha\left(\frac{\overline{p} - p_{0e}}{M_e}\right)\frac{\text{erfc}\left(\dfrac{z}{2\sqrt{c_{ve}t}}\right)}{\text{erfc}\left(\sqrt{\beta/c_{ve}}\right)}, \quad z > \overline{z} \tag{D.15}$$

The corresponding displacement field for $z \leqslant \overline{z}$ is,

$$u_z = \left[-\frac{Sp_{0e}}{\alpha} + \frac{\alpha\left(\overline{p} - p_{0e}\right)}{M_e} - \frac{\alpha\overline{p}}{M_p}\right] z + \left(\frac{\alpha\overline{p}}{M_p}\right)\frac{z - u_{*p}}{\text{erf}\left(\sqrt{\beta/c_{vp}}\right)} + D_1 \tag{D.16}$$

For $z > \overline{z}$,

$$u_z = -\left(\frac{Sp_{0e}}{\alpha}\right) z + \alpha\left(\frac{\overline{p} - p_{0e}}{M_e}\right)\frac{u_{*e}}{\text{erfc}\left[\sqrt{\beta/c_{ve}}\right]} + D_2 \tag{D.17}$$

Integration constants D_1 and D_2 are related through,

$$\left[\frac{\alpha\left(\overline{p} - p_{0e}\right)}{M_e} - \frac{\alpha\overline{p}}{M_p}\right]\overline{z} + \left(\frac{\alpha\overline{p}}{M_p}\right)\frac{\overline{z} - u_{*p}}{\text{erf}\left(\sqrt{\beta/c_{vp}}\right)} + D_1 = \alpha\left(\frac{\overline{p} - p_{0e}}{M_e}\right)\frac{u_{*e}}{\text{erfc}\left(\sqrt{\beta/c_{ve}}\right)} + D_2 \tag{D.18}$$

D.2.1 Particular Case

In the particular case when the constituents are incompressible, i.e., $\alpha = 1$, $S = 0$, $u_z|_{z\to\infty} = 0$, the displacement fields for the poroelastic and poro-elasto-plastic cases become bounded. The corresponding surface displacement is,

For $\sigma_0 \geqslant \sigma_{ep}$,

$$u_z|_{z=0} = \frac{2p_{0e}}{M_e}\sqrt{\frac{c_{ve}t}{\pi}} \tag{D.19}$$

When $\sigma_{ep} > \sigma_0 > \sigma_{fp}$,

$$u_z|_{z=0} = 2\sqrt{t}\left\{\left(\frac{\overline{p}}{M_p}\right)\frac{\sqrt{c_{vp}/\pi}}{\operatorname{erf}\left(\sqrt{\beta/c_{vp}}\right)}\left[1-\exp\left(-\frac{\beta}{c_{vp}}\right)\right]-\left(\frac{\overline{p}-p_{0e}}{M_e}\right)\left[\sqrt{\frac{c_{ve}}{\pi}}\frac{\exp\left(-\beta/c_{ve}\right)}{\operatorname{erfc}\left(\sqrt{\beta/c_{ve}}\right)}\right]\right\} \tag{D.20}$$